Universität Stuttgart

Motile bacteria in complex environments

Von der Fakultät Mathematik und Physik der Universität Stuttgart genehmigte Abhandlung zur Erlangung der Würde eines Doktors der Naturwissenschaften (Dr. rer. nat.)

vorgelegt von

Christoph Lohrmann

aus Kirchheim unter Teck

Hauptberichter:	Prof. Dr. Christian Holm
Mitberichter:	Prof. Dr. Thomas Speck
Mitberichter:	Prof. Dr. Sujit S. Datta

Tag der mündlichen Prüfung: 2 Juli 2024

Institut für Computerphysik
Universität Stuttgart

16 Juli 2024

I'm afraid I haven't done anything that was practical.

— Donna Strickland, 2018,
Physics Nobel Prize announcement [1].

Contents

1 | Abstract

5 | Publications

9 | Chapter 1
Introduction

1.1 Why bacteria? 9

1.1.1 From a physics perspective 9

1.1.2 From an engineering perspective 13

1.1.3 From a medical perspective 17

1.2 Some biology 18

1.2.1 Bacterial motility 19

1.2.2 Chemotaxis 22

1.2.3 Biofilms 22

1.2.4 Bacteriophages 24

29 | Chapter 2
Theory

2.1 Stochastic dynamics 29

2.1.1 Introduction 29

2.1.2 Langevin dynamics 30

2.1.3 Rotational degrees of freedom 37
2.1.4 Active Brownian motion 42
2.1.5 Numerical methods 45
2.2 Hydrodynamics 51
2.2.1 The Navier-Stokes equation 51
2.2.2 The Stokes equation 54
2.2.3 Multipole expansion 58
2.2.4 Numerical methods: Lattice Boltzmann 61
2.3 Porous media 72

75 Chapter 3
Methods: Modeling of bacteria

3.1 Modeling the cell body 75
3.1.1 Rigid body dynamics: Raspberries 75
3.1.2 Interaction potentials 77
3.2 Bacterial swimming 79
3.2.1 "Dry" swimming 80
3.2.2 "Wet" swimming 80
3.2.3 Run-and-tumble dynamics 81
3.2.4 Application in simulations 85
3.3 Implementation 87

91 Chapter 4
The influence of motility on bacterial accumulation in a microporous channel

4.1 Introduction 91

4.2 Methods 93
4.2.1 Geometry and flow 93
4.2.2 Swimmer model 94
4.3 Results 96
4.3.1 Accumulation behind the obstacle 96
4.3.2 Role of lateral walls on accumulation 103
4.3.3 Influence of swimming characteristics 104
4.3.4 Limits of the coarse-grained bacterial model 106
4.4 Conclusions 107

Chapter 5
109 A novel model for biofilm formation in porous media flow

5.1 Introduction 109
5.2 Methods 111
5.2.1 Cell model 111
5.2.2 Surface attachment 111
5.2.3 Cell growth and division 114
5.2.4 Cell-cell interaction 116
5.3 Results 116
5.3.1 Surface attachment in flow 116
5.3.2 Qualitative biofilm morphologies 120
5.3.3 Determination of model parameters 123
5.3.4 Simulation of biofilm formation in porous media 125

5.4 Conclusions 130

Chapter 6

135 Optimal motility strategies for self-propelled agents to explore porous media

6.1 Introduction 135

6.2 Methods 138

6.2.1 Agent model 138

6.2.2 Motility patterns 138

6.2.3 Porous media model 141

6.2.4 Parameter choice 143

6.3 Results 144

6.3.1 Effective diffusivity 144

6.3.2 Run time variation 153

6.4 Conclusions 156

Chapter 7

159 Influence of bacterial swimming and hydrodynamics on infection by phages

7.1 Introduction 159

7.2 Methods 162

7.2.1 Model for phages and bacteria 163

7.2.2 Model of phage infection 165

7.2.3 Continuum modelling 166

7.2.4 Choice of numerical parameters 167

7.3 Results 170

7.3.1 Flow field 170

7.3.2 Phase infection of the cell body 171
7.3.3 Phage infection of the flagellum 178
7.3.4 Total infection rate 180
7.4 Conclusions 182

Chapter 8
185 Emergence of chemotactic strategies with multi-agent reinforcement learning

8.1 Introduction 185
8.2 Theory 187
8.2.1 Actor-critic reinforcement learning 188
8.2.2 Multi-agent reinforcement learning 190
8.3 Methods 191
8.3.1 RL implementation 191
8.3.2 Agent model 191
8.3.3 Reinforcement learning parameters 194
8.3.4 Actions 195
8.3.5 Computational methods 196
8.4 Results 196
8.4.1 Probability of emergent chemotaxis 196
8.4.2 Learning efficiency 199
8.4.3 Policy efficiency 201
8.4.4 Emergent policies 203
8.5 Conclusion 209

211 Chapter 9
Conclusion and outlook

217 Appendix A
Additional information for results chapters

A.1 Additional information for Chapter 4: The influence of motility on bacterial accumulation in a microporous channel 217

A.1.1 Parameter choice 218

A.2 Additional information for Chapter 5: A novel model for biofilm formation in porous media flow 220

A.2.1 Surface attachment in flow with increased attachment time 221

A.2.2 Parameters for simulations 222

A.3 Additional information for Chapter 6: Optimal motility strategies for self-propelled agents to explore porous media 224

A.4 Additional information for Chapter 7: Influence of bacterial swimming and hydrodynamics on infection by phages 225

A.4.1 Far field decay of the swimming flow field 226

A.4.2 Bacterium and phage model calibration 227

A.4.3 Determination of infection rate 227

A.4.4 Exclusion of finite size and density effects 227
A.4.5 Finite attachment rate 229
A.4.6 Puller swimmers 229
A.5 Additional information for Chapter 8: Emergence of chemotactic strategies with multi-agent reinforcement learning 232
A.5.1 Shape studies 233
A.6 Code and data availability 234
243 Appendix B
Miscellaneous
B.1 Scientific curriculum vitae 243
B.2 Zusammenfassung in deutscher Sprache 244
B.3 Erklärung der Selbständigkeit 250
B.4 Erklärung zur Übereinstimmung der digitalen Version mit der vorgelegten Printversion der Dissertation 250
251 Appendix C
Acknowledgements
255 Bibliography

Abstract

In their natural habitats, bacteria are subject to interactions with complex environments. Complexity can arise from, e.g., confinement in porous media, nontrivial external flow conditions or from other particles that bacteria interact with. This thesis reports the development and application of a numerical model for swimming bacteria in such complex environments

The bacterial model is based on coarse-grained molecular dynamics, resolving the trajectories of individual particles, but abstracting physical interactions to the micrometer scale. Bacteria are represented as rigid rods comprising multiple molecular dynamics particles. Their dynamics are described by physical equations of motion, including interactions with an underlying fluid, with boundaries, or with other particles. When required, hydrodynamic interactions are included using the lattice Boltzmann framework.

Biological detail beyond the physical parameters like shape and mass is described in an equally coarse-grained fashion, seeking to only capture the relevant mechanisms for each application. Swimming is realised by a fictitious driving force counterbalanced by a force on the underlying fluid that mimics the propulsion mechanism. Different motility patterns such as run-and-tumble, run-and-reverse or run-reverse-flick are modelled by changes in propulsion force and steering torque. Attachment to surfaces via (non-

)reversible binding is included through breakable bonds as used in the study of polymers. Cell growth and division is modelled by changes in the configuration of the individual particles that make up the bacterial rod.

The model for bacteria is applied to answer relevant questions in the field of research into motile bacteria: The first question concerns the accumulation of cells and the formation of biofilms, i.e., colonies of growing bacteria, in porous media. "How does external flow influence the initiation and formation of biofilms?" This question has two parts. Complex external flow influences swimming bacteria and determines the locations where bacteria accumulate and attach to surfaces. Once bacteria are attached and start forming a colony by growth and division, external flow exerts viscous forces on the colony that detemine the time evolution and final shape of the biofilm. Both aspects will be covered with our cell model.

The second question stays in the realm of porous media, but concerns confinement that is so strong that it reaches the scale of individual cells. "Which is the optimal motility strategy for a bacterium to efficiently explore a porous environment?" In nature, bacteria use different motility patterns, i.e., temporal sequences of forward swimming and (active) rotation, to explore their surroundings. Depending on the level of confinement, we determine which pattern is optimal for porous media exploration, quantified in terms of an effective diffusion coefficient. Based on the insights gained from this investigation, we propose a new, adaptive strategy that outperforms the fixed patterns found in nature.

The third question increases the level of detail even further, delving into the hydrodynamic interactions on scales below the cell size. "What is the influence of bacterial swimming on the infection process between phages and bacteria?" Phages are viruses that kill bacteria, but need physical contact with their prey to initiate the infection. The flow-field generated by swimming bacteria has an influence on the approach of phages to the cell, because phages are advected by it. Following the footsteps of Berg and Purcell, we use our detailed bacterial model to determine the phage infection rate as a function of swim speed. Going beyond Berg and Purcell, we also cover phages that attach to flagella, finding results that are opposite to those for the cell body and highlight the special importance of hydrodynamic interactions.

As an outlook, we show an example of the combination of machine learning methods and our particle simulations to answer a fundamental question about bacterial behaviour in non-homogeneous environments. "What is the influence of size and speed of bacteria on their ability to perform chemotaxis?" Chemotaxis is the directed motion towards the source of a chemical based on sensory input. Bacteria use certain strategies to bias their swimming motion to direct themselves to more favourable environmental conditions even in the presence of random thermal fluctuations. Our reinforcement learning approach finds well known strategies but also uncovers new ones that can inspire the design of artificial microrobots. Furthermore, we find and physically interpret boundaries in parameter space that separate regions where chemotaxis can be learned and regions where chemotaxis is impossible.

In summary, by contributing to answering the aforementioned questions, we demonstrate the applicability of our physics-rooted model to biological systems. This gives us confidence that the tools and methods developed and applied here can be used for further research into motile bacteria in complex environments.

Publications

▶ Part of the thesis

This thesis is based on the following five publications, all of which are published in peer-reviewed journals.

- M. Lee, C. **Lohrmann**, K. Szuttor, H. Auradou, and C. Holm, "The influence of motility on bacterial accumulation in a microporous channel", Soft Matter **17**, 893 (2021)
- C. **Lohrmann** and C. Holm, "A novel model for biofilm initiation in porous media flow", Soft Matter **19**, 6920 (2023)
- C. **Lohrmann** and C. Holm, "Optimal motility strategies for self-propelled agents to explore porous media", Phys. Rev. E **108**, 054401 (2023)
- C. **Lohrmann**, C. Holm, and S. S. Datta, "Influence of bacterial swimming and hydrodynamics on attachment of phages", Soft Matter **20**, 4795 (2024)
- S. J. Tovey, C. **Lohrmann**, and C. Holm, "Emergence of Chemotactic Strategies with Multi-Agent Reinforcement Learning", Machine Learning: Science and Technology, accepted manuscript (2024). Equal contribution with first author.

▶ Not part of the thesis

During the course of my doctorate, I also contributed to the following publications which are not part of the main text of this thesis.

- A. Wagner, E. Eggenweiler, F. Weinhardt, Z. Trivedi, D. Krach, C. **Lohrmann**, K. Jain, N. Karadimitriou, C. Bringedal, P. Voland, *et al.*, "Permeability Estimation of Regular Porous Structures: A Benchmark for Comparison of Methods", Transport in Porous Media **138**, 1 (2021)

- S. Tovey, F. Zills, F. Torres-Herrador, C. **Lohrmann**, M. Brückner, and C. Holm, "MDSuite: comprehensive post-processing tool for particle simulations", Journal of Cheminformatics **15**, 19 (2023)

- S. Tovey, D. Zimmer, C. **Lohrmann**, T. Merkt, S. Koppenhoefer, V.-L. Heuthe, C. Bechinger, and C. Holm, "Environmental effects on emergent strategy in micro-scale multi-agent reinforcement learning", 2023, arXiv:2307.00994

- S. Tovey, C. **Lohrmann**, T. Merkt, D. Zimmer, K. Nikolaou, S. Koppenhöfer, A. Bushmakina, J. Scheunemann, and C. Holm, "SwarmRL: Building the future of smart active systems", submitted to *Journal of Micro and Bio Robotics*. Equal contribution with first author.

- S. Koppenhöfer, C. **Lohrmann**, and C. Holm, "Phase transition of a lattice of rotating rods in a smart active bath", in preparation

- S. Tovey, L. Aigner, F. Zills, C. **Lohrmann**, M. Fleck, N. Hansen, and C. Holm, "Configuration space exploration through the minimum membership kernel", in preparation

Chapter 1

Introduction

1.1 Why bacteria?

1.1.1 From a physics perspective

This thesis about bacteria was written by a physicist at the institute for computational physics, part of the faculty of mathematics and physics, and will be defended in front of a committee of physicists. The main results were published in physics journals such as the ones published by the American Physical Society. Why are all these physicists interested in bacteria?

I think that anyone who has seen bacteria swimming under a microscope or even in a video recording has felt interest towards the fast moving bugs or has at the very least thought "wow, that looks cool". Beyond basic human curiosity, a more physics-inclined observer in such a situation will immediately feel the urge to quantify, to explain: "How fast do these cells swim?", "By what mechanism do they swim?", "How long will they swim?", "Why do they swim?", "What happens if I put many of them together?", "Why did that one just suddenly change direction?"...

These are the questions that have motivated physics research into bacteria for decades and will continue to puzzle physicists for the decades to come.

▶ Statistical mechanics

Swimming bacteria, seen as abstract particles with interesting properties, have sparked the attention of the statistical mechanics community for a while because they behave fundamentally different from non-motile, "dead", colloidal particles of similar size. Colloids move about randomly due to thermal motion, but are ultimately on their way to equilibrium if their environment allows them to. Bacteria on the other hand are living organisms that take up energy from their environment, for example in the form of nutrients, and use their metabolism to power the cell machinery that can include self-propulsion. Because of the permanent energy conversion in the cell, it will never reach an equilibrium state as long as it is alive. The inherent out-of-equilibrium nature of living matter thus poses a major challenge for its statistical description but also opens new avenues of ongoing research.

The term "active matter" has been coined to cover systems where the non-equilibrium state is not caused by external stimuli, but at the scale of the particles that form the system. It includes all living matter, but also artificial, catalytic systems where chemical reactions provide the energy conversion needed to sustain the inherent non-equilibrium nature of the particle. Of particular interest is microscopic motile active matter, where the particles use energy to fuel a self-propulsion mechanism, such that they perform directed motion on top of thermal agitation.

The ability to self-propel leads to unexpected and counterintuitive phenomena, some of which can be explained in surprisingly simple terms.

Active particles are not bound to Boltzmann statistics, so they can have a non-homogeneous distribution in a constant potential. For example, when confined, active particles accumulate at boundaries, even when the potential in the "allowed" region is constant [13, 14]. This is because their active propulsion drives them forward along their internal direction until they hit a boundary. The driving keeps them at the boundary until a torque or rotational thermal motion orients them away from the surface.

An active Maxwell demon can be constructed from an array of funnels, as experimentally verified with bacteria by Galajda *et al.* [15]. Passive particles will have the same density on both sides of the funnels, because the potential and therefore the position probability density is the same on both sides of the funnels. When active particles encounter a funnel "arm", unlike passive particles, they will glide along it due to their persistent motion. In the forward direction, this will lead them to the funnel opening and they transition to the other side. In the backward direction, they will get stuck at the intersection with the next funnel arm, thus staying on their side of the array of funnels. This leads to an accumulation of active particles on one side of the funnels, showing the non-equilibrium nature of the system.

Both of these examples, among many others (see Ref. [13] for an excellent review), highlight the nontrivial outcomes of interactions between active particles with confining geometries and complex

environments. There are a plethora of other phenomena related to the statistical mechanics of active particles that make bacteria interesting to physicists – e.g., flux rectification [16, 17], motility induced phase separation [18], energetics of active engines [19, 20] and generalised thermodynamics concepts [21, 22] – but I will not discuss them here because they are less relevant to the understanding of the work presented in this thesis. This thesis puts emphasis on the interplay between bacterial motility and complex environments, seeking to elucidate the influence that such environments have on the single cells as well as on their collective behaviour.

▶ Hydrodynamics

Bacteria are not driven by external forces, instead they have to generate the propulsion themselves. The most common propulsion mechanism for bacterial swimming in bulk liquid uses flagella, filamentous appendages connected to a molecular motor. Bacterial flagella typically have a semi-rigid helical shape and are connected to a rotating molecular motor, thus generating forward thrust. The hydrodynamics involved in this mechanism are of great physical interest, and many fundamental questions were tackled over the years: How does the rotation of the flagellum lead to a propulsion force [23, 24]? If there are multiple flagella, how do they coordinate their rotation and not hinder each other [25]? Does the location of the flagella matter [26]? How does motility and the flow-field generated by swimming bacteria influence their interactions with their environment [27]? How does the flow-field generated by swimming bacteria influence other particles or organisms suspended in the same liquid [28]? How does an external flow influence the swim-

ming of motile bacteria [29]?

All these questions fall in the realm of basic physics research but have large implications for bacterial communities in nature and in engineering and medical applications as outlined in the following sections. This thesis will contribute to the last two of the questions posed above, focusing on hydrodynamic interactions between bacteria and their complex environment. A detailed introduction to the hydrodynamics of swimming bacteria will be provided in Section 2.2.

1.1.2 From an engineering perspective

▶ Microscopic engineering

Human inventions take inspiration from nature and so it is not a surprise that a masterpiece of evolution like microscopic motility in the bacterial domain has sparked a lot of interest in the microrobotics community. The goal is to engineer microscopic swimmers that are envisioned to perform tasks in, e.g., medical settings, going back to the idea of "swallowing the doctor" from the famous "plenty of room at the bottom" lecture held by Feynman [30]. Other tasks might be removal of microplastics [31] or water remediation and purification [32].

Artificial swimmers on the micrometer scale can be constructed in many different ways [33]. A common way of classification is by their energy source and propulsion mechanism.

Magnetic micro-swimmers are microscopic particles with a magnetic moment that are driven by external magnetic fields. The magnetic field typically rotates to provide a torque to a helical

particle which then propels forward akin to propulsion of flagellated bacteria [34]. This type of swimmer is technically not *self*-propelled as it relies on the external driving, but this driving allows for great control over the swimming trajectory [35]. This control is crucial for microswimmers to perform their intended task.

There is a variety of artificial micro-swimmers that use chemical energy to propel. In most cases, the swimmer is coated in a catalyst that facilitates the reaction of some fuel on the swimmer surface [24]. The catalyst is typically deposited inhomogeneously on the surface, swimmers are then called "Janus" particles after the two-faced Roman god. The spatially asymmetric reaction leads to an inhomogeneous distribution of (charged) chemical species around the swimmer. A famous example is the Janus particle of Paxton *et al.* [36] that is half-coated in platinum to catalyse the decomposition of hydrogen peroxide. The exact mechanism by which this inhomogeneous distribution leads to propulsion is nontrivial and for some application still subject to scientific debate, but species-specific short range interactions ($\rightsquigarrow$ self-diffusiophoresis [37]) and long range electrostatic forces ($\rightsquigarrow$ self-electrophoresis [38]) certainly play a role.

The concept of chemical inhomogeneity for propulsion is also used for self-thermophoretic swimmers [39] and more exotic mechanisms that rely on demixing of binary mixtures [40]. All these mechanisms have in common that they lead to true self-propulsion generated by the swimmer itself, but that they are usually not bio-compatible because of the fuels or external conditions that are required to sustain directed motion. This limits their applicability

in medical settings.

A type of engineered micro-swimmers that is very different from the ones introduced above does not only imitate biological swimmers, but uses them directly. Genetically modified bacteria can be equipped to use light instead of cellular respiration to generate the power needed for self-propulsion [41]. This gives basic experimental control over the microorganisms, enabling researchers to make bacteria perform tasks like cargo delivery [42], powering of microscopic gears [43], or painting the Mona Lisa [44]. Bacteria can also be combined with man-made objects and used as the motor of such a vessel [45–48]. These approaches make the micro-swimmers applicable in all environments in which bacteria can survive, notably the human body.

A better understanding of bacterial swimming and the interactions between swimming particles and their complex environments can guide the design of future artificial micro-swimmers and provide insights into possible applications in such environments. Therefore, bacteria in general and the basic physics research on bacteria presented in this thesis are of interest to the micro-engineering community.

▶ Macroscopic engineering

Bacteria, especially large agglomerates of them, pose a major challenge in many engineering applications. Porous systems such as filters and pipes are prone to contamination and clogging by bacterial colonies. This causes problems for, e.g., irrigation [49], water purification [50], onsite sewage treatment [51], or ground source heat pumps [52].

However, there are also scenarios where bacteria are very beneficial if not necessary for engineering applications. Probably the largest and most established use of bacteria in engineering is wastewater treatment [53, 54]. There, they are commonly employed to remove organic pollutants, which is especially relevant for sewage treatment.

A newer and less established idea is the use of bacteria for biomineralization in porous environments [55]. Precipitation of Calcite from solution can be induced by enzymatic hydrolysis of urea. Some bacteria like *Sporosarcina pasteurii* and *Brevibacterium ammoniagenes* secrete the enzyme urease that facilitates this hydrolysis and leads to localised mineral deposition around bacterial colonies, if a solution rich in calcium ions and urea is provided [56]. Applications of this microbially induced calcite precipitation (MICP) are manyfold.

In the construction sector, self-healing concrete can be created from a mixture of traditional concrete with bacteria, nutrients and additional calcium [57]. The idea here is that as soon as cracks appear, water seeps into the now more porous concrete and wakes the bacteria from their dry slumber. Then, MICP activity will repair the cracks and restore concrete integrity. MICP can also be used to repair cracks in fractured traditional concrete or other building materials by injection of bacteria and nutrient/calcium/urea solution into the cracks [58]. Visitors of the Forum Romanum can see this technology being used to restore the arch of Septimius Severus [59]. One more application in the construction sector is bioconcrete made with bacteria as a tool for concrete 3D-printing.

Here, complex structures are obtained by first depositing sand and sand-bioconcrete-powder in a predefined manner, then flushing the system with a cementation solution containing calcium ions and urea, and finally removing the un-solidified sand [60].

In environmental settings, MICP is used for soil stabilisation, dust suppression, reservoir sealing and remediation of leakage pathways near wellbores [61–63]. A less environmetally friendly application is MICP for enhanced oil recovery, where precipitates block the preferential flow paths of the injection fluid, causing it to explore more of the porous matrix and thereby removing more oil [64].

The study of bacterial colony growth under complex flow conditions in porous media as presented in this thesis can be used to gain a detailled understanding of the microscopic processes involved in the initial stages of MICP and all other application above. Even though the scope of these applications is at the macroscopic scale, the microscopic dynamics play an important role for the success of use of bacteria in engineering.

1.1.3 From a medical perspective

The group of people that are most interested in bacteria are probably patients and medical practicioners that deal with bacterial infections. About one in eight human deaths are related to bacterial pathogens, making bacterial infections the second-leading cause of death after heart diseases [65]. Therefore, research into bacteria at any scale is relevant for mankind as a whole.

Starting from single (motile) cells entering the body and at-

taching to surfaces, bacterial infections occur in complex, confined environments under the influence of complex fluid flow. Many pathogens form biofilms, i.e., colonies of bacteria, that are much less susceptible to antimicrobial treatment because of the protective layer of extracellular polymeric substances [66, 67]. This is particularly important if biofilms cause chronic infections [68] or form on medical implants [69]. Much like single-cell motion, biofilm formation is subject to constraints imposed by the geometry of the surrounding tissue and potential flow of body fluids.

To better understand the process of infection and thus enable better treatment of diseases, research into the physical mechanisms underlying the interplay between bacteria and their host environment is needed.

1.2 Some biology

Before we delve into the physical, mathematical and numerical tools used to describe and investigate the dynamics of motile bacteria in Chapter 2, we first have to lay a very basic biological foundation. We will not go into details of the fascinating world of microbiology concerned with biochemical processes and genetics inside a cell. Instead, we will focus on the aspects that are relevant to the physical modelling of cells as a whole, which will be presented in the later chapters of this thesis.

1.2.1 Bacterial motility

Bacterial motility comes in many forms and not all of them are related to swimming through bulk liquid. Bacteria can attach to surfaces using pili, cell appendages with adhesins on their ends that bind to specific substrates [70]. These appendages are not fixed in length, but are constructed from building block proteins at the cell membrane to extend them further from the cell [71]. When a pilus has attached (or after some predefined time), the bacterium starts removing building blocks from base, leading to a retraction of the appendage. This "grappling hook" mechanism pulls the cell forward and can lead to sustained motion when the cycle of extension and retraction is repeated. Because bacteria typically have many pili that pull in different directions, this propulsion mechanism leads to a "twitchy" trajectory with random direction changes on the surface.

While surface-bound motility is certainly interesting and reference to pilus-mediated surface attachment is made in the modelling section of this thesis, the main emphasis is on swimming motility by flagellar rotation. Such swimming is common in bacteria and extensively studied experimentally for model organisms like *Escherichia coli*, *Bacillus subtilis* and *Salmonella enterica*.

Flagella are cell appendages much like pili, but to facilitate propulsion, they have a semi-rigid, helical structure, see Fig. 1.1. When rotated, the flagella self-organise to form a coherent bundle which produces forward thrust [23, 72, 73]. They are connected to a molecular motor in the cell membrane with the so called "hook", a flexible segment of the flagellum. The hook acts as a universal

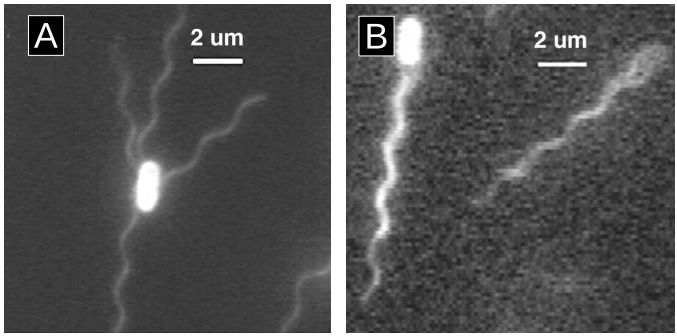

Figure 1.1. Fluorescence microscopy of *E. coli* with stained flagella. A) Dead bacterium with four helical flagella protruding from the cell body. B) Swimming bacteria, the flagella are bundled together behind the cell body. Reproduced from Ref. [74] with permission from the American Society for Microbiology.

joint, allowing the motor to exert a torque on the flagellum even when the flagellar axis is perpendicular to the cell surface.

The flagellar motor is a molecular machine that utilises the proton-motive-force to rotate at very high frequencys of the order of 100 revolutions per second [71, 75–77], with peak rotation rates of 1700 Hz reported in rare cases [78][1]. The bacterium generates an electrochemical gradient of ions (most commonly the namesake H^+, but sometimes also Na^+ or K^+) across its cell membrane such that energy can be harnessed when the ions pass back through the molecular motor. Whenever the ion passes through the stator part of the motor, a torque is generated and the rotor part rotates the flagellum [80, 81]. The energy conversion is estimated to have an

[1] That is a lot faster than the 250 Hz of modern Formula 1 racecar engines [79].

efficiency of 90 % [82]. Usually, the rotor turns in the clockwise direction, but signalling proteins can induce conformational changes in the stator that lead to a reversal of the rotation direction [83].

Some bacteria use this motor reversal switch to achieve more than forward propulsion. When the sense of rotation is reversed, the thrust that the attached flagellum exerts on the cell body is also reversed. If a bacterium has only one flagellum, this can be used to reverse the direction of swimming. If a bacterium has many flagella, the reversal of a single flagellum has more nuanced consequences. When all motors turn in the same direction, hydrodynamic coupling between flagella synchronises the rotation and the flagella form a coherent bundle that produces forward thrust [25]. This mode of swimming is referred to as a "run". When one flagellum rotates in the other direction, it leaves the bundle, disturbs the other flagella and produces thrust in the new direction that it points to [74]. The cell body propels less efficiently and the unbundled flagella exert a torque on it. Thus, the cell rotates, a state that is called "tumbling". Bacteria like *E. coli* switch between the two modes and perform a run-and-tumble motion that results in zig-zag trajectories [84]. The direction of reorientation is random and depends on the location of the counter-rotating flagellum as well as the dynamics of the unbundling of flagella. Despite the randomness, bacteria that can perform tumbing motion have some steering capability and control over their trajectory.

1.2.2 Chemotaxis

Chemotaxis is the directed motion of an organism towards or away from an external chemical stimulus such as a nutrient or a toxin gradient [85–87]. There are other forms of taxis, such as phototaxis, aerotaxis, gravitaxis or thermotaxis, where the stimulus is light, oxygen, gravity or temperature, respectively [88–90]. Chemotaxis is also not unique to bacteria, many other forms of life tax towards chemical stimuli, e.g., sperm towards the egg [91] and some algae towards pheromones [92].

In order to respond to a chemical gradient, bacteria must first sense the gradient. Since relevant gradients are typically very shallow and noisy, and bacteria are very small, they cannot sense a gradient via spatial comparison over their cell body. Therefore, they must resort to temporal sensing and compare chemical concentrations along their trajectory [93].

Bacteria like *E. coli* use the signal of their chemoreceptors to influence their run-and-tumble sequence in order to bias the overall motion. When the signal is positive, run durations are increased, when the signal is negative, run durations are shortened and tumbles become more frequent [94]. Using this strategy, bacteria can navigate towards the source of a nutrient despite only making random direction changes.

1.2.3 Biofilms

As hinted at earlier, biofilms are (sessile, surface-attached) colonies of bacteria, see Ref. [95] for a detailled introduction. They can

consist of a single species, but multi-species biofilms are very common in nature [96]. The colony of bacteria is held together by a matrix of extracellular polymeric substances (EPS), secreted by the bacteria. Bacteria in biofilms are often phenotypically different from free swimming, planktonic bacteria of the same species, where the switch is often related to changes in the environmental conditions like temperature, pH level, nutrient availability or presence of antibiotics [97]. The "biofilm-mode" comes with changes in cell shape, smaller growth rate, loss of motility and, of course, production of EPS.

EPS give the biofilm shape and structural stability against mechanical stresses from, e.g., fluid flowing over the biofilm or attempted mechanical removal. The internal structure can be complex with open channels penetrating the biofilm to give access to nutrients and to enable removal of metabolic products [98]. Biofilms come in many different shapes and forms, and their viscoelastic properties have been widely studied [99, 100].

The EPS matrix does not only provide structural integrity to the biofilm, it also acts as a protective layer against chemical and biological stresses such as antibiotics [67]. Antimicrobials need to diffuse through the biofilm to reach cells deeper in the colony. While doing so, they might get adsorbed to matrix components or cells in the outer layers, reducing penetration. Throughout the biofilm, antimicrobials might also encounter different environments created by bacteria with different access to nutrients. For example, cells on the surface can use an aerobic metabolism while cells deeper in the colony might be anaerobic. The pH might be differ-

ent in certain areas due to metabolic waste products. Cells might be in different growth stages with some bacteria not growing at all. An antimicrobial agent must be able to kill bacteria in *all* these environments and conditions to fully eradicate a biofilm, making it much easier for some bacteria to survive the antibiotic treatment and regrow the full biofilm when the treatment is over.

1.2.4 Bacteriophages

Bacteriophages, often abbreviated to "phages", are viruses that infect and kill bacteria, making them immediately interesting in medical applications [101–104] [2]. As bacteria are ubiquitous in nature, so are phages, with an estimated number of 10^{31} making them the most abundant biological entity on Earth [106, 107]. Locked in an evolutionary arms race, phages have preyed on bacteria for billions of years, coevolving with them in an endless cycle of resistance and counter-resistance [108].

Not technically alive, phages are little more than protein capsules barely large enough to contain their genetic material in the form of RNA or DNA, and a mechanism to bind to bacteria and inject the phage genetic material in the cell (see Fig. 1.2 for an experimental image of phages infecting a bacterial cell). Bacteriophages do not have a metabolism or a means of reproduction on their own, so they rely on hijacking their prey's metabolism to enable the reproduction for them. There are two basic modes of phage infection and reproduction [109]. Lytic phages insert their genetic material

[2] Phages are used in therapy to kill pathogenic bacteria, but some bacteria only become pathogenic when infected by phages [105].

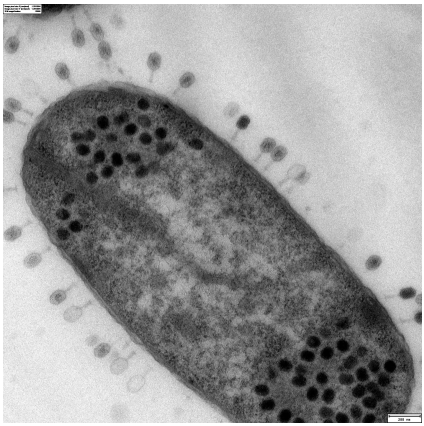

Figure 1.2. T4 bacteriophages infecting an *E. coli* bacterium. A number of phages (small icosahedral capsids with tubular tails) have attached to the cell (large, dark structure). Transmission electron micrograph, reproduced from Ref. [111] with permission of the author.

into a bacterium and force it to produce many new phages before lysing, i.e., destroying their host cell. Lysogenic phages insert their genetic material, but are not immediately harmful. Instead, they integrate their genes into the bacterial chromosome and stay there to be replicated during replication of their host. Some phages even offer benefits to their hosts during this time like protection from superinfection or other resistances against external stresses. At some point however, the phage embedded into the bacterium genome enters a lytic stage, destroying its host[3].

Both replication mechanisms require infection of a host bac-

[3]There is a third mode where the phage does not kill its host in one burst of new phages, but continually produces phage offspring while staying integrated in the host. This "chronic" infection mode seems to be less common [110].

terium, i.e., penetration of the bacterial cell membrane. In a first step, the phage must recognise a suitable host and attach to its surface. To this end, phages are typically equipped with a hollow tail and tail fibers that contain receptor binding proteins which bind specifically to the corresponding receptor on the bacterial cell. These receptors include proteins, sugars and polymers found on the outermost layers of the cell envelope, but also pili or even flagella [112]. Binding can be immediately irreversible or undergo an intermediate, reversible binding state [113]. The tail now penetrates the cell envelope by depolymerising extracellular polysaccharides, thus "drilling" its way to the bacterial cytoplasm [114]. During this process, the phage tail undergoes structural deformation, opening a channel to the capsid. The genetic material is then injected into the cell using the enormous osmotic pressure that the dehydrated DNA or RNA experiences when it is tightly packed in the phage capsid [115]. Finally, phages must overcome the internal defense mechanisms of bacteria such as the now famous CRISPR/Cas system [116] to infect the cell and hijack its metabolism and replication machinery.

As mentioned above, flagella can be receptors for phages, such phages are then called flagellotropic. Phages bind to flagella by wrapping their tail fibers around the flagellum. For infection of the cell, the phages need to reach the cell membrane and inject their genetic material there. Flagella are to small to transport DNA or RNA into the cytoplasm. The mechanism by which phages make their way along the flagellum is akin to the movement of a nut along a bolt [72, 117, 118]. Flagella have a surface structure that

contains helical groves in which the phage's tail fibers come to lie. The phage tail and capsid extend away from the flagellum, so when the flagellum rotates, the phage does not co-rotate at the same frequency due to friction with the surrounding fluid. Like a non-rotating nut on a rotating bolt, the phage is transported to the flagellar base on the cell body where it can complete the infection process.

The process of infection is very involved and much more complex than the basic overview given here. However, it all starts with the physical contact of the phage binding proteins with the receptors on the cell, be it on the cell body or the flagellum. This very fundamental requirement is influenced by the (hydrodynamic) interactions between motile bacteria and the phages that come close to them. A physical description and understanding of these interactions is therefore paramount to an improved understanding of infection of bacteria by phages and all the medical implications that follow from it.

Chapter 2

Theory

2.1 Stochastic dynamics

2.1.1 Introduction

Small particles like bacteria that are suspended in a liquid perform trajectories that appear random when observed through a microscope. This fundamental observation by Robert Brown [119] was explained to be the result of interactions between the invisible molecules of the surrounding liquid and the larger, visible particle [120]. The motion appears random because the fluid molecules cannot be observed and thus only a small subset of the total degrees of freedom that make up the system is accessible to the experimental observer. Although the trajectories are random, we can find a description of the system from which useful information can be extracted. If there are many particles or if particles can be observed over a long time, the specific behaviour of a single particle or the short time dynamics are not the main quantities of interest. Instead, averaged observables are sought after. There are generally two strategies to obtain such averages from a theoretical physicist's

point of view.

First, one can try to find a description where the evolution of a system is described through the time evolution of probability densities describing the state of the system, e.g., the probability density $p(\mathbf{r}, t)$ of finding a particle around location $\mathbf{r}$ at time t. This means averaging out individual particle trajectories to condense the governing physics into a partial differential equation for $p(\mathbf{r}, t)$. From the probability distribution, observables are then obtained by integration [121].

A second approach embraces the stochastic nature of particle motion and seeks to capture realisations of the random process and obtain random trajectories. Observables are then calculated by averaging over such stochastic trajectories. For this thesis, we will focus entirely on the second approach, as it is – in the words of its inventor[1] Paul Langevin – "infinitely more simple" [124, 125].

2.1.2 Langevin dynamics

2.1.2.1 Equation of motion

To describe the dynamics of the position $\mathbf{r}_i$ and velocity $\mathbf{v}_i$ of an isotropic particle i, we use the stochastic Langevin equation of

[1] Louis Bachelier is credited with the invention of stochastic differential equations [122, 123] but he applied them to the French stock market, choosing to invent mathematical finance instead of analysing the motion of particles released from pollen grains in a water droplet.

motion

$$\frac{\mathrm{d}}{\mathrm{d}t}\mathbf{r}_i(t) = \mathbf{v}_i(t), \tag{2.1a}$$

$$m_i\frac{\mathrm{d}}{\mathrm{d}t}\mathbf{v}_i(t) = \mathbf{F}_i^{\mathrm{tot}} = \mathbf{F}_i(\mathbf{r}_i;\{\mathbf{r}_j\}) - \gamma_i^{\mathrm{t}}\mathbf{v}_i(t) + \sqrt{2\gamma_i^{\mathrm{t}}k_{\mathrm{B}}T}\boldsymbol{\xi}_i^{\mathrm{t}}(t). \tag{2.1b}$$

Here, $\mathrm{d}/\mathrm{d}t$ denotes a derivative with respect to time, m the particle mass, $\mathbf{F}^{\mathrm{tot}}$ the total force acting on the particle, $\mathbf{F}_i(\mathbf{r}_i;\{\mathbf{r}_j\})$ a force stemming from interactions between particle i and its environment as well as with other particles j, γ^{t} the translational friction coefficient, $k_{\mathrm{B}} \approx 1.38 \times 10^{-23}\,\mathrm{J\,K^{-1}}$ the Boltzmann constant, T the absolute temperature and $\boldsymbol{\xi}^{\mathrm{t}}(t)$ a random noise term. We introduce the superscript $()^{\mathrm{t}}$ for "translation" to avoid confusion when rotational dynamics are introduced in Section 2.1.3.

Equation (2.1) is very similar to Newton's third law, making it the "natural" extension of deterministic dynamics towards stochastic motion. Langevin made two additions to account for interactions between the particles of interest and the unobserved molecules around them.

The molecules make up a viscous liquid that surrounds the particles which exerts a friction force when the particle moves. For a spherical particle of radius a in a Newtonian fluid with dynamic viscosity μ, the friction coefficient was worked out by Stokes [126], who found

$$\gamma^{\mathrm{t}} = 6\pi\mu a. \tag{2.2}$$

This result was obtained using the continuum description of fluid flow, to which we will return in Section 2.2. From a microscopic

point of view, the friction against particle movement comes from the fact that when the particle moves in one direction, the relative velocity of colliding molecules is larger in the front of the particle than in the back. Consequently, there is a net force resisting the motion.

The second addition is that of the random force $\sqrt{2\gamma_i^{\mathrm{t}} k_{\mathrm{B}} T}\boldsymbol{\xi}_i^{\mathrm{t}}(t)$, which mimics the random impacts of fluid molecules[2]. On average, this force must be zero, i.e.,

$$\left\langle \boldsymbol{\xi}^{\mathrm{t}}(t) \right\rangle = \mathbf{0}. \tag{2.3}$$

Here, the average $\langle\cdot\rangle$ refers to an ensemble average, i.e., an average over many realisations of the random process . The strength of the random force is determined by the prefactor and the correlations of $\boldsymbol{\xi}^{\mathrm{t}}$ given by

$$\left\langle \boldsymbol{\xi}_{i,\alpha}^{\mathrm{t}}(t)\boldsymbol{\xi}_{j,\beta}^{\mathrm{t}}(t') \right\rangle = \delta_{ij}\delta_{\alpha\beta}\delta(t-t'). \tag{2.4}$$

Here, $\boldsymbol{\xi}_{i,\alpha}^{\mathrm{t}}$ denotes component α of the noise of particle i. Equation (2.4) states that the random force is uncorrelated between particles, that it is uncorrelated between directions and that it is uncorrelated in time. The first condition is met if the particles are far enough apart from each other that a molecule impacting particle i does not feel the presence of particle j which might alter

[2]The noise term makes the equation of motion interesting and challenging to physicists concerned with mathematical rigor. What *is* the noise term beyond the two commonly known properties of mean and correlation? How does one define the derivative of a function that has kinks everywhere? We, however, will not worry about such questions and instead rely on using familiar notation to convey the central physical ideas.

the impact dynamics. The second condition is met if the motion of the particle due to the impact from direction α does not change the configuration of the surrounding molecules such that impacts from direction β are affected. The third condition is met if the collision time of the molecules is infinitely short. Of course, there is a finite potential between the particle and the molecules, so there is a finite time associated with the momentum transfer. However, from the perspective of the larger particle, this time is so short that it can be neglected.

The prefactor $\sqrt{2\gamma_i^{\mathrm{t}} k_{\mathrm{B}} T}$ is obtained from requiring that the kinetic energy E_{kin} obey equipartition, i.e., $\langle E_{\mathrm{kin}} \rangle = m \langle \mathbf{v}^2 \rangle / 2 = d k_{\mathrm{B}} T / 2$, where d denotes the number of dimensions (typically $d = 3$). The details to derive the expression for $\langle \mathbf{v}^2 \rangle$ from Eq. (2.1) is worked out in Ref. [127], here we just accept the result and move on.

2.1.2.2 Examples

It is instructive to look at some solutions of Eq. (2.1) for very simple cases (without actually calculating them).

▶ Free particle

For a single particle that isn't subject to any interaction forces, i.e., $\mathbf{F} = \mathbf{0}$, the mean velocity and mean position both remain zero because nothing breaks the symmetry of the system. However, both velocity and position fluctuate around zero. Hence, mean absolute values (or squares) are finite. The mean squared displacement

(MSD) can be obtained analytically [127] and reads

$$\mathrm{MSD}(t) = \left\langle \mathbf{r}^2(t) \right\rangle = 2d\frac{k_\mathrm{B}T}{\gamma^\mathrm{t}}\left[t - \frac{m}{\gamma^\mathrm{t}}\left(1 - \exp\left[-\frac{\gamma^\mathrm{t}}{m}t\right]\right)\right]. \quad (2.5)$$

For small $\frac{\gamma^\mathrm{t}}{m}t$, we expand Eq. (2.5) around $t = 0$ and arrive at

$$\mathrm{MSD}(t \ll m/\gamma^\mathrm{t}) \sim d\frac{k_\mathrm{B}T}{m}t^2. \quad (2.6)$$

The quadratic scaling with t is a signature of ballistic (deterministic) motion like the one generated generated by Newtonian dynamics of a force free particle. There, the position reads $\mathbf{r}(t) = \mathbf{v}_0 t$ with the initial velocity $\mathbf{v}_0$. In our case, we can identify the "initial velocity" with the thermal velocity $v_{th} = \sqrt{\frac{dk_\mathrm{B}T}{m}}$ of our randomly moving particle.

For large $\frac{\gamma^\mathrm{t}}{m}t$, the asymptotic behaviour of Eq. (2.5) is given by

$$\mathrm{MSD}(t \gg m/\gamma^\mathrm{t}) \sim 2d\frac{k_\mathrm{B}T}{\gamma^\mathrm{t}}t. \quad (2.7)$$

The linear scaling with t is a signature of diffusive motion known from, e.g., the squared extent of a dye droplet in water grows linearly with time. We identify the prefactor as the diffusion coefficient

$$D^\mathrm{t} = \frac{k_\mathrm{B}T}{\gamma^\mathrm{t}} \quad (2.8)$$

known from the Einstein-Smoluchowski relation [120, 128].

The time scale separating the ballistic from the diffusive regime is $\tau^\mathrm{t} = \frac{\gamma^\mathrm{t}}{m}$. Below τ^t, momentum plays an important role by carrying a moving particle along its direction of motion. Above τ^t, the motion is determined by noise and friction (and external forces, as we will see in the next example).

▶ Force step

We consider a single particle which is initially at rest with no force applied. At $t = 0$, we switch on a force with constant magnitude F along $\mathbf{e}_x$. Here, we expect a nonzero average velocity along the force direction. Indeed, by applying the ensemble average $\langle\cdot\rangle$ to Eq. (2.1), and solving the resulting ordinary differential equation with $\langle\mathbf{v}\rangle(0) = 0$ as the initial condition, we arrive at

$$\langle\mathbf{v}\rangle(t) = \frac{F}{\gamma^{\mathrm{t}}}\left[1 - \exp\left(-\frac{t}{\tau^{\mathrm{t}}}\right)\right]\mathbf{e}_x. \tag{2.9}$$

This result shows how the particle approaches its terminal velocity $\langle\mathbf{v}\rangle(t \to \infty) = \frac{F}{\gamma^{\mathrm{t}}}\mathbf{e}_x$ exponentially on the time scale $\tau^{\mathrm{t}} = \frac{\gamma^{\mathrm{t}}}{m}$. Again, for short times the velocity increases linearly as expected from the Newtonian dynamics case, while at late times the qualitative physics changes. If the initial setup is reversed, i.e., the particle is dragged by the force F for $t < 0$ and then at $t = 0$ the force is switched off, the general form of the solution remains the same, with the mean velocity decaying exponentially on the time scale τ^{t}.

2.1.2.3 Brownian dynamics

To get an intuition about what Eq. (2.9) means for bacteria, we will plug in some typical numbers. The size scale of bacteria is of the order $a \approx 1\,\mu\mathrm{m}$. Their density is very close to the density $\rho^{\mathrm{water}} \approx 1000\,\mathrm{kg\,m^{-3}}$. Assuming spherical cells and water with $\mu^{\mathrm{water}} \approx 1 \times 10^{-3}\,\mathrm{Pa\,s}$, we can use Eq. (2.2) and get

$$\tau^{\mathrm{t}} = \frac{m}{\gamma^{\mathrm{t}}} = \frac{\frac{4}{3}\pi a^3 \rho^{\mathrm{water}}}{6\pi\mu^{\mathrm{water}} a} \approx 222\,\mathrm{ns}. \tag{2.10}$$

If the bacterium swims at a velocity of $v_{\text{swim}} = 25\,\mu\text{m}\,\text{s}^{-1}$ and the swim force is somehow stopped instantly, the momentum carries the cell for another $\Delta x \sim v_{\text{swim}}\tau^{\text{t}} = 5.55\,\text{pm}$ or about one tenth the atomic radius of hydrogen[3].

This means that when the bacterium experiences a change in force, its mean velocity adapts to the new terminal velocity on an extremely short timescale that is much faster than any of the timescales one is typically interested in when observing bacteria through a microscope for seconds to hours. To reflect this separation of time scales between the change in force ($\sim$ milliseconds to seconds depending on the environment) and the relaxation to the new terminal velocity, we simplify Eq. (2.1b) by setting $m = 0$. This means removing momentum completely from the description and changing τ^{t} from negligibly small to exactly zero.

By removing the left hand side from Eq. (2.1b), we can directly solve for $\mathbf{v}$ and arrive at the equation of motion for so called "overdamped Langevin" or "Brownian" dynamics

$$\frac{\mathrm{d}}{\mathrm{d}t}\mathbf{r}_i = (\gamma_i^{\text{t}})^{-1}\mathbf{F}_i(\mathbf{r}_i;\{\mathbf{r}_j\}) + \sqrt{2(\gamma_i^{\text{t}})^{-1}k_{\text{B}}T}\boldsymbol{\xi}_i^{\text{t}}(t). \tag{2.11}$$

To avoid confusion, Eq. (2.1) is then referred to as "underdamped Langevin" dynamics.

Equation (2.11) preserves the long time behaviour of Eq. (2.1). We can calculate the mean squared displacement of a single, force free Brownian particle with less tedious math than in the under-

[3] Of course, on this length and time scale, a description of particle dynamics using Eq. (2.11) must break down. Still, these extreme numbers show that momentum is a non-factor for bacteria.

damped case and obtain

$$\mathrm{MSD}(t) = 2d\frac{k_\mathrm{B}T}{\gamma^\mathrm{t}}t. \tag{2.12}$$

Here, the MSD is always linear in time, as expected from setting $\tau^\mathrm{t} = 0$.

2.1.3 Rotational degrees of freedom

Most bacteria are not isotropic in shape, i.e., not spherical. Many bacteria have rod-shaped cell bodies and even spherical bacteria might have cell appendages that make them non-isotropic. For this reason, anisotropy must be included in Eqs. (2.1) and (2.11), and the rotational degrees of freedom must be explicitly tracked.

Particle anisotropy matters for the translational dynamics of the particle because for nonspherical shapes, the friction along different directions is not equal.[4] Consider for example a cylindrical object in a viscous liquid, e.g., a very blunt knife in honey. Pulling it in and out of the honey along its symmetry axis will be much easier than stirring the honey by moving it in a perpendicular direction where the cross section is much larger. To capture the direction-dependent friction, we replace the scalar friction coefficient $\gamma^\mathrm{t} \in \mathbb{R}_+$ by a tensorial friction coefficient $\gamma^\mathrm{t} \in \mathbb{R}_+^{d\times d}$. The entries of the friction matrix can be obtained by measuring anisotropic diffusion coefficients in experiments or by theoretical

[4] There are many cases in which the rotational dynamics is relevant even for spherical particles where the friction coefficient is equal in all directions. Think for example of particles with an internal magnetic dipole moment or with an anisotropic density distribution.

calculations in the framework of continuum hydrodynamics, see Section 2.2.3.1. This is, however, not the only difficulty, since γ^{t} is only a constant in the frame of reference of each particle. Because the particle rotates, γ^{t} in the labratory frame, in which Eqs. (2.1) and (2.11) are formulated, is now a function of time through its dependence on the rotation state. The resulting difficulties for solving Eqs. (2.1) and (2.11) numerically will be briefly discussed in Section 2.1.5.

The rotation state of a general anisotropic particle in three dimensions is described with three degrees of freedom, e.g., the two angles describing a main axis in spherical coordinates and an additional angle describing the rotation of the particle around that axis. For this thesis however, we will focus only on particles that have cylindrical symmetry around one axis, e.g., rod-shaped bacterial cells. This symmetry decreases the number of relevant rotational degrees of freedom from three to two. These can be either expressed as two angles or as a normalised vector $\hat{\mathbf{e}}$ pointing along the symmetry axis. The particle direction $\hat{\mathbf{e}}$ takes a similar role to the particle position $\mathbf{r}$, but for its rotational state. In the underdamped Langevin picture it evolves according to

$$\frac{\mathrm{d}}{\mathrm{d}t}\hat{\mathbf{e}}_i(t) = \boldsymbol{\omega}_i(t) \times \hat{\mathbf{e}}_i(t), \tag{2.13a}$$

$$\begin{aligned}\frac{\mathrm{d}}{\mathrm{d}t} I_i \boldsymbol{\omega}_i(t) &= \mathbf{M}_i^{\mathrm{tot}} \\ &= \mathbf{M}_i(\mathbf{r}_i, \hat{\mathbf{e}}_i; \{\mathbf{r}_j\}, \{\hat{\mathbf{e}}_j\}) - \gamma_i^{\mathrm{r}} \boldsymbol{\omega}_i(t) + \sqrt{2\gamma_i^{\mathrm{r}} k_{\mathrm{B}} T}\, \boldsymbol{\xi}_i^{\mathrm{r}}(t),\end{aligned} \tag{2.13b}$$

where $\boldsymbol{\omega}$ denotes the angular velocity, I the moment of inertia (tensor), $\mathbf{M}_i(\mathbf{r}_i, \hat{\mathbf{e}}_i; \{\mathbf{r}_j\}, \{\hat{\mathbf{e}}_j\})$ the interaction torque that depends

on all positions and directions of the particles[5], γ^{r} the rotational friction (tensor) and $\boldsymbol{\xi}^{\mathrm{r}}$ a rotational noise term with the same properties as its translational counterpart $\boldsymbol{\xi}^{\mathrm{t}}$, see Eqs. (2.3) and (2.4).

For some simple shapes, the rotational friction coefficient γ^{r} can be worked out analytically. For a sphere, one obtains [129]

$$\gamma^{\mathrm{r}} = 8\pi\mu a^3. \tag{2.14}$$

As for the translational case, a rotational diffusion coefficient D^{r} can be defined and linked to the rotational friction via the Einstein-Smoluchowski relation

$$D^{\mathrm{r}} = \frac{k_{\mathrm{B}}T}{\gamma^{\mathrm{r}}}. \tag{2.15}$$

The rotational diffusion coefficient has units of 1/[time]. Comparing to the translational friction coefficient with units of [length]^2/[time], we see that we implicitly ignore units of [angle]. All angles are to be measured in radians unless stated otherwise.

2.1.3.1 Examples

Equation (2.13) has the same structure as Eq. (2.1), except that $\hat{\mathbf{e}}$ is a variable that only exists on the unit sphere instead of the entire space. We will therefore skip the discussion of a "mean squared rotation". We can, however, discuss the

[5] When Eq. (2.1) is extended to anisotropic particles, the force also becomes dependent on all particle orientations.

▶ Torque step

Consider a single particle that has initially no angular velocity and there is no torque applied. At $t = 0$, we switch on a torque of magnitude M along $\mathbf{e}_x$. If the particle is isotropic, i.e., both I and γ^{r} can be reduced to scalars, we can solve the differential equation for $\langle \boldsymbol{\omega} \rangle$ analogous to the translational case and obtain

$$\langle \boldsymbol{\omega} \rangle (t) = \frac{M}{\gamma^{\mathrm{r}}} \left[1 - \exp\left(-\frac{t}{\tau^{\mathrm{r}}} \right) \right] \mathbf{e}_x. \tag{2.16}$$

Here, $\tau^{\mathrm{r}} = \frac{I}{\gamma^{\mathrm{r}}}$ is the crossover time between angular momentum-driven motion and random rotational motion. It is also the timescale on which particles adapt their angular velocity to a change in torque acting on them.

2.1.3.2 Rotational Brownian dynamics

Using Eq. (2.14) with $I = \frac{2}{5} m a^2 = \frac{8}{15} \pi \rho^{\mathrm{water}} a^5$ for a solid sphere with $a = 1\,\mu\mathrm{m}$ and the density of water, we obtain $\tau^{\mathrm{r}} \approx 75\,\mathrm{ns}$ for $\mu = \mu^{\mathrm{water}}$. As for the translational case, this time scale is far removed from the time scales we are generally interested in. It seems natural to again simplify the equations of motion by neglecting the inertial term proportional to the moment of inertia I:

$$\begin{aligned} \frac{\mathrm{d}}{\mathrm{d}t} \hat{\mathbf{e}}_i(t) = & \left[(\gamma_i^{\mathrm{r}})^{-1} \mathbf{M}_i(\mathbf{r}_i, \hat{\mathbf{e}}_i; \{\mathbf{r}_j\}, \{\hat{\mathbf{e}}_j\}) + \sqrt{2 (\gamma_i^{\mathrm{r}})^{-1} k_{\mathrm{B}} T} \boldsymbol{\xi}_i^{\mathrm{r}}(t) \right] \\ & \times \hat{\mathbf{e}}_i(t). \end{aligned} \tag{2.17}$$

However, some caveats with respect to Eq. (2.16) have to be kept in mind, because they carry over to the validity of Eq. (2.17).

Stable rotation around the axis along which the torque is applied with terminal angular velocity M/γ^{r} is only possible when the different rotation axes do not couple. This is only the case when both I and γ^{r} can be written as multiples of the unity matrix in d dimensions, i.e., when the particle is spherical with an isotropic density. In all other cases, torque along one axis will also result in rotation around the other axes without a well-defined terminal angular velocity, making the simplification of Eq. (2.13) to Eq. (2.17) unjustified.

For free rotational Brownian motion ($\mathbf{M} = \mathbf{0}$), the (de)correlation

$$\langle \hat{\mathbf{e}}(0) \cdot \hat{\mathbf{e}}(t) \rangle = \exp\left(-\frac{2k_{\mathrm{B}}T}{\gamma^{\mathrm{r}}} t \right) \tag{2.18}$$

of the particle direction can be obtained analytically [130][6]. This equation states that the correlation between the particle direction at time t and its initial direction at $t = 0$ decays exponentially on the time scale

$$\tau^{\mathrm{r}}_{\mathrm{corr}} = \frac{\gamma^{\mathrm{r}}}{2k_{\mathrm{B}}T} = \frac{1}{2D^{\mathrm{r}}}. \tag{2.19}$$

This time scale $\tau^{\mathrm{r}}_{\mathrm{corr}}$ is not to be confused with τ^{r}. The latter relates to the crossover from inertia-driven motion to noise-dominated motion, the former relates to the time that a particle keeps its direc-

[6] Equation (2.17) looks simple and the solution Eq. (2.18) looks very simple, too. However, unlike in the translational case where one can get away with a lot of "intuitive" application of stochastic calculus, the *multiplication* of $\hat{\mathbf{e}}$ and $\boldsymbol{\xi}^{\mathrm{r}}$ in Eq. (2.17) instead of *addition* like in Eq. (2.11) comes with a lot of mathematical intricacy. Thus, in the stochastic dynamics framework, Eq. (2.18) can only be obtained using the rigorous machinery of stochastic calculus [131, p. 104].

tion in the presence of rotational noise.

2.1.4 Active Brownian motion

As introduced in Section 1.2.1, the bacteria of interest for this thesis have the ability to self-propel. The propulsion mechanisms are often complex and rely on hydrodynamic coupling to the underlying fluid. Here however, as a first approximation, we treat bacteria in the framework of Langevin dynamics without explicit consideration of hydrodynamic effects. This picture will be extended in the subsequent sections.

2.1.4.1 Equations of motion

Propulsion is modelled by the addition of a swim force F_{swim} that implicitly captures self-propulsion. The underdamped Langevin equation becomes

$$\frac{\mathrm{d}}{\mathrm{d}t}\mathbf{r}_i(t) = \mathbf{v}_i(t), \tag{2.20a}$$

$$m_i\frac{\mathrm{d}}{\mathrm{d}t}\mathbf{v}_i(t) = \mathbf{F}_i + F_{\mathrm{swim}}(t)\hat{\mathbf{e}}_i(t) - \gamma_i^{\mathrm{t}}\mathbf{v}_i(t) + \sqrt{2\gamma_i^{\mathrm{t}}k_{\mathrm{B}}T}\boldsymbol{\xi}_i^{\mathrm{t}}(t) \tag{2.20b}$$

with its overdamped counterpart

$$\frac{\mathrm{d}}{\mathrm{d}t}\mathbf{r}_i = (\gamma_i^{\mathrm{t}})^{-1}\left[\mathbf{F}_i + F_{\mathrm{swim}}(t)\hat{\mathbf{e}}_i(t)\right] + \sqrt{2(\gamma_i^{\mathrm{t}})^{-1}k_{\mathrm{B}}T}\boldsymbol{\xi}_i^{\mathrm{t}}(t). \tag{2.21}$$

Here, F_{swim} is the force that leads to a terminal swim velocity $v_{\mathrm{swim}} = (\gamma^{\mathrm{t}})^{-1}F_{\mathrm{swim}}$. We keep an explicit time dependence of $F_{\mathrm{swim}}(t)$, because later we will simulate bacteria that can turn off

their swimming motion or reverse the swim direction. Versions of Eqs. (2.20) and (2.21) are known as the equations of motion for a so called *Active Brownian Particle* (ABP) [132]. In literature, typically the two-dimensional overdamped equation of motion with constant F_{swim} is applied.

Equations (2.20) and (2.21) show the necessity of considering rotational degrees of freedom for active particles even if they are isotropic in shape. Translational motion depends on the rotation state because the particle propels along its internal direction $\hat{\mathbf{e}}_i(t)$, breaking the isotropy.

Some bacteria cannot only self-propel but also self-steer, i.e., generate an torque that leads to active rotation. We will incorporate this form of activity in the same way as for translation by extending Eqs. (2.13) and (2.17) to

$$\frac{\mathrm{d}}{\mathrm{d}t}\hat{\mathbf{e}}_i(t) = \boldsymbol{\omega}_i(t) \times \hat{\mathbf{e}}_i(t), \tag{2.22a}$$

$$\frac{\mathrm{d}}{\mathrm{d}t} I_i \boldsymbol{\omega}_i(t) = \mathbf{M}_i + M_{\mathrm{act}}(t)\hat{\mathbf{n}}_i(t) - \gamma_i^{\mathrm{r}}\boldsymbol{\omega}_i(t) + \sqrt{2\gamma_i^{\mathrm{r}} k_{\mathrm{B}} T}\,\boldsymbol{\xi}_i^{\mathrm{r}}(t), \tag{2.22b}$$

for the underdamped case and

$$\frac{\mathrm{d}}{\mathrm{d}t}\hat{\mathbf{e}}_i(t) = \left[(\gamma_i^{\mathrm{r}})^{-1}\left(\mathbf{M}_i + M_{\mathrm{act}}(t)\hat{\mathbf{n}}_i(t)\right) + \sqrt{2(\gamma_i^{\mathrm{r}})^{-1} k_{\mathrm{B}} T}\,\boldsymbol{\xi}_i^{\mathrm{r}}(t)\right] \times \hat{\mathbf{e}}_i(t). \tag{2.23}$$

for the overdamped case. Here, M_{act} is the active torque that leads to rotation with terminal angular velocity $\omega_{\mathrm{act}} = (\gamma^{\mathrm{r}})^{-1} M_{\mathrm{act}}$ and $\hat{\mathbf{n}}_i(t)$ is a vector orthogonal to $\hat{\mathbf{e}}_i(t)$ that sets the direction of active rotation.

2.1.4.2 Mean squared displacement

To gain an intuition about the effect of swimming, we discuss the mean squared displacement of a free, overdamped active Brownian particle. Using Eq. (2.18) in $d = 3$ dimensions, one obtains [133]

$$\mathrm{MSD}^{\mathrm{ABP}}(t) = 6D^{\mathrm{t}}t + 2v_{\mathrm{swim}}^2(\tau_{\mathrm{corr}}^{\mathrm{r}})^2 \left[\exp\left(-\frac{t}{\tau_{\mathrm{corr}}^{\mathrm{r}}}\right) - \left(1 - \frac{t}{\tau_{\mathrm{corr}}^{\mathrm{r}}}\right)\right]. \tag{2.24}$$

On short time scales, it behaves as

$$\mathrm{MSD}^{\mathrm{ABP}}(t \to 0) \sim 6D^{\mathrm{t}}t + v_{\mathrm{swim}}^2 t^2. \tag{2.25}$$

This means that there is a linear regime for $t \lesssim 6D^{\mathrm{t}}/v_{\mathrm{swim}}^2$ in which translational Brownian motion dominates[7]. This regime is followed by a quadratic, i.e., ballistic, regime, in which the MSD is characterised by motion along the particle direction $\hat{\mathbf{e}}$ with velocity equal to the swim speed. For large $t \gg \tau_{\mathrm{corr}}^{\mathrm{r}}$, $\hat{\mathbf{e}}$ decorrelates and the MSD goes back to linear with

$$\mathrm{MSD}^{\mathrm{ABP}}(t \to \infty) \sim 2\left[3D^{\mathrm{t}} + v_{\mathrm{swim}}^2 \tau_{\mathrm{corr}}^{\mathrm{r}}\right] t. \tag{2.26}$$

The form of Eq. (2.26) allows us to identify an effective diffusion coefficient

$$D_{\mathrm{eff}}^{\mathrm{t}} = D^{\mathrm{t}} + \frac{v_{\mathrm{swim}}^2 \tau_{\mathrm{corr}}^{\mathrm{r}}}{3} \tag{2.27}$$

that governs the long-time behaviour.

Plugging in values for a spherical bacterium with radius $a =$

[7] If we had solved for the MSD of an underdamped active Brownian particle, we would have obtained a quadratic regime at even shorter timescales due to particle inertia.

1 µm swimming with $v_{\mathrm{swim}} = 25\,\mu\mathrm{m\,s^{-1}}$ in water at room temperature $T = 300\,\mathrm{K}$, we obtain

$$D^{\mathrm{t}} = 0.22\,\mu\mathrm{m^2\,s^{-1}} \ll 632\,\mu\mathrm{m^2\,s^{-1}} = \frac{v_{\mathrm{swim}}^2 \tau_{\mathrm{corr}}^{\mathrm{r}}}{3}. \tag{2.28}$$

The effective diffusion coefficient is dominated by the active contribution and typically orders of magnitude larger than the thermal diffusion coefficient. Active particles are thus very effective at exploring space due to their persistent motion.

The crossover between ballistic motion at intermediate timescales and the effective diffusion coefficient at long timescales are determined by the *rotational* correlation time $\tau_{\mathrm{corr}}^{\mathrm{r}}$, again highlighting the special importance of rotational degrees of freedom for active particles. The crossover time $\tau_{\mathrm{corr}}^{\mathrm{r}}$ separates the regime where the particle moves along its director more or less ballistically from the regime where it wanders around randomly, but still very fast. The associated length scale

$$l_{\mathrm{p}} = v_{\mathrm{swim}} \tau_{\mathrm{corr}}^{\mathrm{r}} \tag{2.29}$$

is called the *persistence length*. Interesting, non-equilibrium behaviour is expected whenever a length scale in the system (mean particle distance, size of confinement, ...) becomes comparable to l_{p}.

2.1.5 Numerical methods

2.1.5.1 Solving Newton's equation of motion: The velocity Verlet algorithm

Since the Langevin equation is based on Newton's equation of motion, we will start discussing numerical methods with a section on how to solve the latter. Considering only translation, but already including forces that depend on velocities (e.g., the Lorentz force in a magnetic field, later the Langevin friction), the problem is given by

$$m_i \frac{\mathrm{d}^2}{\mathrm{d}t^2}\mathbf{r}_i = \mathbf{F}_i(\mathbf{r}_i, \mathbf{v}_i, \{\mathbf{r}_j, \mathbf{v}_j\}, t). \tag{2.30}$$

There are many ways to solve this ordinary differential equation numerically. Here, we will only describe the one that was used to generate the results in this thesis: The velocity Verlet algorithm as implemented in the ESPResSo [134] simulation package.

The algorithm applies the following steps repeatedly to an initial condition $\mathbf{r}(0)$ and $\mathbf{v}(0)$

1. Calculate velocity at the half step

$$\mathbf{v}(t + \delta t/2) = \mathbf{v}(t) + \frac{\mathbf{F}(\mathbf{r}(t), \mathbf{v}(t - \delta t/2), t)}{m}\frac{\delta t}{2} \tag{2.31}$$

2. Calculate new position

$$\mathbf{r}(t + \delta t) = \mathbf{r}(t) + \mathbf{v}(t + \delta t/2)\delta t \tag{2.32}$$

3. Calculate new velocity

$$\mathbf{v}(t + \delta t) = \mathbf{v}(t + \delta t/2) + \frac{\mathbf{F}(\mathbf{r}(t + \delta t), \mathbf{v}(t + \delta t/2), t + \delta t)}{m}\frac{\delta t}{2} \tag{2.33}$$

Here, δt is the time step of the numerical integration. In the algorithm description, we have omitted the particle indices for clarity, read $\mathbf{r}$ and $\mathbf{v}$ as the position and velocity coordinates of all particles.

The velocity Verlet algorithm is second order accurate in time, i.e., the global truncation error scales as $\mathcal{O}\left(\delta t^2\right)$ for small δt. There are more accurate integration schemes readily available, but for many-particle dynamics, integration speed is often more important than integration accuracy. This is because usually the exact trajectory of each particle is not the quantity of interest but rather an average over many trajectories with random starting conditions. Velocity Verlet is a common choice because it only requires one force calculation per time step (the force calculated for Eq. (2.33) can be reused for Eq. (2.31) in the next step). It also (almost) conserves energy [135, p.72], which makes it very attractive for long simulations.

2.1.5.2 Including noise

The extension from Newtonian to Langevin dynamics does not change the structure of Eq. (2.30), it just adds two terms to the force on each particle. Friction is readily included because the velocities are known. Incorporating the noise term $\boldsymbol{\xi}^{\mathrm{t}}(t)$ is a bit more tricky, because we can't have delta distributions in the time-discretised numerical algorithm. The problem is solved by realising that the shortest time over which a force can act is δt, so we replace the delta-correlation $\left\langle \boldsymbol{\xi}_\alpha^{\mathrm{t}}(t)\boldsymbol{\xi}_\beta^{\mathrm{t}}(t')\right\rangle = \delta_{\alpha,\beta}\delta(t-t')$ by a rectangular

correlation $\left\langle \boldsymbol{\xi}^{\mathrm{t}}_{\alpha}(t)\boldsymbol{\xi}^{\mathrm{t}}_{\beta}(t')\right\rangle = \delta_{\alpha,\beta}\ \frac{1}{\delta t}H(-|t-t'|/2+\delta t)$. Here, $H(\cdot)$ is the heaviside step function. The prefactor $\frac{1}{\delta t}$ makes sure that the integral over the correlation is still unity.

The random force added to the particle in each time step then becomes $\sqrt{2\gamma^{\mathrm{t}}k_{\mathrm{B}}T/\delta t}\,\boldsymbol{\xi}^{\mathrm{t}}_{\mathrm{num}}$, where $\boldsymbol{\xi}^{\mathrm{t}}_{\mathrm{num}}$ is a random number drawn from a distribution with zero mean and unit variance. Some implementations use a Gaussian distribution, but since for the long time behaviour only the two moments are relevant, we can use a uniform distribution, which is the fastest one to sample from numerically.

2.1.5.3 Rotational degrees of freedom

Rotational degrees of freedom can in principle be numerically integrated similarly to the particle translation using a velocity Verlet scheme, because the equation of motion Eq. (2.13) is also a second order ordinary differential equation. However, the constraint $|\hat{\mathbf{e}}(t)| = 1$ and the fact that I depends on the rotation state itself introduces additional complexity. To make the problem more tractable, one can use Euler's formulation of rigid body dynamics which reads

$$I_{\mathrm{body}}\dot{\boldsymbol{\omega}} + \boldsymbol{\omega} \times (I_{\mathrm{body}}\boldsymbol{\omega}) = \mathbf{M}_{\mathrm{body}}, \tag{2.34}$$

where I_{body} and $\mathbf{M}_{\mathrm{body}}$ are moment of inertia and total torque in the particle's rotating frame of reference. The advantage of this reformulation is that now the moment of inertia is a constant. From the cross-product in the second term we see that the price to pay is a quadratic term in $\boldsymbol{\omega}$ that mixes the components, making a specialised treatment necessary. ESPResSo implements a numer-

ical integrator for three-dimensional rotational motion based on a quaternion representation of the rotation state, details can be found in Ref. [136].

2.1.5.4 Why not Fokker-Planck?

In the introduction of this section on stochastic dynamics, I mentioned that we use an approach based on stochastic differential equations (SDEs) rather than partial differential equations (PDEs) for probability densities because it is more simple. After discussing numerical methods, I can now give a less ambiguous justification based on the memory requirements of the two approaches. At first glance, the solution of a PDE seems much more efficient because it has to be done just once, and quantities extracted from it are exact. For the SDE approach, one needs to simulate many realizations of the random process to obtain averages, which will always have some uncertainty associated with them due to the finite set of trajectories used for the average.

However, the memory required to store the PDE solution scales very unfavourably. For N_{part} particles in d dimensions, the solution to the PDE equivalent of Eq. (2.1) is a function of $2dN_{\mathrm{part}}$ variables (position and velocity of all particles, rotation not yet considered). If finite, cubic, space and velocity domains with "volumes" $(L)^d$, $(L_v)^d$ are discretised into cells with side lengths Δx, Δv for numerical solution, we need

$$N_{\mathrm{cells}} = \left(\frac{L}{\Delta x}\frac{L_v}{\Delta v}\right)^{d\cdot N_{\mathrm{part}}} \tag{2.35}$$

values to store the discretised probability density function at each time step, a number that grows exponentially with the number of particles. For a very moderate $N_{\text{part}} = 100$ and a really low resolution of $\frac{L}{\Delta x} = \frac{L_v}{\Delta v} = 10$, we get $N_{\text{cells}} = 10^{600}$ in $d = 3$. There are only about 10^{80} atoms in the universe so it seems unlikely that a memory device will be invented in the near future that can store the solution of the PDE.

To hold a random trajectory, one needs $N_{\text{dof}} = 2d \cdot N_{\text{part}}$ values for each time step, which increases just linearly. We still need to consider many of these trajectories to obtain satisfactory statistics, but the total memory requirements can be handled by current hardware.

2.2 Hydrodynamics

Hydrodynamics or fluid dynamics is the physics and engineering branch that is concerned with the flow of fluids on a continuum level. Liquids are made from particles (atoms, molecules, ...), but if the number of particles approaches infinity, the fluid can be considered a continuum. In practice, this infinite limit is reached surprisingly fast, making the continuum description valid at scales $\gtrsim 50\,\mathrm{nm}$ [137][8]. Bacteria are significantly larger than that, so we will use continuum hydrodynamics for all fluid modeling presented in this thesis.

2.2.1 The Navier-Stokes equation

The Navier-Stokes equation governing the evolution of the velocity field $\mathbf{u}(\mathbf{r}, t)$ and pressure field $p(\mathbf{r}, t)$ of an incompressible Newtonian fluid at density $\rho(\mathbf{r}, t) = \rho = const.$ is given by

$$\rho\left[\partial_t \mathbf{u} + (\mathbf{u}\cdot\nabla)\,\mathbf{u}\right] = -\nabla p + \mu\nabla^2\mathbf{u} + \mathbf{f}^{\mathrm{ext}}, \tag{2.36a}$$

$$\nabla\cdot\mathbf{u} = 0, \tag{2.36b}$$

where $\mathbf{f}^{\mathrm{ext}}$ is an external force density acting on the fluid, e.g., gravity[9]. The left hand side of Eq. (2.36a) expresses the momentum change of an infinitessimal fluid volume at $\mathbf{r}$ caused by the

[8] With careful extension of the Navier-Stokes results and determination of fit parameters, continuum hydrodynamics can be valid at even smaller scales, down to a few molecule diameters [138].

[9] For the rest of this thesis, particle velocities will be denoted by $\mathbf{v}$ and fluid velocities by $\mathbf{u}$.

forces (stresses) given on the right hand side of Eq. (2.36a). The left hand side can be derived rigorously [139], the right hand side follows from modelling assumptions. Forces on the infinitessimal fluid volume come from a change in pressure (∇p), external forces ($\mathbf{f}^{\text{ext}}$) and from internal, viscous friction with the surrounding fluid. The assumption for the Newtonian fluid is that the stress σ associated with viscous friction is linear in the rate-of-strain tensor E, i.e.,

$$\sigma = \mu 2E, \quad E = \frac{1}{2}\left[\nabla \otimes \mathbf{u} + (\nabla \otimes \mathbf{u})^T\right], \tag{2.37}$$

where $\otimes$ denotes the dyadic product. The force density that acts on the fluid is then given by $\nabla \cdot \sigma$.

Equation (2.36b) is an expression of incompressibility of the fluid. It is a short form of the continuity equation $\partial_t \rho = -\nabla \cdot (\rho \mathbf{u})$ using $\partial_t \rho = \nabla \rho = 0$ for the constant density.

2.2.1.1 Boundary conditions

No differential equation is complete without boundary conditions. In the field of hydrodynamics, there are a number of boundary conditions that are frequently used and deserve a short introduction. We use Ω_B to denote the surface at which a boundary condition acts. The fluid domain can be bounded by a number of different boundaries that can each have different conditions associated with them.

▶ No-slip

Typically used to model the boundaries with a solid surface, the no-slip boundary condition requires no fluid flow into or along a

surface Ω_B, i.e.

$$\mathbf{u}(\mathbf{r} \in \Omega_B, t) = \mathbf{0}. \tag{2.38}$$

The normal component encodes the impermeability of the solid surface, the tangential component the interactions of fluid molecules with the (nanoscopic) roughness of the surface.

▶ Constant velocity

A time-constant velocity

$$\mathbf{u}(\mathbf{r} \in \Omega_B, t) = \mathbf{u}_B(\mathbf{r} \in \Omega_B) \tag{2.39}$$

can be employed along a boundary. This is typically used to model moving solid surfaces ($\rightsquigarrow$ no-slip in the comoving reference frame of the surface), or inlets and outlets, e.g., syringes driving fluid at constant velocity through a microfluidic channel.

▶ Constant pressure

A time-constant pressure

$$p(\mathbf{r} \in \Omega_B, t) = p_B(\mathbf{r} \in \Omega_B) \tag{2.40}$$

can be employed along a boundary. This is typically used to model inlets and outlets connected to pressure control systems or "open" boundaries of experimental setups, e.g., an effluent pipe ending in a container at atmospheric pressure.

▶ Periodic

If the system under consideration is periodic with some periodicity $\mathbf{L}$, the boundary condition

$$\mathbf{u}(\mathbf{r}, t) = \mathbf{u}(\mathbf{r} + \mathbf{L}, t) \tag{2.41}$$

for $\mathbf{r} \in \Omega_B$ connects two boundaries of the fluid domain. Despite being a purely theoretical construct, periodic boundary conditions are useful to model porous media which are periodic over some length, or small sections of a very large domain that cannot be treated in full.

▶ Slip

At small length scales, the no-slip boundary condition is not a good approximation of the interaction between a liquid and a solid anymore, because fluid molecules can slide along the particles that make up the solid surface. In this case, one often uses the slip boundary condition [140]

$$\mathbf{u}(\mathbf{r} \in \Omega_B, t) = l_{\text{slip}} 2E\hat{\mathbf{n}}, \tag{2.42}$$

Where $\hat{\mathbf{n}}$ is a vector normal to the surface. Equation (2.42) relates the fluid velocity on the boundary to the viscous stress that acts on the infinitessimal layer of fluid in contact with the solid. The prefactor l_{slip} is called the slip length. It is connected to a fictional surface penetration length that is calculated by extrapolating the velocity field into the solid boundary until it reaches zero.

There are many more boundary conditions, but they are irrelevant to the results presented in this thesis so they are not covered here.

2.2.2 The Stokes equation

Using a characteristic length L of flow features and a characteristic velocity scale U, we can nondimensionalise the Navier-Stokes

equations using $\mathbf{r}^* = \mathbf{r}/L$, $\mathbf{u}^* = \mathbf{u}/U$, $t^* = tU/L$, $p^* = pL/(\mu U)$, $\mathbf{f}^{\text{ext}*} = \mathbf{f}^{\text{ext}} L/(\mu U)$ and obtain

$$\frac{\rho U L}{\mu} \left[\partial_{t^*} \mathbf{u}^* + (\mathbf{u}^* \cdot \nabla_*)\, \mathbf{u}^*\right] = -\nabla_* p^* + \nabla_*^2 \mathbf{u}^* + \mathbf{f}^{\text{ext}*}. \tag{2.43}$$

The dimensionless prefactor

$$\text{Re} = \frac{\rho U L}{\mu} \tag{2.44}$$

on the left hand side is called the Reynolds number and quantifies the relative importance of inertial forces (enumerator) to viscous forces (denominator).

If we plug in the typical velocity scale $U = v_{\text{swim}} = 25\,\mu\text{m}\,\text{s}^{-1}$ for swimming bacteria, a flow length scale of $L = 100\,\mu\text{m}$, and use water as the fluid we arrive at $\text{Re} = 2.5 \times 10^{-3} \ll 1$. This means that very similar to the arguments made for particle inertia in Section 2.1.2.3, fluid inertia can also typically be neglected[10].

Setting $\text{Re} = 0$ and reintroducing the variables with their physical dimensions, we arrive at the time-independent Stokes equation

$$-\nabla p + \mu \nabla^2 \mathbf{u} + \mathbf{f}^{\text{ext}} = 0, \tag{2.45a}$$

$$\nabla \cdot \mathbf{u} = 0. \tag{2.45b}$$

[10]The "smallness" of fluid inertia in this example is less extreme than for the particle inertia in Section 2.1.2.3. By considering a bacterium in external flow with $U = 10 v_{\text{swim}}$ in a porous environment with $L = 1\,\text{mm}$, we can easily increase the the Reynolds number by two orders of magnitude to 0.25. This is still "small", but not small enough to immediately discard fluid inertia in all investigations of bacterial swimming.

Neglecting the left hand side of Eq. (2.36a) leads to two significant simplifications:

▶ Time reversal symmetry

There is no explicit time dependence anymore because the time derivative dropped out. This does not necessarily mean that all flows must be stationary, because the boundary conditions might be time dependent. It does however mean that all flows must instantaneously adapt to any change in boundary condition. All low-Re flows must therefore be time-reversible upon time reversal of the boundary conditions. This simplifies the analytical or numerical solution of hydrodynamic problems, but also has important physical implications for swimming microorganisms: They cannot use a propulsion mechanism based on one, finite degree of freedom. To sustain motion for an extended time, the swimmer has to do some type of cyclic actuation of the degree of freedom. It can vary the actuation with time (e.g., slow in the first half of the cycle, fast in the second half), but at some point it has to return to the initial configuration to start the next cycle. Because the flow fields generated by the actuation are time reversible, the forces on the swimmer are also time reversible. Consequently, when the swimming degree of freedom has returned to its initial value, the time-integrated force on the swimmer over a full cycle comes out to be zero and the total displacement vanishes. This is usually exemplified by the single hinge between the upper and lower shell of a scallop that opens and closes, coining the term "(no) scal-

lop theorem“ [141][11]. There are two main mechanisms by which microswimmers circumvent this constraint.

Some swimmers use more than one degree of freedom for their propulsion. For example, *Chlamydomonas reinhardtii* uses two flexible cilia that open and close in a breast stroke like manner [143]. Unlike the rigid shell of a scallop, the cilia bend in response to actuation, making it possible to define distinct recovery and power strokes based on the shape of the cilia when they are driven fast or slow. The different shape of the cilia in the two halves of the beating cycle makes the propulsion asymmetric with respect to time reversal and thus enables net movement of the cell body.

Other swimmers use one infinite degree of freedom. For example, bacteria such as *E. coli* use *rotational* motors to power flagella. Since the actuated degree of freedom is an angle that can increase to infinity (or is reset mathematically to 0 when one rotation is completed), the bacterium never has to reverse the motor to complete one period of motor driving. Consequently, it can just keep on moving forward.

▶ Linearity

All terms proportional to $\mathbf{u}^2$ dropped out of Eq. (2.36b) and the resulting equation is linear in $\mathbf{u}$ and p. This means that Eq. (2.45)

[11] Scallops are unaffected by the no scallop theorem not only because they swim at larger Reynolds numbers, but mainly because they do not swim by just opening and closing the hinge. Instead, they also open and close membrane valves to suck in fluid from the front and then push it out from the back. With this, they move *forward* when *closing* the shell [142, p. 6]

is a lot more amenable to analytical treatment than Eq. (2.36), examples being shown in the next sections.

2.2.3 Multipole expansion

The Stokes equation being linear, we can look for fundamental solutions (the Green's function) of Eq. (2.45), considering $\mathbf{f}^{\text{ext}}$ as the inhomogeneity. For $\mathbf{f}^{\text{ext}}(\mathbf{r}) = \mathbf{F}\delta(\mathbf{r}-\mathbf{r}_0)$, where $\mathbf{F}$ is a constant and $\mathbf{r}_0$ the location at which the point force acts, and the boundary condition $\mathbf{u}(|\mathbf{r}-\mathbf{r}_0| \to \infty) = \mathbf{0}$, one obtains [144]

$$\mathbf{u}^{\text{FM}}(\mathbf{r};\mathbf{r}_0) = \frac{1}{8\pi\mu} G(\mathbf{r};\mathbf{r}_0)\mathbf{F}, \tag{2.46a}$$

$$p^{\text{FM}}(\mathbf{r};\mathbf{r}_0) = \frac{1}{4\pi|\mathbf{r}-\mathbf{r}_0|^3}\mathbf{F}\cdot(\mathbf{r}-\mathbf{r}_0), \tag{2.46b}$$

where

$$G(\mathbf{r};\mathbf{r}_0) = \frac{1}{|\mathbf{r}-\mathbf{r}_0|}\left[\mathbb{1} + \frac{(\mathbf{r}-\mathbf{r}_0)\otimes(\mathbf{r}-\mathbf{r}_0)}{|\mathbf{r}-\mathbf{r}_0|^2}\right] \tag{2.47}$$

is known as the Oseen tensor. Equation (2.46) is called the "Stokeslet" or "force monopole". Notably, the velocity magnitude decays as $1/|\mathbf{r}-\mathbf{r}_0|$ for large distances, showing the long-ranged effect of flow disturbations.

The solution Eq. (2.46) is not enough to describe all flow fields, as it contains only the contributions that can be produced by point forces. Analogous to electrostatic multipoles, there are infinitely many hydrodynamics multipoles describing the fluid flows that result from point dipoles, point quadrupoles, etc. Source dipoles, source quadrupoles, etc. add another family of fundamental solutions. These are fundamental solutions related to δ-like sources

and sinks of fluid that are infinitely close together. There cannot be a source monopole because we use the incompressible Stokes equation where the total amount of fluid has to be conserved.

All fundamental solutions in the force and source family can be obtained from Eq. (2.46) and the Oseen tensor by derivation with respect to $\mathbf{r}_0$ [145, 146], e.g.

$$\mathbf{u}^{\mathrm{FD}}(\mathbf{r};\mathbf{r}_0) = -\left[\nabla_{\mathbf{r}_0} \otimes \mathbf{u}^{\mathrm{FM}}(\mathbf{r},\mathbf{r}_0)\right]\mathbf{F} \tag{2.48}$$

for the force dipole. The resulting expression is lengthy (for details, see the appendix of Ref. [145]), but from the $|\mathbf{r}-\mathbf{r}_0|$ dependence of the force monopole, it is clear that the dipolar flow field must scale as $|\mathbf{r}-\mathbf{r}_0|^{-2}$. In general, all fundamental solutions of Eq. (2.45) scale as $|\mathbf{u}|(|\mathbf{r}-\mathbf{r}_0| \to \infty) \sim 1/|\mathbf{r}-\mathbf{r}_0|^{\alpha}$ with $\alpha \geq 1$ and $\alpha = 1$ only for the force monopole.

Any flow field can be decomposed into the fundamental solutions, and the far-field will be dominated by the lowest order multipole. For bacteria swimming in bulk fluid, this is always a dipole and never the force monopole. A force monopole can only be created when a net external force is applied to the fluid, for example when a particle sediments under the influence of gravity or a charged colloid is driven through the fluid electrostatically. Bacteria, however, are not externally driven. They produce the swimming force themselves, so by Newton's third law, any forward force on the cells must be countered by an equal and opposite force that the swimmer's propulsion mechanism exerts on the fluid. In total, the system is therefore force free and the flow field generated by swimming microorganisms decays in leading order as $|\mathbf{r}-\mathbf{r}_0|^{-2}$.

2.2.3.1 Friction coefficients

The friction force that a particle experiences when dragged through a fluid at velocity $\mathbf{v}$ can be obtained from the flow field around the swimmer. The force on a surface Ω is calculated by integrating the stress contributions from pressure and viscous dissipation as

$$\mathbf{F}^{\text{frict}} = \int_{\Omega} (\sigma - p\mathbb{1})\hat{\mathbf{n}} \, \mathrm{d}S \,, \tag{2.49}$$

where $\hat{\mathbf{n}}$ denotes the surface normal. For a Newtonian fluid, the viscous stress tensor σ was introduced in Eq. (2.37). In the low Reynolds number world, this force is always linear in the driving velocity $\mathbf{v}$, because time reversal symmetry must be upheld. This allows us to define the friction coefficient via $\mathbf{F}^{\text{frict}} = \gamma^{\text{t}}\mathbf{v}$. Note that γ^{t} does not follow from simple division of the velocity and force norms because the particle might be anisotropic and the two vectors are not necessarily parallel. Rotational friction coefficients can be obtained analogously by integration of torques via

$$\mathbf{M}^{\text{frict}} = \int_{\Omega} \mathbf{r} \times [(\sigma - p\mathbb{1})\hat{\mathbf{n}}] \, \mathrm{d}S \,, \tag{2.50}$$

and $\mathbf{M}^{\text{frict}} = \gamma^{\text{r}}\boldsymbol{\omega}$.

For a sphere, the results were introduced in Eqs. (2.2) and (2.14). Having simulations of rod-like bacteria in mind, we also need friction coefficients for elongated particles. For spheroids, the friction coefficients are a bit more lengthy, but can be worked out analytically, too. Because of the rotational symmetry of the spheroid, the friction tensors have only two independent entries: The axial component $\gamma^{\text{t}}_{\text{ax}}, \gamma^{\text{r}}_{\text{ax}}$ for translation along or rotation

around the symmetry axis, and the equatorial component $\gamma^{\mathrm{t}}_{\mathrm{eq}}, \gamma^{\mathrm{r}}_{\mathrm{eq}}$ for translation along or rotation around all axes perpendicular to the symmetry axis. For a prolate ellipsoid with long (axial) semiaxis a and short (equatorial) semiaxis b, one obtains [147]

$$e = \sqrt{1 - \left(\frac{b}{a}\right)^2}, \tag{2.51a}$$

$$\gamma^{\mathrm{t}}_{\mathrm{ax}} = \frac{16\pi e^3 a}{(1+e^2)\ln[(1+e)/(1-e)] - 2e}\mu, \tag{2.51b}$$

$$\gamma^{\mathrm{t}}_{\mathrm{eq}} = \frac{32\pi e^3 a}{2e + (3e^2-1)\ln[(1+e)/(1-e)]}\mu \tag{2.51c}$$

and [148]

$$p = \frac{a}{b}, \quad \xi = \frac{\sqrt{p^2-1}}{p}, \quad S = \frac{2\,\mathrm{atanh}\,(\xi)}{\xi}, \tag{2.52a}$$

$$F^{\mathrm{perrin}}_{\mathrm{ax}} = \frac{4}{3}\frac{p^2-1}{2p^2-S}, \quad F^{\mathrm{perrin}}_{\mathrm{eq}} = \frac{4}{3}\frac{p^{-2}-p^2}{2-S(2-p^{-2})}, \tag{2.52b}$$

$$\gamma^{\mathrm{r}}_{\mathrm{sphere}} = 8\pi\mu a b^2, \tag{2.52c}$$

$$\gamma^{\mathrm{r}}_{\mathrm{ax}} = F^{\mathrm{perrin}}_{\mathrm{ax}}\gamma^{\mathrm{r}}_{\mathrm{sphere}}, \quad \gamma^{\mathrm{r}}_{\mathrm{eq}} = F^{\mathrm{perrin}}_{\mathrm{eq}}\gamma^{\mathrm{r}}_{\mathrm{sphere}}. \tag{2.52d}$$

2.2.4 Numerical methods: Lattice Boltzmann

Most hydrodynamic problems cannot be solved analytically due to the complexity of the Navier-Stokes Eq. (2.36) and the endless possibilities for the choice of boundary conditions. Complex hydrodynamic problems are highly relevant in many fields of theoretical science and practical engineering, and thus many numerical schemes exist to obtain solutions from computer simulations. Here,

we review the lattice Boltzmann (LB) method because it is used in the research presented in this thesis. It is a very efficient, easy to implement, easy to parallelize Navier-Stokes solver that is very popular in the porous media community due to the straightforward implementation of complex boundary shapes. It is also very useful for the study of swimming microorganisms because schemes have been developed to couple continuum hydrodynamics to moving particles.

This section seeks to give an overview over the basic concepts of the LB methods as well as its strengths and weaknesses without going into detail about advanced methods and implementation. It borrows heavily from the lattice Boltzmann graduate textbook by Krüger *et al.* [149].

2.2.4.1 The Boltzmann equation

The lattice Boltzmann algorithm is based on a mesoscopic description of fluids using kinetic theory of gases and the Boltzmann equation that lends its name to the algorithm. The main quantity of interest is the distribution function $f(\mathbf{r}, \boldsymbol{\xi}, t)$ which is the joint probability density to find a particle at position $\mathbf{r}$ with momentum $\boldsymbol{\xi}$ at time t. The time evolution of f is governed by the Boltzmann equation

$$\partial_t f + \boldsymbol{\xi} \cdot \nabla_{\mathbf{r}} f + \frac{1}{\rho} \mathbf{F} \cdot \nabla_{\boldsymbol{\xi}} f = \Omega(f). \tag{2.53}$$

Here, $\nabla_{\mathbf{r}}$ and $\nabla_{\boldsymbol{\xi}}$ denote partial derivatives with respect to the components of $\mathbf{r}$ and $\boldsymbol{\xi}$, respectively, and Ω denotes the collision operator. Quite similar to the Navier-Stokes Eq. (2.36), the Boltz-

mann Eq. (2.53) describes the change in momentum due to internal momentum transfer and external forces. It is this connection through the fact that both equations represent a continuum version of the conservation laws for mass and momentum that will lead us from an equation for gas particle statistics to a hydrodynamics solver[12].

The collision operator is not known for many types of particle interaction, but there exist some expressions that can be derived using simplifying assumptions. One of them is the *Stoßzahlansatz* by Boltzmann himself which involves integrals over the distribution function f and kernels that take the details of the molecular interactions into account. This is not the form of Ω that is used in the lattice Boltzmann method, instead a much greater simplification is applied. The Bhatnagar, Gross, Krook (BGK) collision operator [152]

$$\Omega^{\mathrm{BGK}}(f) = -\frac{1}{\tau^{\mathrm{BGK}}}\left(f - f^{\mathrm{eq}}\right) \tag{2.54}$$

captures only the most essential, coarse-grained physics of the particle interactions: that – by whatever mechanism – they bring the distribution function towards the equilibrium distribution function f^{eq}, and do so on a time scale τ^{BGK}. Since the equilibrium distri-

[12] One can think of a lot of equations or kinetics that obey mass and momentum conservation, notable examples being smoothed particle hydrodynamics [150] and multi-particle collision dynamics [151]. All of them will lead to some version of the Navier-Stokes equation on a macroscopic scale. The question is then "only" how to relate the parameters of the microscopic desciption to the macroscopic parameters of the fluid that one wants to simulate.

bution is the well known Maxwell-Boltzmann distribution

$$f^{\mathrm{eq}}(\mathbf{r}, \boldsymbol{\xi}, t) = \rho \left(\frac{m}{2\pi k_{\mathrm{B}} T} \right)^{3/2} \exp\left(- \frac{(\boldsymbol{\xi} - \langle \boldsymbol{\xi} \rangle)^2}{2 m k_{\mathrm{B}} T} \right), \tag{2.55}$$

around the mean momentum $\langle \boldsymbol{\xi}(\mathbf{r}, t) \rangle$ at that location, we now have a closed form to solve Eq. (2.53).

2.2.4.2 The lattice Boltzmann algorithm

For a numerical implementation, the continuous spaces of $\mathbf{r}$, $\boldsymbol{\xi}$, t must be discretised. The time stepping is done with a constant time step Δt. For the spatial coordinates, usually a regular grid with grid constant a_{grid} is chosen. For the momentum coordinates, only a small number of distinct directions and magnitudes are included: lattice velocities $\mathbf{c}_i$ that upon multiplication by Δt lead from one grid cell to its neighbours. The number of neighbours that are considered in the discrete velocity set varies with accuracy requirements, but in 3D usually the lattice point itself (zero velocity) and 18 neigbours are chosen. These are the six nearest neighbours and the twelve next-nearest neighbors located on the edges of the cube of side length $2a_{\mathrm{grid}}$ with the central position in the middle. In conclusion, the continuum $f(\mathbf{r}, \boldsymbol{\xi}, t)$ is replaced by $f_i(\mathbf{r}_j, n\Delta t)$, $i \in \{0, 18\}$. The discretised probabilities f_i at each location are referred to as "populations".

Numerical integration of the Eq. (2.53) is typically split into two steps.

▶ Collision

First, the discretised collision operator is applied at each node

$$f_i^\star(\mathbf{r},t) = f_i(\mathbf{r},t) - \frac{\Delta t}{\tau^{\mathrm{BGK}}}\left[f_i(\mathbf{r},t) - f_i^{\mathrm{eq}}(\mathbf{r},t;f_i)\right]. \tag{2.56}$$

The dependence of f_i^{eq} on f_i comes from the fact that the mean momentum must be known to calculate Eq. (2.55).

▶ Streaming

After applying the collision, the populations are moved to the neighboring nodes according to

$$f_i(\mathbf{r}+\mathbf{c}_i\Delta t, t+\Delta t) = f_i(\mathbf{r},t). \tag{2.57}$$

Here, we have only discussed the most simple lattice Boltzmann algorithm. While the generic principles of collision and streaming remain the same among the LB variants that are used in research, usually more complex algorithms are used. For example, many relevant implementations are based on two- or multirelaxation time (STR, MRT) algorithms with more elaborate collision operators that offer more parameters than the single relaxation time τ^{BGK} [134, 153]. Typically, they use a moment representation of the populations (see also Section 2.2.4.3 for the relevance of moments of f) to simplify the calculations.

Thermal fluctuations of a microscopic fluid can be relevant on the length scales of bacteria. These can be taken into consideration in the framework of stochastic hydrodynamics [154]. Analogous to the particle momentum fluctuations modelled with a stochastic force the Langevin equation 2.1, fluctuating hydrodynamics are

obtained by introducing a stochastic stress in addition to the deterministic contributions from pressure and dissipation. Lattice Boltzmann extensions are available to include these fluctuations in the discretised algorithm [155].

One of the main advantages of the LB method is that only during the streaming step information is passed between lattice nodes. Since only a few neighboring nodes are considered, nodes far from each other do not have any explicit interaction. This makes parallelisation of the numerical algorithm very straightforward. Each computational unit (CPU thread or GPU) performs streaming and collision on a subdomain of the fluid. During streaming, information between computational units must only be shared in the very thin layer of nodes that "touches" neighbouring subdomains. Because the surface of the subdomain typically contains much fewer nodes than the volume contained in it, only a small fraction of information has to be shared between computational units, making parallelisation very efficient.

2.2.4.3 Recovering macroscopic quantities

The lattice Boltzmann algorithm – Eqs. (2.56) and (2.57) – solves the discretised version of the Boltzmann equation, giving us the time evolution of the discretised probability function f. However, we are interested in a solution of the macroscopic Navier-Stokes Eq. (2.36). To obtain the macroscopic quantites of interest, we use the definition of f and find that they are calculated as moments

of the probability function

$$\rho(\mathbf{r},t) = \int_{\mathbb{R}^3} f(\mathbf{r},\boldsymbol{\xi},t)\,\mathrm{d}^3\boldsymbol{\xi}\,, \tag{2.58a}$$

$$\mathbf{u}(\mathbf{r},\boldsymbol{\xi},t) = \frac{1}{\rho(\mathbf{r},t)}\int_{\mathbb{R}^3} \boldsymbol{\xi} f(\mathbf{r},\boldsymbol{\xi},t)\,\mathrm{d}^3\boldsymbol{\xi}\,. \tag{2.58b}$$

For the discretised algorithm, the integrals are replaced by summations over the velocity set $\{\mathbf{c}_i\}$.

The connection of the mesoscopic quantities f and τ^{BGK} to other macroscopic quantities like pressure or viscosity is much more difficult to find. The mathematical formalism is known as the Chapman-Enskog analysis [156]. For the BGK collision operator in Eq. (2.54), it leads to

$$p = c_s^2\rho \tag{2.59}$$

and

$$\mu = \rho c_s^2\left(\tau^{\mathrm{BGK}} - \frac{\Delta t}{2}\right), \tag{2.60}$$

where $c_s = \sqrt{1/3}\frac{a_{\mathrm{grid}}}{\Delta t}$ is the lattice speed of sound. The lattice speed of sound does not correlate with the physcial speed of sound. The equation of state (2.59) is therefore only to be used to calculate p, and the results can only be trusted if the resulting pressure differences are small.

2.2.4.4 Application of forces

There are different ways to include the (position dependent) external force $\mathbf{f}^{\mathrm{ext}}$ of Eq. (2.36) (or equivalently $\mathbf{F}$ in Eq. (2.53)) into the lattice Boltzmann algorithm. A popular one is the so called Guo forcing which corresponds to the inclusion of an additional

momentum source term in the collision step and a modification of the velocity calculation [157].

2.2.4.5 Boundary conditions

To implement the hydrodynamic boundary conditions mentioned in Section 2.2.1.1 into the lattice Boltzmann framework, different algorithms have to be applied for each condition. For the purposes of this thesis, only two hydrodynamic boundary conditions were used in simulations: No-slip and periodic boundary conditions. Other types of boundary conditions are approximated by interactions with particles, see Section 2.2.4.6.

Periodic boundary conditions are implemented by simply connecting the lattice nodes at the edge of the computational domain to their periodic couterparts on the other side of the domain in the streaming step. Populations get communicated between these two layers of nodes as they get communicated everywhere else in the system.

No-slip (and constant velocity) boundary conditions are often implemented using the "halfway bounce-back" scheme. As the name suggests, fluid populations that try to enter a lattice node that is marked as a boundary get streamed back to the node they originated from. The velocity vector $\mathbf{c}_i$ of the reflected population is inverted such that the fluid node receives a population just as if there was another fluid node adjacent. This scheme leads to a "physical" boundary approximately halfway between the nodes that are marked as boundaries and the adjacent fluid nodes. "Physical" is to be understood in the sense that if one extrapolates

the fluid velocity from the fluid domain, it will reach zero *inbetween* nodes and not *on* the boundary nodes. Because solid boundaries are defined on the level of lattice nodes, all boundary surfaces are represented as a set of cubes. This "staircase" or "LEGO" approximation of curved boundary surfaces is a limitation of the bounce-back method and has its roots in the regular grid used for discretisation. It is also one of the advantages of bounce-back and lattice Boltzmann in general, because any boundary shape, no matter how geometrically complex, can be approximated as a LEGO model and then included in the hydrodynamic simulations without any more difficulty than a flat wall. The bounce-back boundary condition is also popular because it acts only on local populations during the streaming step, so the ease of parallelisation is not impeded and the collision step is agnostic of boundaries. Furthermore, the populations are reversed and not altered in any other way, so the total amount of fluid mass is conserved exactly.

2.2.4.6 Particle coupling

To couple particle based methods like the ones introduced in Section 2.1 to a continuum description of liquids in the lattice Boltzmann framework, different methods exist. We will not discuss moving boundary methods [155], even though they are certainly a valuable tool for many applications, including microswimmers [158]. To obtain the results presented in this thesis, we instead employ a friction coupling scheme originally developed for polymer simulations [159]. It is based on an extension of the Langevin Eq. (2.1)

to moving carrier fluids. Here, the friction force on particle i reads

$$\mathbf{F}_i^{\text{frict}}(t) = -\gamma_i^{\text{t}} \left[\mathbf{v}_i(t) - \mathbf{u}(\mathbf{r}_i(t), t)\right] \tag{2.61}$$

and replaces the original $-\gamma_i^{\text{t}}\mathbf{v}_i(t)$. In this sense, the Langevin equation can be seen as a simplification where $\mathbf{u}(\mathbf{r}, t) = \mathbf{0}$.

Since $\mathbf{r}_i(t)$ does not have to coincide with a lattice lattice node, $\mathbf{u}(\mathbf{r}_i(t), t)$ needs to be obtained by interpolation. Usually, we use a linear interpolation that takes the eight nearest nodes into account.

If the friction force is only applied to the particle, the total system comprising particles and fluid is not momentum conserving and the particle has no influence on the fluid, i.e., no hydrodynamic interation between particles is possible. Hence, the friction force must also be applied to the fluid, but in the opposite direction. To this end, $-\mathbf{F}^{\text{frict}}$ is interpolated back linearly to the same eight nodes that the velocity was interpolated from. The force on the fluid is then applied according to Section 2.2.4.4.

When thermal fluctuations are considered, one cannot treat the stochastic forces on the particles and on the fluid as independent. Both the deterministic dissipative and the random forces stem from the same nanoscopic interactions between fluid and particle. Newton's third law demands that the force on the fluid be the negative force on the particle. Therefore, a thermal coupling must not only apply $\mathbf{F}^{\text{frict}}$ to the fluid, but also the *same* random force proportional to $\boldsymbol{\xi}_i^{\text{t}}(t)$ that appears in Eq. (2.1).

The frictional coupling and Eq. (2.61) in combination with lattice Boltzmann simulations is a good model for the interaction of "small" particles with larger volumes of fluid or particles at large

distances. Equation (2.61) does not resolve the shape of the particle beyond its (anisotropic) friction coefficient. From the perspective of the fluid, the force originates form a point particle somewhere inside a single lattice cell. Therefore, this coupling cannot resolve near-field hydrodynamic interactions between particles or between particles and surfaces. It also cannot handle particles with a size that approaches the size of a lattice cell, since the friction force is only applied to nodes in that cell.

Both problems can be alleviated by constructing rigid bodies out of point particles, such that the combined particle collection can span multiple lattice cells and interact with all of them [160–162]. These rigid bodies are often called "raspberries" because of their similarity to the fruit when the individual particles are visualised with spheres. The constronstruction of raspberry particles to model bacteria will be discussed in more detail in Section 3.1.1.

The finite size of lattice cells already leads to deviations from the expected dissipative and diffusive behaviour even when particles are still small, but not very small compared to the lattice size. In this case however, there is an approximate correction to the friction coefficient, such that γ^{t} is replaced by

$$\gamma^{t\star} = \left[\frac{1}{\gamma^{\mathrm{t}}} - \frac{1}{g a_{\mathrm{grid}} \mu}\right]^{-1}, \tag{2.62}$$

where $g \approx 25$ is the numerical correction factor [159].

2.3 Porous media

In this short section, we will revise some of the fundamentals of the description of flow in porous media.

In the most simple terms, a porous medium is by definition divided into two domains[13]: the solid domain, also called the "matrix", and the void space. The former comprises sand grains, soil particles, fibers, or any other rigid structure that is impermeable to fluid flow. The latter comprises the pores that can be filled with some fluid like air or water.

The porosity

$$\phi = \frac{V^{\text{void}}}{V^{\text{void}} + V^{\text{solid}}} \tag{2.63}$$

of a porous medium describes the ratio of the void space volume V^{void} to the total volume $V^{\text{void}} + V^{\text{solid}}$, where V^{solid} is the volume of the solid domain.

Many relevant porous media are highly disordered at the pore scale and fluid flow is very complex due to the complex geometry. However, there are descriptions on a continuum scale, where the pore scale details are averaged out into a "resistance" that the porous medium imposes against fluid flow driven through it.

On the macroscopic scale, for a porous medium with cross sectional area A and length L, Darcy's law [163, note D, p. 570]

$$Q = \frac{KA}{\mu}\left[\frac{\Delta p}{L} + f^{\text{ext}}\right] \tag{2.64}$$

[13] We will not discuss porous media made from heterogenious materials or multiphase flow.

describes the relationship between an applied pressure difference Δp and external force density f^{ext}, and the resulting volume flux Q of fluid through the porous medium.

The proportionality factor K is called permeability and quantifies the "resistance" of the porous medium. By factoring out the fluid's dynamic viscosity μ, K is a property solely of the porous medium and once determined can be used to calculate fluxes of different fluids. One can analytically calculate K for a number of simple geometries such a bundle of tubes or stacked parallel plates where the pore scale flow field governed by Eq. (2.45) with the respective boundary conditions is known. In most cases however, K needs to be determined by numerical simulation or experiments.

The flux density $q = Q/A$ with units [volume]/[time $\cdot$ area] = [velocity] measures the throughput of fluid per cross sectional area. It is also a velocity in the sense of a spatial average in which the solid domain contributes with zero velocity. This means that the average of the actual velocity of the fluid at the pore scale v^{pore} is related to the flux density q via $\langle v^{\text{pore}} \rangle = q/\phi$.

The proportionality between Q and $\frac{\Delta p}{L} + \mathbf{f}^{\text{ext}}$ is a result of the low Reynolds number nature of flow for the same reason that the velocity of a particle driven through a fluid must be proportional to the driving force. Therefore, Darcy's law can only be applied in situations where the typical pore size and the typical flow velocity are small enough to ensure $\text{Re} \ll 1$. The continuum picture of fluid flow is only justified when L not only exceeds the typical pore size, but also exceeds the length scale of geometry variation between pores, leading to the notion of a representative elementary

volume (REV). Within the REV all pore scale details must be contained, such that beyond the REV, the permeability K captures all properties of the porous medium.

Most of the theoretical research on flow in porous media at the continuum scale is done using a PDE version of Eq. (2.64), in which $\Delta p/L$ is replaced by a pressure gradient ∇p and q is allowed to be space and time dependent to cover various boundary conditions. For the purposes of this thesis however, the macroscopic version presented here is sufficient so I will not go into more detail.

Chapter 3

Methods: Modeling of bacteria

This chapter outlines the bacterial model that is developed and used in this thesis. It contains the modeling aspects that are common to the models used to obtain the results presented in Chapters 4 to 7. In each of these chapters, a different flavour of the bacterial model will be used. Thus, they will have their own "methods" sections going into more detail and describing the modifications and extensions to the basic model outlined here.

3.1 Modeling the cell body

3.1.1 Rigid body dynamics: Raspberries

As mentioned in Section 2.2.4.6, coupling of particle based molecular dynamics algorithms to a continuum description of hydrodynamics in the lattice Boltzmann framework can be achieved via a two-way friction force. However, the basic point-friction coupling does not allow simulations of particles larger than a lattice Boltzmann grid cell. This limitation needs to be overcome for simulations of bacteria, because the flow fields generated by swim-

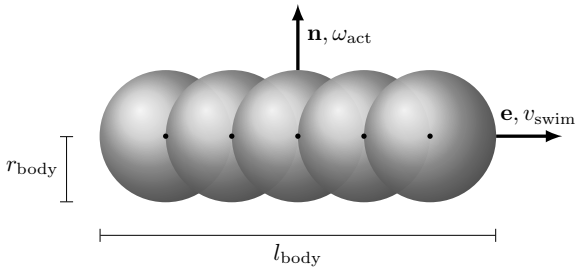

Figure 3.1. Schematic representation of the geometry of the rigid body agent with the definition of geometric parameters $r_{\text{body}}, l_{\text{body}}$. Black points show the location of $\mathbf{r}_i^{(j)}$, grey spheres indicate the extent of repulsive interactions. Reproduced from Ref. [4] with permission from the American Physical Society.

ming bacteria have features on the same length scale as the cell length, which need to be resolved by a finer LB grid. For the bacterial model presented in this thesis, we consider the extended, rod-like cell body of many relevant bacterial species such as *E. coli* or *Pseudomonas aeruginosa*. To construct the *in silico* counterpart, we use an algorithm for rigid body dynamics based on previous work [164]. Here, a rigid body is assembled from a number of spherical particles ("beads") connected to a central particle as shown in Fig. 3.1. Only the central particle's position and orientation are governed by Eqs. (2.1) and (2.13), the other, "virtual" particles are rigidly connected to the central particle. This means that they have a fixed relative position and orientation relative to the central particle. The virtual particles contribute to the dynamics of the overall rigid body via the forces they are subject to. The force $\mathbf{F}_i$ and torque $\mathbf{M}_i$ on the central particle i that enters

Eqs. (2.1) and (2.13) is the sum of the forces and torques on all particles j of the rigid body according to

$$\mathbf{F}_i = \sum_{j=1}^{N^{\text{bead}}} \mathbf{F}_j, \tag{3.1a}$$

$$\mathbf{M}_i = \sum_{j=1}^{N^{\text{bead}}} (\mathbf{r}_i^{(j)} - \mathbf{r}_i) \times \mathbf{F}_j. \tag{3.1b}$$

Here, N^{bead} is the number of particles that comprise the rigid body, $\mathbf{r}_i^{(j)}$ the position of particle j associated with rigid body i and $\mathbf{F}_j$ the total force that this particle j experiences from, e.g., interactions with other particles or a lattice Boltzmann fluid. Since $\mathbf{r}_i^{(j)}$ depends both on the position and the orientation of the rigid body, $\mathbf{F}_i$ and $\mathbf{M}_i$ are a function of position and orientation of all particles in a given system.

The rigid bodies used to model bacteria in Chapters 4 to 7 have different levels of geometric detail and a different numbers of beads per raspberry, depending on the application. The details will be given in the respective chapters.

3.1.2 Interaction potentials

3.1.2.1 Lennard-Jones and WCA

In this thesis, interactions between bacteria and their environment are usually modeled by the Lennard-Jones potential [165, 166]

$$V^{\text{LJ}}(r) = 4\epsilon^{\text{LJ}} \left[\left(\frac{\sigma^{\text{LJ}}}{r} \right)^{12} - \left(\frac{\sigma^{\text{LJ}}}{r} \right)^{6} + c_{\text{shift}} \right] H(r_{\text{cut}} - r), \tag{3.2}$$

where r denotes the distance between bacterial beads or the distance between a bacterial bead and a solid surface, ϵ^{LJ} denotes the potential strength parameter, σ^{LJ} the potential range parameter, r_{cut} the cutoff radius and c_{shift} a shift parameter that makes V^{LJ} continuous at r_{cut}. The potential is not derived from any physical interactions between bacteria and their environment but rather seeks to capture some very generic features of a possible interaction. For $r < 2^{1/6}\sigma^{\mathrm{LJ}}$ the potential is repulsive and diverges for $r \to 0$ with a zero crossing at $r = \sigma^{\mathrm{LJ}}$. This gives the bacterial bead a notion of a radius that contains an excluded volume. For bacteria-bacteria interactions, $2^{1/6}\sigma^{\mathrm{LJ}} = 2r_{\mathrm{body}}$ defines the radius of the cell body. For $2^{1/6}\sigma^{\mathrm{LJ}} < r < r_{\mathrm{cut}}$ the potential is attractive with an attraction well depth ϵ^{LJ}. We will later use this generic attraction to model bacterial cohesion in biofilms in Chapter 5. The finite cutoff radius r_{cut} limits the range of the potential which is necessary for efficient computations.

The choice $r_{\mathrm{cut}} = 2^{1/6}\sigma^{\mathrm{LJ}}$ can be used to remove the attractive part of the potential entirely, which we will use to model steric repulsion. The potential is then known as the Weeks-Chandler-Anderson potential [167].

3.1.2.2 Gay-Berne

Sometimes it is convenient to encode particle anisotropy directly in the interaction potential without having to resort to raspberry methods. A popular choice for anisotropic but spheroidal particles is the Gay-Berne potential [168, 169]. It extends the Lennard-Jones potential by also including the directors $\hat{\mathbf{e}}_i$ of the two interacting

particles when determining the interaction force. For, e.g., prolate particles, the head-to-head interaction potential has a longer range than the side-to-side potential. The potential reads

$$V^{\mathrm{GB}}\left(\hat{\mathbf{e}}_i, \hat{\mathbf{e}}_j, \mathbf{r}_{ij}\right) = \epsilon_{\mathrm{GB}}\left(\hat{\mathbf{e}}_i, \hat{\mathbf{e}}_j, \mathbf{r}_{ij}\right) \times \left[\left(\frac{\sigma_0}{r_{ij} - \sigma_{\mathrm{GB}}\left(\hat{\mathbf{e}}_i, \hat{\mathbf{e}}_j, \mathbf{r}_{ij}\right) + \sigma_0}\right)^{12} - \left(\frac{\sigma_0}{r_{ij} - \sigma_{\mathrm{GB}}\left(\hat{\mathbf{e}}_i, \hat{\mathbf{e}}_j, \mathbf{r}_{ij}\right) + \sigma_0}\right)^{6}\right] \times H(|\mathbf{r}_{ij}| - r_{\mathrm{GB}}^{\mathrm{cut}}), \tag{3.3}$$

where $\mathbf{r}_{ij} = \mathbf{r}_j - \mathbf{r}_i$ is the vector distance between the center of mass of each particle and $\epsilon_{\mathrm{GB}}\left(\hat{\mathbf{e}}_i, \hat{\mathbf{e}}_j, \mathbf{r}_{ij}\right)$, and $\sigma_{\mathrm{GB}}\left(\hat{\mathbf{e}}_i, \hat{\mathbf{e}}_j, \mathbf{r}_{ij}\right)$ are additional functions depending on the orientations of the particles. We use the parametrisation

$$\epsilon_{\mathrm{GB}}\left(\hat{\mathbf{e}}_i, \hat{\mathbf{e}}_j, \mathbf{r}_{ij}\right) = \epsilon_{\mathrm{GB}}^0\left[1 - \chi^2(\hat{\mathbf{e}}_i \cdot \hat{\mathbf{e}}_j)\right]^{-1/2} \tag{3.4}$$

and

$$\sigma_{\mathrm{GB}}\left(\hat{\mathbf{e}}_i, \hat{\mathbf{e}}_j, \mathbf{r}_{ij}\right) = \sigma_{\mathrm{GB}}^0\left(1 - \frac{\chi}{2}\left[\frac{(\hat{\mathbf{r}}_{ij} \cdot \hat{\mathbf{e}}_i + \hat{\mathbf{r}}_{ij} \cdot \hat{\mathbf{e}}_j)^2}{1 + \chi \hat{\mathbf{e}}_i \cdot \hat{\mathbf{e}}_j} + \frac{(\hat{\mathbf{r}}_{ij} \cdot \hat{\mathbf{e}}_i - \hat{\mathbf{r}}_{ij} \cdot \hat{\mathbf{e}}_j)^2}{1 - \chi \hat{\mathbf{e}}_i \cdot \hat{\mathbf{e}}_j}\right]\right)^{-1/2} \tag{3.5}$$

for these functions. Here, $\chi = (l_{\mathrm{GB}}^2 - 1)/(l_{\mathrm{GB}}^2 + 1)$ encodes the particle aspect ratio l_{GB}.

3.2 Bacterial swimming

3.2.1 "Dry" swimming

In simulations where the hydrodynamics of swimming bacteria are neglected, we use Eqs. (2.20) and (2.22) to model swimming motility. The swim force $F_{\text{swim}}\hat{\mathbf{e}}$ is applied to the central particle of the rigid body to obtain the desired swim velocity v_{swim}. All "virtual" raspberry particles experience forces from interactions, but not from friction or thermal noise. Dissipative and random forces are instead only applied to the central particle, where the anisotropic friction tensors γ^{t} and γ^{r} with components obtained from Eqs. (2.51) and (2.52) capture the elongated shape.

3.2.2 "Wet" swimming

In simulations where hydrodynamics of swimming bacteria are considered, we still use Eqs. (2.20) and (2.22) for particle dynamics, but also couple the swimmer to a lattice Boltzmann fluid as described in Section 2.2.4.6. All beads of the swimmer interact with the fluid through a "bare" friction coefficient $\tilde{\gamma}$. This friction coefficient is not related to the size r_{body} of a bead in the raspberry model. Instead, the combined effect of all the friction coupling points that make up the rigid body leads to an effective friction coefficient for the whole cell. Usually, $\tilde{\gamma}$ is chosen as large as numerical stability permits in order to "bind" the fluid of the LB cells to the swimmer that encompasses them as strongly as possible to reduce artefacts of fluid moving through the swimmer volume.

As described in Section 2.2.3, the hydrodynamics of bacterial swimming are not equivalent to the hydrodynamics of a cell

body being driven through the fluid by external forces. Instead, the propulsion mechanism and its effect on the fluid need to be taken into account. Our modeling approach for propulsion follows refs. [164, 170] for the introduction of a force on the fluid that mimics the effect of a flagellum or flagellar bundle. However, we add more geometric detail to the description.

The basic idea of the propulsion model is that the forward force $F_{\text{swim}}\hat{\mathbf{e}}$ that drives the cell forward must be generated by the flagella. Flagella generate forward thrust by pushing fluid backwards and Newton's third law demands that the total force on the fluid must be $-F_{\text{swim}}\hat{\mathbf{e}}$. Therefore, we introduce a special new type of particle to the rigid body, that implicitly captures this effect of the flagella. This new type is still rigidly connected to the central particle of the cell body, but unlike the other beads, it does not experience friction or random forces. Instead, it applies a force $-F_{\text{swim}}\hat{\mathbf{e}}/N_{\text{flag}}^{\text{bead}}$ to the fluid that is interpolated to nearby lattice nodes like the other coupling forces. Here, $N_{\text{flag}}^{\text{bead}}$ is the number of beads that make up the flagellum. A graphical representation will be shown in Section 7.2, Fig. 7.1.

3.2.3 Run-and-tumble dynamics

Many bacteria cannot only self-propel, but also self-steer to some degree. We capture both modes of active motion in the framework of Eqs. (2.20) and (2.22) with time-dependent F_{swim} and M_{act} or, equivalently, time-dependent v_{swim} and ω_{act}.

As mentioned in Section 1.2.1, a swimming pattern often found in bacteria such as *E. coli* is the so-called run-and-tumble pattern.

Other patterns, i.e., sequences of propulsion and steering, exist and will be discussed in Chapter 6.

During a run, the bacterium swims along its body axis $\hat{\mathbf{e}}$ with approximately constant speed. During a tumble, the bacterium stops propelling forward, and instead rotates to a new direction. Because the duration of the molecular motor reversal that triggers the tumble is random and the flagellar dynamics during tumbling appear chaotic, the angle of reorientation Θ_{tumble} does not have a fixed value, but rather follows a broad distribution [84].

The algorithm we use to model run-and-tumble behaviour seeks to capture the essential features of this stochastic reorientation by random torques. It follows previous models for bacterial tumbling [171] and their implementation into the framework of our rigid body cells [172].

The durations t_{run} and t_{tumble} of runs and tumbles are both exponentially distributed as

$$p(t_\star) = \frac{1}{\langle t_\star \rangle} \exp(-t_\star / \langle t_\star \rangle), \tag{3.6}$$

where p denotes the probablility density and $\star \in \{\text{run}, \text{tumble}\}$. The respective means $\langle t_{\text{run}} \rangle$ and $\langle t_{\text{tumble}} \rangle$ are adjustable parameters of the model.

For numerical implementations with large time steps or for comparison with experiments that have limited time resolution, the geometric distribution can be used instead. It represents a discrete version of the exponential distribution and reads

$$P(k; q_\star) = (1 - q_\star)^{k-1} \, q_\star. \tag{3.7}$$

Here, $P(k; q_\star)$ is the probability that after k "steps" the current state (run or tumble) is terminated and the bacterium switches to the next state. The mathematical "step" mentioned here is identified with the numerical model evaluation time step Δt or with the experimental time step. The assumption of the geometric distribution is that for all steps, the probability of leaving the current state is constant. The termination rates $q_\star$, where again $\star \in \{\text{run}, \text{tumble}\}$, are related to the respective mean times via

$$\langle t_\star \rangle = \Delta t \, \langle k \rangle = \frac{\Delta t}{q_\star}. \tag{3.8}$$

To obtain the tumble angle distribution, we approximate the directional change as a diffusive rotation process with diffusion coefficient $D_{\text{rot, tumble}}$. For random, unbiased diffusion of the bacterial director $\hat{\mathbf{e}} = (\sin(\theta)\cos(\phi), \sin(\theta)\sin(\phi), \cos(\theta))$ we have in spherical coordinates

$$\partial_t p(\theta, \phi, t) = D_{\text{rot, tumble}} \nabla^2 p(\theta, \phi, t) \tag{3.9}$$

for the probability density p of orientation (θ, ϕ) after time t. With $p(\theta, \phi, 0) = \delta(\theta)$ as the inital condition, this equation has an analytical solution given by

$$p(\theta, \phi, t) = \sum_{l=0}^{\infty} \frac{2l+1}{2} \exp[-l(l+1) D_{\text{rot, tumble}} t] P_l(\cos\theta) \sin(\theta), \tag{3.10}$$

where P_l denotes the Legendre polynomial of order l.[1]

In our model, we draw a tumble time t_{tumble} from Eq. (3.6) or Eq. (3.7) and then insert it into Eq. (3.10) to generate a distribution of tumble angles Θ_{tumble}. From this tumble angle distribution, we draw an angle and apply a steering torque with associated angular velocity $\omega_{\text{act}} = \Theta_{\text{tumble}}/t_{\text{tumble}}$ to the cell center of mass for the duration of the tumble to rotate it to the new direction. The direction $\hat{\mathbf{n}}$ of rotation is kept constant during the tumble. It is chosen at random (Eq. (3.10) does not depend on ϕ), but fulfills $\hat{\mathbf{n}} \cdot \hat{\mathbf{e}} = 0$ at the beginning of the tumble. The mean tumble angle can be calculated as

$$\langle \cos(\Theta_{\text{tumble}}) \rangle = \frac{1}{2D_{\text{rot, tumble}} \langle t_{\text{tumble}} \rangle + 1} \tag{3.11}$$

in the time-continuous version and

$$\langle \cos(\Theta_{\text{tumble}}) \rangle = \frac{\Delta t / \langle t_{\text{tumble}} \rangle}{\exp(2D_{\text{rot, tumble}} \Delta t) + \Delta t / \langle t_{\text{tumble}} \rangle - 1} \tag{3.12}$$

in the discrete formulation [172]. From these results, we tune $D_{\text{rot, tumble}}$ such that $\langle \Theta_{\text{tumble}} \rangle$ coincides with experimentally observed values.

For "dry" swimming, the application of the rotating torque $\gamma^{\text{r}} \omega_{\text{act}} \hat{\mathbf{n}}$ is enough to describe tumbles. For "wet" swimming however, the torque applied to the cell must be counterbalanced by

[1] This framework of treating rotational diffusion with continuum equations can be used to derive Eq. (2.18) in a much simpler way than by invoking stochastic calculus. Noting that $\langle \hat{\mathbf{e}}(0) \cdot \hat{\mathbf{e}}(t) \rangle = \langle \cos(\theta) \rangle (t)$ we can use the solution given in Eq. (3.10) to calculate the mean on the right hand side by using orthogonality relations of the Legendre polynomials.

a torque on the fluid to mimic hydrodynamic *self*-rotation analogous to self-propulsion: The tumble rotation is not generated by an external torque, but by a torque that the bacterium generates through flagellar actuation and fluid interaction. The countertorque is realised be two opposing forces on the fluid that act perpendicular to the cell orientation, in the plane of rotation. To achieve this, we use the "flagellar" particles introduced in Section 3.2.2. Here however, instead of connecting them to the cell body in a straight line behind the cell body pointed backwards, we connect one of them to the first bead of the raspberry and one to the last bead (see Ref. [172] for more detail). The flagellar particles are pointed perpendicularly outward from the cell's symmetry axis to apply a torque to the fluid but no net force. Since the flagellar particles are connected rigidly to the cell raspberry, they follow the rotation of the cell body, maintainng the correct orientation.

3.2.4 Application in simulations

3.2.4.1 Time discretisation

The Langevin equations of motion for the particle position and orientation as well as the Navier-Stokes equations for the fluid are discretised in time according to Sections 2.1.5 and 2.2.4.2 with a time step δt. The algorithms for bacterial control (e.g., changes to $F_{\text{swim}}(t)$ or $M_{\text{act}}(t)$) are evaluated with the model time step Δt. Necessarily, Δt is an integer multiple of δt, but they do not have to be the same. Typically, we choose Δt five to one hundred times larger than δt. This reflects the difference in timescale between

particle momentum relaxation (fast) and changes in the cell state (slow). It also greatly increases the computational efficiency of the bacterial control algorithms.

3.2.4.2 Density scaling

As outlined in Section 2.1.2.3, the natural description of the stochastic motion of micrometer-sized particles such as bacteria is the Brownian or "overdamped" equation of motion due to the extremely short momentum relaxation time $\tau^{\mathrm{t}} = m/\gamma^{\mathrm{t}}$ of such particles. However, the hydrodynamic Navier-Stokes equations that the lattice Boltzmann method solves are based on a description of the fluid motion that contains momentum. Furthermore, the coupling between particles and fluid outlined in Section 2.2.4.6 is based on velocities, which are not well defined in the Brownian dynamics picture.

Therefore, to have consistency in the inclusion of momentum as well as to facilitate the fluid coupling, we must use the Langevin, "underdamped" Eqs. (2.20) and (2.22) to obtain particle trajectories[2]. The extremely short (angular) momentum relaxation time scales τ^{t} and τ^{r} now pose a problem for numerical integration, because the numerical time step δt must be smaller than $\min(\tau^{\mathrm{t}}, \tau^{\mathrm{r}})$ to resolve the adaption of the particle (angular) momentum to a

[2]The introduction and discussion of (rotational) Brownian dynamics in Chapter 2 were not in vain, despite the fact that they are not used in the numerical scheme. The motion of bacteria *is* overdamped on any timescale that we are interested in for the purposes of this thesis. The analytical results obtained from the overdamped equations of motion stay valid, and we will make reference to them when discussing our results.

change in forces or torques.

To alleviate this problem, we artificially increase $\tau^{\mathrm{t}} = m/\gamma^{\mathrm{t}}$ and $\tau^{\mathrm{r}} = I/\gamma^{\mathrm{r}}$ in simulations by increasing the particle mass and rotational moment of inertia, or equivalently, the particle mass density ρ. Of course, we must take care not to increase τ^{t} so much that it becomes comparable to any timescale of interest. The mass increase must be small enough to have no impact on any observable that we extract from simulations. For example, if we simulate a system in which the mean tumble time $\langle t_{\mathrm{tumble}} \rangle = 0.1\,\mathrm{s}$ is the smallest time scale of physical relevance and the rotational momentum time scale is $\tau^{\mathrm{r}} = 75\,\mathrm{ns}$ as in the example in Section 2.1.3.2, we would choose a bacterial density $\rho = 10^4 \rho^{\mathrm{water}}$ to bring τ^{r} to around $1\,\mathrm{ms} \ll \langle t_{\mathrm{tumble}} \rangle$. This would leave the results we obtain from simulations virtually unchanged, but allows us to speed up simulations by a factor of 10^4 by increasing the numerical time step δt.

3.3 Implementation

The bacterial model described in this chapter as well as the extensions that will be introduced in Chapters 5 to 7 are implemented in a python package. This package is employed in all simulations that were used to obtain the results presented in the aforementioned chapters. Different versions of the code are publicly available in the datasets [173–175] that accompany the publications [3–5] on which the chapters are based.

The implementation is based on ESPResSo [134] as the simula-

tion engine to solve the stochastic equations of motion, Eqs. (2.20) and (2.22). ESPResSo also handles the rigid body dynamics (Section 3.1.1), the lattice Boltzmann algorithm (Section 2.2.4), the particle coupling (Section 2.2.4.6) and the "wet" swimming algorithm (Section 3.2.2).

My custom code on top of ESPResSo is centered around the `Swimmer` class. It wraps the ESPResSo particles that comprise the rigid body we use to model bacteria. It provides an intuitive interface to create the rigid bodies based on the geometrical parameters $r_{\text{body}}, l_{\text{body}}, N^{\text{bead}}$ and to add them to an ESPResSo simulation system. It also takes care of the calculation of particle properties like mass, moment of inertia and friction coefficients.

During a simulation, various class methods implement the (time-dependent) motility patterns such as run-and-tumble, or the growth and cell division algorithm detailed in Chapter 5. This makes it easy to perform simulations of motile and/or growing bacteria in complex environments, because the basic physical entity, the cell, is represented by the basic software entity, the `Swimmer`. The custom package also offers a variety of utility functionality to, e.g., set up complex boundary shapes, interactions or deal with logging and parameter handling.

In a typical simulation, ESPResSo does most of the "heavy lifting" in terms of computational expense, meaning that the execution time is dominated by solving the equations of motion rather than evaluating the bacteria-related algorithms. There are some performance relevant algorithms, for example the calculation of the tumble angle distribution Eq. (3.10) or the neighbour search

needed to simulate phage infection in Chapter 7. In these cases, the code is optimised for speed using, e.g., function return caches or reformulation of the problem into set operations with constant execution time. This ensures that the execution time footprint of the bacterial modeling always stays low.

The python package is built in a modular way following coding best practices. It is version controlled and well tested, ensuring that all components continue to work well whenever the software or its dependencies change. Versions of the package used to perform the research presented in the following chapters are publicly available at Refs. [173–175], the development version will be published on GitHub. At the time of writing this thesis, the software is under continued development. If you are interested in learning or using or contributing to the package, feel free to contact me.

Chapter 4

The influence of motility on bacterial accumulation in a microporous channel

This chapter contains in large parts text that is taken verbatim from M. Lee, C. **Lohrmann**, K. Szuttor, H. Auradou, and C. Holm, "The influence of motility on bacterial accumulation in a microporous channel", Soft Matter **17**, 893 (2021), a publication to which I contributed preparation of figures and co-writing of the manuscript draft.

4.1 Introduction

The first complex environment we consider for our motile bacteria is the one that most surface-based microorganisms on our planet face: Porous confinement with external flow. Many relevant habitats such as soil, aquifers, larger host organisms like humans or man-made environments like filtration systems fall in this cate-

gory.

On a large scale, confinement and flow determine the dispersion behaviour of bacteria [176], but the underlying mechanisms can only be understood by considering the scale of single pores. Even in simple systems consisting only of basic geometries such as flat walls or straight channels, the interplay between bacterial swimming, confinement and external flow can lead to interesting and sometimes counterintuitive phenomena [29]. These include, e.g., upstream swimming [177–179], drift trajectories on surfaces [180, 181] or helicoidal trajectories [182, 183]. The distribution of bacteria is also affected in nontrivial ways, exemplified by shear-induced depletion [184], or accumulation of bacteria on the rear ends of surfaces in flow [185–187]. The distribution of bacteria, especially in the vicinity of surfaces, is very relevant for the formation of biofilms and therefore of interest in a wide area of engineering and medical applications.

In this chapter, we seek to use our bacterial model to reproduce and explain the experimental results of Miño *et al.* [187]. In their study, they use a rectangular channel with a single cylindrical obstacle to study the influence of external flow on the distribution of motile bacteria and find an accumulation *behind* the obstacle. The scale of their experiment is perfectly suited for our numerical model as we are able to recreate their experimental setup and explicitly model individual swimming bacteria. Going beyond the experimental design, we also investigate the influence of swimming parameters as well as the choice of geometry.

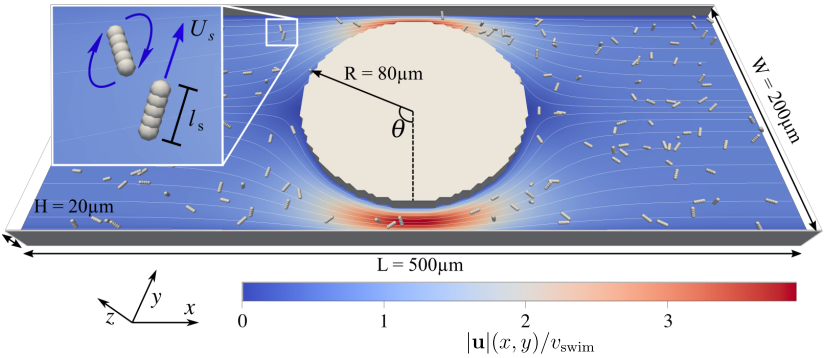

Figure 4.1. The simulation set-up consists of a rectangular fluid-filled channel of size $(L, W, H) = (500\,\mu\text{m}, 200\,\mu\text{m}, 20\,\mu\text{m})$ with a cylindrical obstacle of radius 80 μm placed at the center of the box. Inside the channel are up to 159 swimmers, each consisting of five interaction sites with the lattice-Boltzmann fluid, that are capable of performing run-and-tumble as indicated on the inset. The fluid is driven by an external force density. The stream lines and the colormap represent the driven flow-field projected on to the xy-plane normalized by the swimming speed v_{swim}. Reproduced from Ref. [2] with permission from the Royal Society of Chemistry.

4.2 Methods

4.2.1 Geometry and flow

The boundary geometry for the fluid and the bacteria is set up according to the experimental design in Ref. [187] as shown in Fig. 4.1. It comprises a rectangular channel of size $L \times W \times H$ and a cylindrical obstacle of radius R in the center of the channel, which we define as the origin of our coordinate system. The frame of reference is the laboratory frame. Fluid flow is simulated using

the lattice Boltzmann method with bounce back boundary conditions on the solid surfaces as introduced in Section 2.2.4. Along the x-direction, i.e., along the channel, we employ periodic boundary conditions.

The flow is driven through the channel by applying a constant force density onto each lattice-Boltzmann node.

The system's geometry and the resulting flow field are depicted in Fig. 4.1. We characterize the flow strength by the average value $\langle |\mathbf{u}| \rangle := \frac{1}{W \times H} \int_{-H/2}^{H/2} \int_{-\frac{W}{2}}^{\frac{W}{2}} |\mathbf{u}|(x = 250\,\mu\text{m}, y, z)\,\mathrm{d}y\,\mathrm{d}z$, measured at the outlet of the channel. For all simulations, the Reynolds number of the flow is very small $\mathrm{Re} \sim 10^{-2}$. This is manifested through the spatial symmetries of the flow field with respect to the center of the box. Note that from now on, we always normalize the flow strength by the swimming speed v_{swim} of our model bacteria unless otherwise stated.

4.2.2 Swimmer model

We use the $N^{\text{bead}} = 5$ cell model with $l_{\text{body}} \sim 5\,\mu\text{m}$ and $r_{\text{body}} = 0.5\,\mu\text{m}$ as introduced in Section 3.1. The purely repulsive WCA potential (see Section 3.1.2.1) captures steric interactions among swimmers and between swimmers and surfaces. The fluid coupling follows the principles of of "wet" swimming with $N_{\text{flag}}^{\text{bead}} = 1$, as described in Section 3.2.2. Cells perform run-and-tumble dynamics according to the algorithm outlined in Section 3.2.3. The swimmers' motion can thus be characterized by the mean run and tumble durations $\langle t_{\text{run}} \rangle$, $\langle t_{\text{tumble}} \rangle$ as well as the swimming speed v_{swim}.

The numerical parameters (listed in Appendix A.1) are chosen such that $v_{\mathrm{swim}} = 24\,\mu\mathrm{m\,s}^{-1}$, which is very close to the average velocity of the bacteria used in Ref. [187].

We introduce $N = 159$ swimmers to the system to achieve the same low density of bacteria that is used in the experiment. In the following we analyze the swimmer distribution in the channel in various situations. We hence define the swimmer distribution $\rho(\mathbf{r})$ as

$$\rho(\mathbf{r}) = \frac{1}{\mathcal{T}} \sum_{i=1}^{N} \int_0^{\mathcal{T}} \delta^3(\mathbf{r}_i(t) - \mathbf{r})\,\mathrm{d}t\,, \tag{4.1}$$

where $\mathbf{r}_i(t)$ is the ith swimmer's position at time t, and $\mathcal{T}$ the total simulation duration. It is a time-averaged one-particle distribution. The projection onto the xy-plane is then done by taking the average over the z-direction: $\rho(x, y) = \frac{1}{H} \int_{-H/2}^{H/2} \rho(\mathbf{r})\,\mathrm{d}z$. We make the swimmer distribution $\rho(\mathbf{r})$ dimensionless by normalizing it with the homogeneous swimmer density $\rho_{\mathrm{h}} = N/V_{\mathrm{box}}$, where V_{box} is the volume of the simulation box that is accessible to swimmers, i.e., excluding the volume occupied by the obstacle.

Next, we define some quantities that will be useful for describing our observations. The swimmer distribution around the obstacle $\rho_{\mathrm{obs}}(\theta)$ as a function of polar angle θ is given by $\rho_{\mathrm{obs}}(\theta) = \frac{1}{850\,\mu\mathrm{m}^2} \int_{80\,\mu\mathrm{m}}^{90\,\mu\mathrm{m}} \rho(r, \theta) r\,\mathrm{d}r$. Similarly, the swimmer distribution on the lateral walls $\rho_{\mathrm{wall}}(x)$ at $y = -W/2$ and $y = W/2$ as a function of lateral position x is $\rho_{\mathrm{wall}}(x) = \frac{1}{2\times 10\,\mu\mathrm{m}} (\int_{-100\,\mu\mathrm{m}}^{-90\,\mu\mathrm{m}} \rho(x, y)\,\mathrm{d}y + \int_{90\,\mu\mathrm{m}}^{100\,\mu\mathrm{m}} \rho(x, y)\,\mathrm{d}y)$. Consequently, we calculate the swimmer density behind the obstacle using $\overline{\rho_{\mathrm{obs}}^{\mathrm{behind}}} = \frac{1}{\pi} \int_{\pi}^{2\pi} \rho_{\mathrm{obs}}(\theta)\,\mathrm{d}\theta$ and on the lateral walls using $\overline{\rho_{\mathrm{wall}}} = \frac{1}{L} \int_{-L/2}^{L/2} \rho_{\mathrm{wall}}(x)\,\mathrm{d}x$.

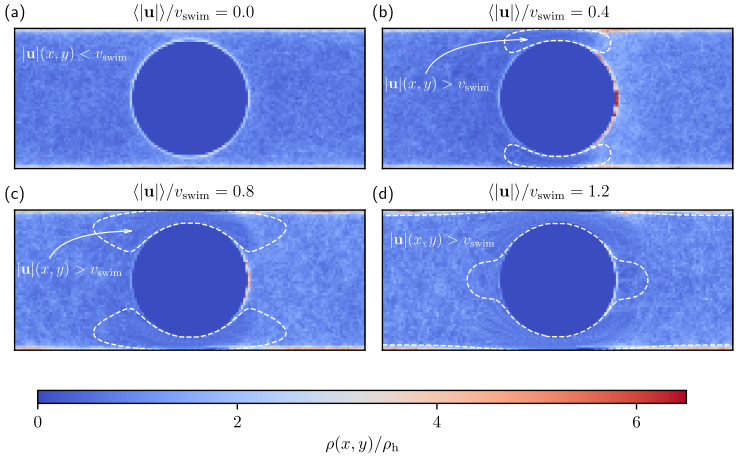

Figure 4.2. The swimmer distribution $\rho(x, y)$ normalized with the homogeneous swimmer density ρ_{h} in the channel for various external flow inputs. The dashed lines are contours, separating the regions where the magnitude of flow velocity $|\mathbf{u}|(x, y)$, averaged in the z-direction, is greater than the magnitude of the swimming velocity v_{swim}. Reproduced from Ref. [2] with permission from the Royal Society of Chemistry.

4.3 Results

4.3.1 Accumulation behind the obstacle

Figure 4.2 shows the spatial distribution of swimmers calculated using Eq. (4.1) inside the channel for different flow conditions. Additionally, Fig. 4.3(a) and Fig. 4.4 quantitatively present the spatial distribution of the swimmers around the obstacle and on the lateral walls, respectively. Notice first that, in the absence of flow, a significant fraction of swimmers (i.e., $\rho > \rho_{\mathrm{h}}$) is distributed

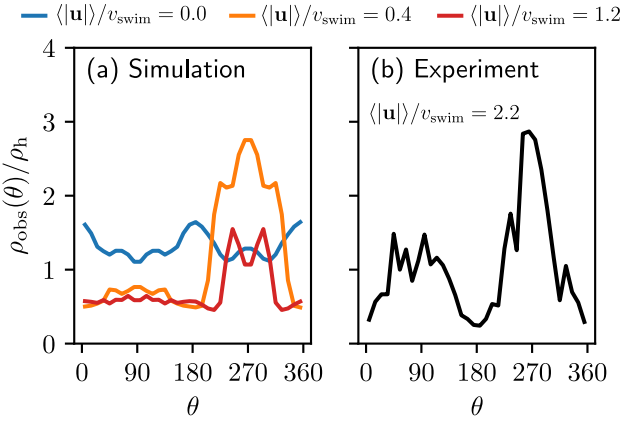

Figure 4.3. The normalized swimmer distribution around the obstacle $\rho_{\mathrm{obs}}/\rho_{\mathrm{h}}$ in (a) the simulation and (b) the experiment (Ref. [187]) as a function of the polar angle around the center of the obstacle. $\theta = 0$ and 180 correspond to the lateral sides, and $\theta = 90°$ and $\theta = 270°$ to the upstream and downstream sides, respectively. The blue, orange and red lines in (a) stand for the velocity ratios $\langle|\mathbf{u}|\rangle/v_{\mathrm{swim}} = 0.0$, 0.4, and 1.2. Reproduced from Ref. [2] with permission from the Royal Society of Chemistry.

both on the lateral walls and around the obstacle. The maxima of the blue curve in Fig. 4.3(a) at $\theta = 0°$ and 180°, as well as that of the blue curve in Fig. 4.4 at $x = 0$ show a small enhancement of the accumulation at places where the obstacle and the lateral walls are closest. We refer to these regions as constrictions. The homogeneous swimmer accumulation on the surfaces, i.e., both on the lateral walls and on the obstacle, is to be expected [188–191], since at the chosen running duration, the persistence length $l_{\mathrm{p}} =$

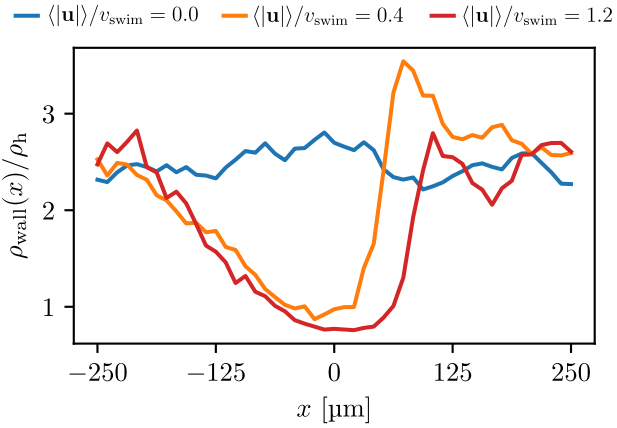

Figure 4.4. The normalized swimmer distribution along the lateral walls $\rho_{\text{w}}/\rho_{\text{h}}$ for different flow velocities. The blue, orange and red lines stand for $\langle|\mathbf{u}|\rangle/v_{\text{swim}} = 0.0$, 0.4, and 1.2, respectively. Reproduced from Ref. [2] with permission from the Royal Society of Chemistry.

24 µm is comparable to the length scale of the channel. Because the swimmers tumble and swim in all possible directions with equal probability, at some point they will touch a surface and stay there until tumble events orient their swimming directions away from the surface.

Additionally, we observe that more swimmers are accumulated on the lateral walls than around the obstacle. This can be explained by the geometric characteristics of the surfaces. The obstacle is a convex surface, and not capable of containing swimmers for as long as the flat walls can do, as observed in other studies as well [192, 193]. We attribute this to the simple fact that the

swimmers will depart from any convex surface merely by swimming straight in any direction that was initially tangent to the surface. The influence of the convexity will become more significant with increasing running duration t_{run}.

Introducing an external flow, we measure an inhomogeneous distribution of swimmers on the surfaces. A larger number of swimmers accumulates on the downstream side of the obstacle while the density of swimmers on the upstream side of the obstacle is reduced, falling below the homogeneous swimmer density ρ_{h}. For $\langle|\mathbf{u}|\rangle / v_{\mathrm{swim}} = 0.2$ nearly three times more swimmers per unit of volume are located at the rear of the obstacle than anywhere else in the fluid. This finding is in agreement with the observation made in the experiment [187].

We find that stronger flow velocities reduce the extension of the regions where the accumulation is observed. Consequently, the swimmer densities $\overline{\rho_{\mathrm{obs}}^{\mathrm{behind}}}$ behind the obstacle and $\overline{\rho_{\mathrm{wall}}}$ on the lateral walls reduce with increasing external flow strength, as indicated by the solid lines in Fig. 4.5. To further explain this, we mark the regions where the magnitude of the local flow velocity $|\mathbf{u}|$ is higher than the swimming velocity v_{swim} in Fig. 4.2. For $\langle|\mathbf{u}|\rangle / v_{\mathrm{swim}} < 1.0$, the regions where $|\mathbf{u}| > v_{\mathrm{swim}}$ are localized in the constrictions. At the strongest external flow ($\langle|\mathbf{u}|\rangle / v_{\mathrm{swim}} = 1.2$), the region covers the entire channel apart from two small domains located at the rear and front of the obstacle, and parts of the lateral walls located away from the constrictions.

Higher local flow speed regions act as one way streets; all swimmers are moving down-stream regardless of their swimming direc-

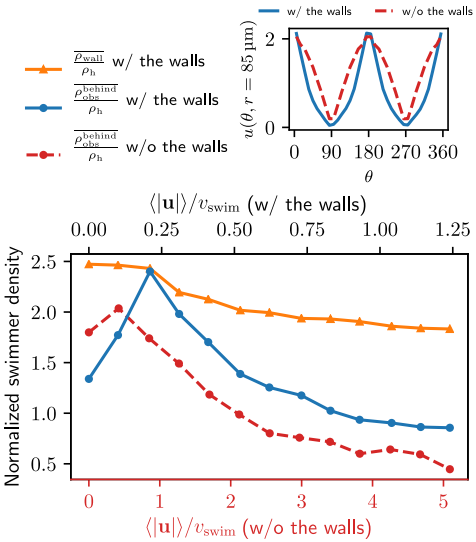

Figure 4.5. Main: The average swimmer density $\overline{\rho_{\text{obs}}^{\text{behind}}}$ behind the obstacle (blue solid line), and $\overline{\rho_{\text{wall}}}$ on the walls (orange solid line) as a function of the external flow strength $\langle|\mathbf{u}|\rangle/v_{\text{swim}}$ in the presence of the lateral walls, as well as the average swimmer density behind the obstacle in the absence of the lateral walls (red dashed line). Top inset: the flow velocity $u(\theta, r = 34\sigma)/\langle|\mathbf{u}|\rangle$ around the obstacle as a function of polar angle θ for both cases, with (blue), and without (red) the lateral walls. Reproduced from Ref. [2] with permission from the Royal Society of Chemistry.

tion, since they cannot compete with the flow. In regions with lower local flow speed, bacteria can swim in all directions, including upstream. The borders of the stronger flow regions therefore act as an additional boundaries to upstream swimmers. Just like the "real" boundaries, swimmers cannot cross so they accumulate there until they are oriented away by shear or tumbles. This effect leads to an asymmetric distribution of swimmers, with a higher density in the right half of the channel.

Our argument implies that many swimmers that accumulate behind the obstacle are swimming against the local flow direction. To support this idea we calculate, as shown in Fig. 4.6, the ratio of the number of events where a swimmer enters the accumulation region by swimming upstream $\mathcal{E}_{\mathrm{up}}$ to the total number of entering events $\mathcal{E}$. This ratio stays roughly constant at a high value of about 70% irrespective of the increasing external flow. This is in contrast to the ratio of upstream swimming bacteria in the whole system (N_{up}/N), which decreases monotonically with increasing external flow. From the two curves we can conclude that the smaller number of accumulated swimmers behind the obstacle at large external flow speeds is due to the fact that the total number of swimmers that are capable of accumulating is reduced. The mechanism of accumulation itself (upstream swimming into niches bordering a surface or a strong flow region) remains unaltered despite the increasing external flow.

The accumulation behind the obstacle (blue curve in Fig. 4.5) displays a non-monotonic behavior which can be explained as follows. With a very weak external flow, the available space for the

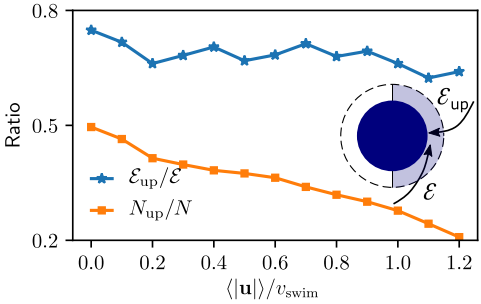

Figure 4.6. Blue solid line: The ratio of the number $\mathcal{E}_{\mathrm{up}}$ of events where upstream swimmers enter behind the obstacle to that of $\mathcal{E}$ events where swimmers enter behind the obstacle regardless of their swimming directions. Orange: The time averaged ratio of the number N_{up} of swimmers that swim upstream in the whole system to the total number N of swimmers. A swimmer is counted as upstreaming if the x-component of its velocity in the laboratory frame is negative. Inset: A schematic visualization of events counted by $\mathcal{E}$ and $\mathcal{E}_{\mathrm{up}}$. Reproduced from Ref. [2] with permission from the Royal Society of Chemistry.

swimmers to accumulate is relatively large. The number of swimmers reaching the rear is thus reduced, because a large fraction is accumulated elsewhere. The accumulation exhibits a maximum around $\langle|\mathbf{u}|\rangle/v_{\mathrm{swim}} = 0.2$. This value coincides with the flow strength at which the local flow speed at the constriction becomes larger than the bacterial swimming speed. The one way street mechanism now leads to the maximum accumulation because the constrictions effectively block the upstream swimmers but the overall flow speed is not yet strong enough to flush the swimmers. With a further increase of the external flow strength, the size of the small flow niche shrinks, as can be observed in Fig. 4.2. Naturally, this

limits the accessible surface area, and therefore the accumulation decreases.

4.3.2 Role of lateral walls on accumulation

In this section we will analyze in detail the effects that the lateral walls play in the bacterial accumulation. Looking back again into Fig. 4.2, we note the preferential accumulation of the bacteria in the right half of the channel. Moreover, a significant number of bacteria accumulate on the walls regardless of external flow strength. We argue that these accumulated swimmers on the walls can potentially migrate to the obstacle.

Due to the geometry, the lateral walls orient the swimmers to the $\pm\mathbf{e}_x$ directions as they slide along. The upstreaming fraction can travel along the channel even under strong external flow, as the no-slip boundary condition provides niches of low flow velocities. Using this route, a swimmer can move up to the constriction with a high probability. Behind the constriction, the streamlines fan out and depart from the wall. This flow away from the walls causes the bacteria to reorient and turn towards to the cylinder.

To quantify our argument, we also performed a new set of simulations in which the lateral walls were removed and replaced by a periodic boundary condition in the y direction. To make the new system as comparable to the one with walls, the system size is also changed to $(L, W, H) = (500\,\mu\text{m}, 500\,\mu\text{m}, 20\,\mu\text{m})$. In addition, we adjusted the force densities, such that the flow velocity and profile around the obstacle are as close as possible to the original geometry (see the top right inset in Fig. 4.5). The total number of

swimmers is changed from 159 to 248 to obtain better statistics. Notice that the change in the total number of swimmers does not affect the overall dynamics of the total system since we remain in the low density limit.

In the absence of lateral walls, a smaller accumulation behind the obstacle is found, except for the first two smallest external flow conditions as represented by the red dashed line in Fig. 4.5. This is because with a very weak external flow strength, the swimmers can accumulate on any surface. Without the lateral walls, it is thus natural that more swimmers accumulate at the cylinder. With a stronger external flow strength, however, the swimmers without a lateral confinement will only end up behind the obstacle if a tumble happens at the right time with the right angle to allow them to come close to the surface of the obstacle. Therefore, for most of the time, the bacteria just follow the fluid flow.

4.3.3 Influence of swimming characteristics

In order to elucidate the influence of bacterial parameters on donwstream accumulation, we now vary the running duration t_{run}. We keep the external flow strength fixed at $\langle |\mathbf{u}| \rangle = 0.6 v_{\mathrm{swim}}$.

In Fig. 4.7 we display the swimmer densities behind the obstacle and on the lateral walls as a function of $\langle t_{\mathrm{run}} \rangle \in [0.16\,\mathrm{s}, 21\,\mathrm{s}]$. Intriguingly, the swimmer accumulation behind the obstacle peaks, and then decreases, whereas the bacterial density on the walls monotonically increases.

When $\langle t_{\mathrm{run}} \rangle$ is very small, the behavior of the swimmers is similar to Brownian motion of passive particles. As they change their

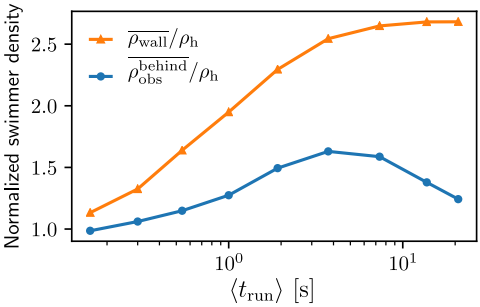

Figure 4.7. The normalized swimmer density $\overline{\rho_{\text{obs}}^{\text{behind}}}/\rho_{\text{h}}$ behind the obstacle (blue solid line) and $\overline{\rho_{\text{wall}}}/\rho_{\text{h}}$ on the lateral walls (orange solid line) as a function of the swimming Péclet number Pe_s. Reproduced from Ref. [2] with permission from the Royal Society of Chemistry.

direction rapidly, their swimming only leads to enhanced diffusion, but not to persistent motion. The lack of persistent motion yields a very small accumulation density on the boundaries.

As $\langle t_{\text{run}} \rangle$ increases, the swimmers start showing an increasingly persistent and directed motion that allows them to swim for a sufficient amount of time to reach the boundaries.

With a large $\langle t_{\text{run}} \rangle > 7\,\text{s}$, however, the situations on the walls and behind the obstacle start diverging. This is primarily due to the shape of the boundaries as mentioned in Section 4.3.1. The swimmers with very high $\langle t_{\text{run}} \rangle$ rarely change their directions. Therefore, the walls can trap swimmers much longer than the convex obstacle.

Fixed by the system's geometry, we can find the optimal running duration for the accumulation behind the obstacle around

$\langle t_{\mathrm{run}} \rangle \sim 4\,\mathrm{s}$ from Fig. 4.7. It is worth noting that the swimming Péclet number, the ratio of the persistence length to the body size, is not a dimensionless parameter that can capture the essential aspects of bacterial accumulation in porous media. This is because the ratio of local fluid flow speed to the swimming speed also affects the accumulation as discussed above.

4.3.4 Limits of the coarse-grained bacterial model

Our bacterial model and the simulation could reproduce qualitatively the preferred accumulation behind the obstacle as observed in the experiment of Miño *et al.* [187], but there remains a quantitative discrepancy. The simulations overall yielded a smaller accumulation density around the obstacle than found in the experiment. In the simulation, the swimmers were mostly washed away when the average flow speed exceeded $\langle |\mathbf{u}| \rangle = 1.2 v_{\mathrm{swim}}$, whereas in the experiment, the bacteria managed to accumulate even under a stronger external flow of $\langle |\mathbf{u}| \rangle \sim 2.2 v_{\mathrm{swim}}$. The difference in accumulation density was found particularly pronounced in front of the obstacle.

We present two reasons for this discrepancy. First, the swimming speed of our bacterial model was kept constant in the simulation in order to achieve a better understanding of the interplay between the local flow field and the swimmers' motility. In the experiment, the bacterial swimming speed distribution follows a half-normal distribution with a standard deviation that is as large as the mean v_{swim} [187]. This means that numerous bacteria are able to swim faster than v_{swim} and therefore more of them can

accumulate behind the obstacle at large $\langle|\mathbf{u}|\rangle$.

Second, we neglected the rotation of the bacterial body around its main axis and the counter-rotation of the flagella that causes the bacteria to swim in circular trajectories on surfaces [180]. Cirle swimming results in a lower effective diffusivity, and can cause the bacteria to explore less space in a given time compared to straight swimming. In front of the obstacle, bacteria escape the region of small flow by swimming in any direction (except straight into the cylinder), so only circular swimming could cause the prolonged residence time in this area.

4.4 Conclusions

Our simulations demonstrated that motile microorganisms preferably accumulate at the downstream side of surfaces. The reason why these surfaces are preferred over upstream oriented surfaces is linked to upstream swimming of motile bacteria. Unlike passively advected partcicles such as colloids, swimming bacteria can swim against the flow until they either reach a downstream surface or a region where the local flow speed is larger than the swimming speed. There, they accumulate. Downstream swimming bacteria also accumulate on upstream surfaces to some extent, but because the flow drags them along the surface into regions with larger local flow speed where they get washed away, this accumulation is less pronounced.

This result is in line with the recent results reported by Alonso-Matilla *et al.* [194]. In their study, they investigated the dispersion

of swimmers in a matrix of obstacles, whose shape is systematically altered from a circle to an ellipsoid and to a triangle. They showed that, as long as an external flow is moderate, an upstream swimming pattern can be observed not only with circular obstacles but also with triangular obstacles, the edges of which are pointing to the downstream direction. This suggests that the downstream accumulation is not restricted to a specific obstacle shape.

In the present study, the confinement by lateral walls plays a substantial role on the swimmer accumulation behind the obstacle. The walls generate additional zones of small fluid velocity due to the no-slip boundary condition which provide a pathway for the bacteria to swim upstream. This mechanism is an important element since it allows swimmers to come closer to the constrictions, from which the swimmers can migrate to the obstacle. The migration of bacteria from the walls to the cylinder surface is triggered by the local shear that reorients the bacteria toward the cylinder. This effect can only be captured by models like ours that have sufficient resolution of the bacterial shape and do not reduce them to point particles. Finally, we observe that an optimal bacterial accumulation can be achieved when the running duration is around 4 s for our geometry.

Our observations can help to design and optimize strategies to sort and trap microorganisms. They can also reveal insights into the physical mechanisms governing the filtration of motile bacteria in porous media on a larger scale.

Chapter 5

A novel model for biofilm formation in porous media flow

This chapter contains in large parts text that is taken verbatim from C. **Lohrmann** and C. Holm, "A novel model for biofilm initiation in porous media flow", Soft Matter **19**, 6920 (2023), a publication to which I contributed the modelling, simulations, data analysis and writing of the manuscript draft.

5.1 Introduction

After having elucidated the intricacies of the interplay between bacterial motility and porous media flow in the previous chapter, we now continue the investigation beyond the planktonic, i.e., freely swimming, stage of bacterial life. A significant fraction of bacteria in surface habitats live in biofilms [195]. As mentioned in Chapter 4, these habitats are often porous and external flows are relevant. This does not only affect the swimming of bacteria, but also the initiation and formation of biofilms. They have to

withstand the shear forces but they also benefit from flows since they provide nutrients.

Biofilms can have profound positive and negative impact in medical and engineering settings, see Sections 1.1.2 and 1.1.3. It is therefore paramount to understand how fluid flow impacts biofilm formation, and what the qualitative and quantitative consequences are for the properties of the porous medium.

Experiments show interesting and nontrivial behaviour of bacteria and biofilms in porous media flow: Biofilms do not form homogeneously on all surfaces, but preferentially on the downstream side of obstacles or corrugated surfaces [185, 187]. There can be (visco-) elastic deformation [196] and a change of the internal structure of the biofilm [197]. Under the right conditions, streamers, i.e., filamentous biofilms suspended in flow, form and can cause rapid clogging of porous structures [198, 199]. All these effects are relevant in the early stages of bacterial colony formation and have an influence on the growth of biofilms in porous media on a larger scale [200, 201]

On the theoretical side, many models exist for bacteria and biofilm formation with different levels of detail, e.g., individual bacteria [202–205], cellular automata [206–209] and continuum approaches [210–213]. Often, the assumption is that the biofilm is rigid and there is only a one-way mechanical coupling between flow and biofilm via boundary conditions for the fluid. Also, in individual based models, the initial positions of biofilm formation are commonly assumed to be randomly distributed.

In this chapter, we propose a novel model that explicitly

takes into account the influence of complex flow environments on the initial stages of biofilm formation. In the planktonic phase, we capture the interplay between external flow, bacterial motility and surface adhesion, and in the biofilm growth phase we include the influence of a flow on a soft biofilm and vice versa. Our results on selected applications show that in both of the two bacterial phases flow leads to nontrivial, and sometimes even counterintuitive behaviour.

5.2 Methods

5.2.1 Cell model

We use the bacterial cell model described in Section 3.1 with $N^{\text{bead}} = 5$ and no explicit modelling of the flagellum as shown in Fig. 3.1. The following sections detail the extensions of the basic cell model that enable simulations of biofilm forming bacteria which adhere to surfaces, grow and divide.

5.2.2 Surface attachment

For simulations of biofilm formation in porous media, surface interactions are crucial. For the fluid, confining surfaces are built by using the standard bounce-back boundary condition that ensures no slip of fluid. The ability of lattice Boltzmann to discretise arbitrary boundary shapes on its regular grid is one of its main advantages and one of the reasons for its popularity in porous media research [214]. Bacteria interact with surfaces through a force

that acts perpendicular to the surface, with magnitude depending on the minimum distance between a particle and the boundary. We use the short-ranged, purely repulsive Weeks-Chandler-Anderson potential (see Section 3.1.2.1) to mimic steric repulsion. Additionally, we employ a model for reversible surface attachment based on dynamic bond creation and deletion.

In our algorithm we represent surface binding via, e.g., pili, by bonds like the ones used in coarse-grained simulations of polymers, i.e., distance dependent potentials between only two particles [215]. When a bacterium is attached to a surface, a "virtual" particle is placed on the surface with which the bond is formed. The virtual particle is fixed in space and does not interact with any other component of the simulation. This type of anchoring is preferred over a purely distance dependent interaction between the surface itself and the bacteria, because the latter would allow the bacteria to slip along the surface.

For the bond potential we have chosen a harmonic potential of the form

$$V^{\text{attachment}}(\mathbf{r}_i, \mathbf{r}_{anchor,i}) = k_{\text{harm}}(|\mathbf{r}_i - \mathbf{r}_{anchor,i}| - r_{\text{bond}})^2, \quad (5.1)$$

where $\mathbf{r}_{anchor,i}$ is the position of the anchor particle associated with the bacterium bead i, r_{bond} the equilibrium extension of the bond and k_{harm} the stiffness of the interaction. Other bonds that resemble the experimentally measured force-elongation curve of a pilus [216] can easily be included if that level of detail is required or desired.

The decision of whether to form a bond is based on a stochastic distance criterion. When a bead of a bacterium is within a certain

range r_{attach} of a surface, there is a probability p_{attach} for attachment and bond formation within the time step Δt. This means that the time to attachment, t_{attach}, is exponentially distributed and characterised by its mean

$$\langle t_{\text{attach}} \rangle = \Delta t / p_{\text{attach}}. \tag{5.2}$$

Setting $p_{\text{attach}} = 1$ leads to a deterministic bond formation upon surface contact.

The maximum number of bonds, N_{anchor}, formed by a single bacterium can be chosen up to the number of beads N^{bead}, but at least two are necessary to not only bind the bacterium to a surface but also to fix its orientation.

Note that our attachment to a surface is reversible. We use a model for detachment where the bond and the anchor particle is removed if the distance of the bacterium bead to its anchor point reaches a certain threshold r_{detach}. The distance can be reached if viscous drag forces from a surrounding fluid act on the cell, or if cells push each other. The maximum distance criterion is equivalent to a maximum force criterion if the bacterium gets pulled from the surface. For the harmonic potential, the maximum force follows simply from $F_{\text{detach}} = k_{\text{harm}} \cdot (r_{\text{detach}} - r_{\text{bond}})$. It can be tuned to experimental values for the attachment strength of pili to capture the attachment capabilities of the species under consideration.

5.2.3 Cell growth and division

Once the bacteria are attached to a surface, the biofilm will grow by growth and division of the individual cells. Assuming a sufficient supply of nutrients, growth is exponential with a constant rate r_{growth} such that the cell length l_{body} follows

$$l_{\text{body}}(t) = l_{\text{body}}(0) \exp(r_{\text{growth}} t). \tag{5.3}$$

The doubling time (or "generation time") τ_2 can be calculated as $\tau_2 = \ln(2)/r_{\text{growth}}$.

To adapt a bacterium to a new length in the simulation, the rod is extended by placing the beads successively further apart from the central bead, and keeping the centre of mass fixed. This "unphysical" movement of particles requires that the simulation time step is small compared to the relaxation time of particles in a dense biofilm. Only then the displacements of bacterial beads are small enough so that there is sufficient time for the biofilm configuration to adapt to the new length of cells before their size is changed again.

When a bacterium grows while being attached to a surface with an anchor as described in Section 5.2.2, the bonds will break at some point. However, since the beads are still close to the surface, new bonds can reform with a high probability and therefore keep the bacterium attached. The same applies to cells at the edge of a growing colony that get pushed by their growing neighbours.

When the bacterium size l_{body} reaches a threshold length $l_{\text{body, max}}$, a division event is triggered. Upon cell division, the parent cell is replaced by two daughter cells that together occupy

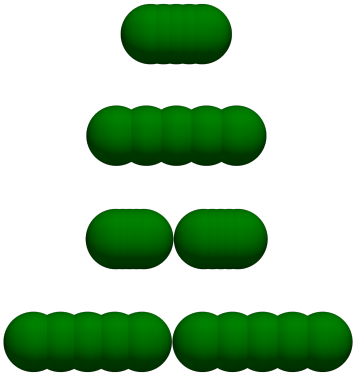

Figure 5.1. Snapshots illustrating the growth and division algorithm. Reproduced from Ref. [3] with permission from the Royal Society of Chemistry.

the same space as the parent cell, see Fig. 5.1. The daughter cells do not have exactly the same length, instead the point of division is selected from a narrow distribution around the centre of the parent cell. We use a uniform distribution with a width of $0.05 l_{\text{body, max}}$. This not only represents bacterial cell division closer than an equal splitting, but also remove the unnatural synchronisation of all subsequent division events of the cell lineage.

When a cell is attached to a surface while dividing, the daughter cells inherit the surface anchor sites at the beads that are closest to the parent binding sites.

5.2.4 Cell-cell interaction

Having many bacteria closely packed in a colony gives special importance to the interactions between them. Obviously bacteria repel each other at very short distances due to their excluded volume. In colonies, bacteria secret extracellular polymeric substances (EPS) that act as an effective binder between cells and stabilise the biofilm. With our model, we aim to find an interaction potential for the bacteria that captures macroscopic properties such as the cohesive strength of the biofilm. For simplicity we have chosen the truncated shifted Lennard-Jones potential as introduced in Section 3.1.2.1. With σ^{LJ} fixed by the cell diameter $2r_{\mathrm{body}}$, we can use the only free parameter ϵ^{LJ} to match a macroscopic biofilm property as illustrated in Section 5.3.3.

5.3 Results

5.3.1 Surface attachment in flow

As a first step of surface colonisation and biofilm formation, we simulate the attachment of bacteria to surfaces in flow. To model the porous geometry we have chosen a staggered regular array of cylindrical obstacles with periodic boundary conditions in all three dimensions. The radii are $R_{\mathrm{cyl}} = 20\,\mu\mathrm{m}$, and the distance of the cylinders is $60\,\mu\mathrm{m}$ in both $x-$ and y-direction. Figure 5.2 shows the unit cell we have simulated and the flow-field that results from requiring the mean flow velocity $\langle|\mathbf{u}|\rangle$ to be twice the swimming velocity of $v_{\mathrm{swim}} = 25\,\mu\mathrm{m\,s}^{-1}$. Since the flow-field al-

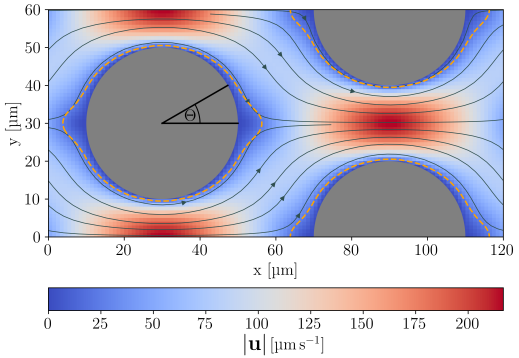

Figure 5.2. Set-up of the porous model geometry for the simulations of cell attachment in flow. The mean (Darcy) velocity is chosen as $|\langle \mathbf{u} \rangle| = 2v_{\text{swim}} = 50\,\mu\text{m}\,\text{s}^{-1}$. Solid, grey lines show flowlines, the dashed, orange line marks where $|\mathbf{u}| = v_{\text{swim}}$. We use the angle θ to describe where bacteria are attached on the cylinders. Reproduced from Ref. [3] with permission from the Royal Society of Chemistry.

terations induced by planktonic bacteria are negligible compared to the external flow, we do not run the lattice Boltzmann fluid dynamics during the whole simulation. Instead, we calculate the flow-field once in the beginning without added bacteria and then keep it constant when simulating bacterial attachment.

The model parameters of the bacteria are chosen as $l_{\text{body}} = 3\,\mu\text{m}$, $r_{\text{body}} = 0.5\,\mu\text{m}$, $N^{\text{bead}} = 5$, $\langle t_{\text{run}} \rangle = 1\,\text{s}$, $\langle t_{\text{tumble}} \rangle = 0.1\,\text{s}$, $\langle \cos(\Theta_{\text{tumble}}) \rangle = 0.5$. Since the flow-field is set constant, the total friction of the rod is additive in the number of coupling points N^{bead}. Using this, the friction coefficient $\tilde{\gamma}$ is calculated such that

the total friction of the five-bead rod matches the longitudinal friction of a spheroidal particle (see Section 2.2.3.1) with half-axes corresponding to $l_{\text{body}}/2$ and r_{body} in water with dynamic viscosity $1 \times 10^{-3}\,\text{Pa}\,\text{s}$. To investigate the low-density limit of few bacteria, we do not consider interactions between bacteria and only focus on their interaction with the fluid and the surfaces. We set the attachment, bond and detachment range to $r_{\text{attach}} = r_{\text{bond}} = 1\,\mu\text{m}$ and $r_{\text{detach}} = 1.5\,\mu\text{m}$, respectively. The maximum attachment strength is set to 200 pN, as observed for *E. coli* [216]. We choose $p_{\text{attach}} = 1$ corresponding to instant attachment upon surface contact. Increasing the average attachment time up to $\langle t_{\text{attach}} \rangle = 10\,\text{s}$ yields qualitatively the same results (see Appendix A.2) Note that for the flow rate considered here, the viscous forces are not strong enough to cause a detachment of cells.

As a starting point for the attachment simulation we choose the steady state formed after a warm-up period of $t_{\text{warmup}} = 10 L_x / v_{\text{swim}}$, where L_x is the length of the simulation domain along the flow direction. The simulation ends when all cells are attached to a surface. We simulated 20000 trajectories of motile bacteria and the same number of trajectories for non-motile bacteria ($v_{\text{swim}} = 0$ and no tumbling) with otherwise identical parameters.

Figure 5.3 shows the distribution of attachment points on the cylinder surface parametrized by the angle θ. The distribution for non-motile bacteria is peaked at the side of the cylinder ($\theta \approx \pi/2$) and at the front ($\theta \approx \pi$). It is very unlikely that they can approach the cylinder from the downstream side, because that requires diffusion against the external flow. Instead, the attachment probability

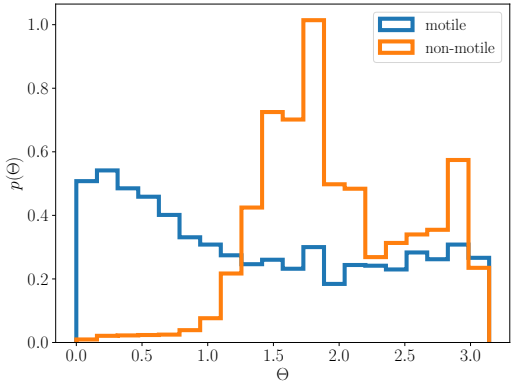

Figure 5.3. Normalized histogram of the angular position of attachment for motile and non-motile bacteria. Reproduced from Ref. [3] with permission from the Royal Society of Chemistry.

is highest where the least amount of cross-streamline diffusion is required to reach the surface, which is the narrow constriction between the cylinders. The same effect is observed in experimental studies of similar geometries, but only when the flow velocity is much larger than the bacterial swim velocity and swimming can therefore be neglected [217]. There is also a peak of attachment probability in the front of the obstacle. Here, the flow velocity is low in a larger region, allowing the cells to diffuse to the surface without being carried away by the flow.

The distribution for motile bacteria looks qualitatively different: In accordance with the results presented in the previous chap-

ter[1] , there is a large probability for attachment on the downstream side of the obstacles ($\theta < \pi/2$) and a peak around $\theta = 0$. Motile bacteria can cross streamlines due to their forward propulsion and active reorientation during tumbles, which is much more efficient than translational and rotational Brownian motion. They can also reach the cylinder surface from the downstream side when they swim against the local flow. On both, the upstream and downstream end of the cylinders, bacterial swimming is faster than the external flow, so given the correct orientation, they can easily reach the surface and attach. The effect is more pronounced at the downstream end, because here the local flow helps the cells to stay in the vicinity of the surface: A bacterium swimming parallel to the cylinder away from $\theta = 0$ is slowed down and pushed back towards $\theta = 0$. On the upstream side, a bacterium swimming parallel to the cylinder away from $\theta = \pi$ is accelerated by the flow and transported towards the region of high local flow, where it will consequently be washed away. The probability of attachment is smallest around $\theta = \pi/2$, because here the local flow is high, so that bacteria are fast and have the least amount of time to tumble and swim to the surface.

5.3.2 Qualitative biofilm morphologies

To showcase the capabilities of our model to reproduce different biofilm morphologies, we simulate biofilm growth in a very sim-

[1] It is not *a priori* clear that these results must be the same. In Chapter 4, we investigated a particle density, whereas here we are interested in a first-passage problem that can in principle yield very different outcomes.

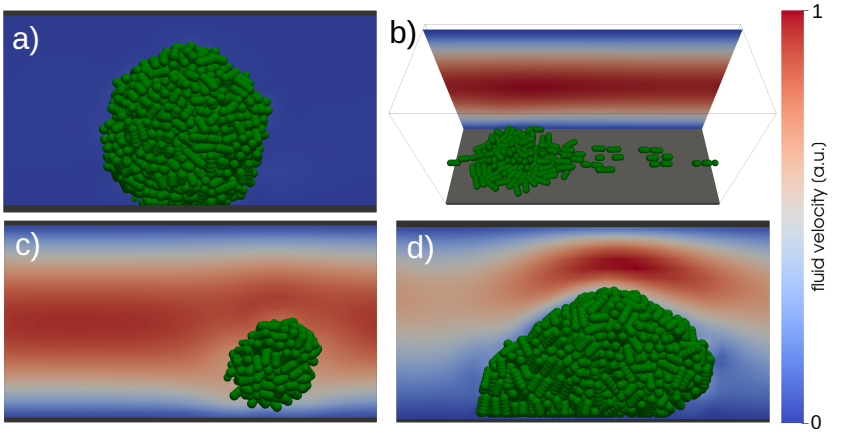

Figure 5.4. Biofilm morphologies obtained in different parameter regions determined by maximum fluid shear rate $\dot{\gamma}_{\text{wall}}$, surface adhesion strength k_{harm} and cell-cell attraction strength ϵ^{LJ}. Only qualitative results are shown here, exact values are listed in Appendix A.2. a) $\dot{\gamma}_{\text{wall}} = 0$, intermediate k_{harm}, intermediate ϵ^{LJ}. b) Intermediate $\dot{\gamma}_{\text{wall}}$, intermediate k_{harm}, small ϵ^{LJ}. c) Intermediate $\dot{\gamma}_{\text{wall}}$, small k_{harm}, intermediate ϵ^{LJ}, d) Intermediate $\dot{\gamma}_{\text{wall}}$, intermediate k_{harm}, intermediate ϵ^{LJ}. Reproduced from Ref. [3] with permission from the Royal Society of Chemistry.

ple geometry. We confine cells and fluid in z-direction between two parallel plates with periodic boundary conditions along the x- and y-direction. The biofilm starts from one founder cell initially located in contact with the bottom surface. Additionally, we impose a constant force $\mathbf{f}^{\text{ext}}$ on the fluid along x, which results in a parabolic flow profile in the empty channel. By varying $\mathbf{f}^{\text{ext}}$, the biofilm cohesiveness parameter ϵ^{LJ} and the adhesive strength determined by k_{harm}, different morphologies are obtained. In the

following, we discuss qualitative results in certain general parameter regimes, the exact parameters to obtain the results are listed in Appendix A.2.

If there is no external flow, rotational symmetry is not broken and a biofilm simulated on a flat surface will grow into a shape that resembles a spherical cap as shown in Fig. 5.4a). If, however, there is a very strong flow, or the biofilm is very soft, bacteria adhere only to the surface and any cells that get pushed from the surface are washed away with the flow. In this case, the biofilm consists only of a single layer of cells, see Fig. 5.4b), but is still able to cover the surface. The shapes shown in Fig. 5.4a) and b) bear strong resemblance to the shapes of *Vibrio cholerae* biofilms grown under conditions of varying levels of shear [197]. For strong flow and cohesion but weak adhesion, the colony detaches from the surface as a whole and grows into a sphere while being transported with the flow, see Fig. 5.4c). The biofilm then rolls along the surface as observed in experiments [218]. In the simple geometry considered here, the rolling will continue until the biofilm fills the entire channel. In a more complex environment, the detached biofilm could reach a region of smaller flow and attach to a surface there. In the intermediate regime, where the parameters are balanced, we can see the two-way coupling between particles and fluid as shown in Fig. 5.4d). The biofilm grows into a slanted shape dictated by the forces exerted from the flow. At the same time the fluid has to flow around the biofilm that constricts the channel until it is finally fully clogged. On the upstream end of the biofilm one can see that the cells become ordered with a common direction perpendicular

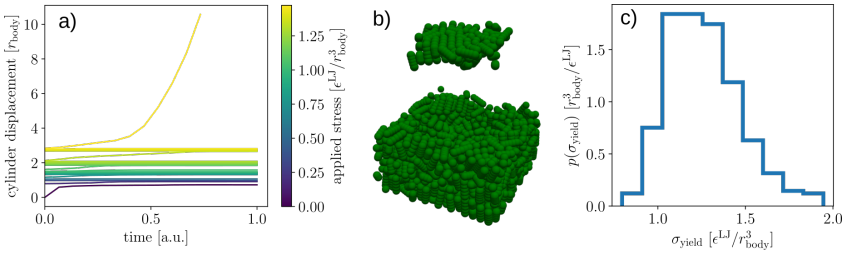

Figure 5.5. a) Z-cooridinate of the cylinder during retraction from the biofilm. The color-code shows the applied stress at each iteration. b) A circular segment detaches from the main biofilm as yield stress is reached (cylinder not shown). c) Normalized histogram of the yield stress. Reproduced from Ref. [3] with permission from the Royal Society of Chemistry.

to the surface, indicating a local nematic ordering that was also observed experimentally [197, 219].

5.3.3 Determination of model parameters

Most model parameters such as the size of the bacterium, the growth rate, or even the maximum surface attachment force can be obtained directly from experiments. The cell-cell interaction strength ϵ^{LJ}, however, is a very coarse-grained quantity that implicitly models complex interactions mediated by EPS. Therefore, we need to match coarse-grained biofilm properties between experiment and simulation to determine ϵ^{LJ} for the bacterial species under consideration.

Since we want to model biofilms in environments with potential strong local flow, rupture and detachment of biofilm parts must be

well represented. Therefore, we propose to use the biofilm yield stress σ_{yield} for parameter calibration. We obtain the yield stress by performing a simulation that recreates the experiments performed by Aggarwal *et al.* [220, 221].

First we simulate biofilm growth between two parallel plates. We choose the size of the simulation domain and the distance between the plates in a way that the volume can contain approximately 1000 bacteria. This is the order of magnitude for cells in a cohesive biofilm section we aim for in later simulations in porous media. To ensure a flat biofilm, multiple bacteria are initially placed on the surface. Since the experiment is performed without external flow, we do not use the lattice Boltzmann method to simulate a flow field and instead assume a quiescent background field with a constant friction coefficient. As soon as the volume between the plates is filled with bacteria, the top surface is removed.

We then introduce a cylindrical boundary from the top such that bacteria can attach to it. Its size is chosen such that around 50 cells can anchor on its base. Once the bacteria have attached, we apply a force on the cylinder perpendicular to the surface (i.e., a tensile stress) and thereby pull on the biofilm. The force is increased in small steps until failure is reached and the cylinder with some broken off pieces of biofilm retracts fully. An example trajectory of the cylinder position and the final state with retracted cylinder are shown in Fig. 5.5a) and b), respectively. The expansion at zero applied stress is due to the fact that the cylinder was kept fixed during biofilm growth.

Performing this simulation for 360 random starting positions,

we obtain the tensile strength of $\sigma_{\text{yield}} r_{\text{body}}^3 / \epsilon^{\text{LJ}} = 1.26 \pm 0.01$. The uncertainty reported here is the standard error of the mean. The distribution of tensile strength values follows a broader distribution with a standard deviation of around 0.21, see Fig. 5.5a). This is because of the randomness of the length of the bacteria attached to the cylinder: Many small (i.e. young) bacteria have a stronger attraction to neighboring cells than few large (i.e. old) bacteria since the density of force coupling points is bigger for small bacteria (N^{bead} is constant but l_{body} increases with cell age).

Assuming a value of 3000 Pa for *Pseudomonas aeruginosa* biofilm tensile strength [220] and a cell radius of $r_{\text{body}} = 0.5\,\mu\text{m}$, we determine $\epsilon^{\text{LJ}} \approx 3 \times 10^{-16}\,\text{J}$.

5.3.4 Simulation of biofilm formation in porous media

To demonstrate the applicability of our model in a porous media setting we simulate biofilm growth on a porous geometry similar to the one used in Section 5.2.2. Here, we additionally confine the computational domain with flat walls at the top and bottom of the channel. We also simulate a larger segment of the periodically repeated staggered grid, because when bacteria grow and divide, the biofilm exceeds the minimal repeating unit. Along the x-direction we apply a force to the fluid, resulting in a flow from left to right. We employ the full, two-way particle-fluid coupling.

In order to simulate such a system with vastly different time scales (fast motion of the fluid, slow growth of the biofilm), we need to scale some input parameters: Since from the perspective of the fast-moving fluid the biofilm is always approximately at rest,

it does not matter exactly how much slower the biofilm growth is than the fluid flow, as long as the time scales are separated. To bring the time scales closer, we reduce the fluid velocity in our simulation by a factor f. This affects the Reynolds number $\mathrm{Re} = \rho|\langle \mathbf{u} \rangle|h/\mu$, where ρ is the fluid density, $|\langle \mathbf{u} \rangle|$ the average fluid velocity, h the channel height and μ the dynamic viscosity. To keep Re at its original value and thereby recover the original fluid physics up to scaling, we also reduce the viscosity by the factor f. This means that according to Eq. (2.37), the force the fluid exerts on boundaries and the bacteria is reduced by f^2. Reflecting this change in fluid properties, we scale down ϵ^{LJ} and k_{harm} by f^2 to recover the original physics of the biofilm-fluid interaction.

Using the parameter set listed in Appendix A.2, we show the qualitative behaviour of the growing biofilm in porous media flow. In the starting phase, we initialize a layer of bacteria attached to the downstream end of a cylindrical obstacle (see Fig. 5.6, top row), according to our observations in Section 5.2.2. While the biofilm remains in the region of small local flow velocities, the growth is approximately spherical. However, when the biofilm grows further away from the surface, it encounters stronger flows which cause the sphere to deform into an elongated filament, a process very similar to the experimentally observed transition from bioaggregates to streamers [217]. This filament extends downstream and upon further growth, covers the fluid constriction between the cylinders of the next column in the staggered grid. As the fluid cannot penetrate the biofilm with considerable velocity, this flow path is blocked by the biofilm. Driven by the growth pressure from in-

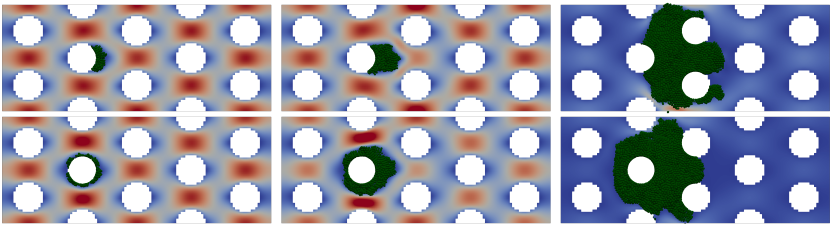

Figure 5.6. Top row: Evolution of biofilm formation for downstream seeding of the initially attached bacteria. Bottom row: Evolution for uniform seeding. For both simulations, we use the same biofilm yield stress $\sigma_{\text{yield}} = 3000\,\text{Pa}$ and initial $\text{Re} = 0.6$. Reproduced from Ref. [3] with permission from the Royal Society of Chemistry.

side the biofilm that is firmly attached to the cylinders and the top and bottom wall, bacteria now also extend into the remaining open flow path and eventually clog the whole porous geometry. On a qualitative level, the clogging of flowpaths and thereby redirection of fluid to new flowpaths matches well with experimental investigations [222, 223]. It is this mechanism that makes microbes well suited for enhanced recovery of substances trapped in porous media such as oil or contaminants.

For very soft biofilms, the dynamics are markedly different, because the shear forces do not only deform the colony, but can also rupture it. Figure 5.7 shows an event where a piece of biofilm originally grown on the left cylinder gets detached by the flow and transported downstream to the next cylinder, where there is already a sizeable colony formed by previous biofilm transport events. To our knowledge, our biofilm model is the only computational model

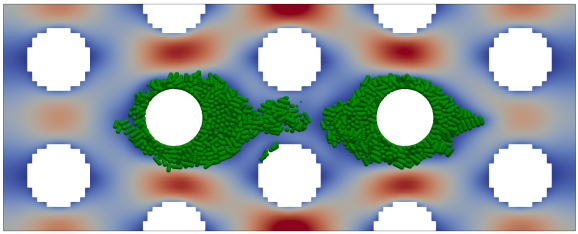

Figure 5.7. Snapshot of biofilm formation for soft ($\sigma_{\text{yield}} = 500\,\text{Pa}$) biofilm. Inbetween the central cylinders a section of biofilm is being advected to the right. Reproduced from Ref. [3] with permission from the Royal Society of Chemistry.

that can predict such events.

To quantify the clogging behaviour, we show in Fig. 5.8 the reduction of permeability $K/K(0) = |\langle \mathbf{u} \rangle|/|\langle \mathbf{u}(0) \rangle|$, see Section 2.3. We keep the initial fluid velocity corresponding to $\text{Re} = 0.6$ for all simulations. For comparison, we also show the permeability reduction over time for the case where we initialize the biofilm not on the downstream end of a cylinder, but uniformly around the whole surface, with the same number of initial bacteria (see Fig. 5.6, bottom row). A single bacterium as well as the total colony grow exponentially, so the clogging behaviour is expected to be slow in the beginning and fast in the end. For soft biofilms ($\sigma_{\text{yield}} = 500\,\text{Pa}$), there is no qualitative difference between the two initialization methods. In both cases, biofilm growth is characterised by events where sections of the biofilm detach from the initial cylinder, get transported with the flow and attach on downstream obstacles, Clogging happens late, because rather than being concentrated around a few critical flowpaths, the biomass is

more evenly distributed throughout the whole geometry.

The difference between the two initialization methods manifests itself when stiffer biofilms are considered. Here, the permeability curves for downstream seeding show two inflection points that are absent for uniform seeding. In the beginning, clogging is slower for the downstream initialized colony, because unlike the uniformly-seeded biofilm, it grows in a region of small fluid velocity where clogging does not have a large overall effect. The faster clogging in the following regime is the consequence of the filament extending into the central flow path and blocking it. Around the second inflection point, clogging is slower again. This is due to the fact that while the central flow path is being blocked, it will take a longer time until the biofilm extends into the second flow path. In the final clogging regime, the seeding method does not have a large influence anymore, since in both cases the biofilm is well connected to the neighbouring cylinders and the top and bottom wall. Here, only the total volume of clogging biofilm is relevant, which is the same for both seeding methods. Overall, clogging gets faster the harder the biofilm is, but the effect is rather small once σ_{yield} is large enough to keep the bacteria attached to the initial cylinder as one cohesive colony.

The permeability does not go exactly to zero because of our method for fluid-particle coupling: The coupling is realised by a finite friction, so a non-moving biofilm slows down the fluid significantly, but does not constitute a perfect non-slip boundary condition as the geometrical surfaces do. In our case, we stop the simulations when $K/K(0) < 0.05$, because after this, the permeability

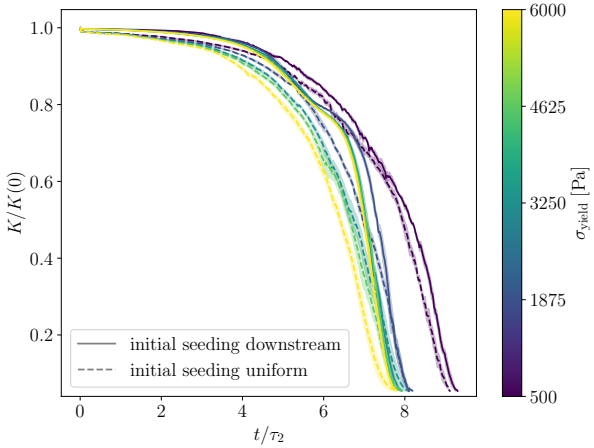

Figure 5.8. Permeability reduction as a function of time. The line color corresponds to the biofilm stiffness quantified by the yield stress σ_{yield}, see color bar. Solid and dashed lines indicate downstream and uniform initial seeding of the biofilm, respectively. The shaded region denotes the standard error of the mean over 5 statistically independent simulations, all simulations start with Re = 0.6. Reproduced from Ref. [3] with permission from the Royal Society of Chemistry.

does not reduce significantly anymore. Moreover, the simulations become unstable due to the exponentially increasing number of particles.

5.4 Conclusions

We have developed an agent-based model of bacteria for biofilm initiation and showed how porous media flow affects all stages of

colony formation. For the first stage of biofilm initiation, that is the initial attachment of planktonic bacteria to a surface, we demonstrate the importance of bacterial motility when determining the likely locations of surface adhesion: Unlike passive particles, motile bacteria can cross streamlines easily and even swim against an external flow. This leads to the counterintuitive phenomenon that bacteria attach on the downstream end of obstacles rather than on the upstream end or the narrow constrictions between obstacles, as explained in Chapter 4.

In the biofilm growth stage, where bacteria are attached to a surface, grow and divide, we first show the capability of our model for soft, deformable biofilms to capture qualitative behaviour of biofilm growth under shear conditions. We explore the different parameter regimes and find distinct morphologies: spherical growth when there is no shear in the surrounding fluid, flat, monolayer growth when shear is very strong, detachment of the entire biofilm when shear is strong and adhesion weak and finally an asymmetric growth when the biofilm and fluid parameters are balanced.

To connect our model parameter for biofilm cohesion to experimentally accessible, macro-scale quantities, we perform biofilm rupture simulations and obtained the yield stress of a bacterial colony. For this, we let the top layer of bacteria in a biofilm attach to a cylinder and apply an increasing force to the cylinder until it detaches from the main biofilm. Using the parameters from these simulations, we perform a full biofilm growth simulation in a model porous medium with external flow. Here we show how the fluid influences the colony shape, forming an elongated filament extend-

ing from the surfaces into the flow. We further observe how in turn the biofilm influences the fluid, blocking flow paths and eventually clogging the entire porous geometry. We also show how the initial seeding of the biofilm (uniform around an obstacle or located on the downstream end) quantitatively changes the evolution of the permeability over time.

All the different applications of our model show the importance of the interplay between bacterial motility, biofilm softness and external flow, especially in a porous media context. With our model, investigations of this interplay are possible because it explicitly includes particle motility as well the possibility of biofilm deformation by viscous forces applied to the colony boundary. This represents a large step forward in biofilm modelling, where many models do not consider the initial surface attachment at all and treat the biofilm as a rigid boundary with only a one-way coupling to the fluid. We thus expect that our model can be applied beyond the cases we have shown in this article and facilitate further insight into the rich phenomenology of biofilm growth in porous media.

We have applied our model for swimming, attaching, and growing bacteria to geometries where the typical length scale is much larger than the size of a single cell. This is a very relevant length scale, as many pores in the soil or the human body are big enough to accomodate many bacteria. They have to be large enough for biofilm formation to occur on non-metabolisable substrates, because supply of nutrients from a (larger) body of fluids is necessary to sustain growth. However, in the planktonic stage, single bacteria in their search for new, nutrient rich surfaces to colonise, might

face much tighter confining geometries. The efficiency of different motility strategy to facilitate this search in porous environments with very small pores will be the focus of the next chapter.

Chapter 6

Optimal motility strategies for self-propelled agents to explore porous media

This chapter contains in large parts text that is taken verbatim from C. **Lohrmann** and C. Holm, "Optimal motility strategies for self-propelled agents to explore porous media", Phys. Rev. E **108**, 054401 (2023), a publication to which I contributed the modelling, simulations, data analysis and writing of the manuscript draft.

6.1 Introduction

For bacteria to colonise new terrain and for micro-robots to properly fulfill their (medical) function, it is important that both types of micro-swimmers are able to traverse a highly confining, disordered porous environment before reaching their target.

Self-propulsion is a necessary ingredient for the efficient exploration of such an environment, however, self-steering can im-

prove the performance significantly. Microorganisms achieve directional control by changing the beating patterns and synchronisation of their propelling cilia [224] or flagella [225, 226]. Many basic artificial microswimmers on the other hand are unable to steer, especially if their propulsion mechanism relies on chemical reactions [36, 227, 228]. However, progress has been made in the control of individual artificial swimmers that are actuated by light [229–231] or magnetic fields [232–234], endowing them with a steering feature.

Biological microswimmers are known to possess various motility patterns [235, 236], i.e., strategies to use a combination of self-propulsion and self-steering to navigate through their environment: *P. Aeruginosa* and many marine bacteria can reverse their locomotion and perform a run-and-reverse pattern in which they alternate between forward and backward swimming [235]. Bacterium *E. coli* interrupts its forward swimming mode ("run") with reorientation events ("tumble"), where the bacterium rotates before continuing to swim in a new direction [84]. *V. alginolyticus* alternates between swimming forward, swimming backward and flicking its orientation by 90°, a pattern called run-reverse-flick [237]. In the following we will use these motility patterns as a starting point to investigate optimal strategies for porous media exploration and navigation.

The spreading behaviour of active particles with different motility patterns has been well studied in unconfined fluids [238] and weakly confined environments [13]. Diffusive properties under strong confinement have also been the subject of a number of experimental and theoretical works: Zeitz *et al.* investigated in

detail the mean-squared displacement of disk-like active Brownian particles in a porous environment close to the percolation threshold [191]. Bhattacharjee & Datta tracked *E. coli* cells in three-dimensional porous media and found that the bacterial trajectories cannot be identified as run-and-tumble anymore. Instead, they identified a sequence of hopping events through the channels, with the bacteria being intermittently trapped in small pores [239, 240]. Theoretical studies of run-and-tumble-swimmers in porous media find a maximal effective diffusivity by optimizing the duration of runs for specific pore configurations [241–244]. Similarly, numerical simulations of run-and-reverse-swimmers show that the optimal run length can be inferred from the distribution of the lengths of straight paths in a porous medium [245].

While the aforementioned works have optimized the parameters of specific patterns for porous media exploration, in this chapter, we will attempt to optimize the motility pattern itself. We study the qualitative features of different patterns when used by otherwise identical agents in various three-dimensional, disordered environments. We cover the range of all relevant pore sizes from bulk fluid to confinement ranging down to the size of the microswimmer. Using the insights gained from our analysis of biologically inspired motility patterns, we develop a new pattern which requires the agents to be capable of sensing whether they are trapped or not. This pattern, which can be deployed by artificial autonomous self-propelled agents, performs best across all investigated environments, and can be a basis for developing further optimal navigation strategies.

6.2 Methods

6.2.1 Agent model

We use the bacterial cell model described in Section 3.1 with $N^{\text{bead}} = 5$ as shown in Fig. 3.1 to represent the agents. In the following, we refer to the micro-swimmers as "agents" because our results apply to bacteria as well as to artificial swimmers. For this study, we do not consider hydrodynamic fields because the agents' dynamics in tightly confining geometries are dominated by steric interactions rather than hydrodynamic interactions. As such, we do not use any lattice Boltzmann or particle-fluid coupling and instead apply the "dry" model outlined in Section 3.2.1. We want to investigate the single-swimmer, low density limit behaviour of active agents and therefore do not consider interactions between agents. Agents do however interact with their environment as detailled in Section 6.2.3.

6.2.2 Motility patterns

We create motility patterns by combining phases of self-propulsion and self-rotation, prescribing the durations of the phases and their temporal sequence. In the following, we list the algorithms of the patterns used in this study, example trajectories are shown in Fig. 6.1.

▶ Straight swimming

A constant force along the symmetry axis is applied, there is no active rotation. The only source of randomness in the trajec-

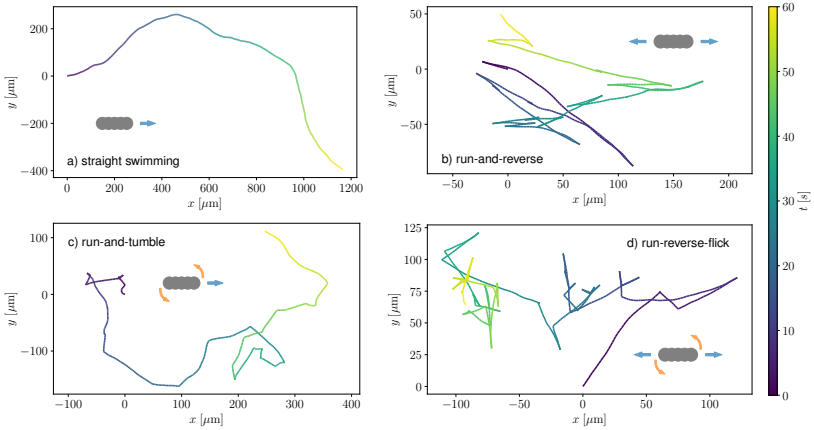

Figure 6.1. Two-dimensional projections of example trajectories without confinement for the four biologically inspired motility patterns. The pictograms (not to scale) show the phases involved in the respective pattern, i.e., forward swimming, backward swimming and rotation. The trajectory for reverse-when-stuck is not depicted, as this pattern reduces to straight swimming if there are no pores to get trapped in. For easier distinction, the temperature is reduced by a factor of 60 compared to the simulations used in our analysis. Reproduced from Ref. [4] with permission from the American Physical Society.

tory is the translational and rotational diffusion. Aside from the anisotropic shape of the self-propelled agent, this pattern is an implementation of a 3D active Brownian particle (ABP).

▶ Run-and-reverse

With this motility pattern, agents swim at constant speed v_{swim} ("run") but can reverse their swimming direction, realised by a change in sign of the self-propulsion velocity $v_{\text{swim}} \to -v_{\text{swim}}$. The

reversal algorithm thus implies that agents reverse their swimming propulsion and not the direction of their body, in accordance with observations in nature [246, 247]. No active torques are applied. The durations t_{run} of runs are commonly found to be exponentially distributed for bacteria [248, 249], therefore we draw them from an exponential distribution, Eq. (3.6). The only adjustable parameter of the run-and-reverse pattern is $\langle t_{\mathrm{run}} \rangle$.

▶ Run-and-tumble

We implement run-and-tumble according to Section 3.2.3.

▶ Run-reverse-flick

This motility pattern can be found in marine bacteria *V. alginolyticus* [237] and combines elements from run-and-reverse and run-and-tumble. Here, runs (of exponentially distributed durations t_{run}) are interrupted by both, reversals and flicks. A flick is a tumble with a constant angle $\Theta_{\mathrm{flick}} = \pi/2$ and duration t_{flick}. Reversals and flicks occur in alternating fashion.

▶ Reverse-when-stuck

Leaving the realm of motility patterns that occur in nature, we propose a hypothetical optimal pattern for porous media navigation that combines straight swimming and reversals. For this pattern, the agent must be endowed with sensing capabilities, a way to store a memory over a limited amount of time, and an intelligence unit to make simple decisions. Together, these capabilities enable smart reactions to the environment beyond following a predetermined order of self-propulsion and -rotation. Using a position sensor, the agent constructs a memory of its trajectory within a time frame

t_{memory}. If it did not move more than one body length l_{body} in that time, a reversal is triggered. Upon reversal, the memory is reset.

This algorithm is used as a representative of the whole class of motility patterns in which the agent is able to sense if it is stuck in a pore. A position sensor is not necessarily required, agents could also obtain this information from a sensor for swimming speed. Mechanical sensors on the agent body or propulsion mechanism such as the ones found in bacteria [250] could determine a trapped state as well.

6.2.3 Porous media model

Inspired by the experimental setup of Bhattacharjee & Datta [239], we model the porous environment with overlapping spheres of radius $R_{\text{sphere}} = 15 r_{\text{body}}$. The spheres are placed randomly throughout the simulation box and fixed in space for the entire duration of the simulation. An example is shown in Fig. 6.2.

As an approximation of hardcore repulsion, all individual particles of the swimmer rods interact with all spheres with a shifted WCA potential

$$\begin{aligned} V(r) =& 4\epsilon^{\text{LJ}} \left[\left(\frac{\sigma^{\text{LJ}}}{r - R_{\text{sphere}}} \right)^{12} - \left(\frac{\sigma^{\text{LJ}}}{r - R_{\text{sphere}}} \right)^{6} + \epsilon^{\text{LJ}} \right] \\ & \times H(R_{\text{sphere}} + r_{\text{body}} - r), \end{aligned} \tag{6.1}$$

where r is the distance between the particle and the sphere center, $\sigma^{\text{LJ}} = 2^{-\frac{1}{6}} r_{\text{body}}$ and all other parameters have an interpretation analogous to the "standard" Lennard-Jones potential.

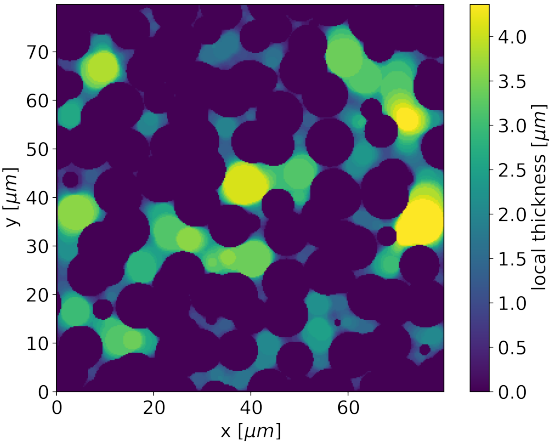

Figure 6.2. A two-dimensional slice through a typical randomly generated porous geometry with mean pore radius $r_\mathrm{p} \approx 2.6\,\mu\mathrm{m}$. The colors indicate the local thickness, a measure for the pore size, see main text. Reproduced from Ref. [4] with permission from the American Physical Society.

The reason we do not use the unmodified WCA potential introduced in Section 3.1.2.1 is that with the distance offset introduced here, the stiffness of the potential is independent of the sphere radius R_sphere. Because $R_\mathrm{sphere} \gg r_\mathrm{body}$, a comparatively large $\sigma^\mathrm{LJ} \gg r_\mathrm{body}$ would be required in the unmodified Lennard-Jones potential which would make the interaction "soft" on the scale of an agent. All simulations are performed in a cubic, $L \times L \times L$ domain with periodic boundary conditions, where L denotes the simulation box size. The control parameter for the porous geometry is the number of spheres. To analyse the porous geometry,

we first use the positions of the spherical obstacles to generate a binary image of the pore space at a resolution of $\Delta x = 0.25\,\mu\text{m}$. Then we use the porespy [251] python package to obtain quantitative measures such as porosity ϕ, local thickness $\tau(\mathbf{r})$, and the pore size distribution. The local thickness represents the radius of the largest sphere that contains the point $\mathbf{r}$ and fits entirely in the void space between the obstacles as seen in Fig. 6.2. The mean pore radius r_p is determined by calculating the mean of $\tau(\mathbf{r})$ in the regions where it is non-zero.

6.2.4 Parameter choice

To compare the motility patterns against each other, we choose the same physical parameters for all simulations: $l_\text{body} = 2\,\mu\text{m}$, $r_\text{body} = 1/3\,\mu\text{m}$, $v_\text{swim} = 28\,\mu\text{m}\,\text{s}^{-1}$, $T = 300\,\text{K}$, $\mu = 8.9\times10^{-4}\,\text{Pa}\,\text{s}$, $R_\text{sphere} = 5\,\mu\text{m}$, $\epsilon^\text{LJ} = k_\text{B}T$ and $L = 80\,\mu\text{m}$. In Appendix A.3 we report effective diffusivities for $R_\text{sphere} = 10\,\mu\text{m}$. The results are in very good agreement with Fig. 6.4, hinting at the independence of our conclusions from the details of the porous medium model. Unless noted otherwise, we set the average run times for run-and-reverse, run-and-tumble and run-reverse-flick to $\langle t_\text{run}\rangle = 1\,\text{s}$, the average time of rotation for run-and-tumble and run-reverse-flick to $\langle t_\text{tumble}\rangle = t_\text{flick} = 0.1\,\text{s}$ and the memory time for reverse-when-stuck to $t_\text{memory} = 1\,\text{s}$. For run-and-tumble, we set $D_\text{rot, tumble} = 5\,\text{s}^{-1}$, which results in $\langle\Theta_\text{tumble}\rangle \approx 56°$, close to values observed in *E. coli* [84]. These might not be the optimal parameters for each of the patterns for all pore sizes, but they serve as a common ground for the evaluation of the pattern performance.

For agents of this size at the density of water $\rho^{\text{water}} = 1 \times 10^3\,\text{kg}\,\text{m}^{-3}$, the diffusive relaxation time $\tau^{\text{t}} = m/\gamma^{\text{t}} \approx 7 \times 10^{-8}\,\text{s}$ is very small compared to all other timescales of the system. Following Section 3.2.4.2, we choose $\rho = 10^5 \rho^{\text{water}}$, allowing time steps $\Delta t = 15\delta t = 5 \times 10^{-3}\,\text{s}$. Simulations are performed with $N = 100$ agents and run for $\mathcal{T} = 6000\,\text{s}$ to collect a sufficient amount of stochastic data, with an additional 600 s warm-up phase before data collection starts. They are repeated N_{ensemble} times with different random seeds, i.e., different geometries, particle starting positions and noise realisations. Error quantifications shown in the following sections represent the standard error of the mean over different simulations.

6.3 Results

6.3.1 Effective diffusivity

From the scale of the different trajectories in Fig. 6.1 one can already get a qualitative understanding of how efficient agents can explore unconfined spaces depending on the strategy they employ. To quantify the efficiency of exploration in both, unconfined space and porous media, we calculate the mean-squared displacement (MSD)

$$\text{MSD}(t) = \frac{1}{N} \sum_{i=1}^{N} \frac{1}{\mathcal{T} - t} \int_0^{\mathcal{T}-t} \left| \mathbf{r}_i(t' + t) - \mathbf{r}_i(t') \right|^2 \text{d}t' \,, \tag{6.2}$$

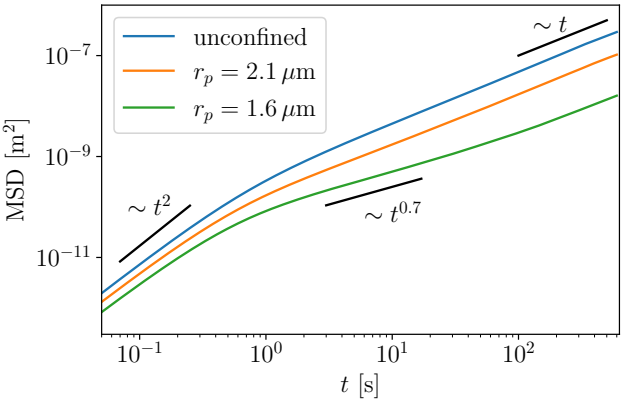

Figure 6.3. Mean-squared displacement of the run-and-reverse pattern at various mean pore sizes r_p. The black lines indicate different scaling behaviours as a guide to the eye. Reproduced from Ref. [4] with permission from the American Physical Society.

where $\mathcal{T}$ is the duration of the simulation, and $\mathbf{r}_i$ the center of mass position of agent i[1].

An example for run-and-reverse is shown in Fig. 6.3. It contains the qualitative features that are present in the MSDs for all motility strategies: For short timescales it is super-diffusive with $\mathrm{MSD}(t) \sim t^2$, where the ballistic contribution of self-propulsion dominates over random motion and interactions. For intermediate timescales there is a sub-diffusive regime, i.e., $\mathrm{MSD}(t) \sim t^\alpha$ with $\alpha < 1$. This is a result of trapped agents that spend significant time not moving in narrow pores, waiting for a random event to

[1]To approximate the ensemble average of the theoretical MSD definition from Section 2.1, we use an average over time and different trajectories.

allow them to escape. For long timescales, the motion is diffusive, i.e., $\mathrm{MSD}(t) \sim 6D^{\mathrm{t}}_{\mathrm{eff}}t$ with an effective diffusion coefficient $D^{\mathrm{t}}_{\mathrm{eff}}$. This holds true without confinement, and also in porous media as long as the confinement is not strong enough to prohibit agents from moving altogether. We use $D^{\mathrm{t}}_{\mathrm{eff}}$ as the key metric to rank the different motility patterns.

Figure 6.4 shows $D^{\mathrm{t}}_{\mathrm{eff}}$ as a function of mean pore radius r_{p} of the confining geometry. Without confinement (mean pore radius $r_{\mathrm{p}} \to \infty$), straight swimming leads to a larger effective diffusion than any of the other patterns, but only by a factor of about 2 to 3. This ratio is quite small considering that there are active reorientations in the other motility patterns while for the straight swimmers the rotational diffusion is the only source of deviation from ballistic motion. Due to the small size of the particles, rotational diffusion has a strong effect on swimming regardless of the specific pattern: From the rotational friction coefficient γ^{r} follows the typical timescale $\tau^{\mathrm{r}}_{\mathrm{corr}}$ for rotational diffusion via the Einstein-Smoluchowski relation

$$\tau^{\mathrm{r}}_{\mathrm{corr}} = \frac{1}{2D^{\mathrm{r}}} = \frac{\gamma^{\mathrm{r}}}{2k_{\mathrm{B}}T}, \tag{6.3}$$

see Section 2.1.2.3. For the parameters of the agents simulated here, we obtain $\tau^{\mathrm{r}}_{\mathrm{corr}} \approx 0.7\,\mathrm{s}$. This timescale is comparable to the typical time $\langle t_{\mathrm{run}} \rangle = 1\,\mathrm{s}$ between active reorientations in non-straight swimming patterns, causing the relatively small ratio of $D^{\mathrm{t}}_{\mathrm{eff}}$ between the patterns when there is no confinement. For bigger agents or flagellated bacteria, where $\tau^{\mathrm{r}}_{\mathrm{corr}}$ is typically much larger than $\langle t_{\mathrm{run}} \rangle$, the difference in free-space diffusivity between straight

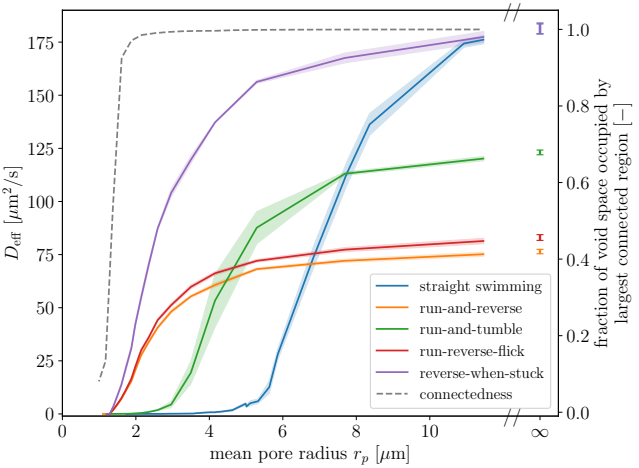

Figure 6.4. Solid, colored lines, left axis: Effective diffusion coefficient $D^{\text{t}}_{\text{eff}}$ as function of average pore size for all motility strategies. Dashed, grey line, right axis: Connectedness of the accessible void space measured as the fraction of the void space occupied by the largest connected region with local thickness $\tau(\mathbf{r}) > r_{\text{body}}$. The shaded areas denote one standard error of the mean over $N_{\text{ensemble}} = 7$ statistically independent simulations. Reproduced from Ref. [4] with permission from the American Physical Society.

swimming and the other patters would be greater.

In the absence of obstacles, the effective diffusion coefficient of the straight swimmer can be calculated analytically, see Section 2.1.4.2, and reads

$$D^{\text{t}}_{\text{eff, ABP}} = \frac{k_{\text{B}}T}{\gamma^{\text{t}}} + \frac{1}{3}\tau^{\text{r}}_{\text{corr}} v^2_{\text{swim}}. \tag{6.4}$$

Here, we obtain $D^{\text{t}}_{\text{eff, ABP}} \approx 183\,\mu\text{m}^2\,\text{s}^{-1}$ as confirmed in Fig. 6.4.

Without confinement, the other patterns show a smaller effective diffusivity than the straight swimmers, because in addition to rotational diffusion, they use active reorientations. Since for run-and-tumble the average reorientation angle is $\langle \Theta_{\text{tumble}} \rangle \approx 56°$, it results in more persistent motion than run-and-reverse with a reorientation angle of 180°. Run-reverse-flick performs slightly better than run-and-reverse because the flicks lead to less retracing of the trajectory compared to reversals.

For decreasing pore size, i.e., stronger confinement, agents that employ straight swimming are the first to become ineffective at navigating through their environment. Even though the porous geometry is made of spheres, i.e., convex surfaces, overlap between them can generate concave pore shapes in which elongated swimmers get stuck. Straight swimmers have to rely on thermal motion to randomly reorient themselves away from such pores to escape. Escapes are additionally hindered by the constant forward propulsion that drives them into the pore, such that translational diffusion is very unlikely to lead to a displacement out of the pore. The occurrence of concave, trapping pores happens at porosities where the average pore radius is still much larger than the size of the swimmer. Only a few of such pores significantly decrease the effective diffusivity because straight swimmers can get trapped for long durations.

The next pattern to become ineffective is run-and-tumble, but there is a range of pore sizes where run-and-tumble outperforms straight swimming. Here, tumble events make it possible to escape from pores where rotational diffusion is not strong enough to lead

to sufficient reorientations. Since the tumble angle is drawn from a distribution over $[0, \pi]$, there is a probability for tumbles with $\Theta_{\text{tumble}} > \pi/2$, pointing the swimmer out of the pore and back to an open channel. Yet, the pore size at which run-and-tumble becomes ineffective is still significantly larger than that of run-reverse-flick or run-and-reverse. This is because swimmer reorientation and pore escape requires rotation of the elongated swimmer body in space, which can be suppressed by confinement. To illustrate this point, we show the probability density of attempted tumble angles Θ_{tumble} and the actual angle Θ^*_{tumble} between start and finish of a tumble in Fig. 6.5 for one typical simulation.

Without rotational Brownian motion or obstacles, there would only be non-zero values on the angle bisector of the coordinate axes with magnitude according to the distribution of attempted tumble angles. However, in porous confinement, the deviation from $\Theta_{\text{tumble}} = \Theta^*_{\text{tumble}}$ is strongly asymmetric with the majority of actual tumble angles happening close to zero. Most tumbling, especially for larger angles, is suppressed by confinement, leaving agents trapped in pores despite their attempts to escape. To quantify this effect, we show the average actual tumble angle $\langle\Theta^*_{\text{tumble}}\rangle$ for different mean pore sizes in Fig. 6.6. The suppression of tumbles with decreasing mean pore radius starts around $r_{\text{p}} \approx 5\,\mu\text{m}$, the same value where $D^{\text{t}}_{\text{eff}}$ begins to drop significantly for run-and-tumble agents. We note that at this mean pore size, only a relatively small fraction of pores has a smaller diameter than the length l_{body} of an agent (orange curve). It is enough to cause a significant deviation of Θ^*_{tumble} from the target tumble angle Θ_{tumble}

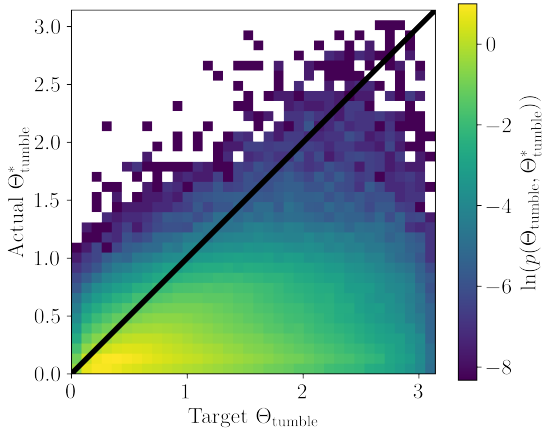

Figure 6.5. Joint probability density of attempted tumble angle Θ_{tumble} and actual tumble angle $\Theta^*_{\mathrm{tumble}}$ between start and end of a tumble at mean pore radius $r_{\mathrm{p}} \approx 2\,\mu\mathrm{m}$. The black line indicates $\Theta^*_{\mathrm{tumble}} = \Theta_{\mathrm{tumble}}$. Reproduced from Ref. [4] with permission from the American Physical Society.

because self-propelled agents are much more likely to encounter the small, trapping pores than passive particles would be: Active agents tend to be in contact with surfaces over long periods of time and slide along the pore walls due to their persistent motion. This increases the chance of entering a location of strong confinement.

Run-and-reverse and run-reverse-flick swimmers can explore environments with average pore sizes ranging down to the size of a single agent. This is not only because of the large probability of reversal events (certainty for run-and-reverse, 50% for run-reverse-flick), but also because they lead to a guaranteed pore escape,

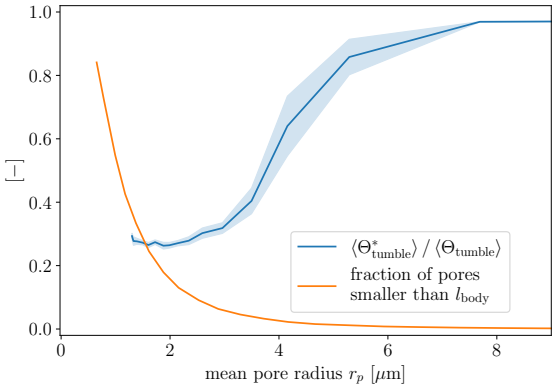

Figure 6.6. Two dimensionless quantities as a function of the mean pore size. Blue: The mean actual tumble angle $\langle\Theta^*_{\text{tumble}}\rangle$ normalized by the mean attempted tumble angle $\langle\Theta_{\text{tumble}}\rangle$. Orange: The fraction of pores smaller than the agent size, i.e., with $\tau(\mathbf{r}) < l_{\text{body}}/2$. The shaded areas denote one standard error of the mean over $N_{\text{ensemble}} = 7$ statistically independent simulations. For further explanations, see the main text. Reproduced from Ref. [4] with permission from the American Physical Society.

unlike large tumble angles with run-and-tumble. For example, a tumble with $\Theta_{\text{tumble}} = \pi$ is not equivalent to a reversal event in run-and-reverse. In the former, there needs to be enough space to allow the rotation of the swimmer body whereas in the latter, the propulsion is reversed without affecting the swimmer orientation. Run-reverse-flick reduces to run-and-reverse because flicks are geometrically suppressed just as tumbles are. Its effective diffusivity is slightly larger than that of run-and-reverse because the smaller frequency of reversals allows the agents to move faster through open

channels inbetween trapping pores. Both patterns become ineffective at porous media exploration only when the available void space becomes disconnected and motion is only possible within a finite volume. To quantify this, we calculate the volumes of connected regions with local thickness $\tau(\mathbf{r}) > r_{\text{body}}$. The dashed grey line in Fig. 6.4 shows the ratio between the volume of the largest of these regions and the total void space $V_{\text{void}} = \phi L^3$, where ϕ is the porosity of the porous geometry and L the length of the cubic simulation domain. There is only one such region for $r_{\text{p}} \gtrsim 2\,\mu\text{m}$, but around $r_{\text{p}} \approx 1.5\,\mu\text{m}$ the void space splits into many smaller regions such that even for the larger ones there can be no more percolating motion through the simulation box.

Kurzthaler *et al.* [245] find that there is no significant difference between the effective diffusivity of run-and-tumble and run-and-reverse in porous media. However, their implementation of run-and-tumble includes a 50% chance of reversing when tumbling, so we would classify that pattern as run-and-tumble-or-reverse. According to our observation of suppressed tumbles, this pattern will reduce to run-and-reverse when sufficiently confined, at which point our results are in agreement with theirs.

Run-and-reverse and run-reverse-flick are the best biologically inspired patterns for porous media exploration at very small pore sizes, but they do not perform well for larger porosities, where straight swimming is optimal. This inspired the creation of the reverse-when-stuck pattern, combining the best features of straight swimming and run-and-reverse, especially propulsion reversal without rotation of the swimmer body. As expected, it

results in the largest effective diffusivity and therefore best exploration efficiency over the whole range of pore sizes. At very small pore sizes, reverse-when-stuck performs better than run-and-reverse and run-reverse-flick, because the agent only performs reversals when they are needed for pore escape. When it has found an open channel through the porous medium, it follows that channel until it gets stuck at the end without being interrupted by a randomly triggered reversal event.

6.3.2 Run time variation

While the previous section focused on the influence of confinement on the dynamics of agents with fixed parameters, we now explore the influence of motility strategy parameters with fixed level of confinement. We assume the agents' shape and propulsion speed to be given and vary only the internal parameters that are directly linked to the strategy. We choose the run time parameter $\langle t_{\mathrm{run}} \rangle$ for comparison as it is common amongst the biologically inspired patterns run-and-reverse, run-and-tumble and run-reverse-flick. We do not change tumble or flip parameters, because they interpolate between straight swimming and run-and-tumble as well as between run-and-reverse and run-reverse-flick, and we want to preserve the essential features of each motility strategy. Simulations are performed at three levels of confinement $r_{\mathrm{p}} \in \{2\,\mu\mathrm{m}, 4\,\mu\mathrm{m}, 6\,\mu\mathrm{m}\}$ where we expect to see the most geometry-related differences between the motility strategies. The results are shown in Fig. 6.7.

All motility strategies perform very badly with $\langle t_{\mathrm{run}} \rangle \to 0$, as in this limit, agents reduce to particles without active propulsion

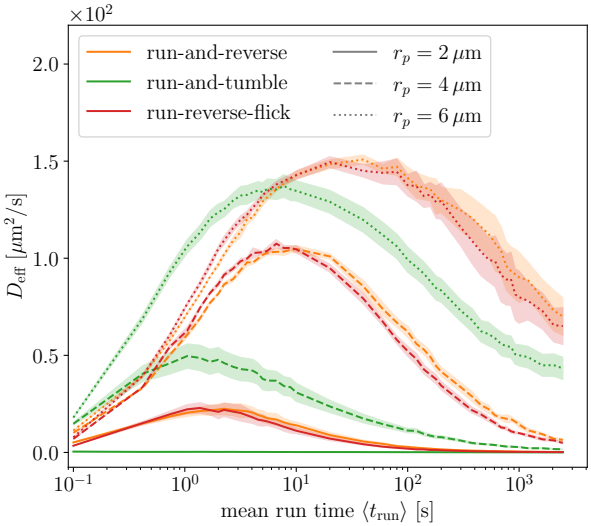

Figure 6.7. Effective diffusion coefficient as a function of mean run time. Colors denote the motility stategy. Solid, dashed and dotted lines correspond to different mean pore sizes. The shaded areas denote one standard error of the mean over $N_{\mathrm{ensemble}} = 5$ statistically independent simulations. Reproduced from Ref. [4] with permission from the American Physical Society.

that rely solely on thermal diffusion for exploration of their environment.

For the largest mean pore radius $r_{\mathrm{p}} = 6\,\mu\mathrm{m}$, run-and-tumble is most efficient for short mean run times $\langle t_{\mathrm{run}} \rangle \lesssim 7\,\mathrm{s}$. In this regime, agents perform active reorientations frequently, so they spend more time swimming through open channels in the porous medium than being trapped. Here, run-and-tumble agents benefit from larger

persistence than the patterns with reversals. However, tumbles are less likely to lead to an escape from narrow pores than reversals. This is why with increasing $\langle t_{\mathrm{run}} \rangle$, the effective diffusivity for run-and-tumble reaches its maximum earlier and at a lower value than the effective diffusivity of the other two patterns. For long mean run times, swimmers spend more time trapped than swimming freely due to less frequent escape attempts. Pore escape efficiency becomes more important than large persistence in open channels, so run-and-reverse and run-reverse-flick perform best. In the limit $\langle t_{\mathrm{run}} \rangle \to \infty$, all motility patterns reduce to straight swimming and must have the same $D^{\mathrm{t}}_{\mathrm{eff}}$. In our simulations, this limit will be reached only at mean run times $\langle t_{\mathrm{run}} \rangle \gg 2000\,\mathrm{s}$, far beyond biologically reasonable timescales.

For intermediate and tight confinement ($r_{\mathrm{p}} = 4\,\mu\mathrm{m}, 2\,\mu\mathrm{m}$), the same qualitative behaviour is observed. However, because open channels are fewer and shorter, and trapping pores are encountered more often, pore escape by motility reversal becomes more relevant at smaller $\langle t_{\mathrm{run}} \rangle$. At $r_{\mathrm{p}} = 4\,\mu\mathrm{m}$, run-and-tumble shows only a marginally larger effective diffusivity than run-and-reverse and run-reverse-flick for $\langle t_{\mathrm{run}} \rangle \lesssim 0.7\,\mathrm{s}$. For larger mean run times, the performance is significantly worse. This mean pore size coincides with the r_{p} at which tumbles are still possible, but begin to be suppressed, see Fig. 6.6, reducing the efficiency of pore escape. At $r_{\mathrm{p}} = 2\,\mu\mathrm{m}$, run-and-tumble agents are not able to explore the medium at any mean run time, as tumbling is completely suppressed.

The nonmonotonic behaviour and shift in the maximum of $D^{\mathrm{t}}_{\mathrm{eff}}$

for all motility patterns was observed and explained for run-and-reverse in Ref. [245]: When the length of free paths in the porous medium coincides with the average run length $l_{\mathrm{run}} = \langle t_{\mathrm{run}} \rangle v_{\mathrm{swim}}$, the effective diffusivity is optimal. Deviations lead to a decrease in $D_{\mathrm{eff}}^{\mathrm{t}}$, either due to premature cancellation of a run phase that could have followed a free path for a longer time or due to long trapping times that could have been avoided by more frequent reversals.

In general, these observations support the qualitative conclusions drawn from the simulations performed at fixed $\langle t_{\mathrm{run}} \rangle$. For all three levels of confinement, the ranking of motility strategies remains the same for small $\langle t_{\mathrm{run}} \rangle$. However, by tuning the run length, run-and-reverse agents can outperform run-and-tumble agents. We therefore suggest that if manufacturing or genetically creating a reverse-when-stuck agent is not feasible, optimizing a run-and-reverse swimmer is the best choice when creating an agent for porous media exploration.

6.4 Conclusions

We have performed Langevin dynamics simulations of rod-shaped, self-propelled and self-steered agents with various motility patterns in porous model geometries spanning a large range of porosities and pore sizes. By quantifying their long-time, effective diffusivity, we evaluated their ability to explore these porous environments: At high porosity, i.e., large pore sizes, straight swimming performs best due to the absence of active rotation. At intermediate pore sizes, run-and-tumble has the largest effective diffusivity. Here, the

agents can escape the pores by tumbling, which straight swimmers cannot, and they can explore the larger pore spaces with a more persistent motion than run-and-reverse or run-reverse-flick. At very small pore sizes, rotation of the rods is suppressed by confinement, causing run-and-tumble swimmers to get stuck and preventing run-reverse-flick swimmers from flicking. In this regime, run-and-reverse and run-reverse-flick swimmers can still escape small pores because their reversal mechanism enables them to reverse propulsion without rotation of the agent itself, making them the only viable strategies in tight confinement. By optimizing the run length of the different motility strategies and thus exhausting the full potential of each pattern, we find that in all geometries investigated, run-and-reverse can surpass the other strategies, making it the optimal biologically inspired motility pattern considered in this study.

These results prompted us to develop a motility pattern that outperforms the biologically inspired patterns by endowing the active agents with memory and the ability to sense position (or velocity) for some time span, and an intelligence feature that makes a decisions based on this memory: If the agent only reverses when it is stuck, defined as not moving more than its own length in its memory time, it can optimally explore open channels in the porous geometry while still being able to escape trapping pores.

With or without intelligence, we suggest that being able to reverse propulsion without rotation of the agent itself should be a high priority when designing active micro-agents for medical and engineering applications in confined spaces. Only with this ability

they can efficiently navigate the inevitably porous geometries in which they are deployed. After all, the need for miniaturisation of agents in these applications arises from the highly confined environments in which their tasks are to be performed. Furthermore, our results can serve as a basis for developing other optimized navigation strategies for specific environments.

Chapter 7

Influence of bacterial swimming and hydrodynamics on infection by phages

This chapter contains in large parts text that is taken verbatim from C. **Lohrmann**, C. Holm, and S. S. Datta, "Influence of bacterial swimming and hydrodynamics on attachment of phages", Soft Matter **20**, 4795 (2024), a publication to which I contributed the modelling, simulations, data analysis and writing of the manuscript draft.

7.1 Introduction

For the next investigation of motile bacteria in complex environments we turn to an environment where the complexity does not stem from confining geometries, but rather from other particles suspended in the same fluid as the bacteria. As introduced in Section 1.2.4, bacteriophages play an important role in bacterial

ecology in nature, but also have a great prospect for medical use.

Extensive research has focused on documenting various biological and chemical factors that influence interactions between bacteria and phages; nevertheless, the basic physical processes underlying how bacteria encounter and thereby become infected by phages in the first place remain poorly understood. For example:

How does swimming influence the rate at which bacteria encounter and become infected by phages, if at all? Despite its apparent simplicity, this question still does not have a clear answer [252]—even for the illustrative, idealized case of a cell swimming at a constant velocity v_{swim} in an unbounded, uniform, Newtonian fluid at low Reynolds number. One might expect that the rate at which the cell is infected by phages simply increases proportionately with its swimming speed as it explores more space [253]; however, this expectation does not consider the complex flow field generated by the bacterium around itself as it swims, which can advect surrounding phages in a non-trivial manner [254]. The importance of these hydrodynamics is highlighted by examining the Péclet number comparing the characteristic rates of phage transport by fluid advection and thermal diffusion, $\mathrm{Pe}_{\mathrm{phage}} \equiv v_{\mathrm{swim}} r_{\mathrm{body}} / D_{\mathrm{P}}^{\mathrm{t}}$, which exceeds unity for typical values of the bacterial swimming speed $v_{\mathrm{swim}} \sim 10 - 100\,\mu\mathrm{m\,s}^{-1}$, size $r_{\mathrm{body}} \sim 1\,\mu\mathrm{m}$, and phage diffusivity $D_{\mathrm{P}}^{\mathrm{t}} \sim 1 - 10\,\mu\mathrm{m}^2\,\mathrm{s}^{-1}$. Hence, the rate at which a bacterium encounters and becomes infected by phages is likely highly sensitive to the nature of the flow field it generates by swimming.

In a classic study [255], Berg and Purcell examined the in-

fluence of these hydrodynamics by treating the swimming bacterium as an externally-driven sphere. Building on prior calculations [256, 257], the authors concluded that because the cell pushes fluid around it as it moves, "motility cannot significantly increase the cell's acquisition of material", and the phage infection rate only increases sublinearly with swimming speed. However, while instructive, this analysis neglects two crucial features of flagellated bacteria—which are not uniform spheres, but are typically comprised of an elongated cell body driven by an adjoined elongated flagellar propeller. First, it is now well known that many such bacteria (including *E. coli*, *Bacillus subtilis*, and *Salmonella enterica*) are force-free "pushers": Each cell pushes on surrounding fluid with an equal and opposite force to the one generated by its flagella as it swims [254, 258, 259]. As a result, the fluid boundary conditions are distinct for the cell body and the flagella, and phage infection rates may thus differ considerably between the two. Second, the flow field away from a swimming bacterium has a dipolar shape with a fluid velocity magnitude $|\mathbf{u}|$ that decays with distance r away from the cell as $\sim 1/r^2$, see Section 2.2.3. This qualitatively different from the longer-ranged $|\mathbf{u}(r)| \sim 1/r$ decay characteristic of a driven sphere. How these two features influence the manner in which swimming bacteria encounter and become infected by phages is as yet unknown.

Here, we address this gap in knowledge using simulations of a "pusher"-type bacterium swimming through a fluid containing uniformly-dispersed phages. We use particle-resolved molecular dynamics to explicitly treat the cell body, flagellar propeller (here-

after referred to as the flagellum for convenience), and individual phages, all of which are coupled to and interact via an underlying fluid which we simulate using a lattice Boltzmann algorithm. We find that while swimming increases the rate at which the cell body is infected by phages, the dipolar flow thereby generated advects phages away from the forward-facing "head" of the cell body, thereby suppressing this increase by as much as twofold—as suggested by Berg and Purcell. However, this dipolar flow field also pumps phage-containing fluid to the flagellum. As a result, the phage infection rate at the flagellum is appreciable and increases nearly linearly with swimming speed, in stark contrast to the findings of Berg and Purcell. Altogether, our work suggests that while the fluid flow generated by swimming helps to protect the bacterial cell body from phages, it *promotes* phage infection at the flagellum—an effect that, to the best of our knowledge, has been overlooked in previous work. This effect may be exploited by flagellotropic phages, i.e., phages that initiate infection by attaching to the host flagellum, which are increasingly being recognized as key constituents of natural microbial communities and potentially useful therapeutics against pathogenic bacteria [117, 260]. More broadly, our findings highlight the pivotal influence of hydrodynamics on the interactions between bacteria and phages, as well as other diffusible species in microbial environments.

7.2 Methods

7.2.1 Model for phages and bacteria

▶ Phages

For simplicity, we treat phages as uniform spherical particles with radius r^{P}. Their motion in three spatial dimensions is described by Langevin dynamics. Phages do not swim actively, so we use the equation of motion 2.1 for passive particles. Furthermore, since they are assumed to be spherical, their rotational dynamics can be neglected. Phages are coupled to an underlying lattice Boltzmann fluid according to Section 2.2.4.6 and thus interact hydrodynamically with other phages and bacteria. Our focus here is on phage-bacteria encounters, and we therefore do not consider any explicit phage-phage interactions.

▶ Bacterium

The model for the cell body is a geometric refinement of the basic model described in Section 3.1. We use the basic model and a WCA potential for interactions with phages, i.e., $\sigma^{\mathrm{LJ}} = 2^{-1/6}(r_{\mathrm{body}}+r^{\mathrm{P}})$. In addition, we introduce fluid coupling points on the surface of the cell body as shown in Fig. 7.1, increasing the number of raspberry particles with respect to the model used in the previous chapters. These additional coupling points do not interact with phages, but are coupled to the underlying lattice Boltzmann fluid to better represent the surface of the cell. The addition is necessary because we will consider fine lattice Boltzmann grids to accurately resolve the flow field generated by bacterial swimming.

We model the volume of the flagellar bundle by particles that interact with phages through a WCA potential with $\sigma^{\mathrm{LJ}} =$

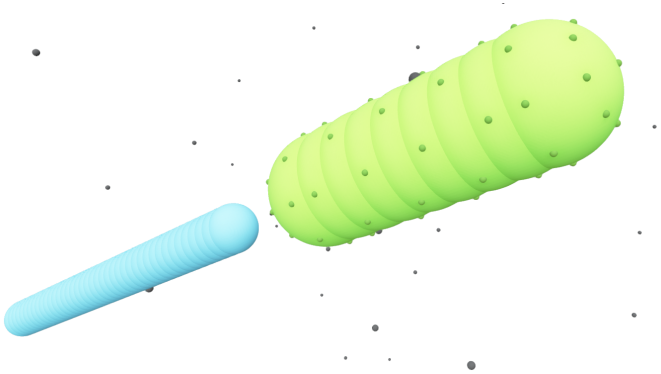

Figure 7.1. **Rendering of our rigid-body, coarse-grained molecular dynamics model of a swimming bacterium.** Large green and medium blue spheres comprise the cell body and flagellum, respectively. Small, darker green spheres mark the locations of particle-fluid coupling points. Small gray spheres represent phages dispersed in the surrounding fluid. Reproduced from Ref. [5] with permission from the Royal Society of Chemistry.

$2^{-1/6}(r_{\text{flag}}+r^{\text{P}})$, where r_{flag} denotes the radius of the flagellar bundle. The fluid coupling of the flagellar particles follows the modelling principles for "wet" swimming as outlined in Section 3.2.2.

This model represents a coarse-grained picture of a swimming bacterium that does not take into account the helical geometry of a flagellum or the intricate inner structure of a flagellar bundle. Rather, it seeks to capture four essential features of the bacterial flagellar bundle: it is permeable to fluid, exerts a force on the fluid, occupies a non-zero volume, and crucially, phages can attach to it.

7.2.2 Model of phage infection

We consider a phage as being in contact with the bacterium (either the cell body or flagellum) if the surface-to-surface distance is smaller than a prescribed encounter distance d_{enc}. Once it contacts the bacterium, the phage attaches and infects the cell at a rate k^{att}, which is a lumped parameter that describes the complex process of binding to specific receptors [261, 262]. As we show below, the overall qualitative insights that result from our simulations are insensitive to the specific choice of k^{att}. In our model, this attachment step completes the infection; because our focus is on the purely physical processes underlying phage encounter and infection, we do not consider the subsequent biological steps needed for the phage to actually insert its genetic material into the cell.

In our time-discretised numerical implementation, we check for phages in contact with the bacterium after every successive time interval Δt. For such contacting phages, we calculate the attachment probability $p_{\mathrm{attach}} = \Delta t k^{\mathrm{att}}$. Based on this probability, using a random number generator, we choose whether the phage remains free or it successfully attaches and infects the cell. If infection happens, we register the time and relative position of the phage encounter on the bacterium surface. We then move the phage to a random position outside the encounter region defined by d_{enc} to prevent double-counting; this procedure mimics the case of a bacterium swimming in an infinite fluid reservoir with constant phage number density.

We apply the same model for phage infection to both the cell body and the flagellar bundle. We thus use contact with the flag-

ellar bundle as the criterion for attachment instead of contact to individual flagella, which are not explicitly resolved in our coarse-grained approach. This simplifying assumption is justified because the fast motion of individual flagella, the complex flow field inside the bundle and the large surface-to-volume ratio of flagella all promote contact with phages once they have entered the bundle, making the approach *to* the bundle the limiting step.

We determine the overall infection rate $J = \lim_{t\to\infty} \frac{N^{\mathrm{att}}(t)}{t}$ from a linear fit to the computed number of phages that have infected the cell at time t, $N^{\mathrm{att}}(t)$, see Appendix A.4.3. For the case of $k^{\mathrm{att}} \to 0$ ($p_{\mathrm{attach}} \to 0$), the number density of phages in the encounter region is asymptotically independent of k^{att}. Hence, J scales linearly with k^{att}, and we only need to determine the number density of phages in the encounter region. Therefore, for simulations of $k^{\mathrm{att}} \to 0$, we compute J by tracking the trajectories of phages in the contact region to obtain their number density.

7.2.3 Continuum modelling

To compare the results of our particle-based simulations to those of Berg and Purcell [255], we follow their approach and solve the continuum advection-diffusion equation

$$D_{\mathrm{P}}^{\mathrm{t}} \nabla^2 c(\mathbf{r}) + \mathbf{u}_{\mathrm{Stokes}}(\mathbf{r}) \cdot \nabla c(\mathbf{r}) = 0 \tag{7.1}$$

for the phage concentration c, where $D_{\mathrm{P}}^{\mathrm{t}}$ is the phage diffusion coefficient. As in their work, we model the bacterium as a perfectly-absorbing volume-equivalent sphere of radius $r_{\mathrm{eq}} = \sqrt[3]{3r_{\mathrm{body}}^2 l_{\mathrm{body}}/4}$ in an infinite reservoir of phages, with boundary

conditions $c(|\mathbf{r}| = r_{\mathrm{eq}}) = 0$ and $c(|\mathbf{r}| \to \infty) = c_0$. The Stokes flow field is given by

$$\mathbf{u}_{\mathrm{Stokes}}(\mathbf{r}) = u_r \mathbf{e}_r + u_\Theta \mathbf{e}_\Theta, \tag{7.2}$$

$$u_r = -v_{\mathrm{swim}} \cos(\Theta) \left(1 - \frac{3r_{\mathrm{eq}}}{2r} + \frac{r_{\mathrm{eq}}^3}{2r^3}\right), \tag{7.3}$$

$$u_\Theta = v_{\mathrm{swim}} \sin(\Theta) \left(1 - \frac{3r_{\mathrm{eq}}}{4r} - \frac{r_{\mathrm{eq}}^3}{4r^3}\right) \tag{7.4}$$

in the comoving frame of reference; here, r and Θ denote the radius and polar angle in spherical coordinates, and $\mathbf{e}_r, \mathbf{e}_\Theta$ the corresponding basis vectors. The infection rate is then given by the flux of phages into the absorbing sphere surface Ω_s; we compute it directly from the solution of the concentration field via the relation

$$J_{\mathrm{Berg}} = -D_{\mathrm{P}}^{\mathrm{t}} \int_{\Omega_s} \mathbf{e}_r \cdot \nabla c \, \mathrm{d}S \,. \tag{7.5}$$

.

In practice, we solve Eqs. (7.1)–(7.4) using a finite element algorithm [263] with the boundary condition $c(|\mathbf{r}| = R) = c_0$ with $R = 50\,\mu\mathrm{m} \gg r_{\mathrm{eq}}$. The finite size effects from restricting the simulation domain to this radius are negligible, and the infection rate for $v_{\mathrm{swim}} = 0$ obtained with finite R deviates from the analytical solution for $R \to \infty$ only by $\approx 1\,\%$.

7.2.4 Choice of numerical parameters

For the phages, we choose $r^{\mathrm{P}} = 50\,\mathrm{nm}$, which is comparable to the size of many commonly-studied phages, including T4 [264] and the

flagellotropic phages χ and PBS1 [260]. We calculate the phage friction coefficient from Eq. (2.2).

The numerical friction coefficient then follows from the lattice correction given by Eq. (2.62).

The phage diffusion coefficient is given by the Einstein-Smoluchowski relation $D_{\mathrm{P}}^{\mathrm{t}} = k_{\mathrm{B}}T/\gamma_{\mathrm{P}}^{\mathrm{t}} \approx 4.4\,\mu\mathrm{m}^2\,\mathrm{s}^{-1}$ at our choice of $T = 300\,\mathrm{K}$, which is in good agreement with experimental measurements [253, 265].

Assuming water density for phages, the time scale for momentum relaxation $\tau_{\mathrm{P}}^{\mathrm{t}} = m^{\mathrm{P}}/\gamma_{\mathrm{P}}^{\mathrm{t}} \approx 5.6 \times 10^{-10}\,\mathrm{s}$ is much smaller than any time scale of interest in our system. Anologous to the arguments made in Section 3.2.4.2, we choose $\rho^{\mathrm{P}} = 10^5 \rho^{\mathrm{water}}$, which leaves the dynamics still overdamped but allows us to use a larger numerical integration time step $\delta t = 3.33 \times 10^{-5}\,\mathrm{s}$.

To mimic the commonly-studied flagellated bacterial species *E. coli* [225] and *S. enterica* [266], we choose $l_{\mathrm{body}} = 3\,\mu\mathrm{m}$ and $r_{\mathrm{body}} = 0.5\,\mu\mathrm{m}$, with ${N^{\mathrm{bead}}}_{\mathrm{body}} = 9$ and ${N^{\mathrm{bead}}}_{\mathrm{coupl}} = 62$ to obtain a sufficiently well-resolved cell surface. The bacterial mass is approximated by $m^{\mathrm{B}} = \rho^{\mathrm{B}} \pi r_{\mathrm{body}}^2 l_{\mathrm{body}}$; as detailed above for the phages, the diffusive time scale for bacteria is very small and the dynamics are overdamped, so we choose $\rho^{\mathrm{B}} = 5 \times 10^3 \rho^{\mathrm{water}}$.

For simulations without hydrodynamics, we calculate friction coefficients according to Section 2.2.3.1, using $l_{\mathrm{body}}/2$ and r_{body} as the long and short semiaxis, respectively.

For simulations with hydrodynamics, we set $\tilde{\gamma} = 2.4 \times 10^{-9}\,\mathrm{kg\,s}^{-1}$, which represents the largest value that we can use without impeding numerical stability to most closely approxi-

mate a no-slip boundary condition. The relation between F_{swim} and v_{swim} is nontrivial because of the complex flow field and the many coupling points; however, empirically, we find that using $F_{\mathrm{swim}} = \gamma^{\mathrm{eff}} v_{\mathrm{swim}}$ with an effective friction coefficient $\gamma^{\mathrm{eff}} = N^{\mathrm{bead}}{}_{\mathrm{body}} \tilde{\gamma}/0.825$ yields good agreement between the desired and actual swimming velocity, as detailed further in Appendix A.4. The flagellum is $l_{\mathrm{flag}} = 5\,\mu\mathrm{m}$ long with a radius of $r_{\mathrm{flag}} = 0.25\,\mu\mathrm{m}$ at a distance $l_{\mathrm{dipole}} = 5\,\mu\mathrm{m}$, and we take $N^{\mathrm{bead}}{}_{\mathrm{flagellum}} = 41$. For comparison to other kinds of microswimmers, we also perform all our simulations with a puller-type swimmer with $l_{\mathrm{dipole}} = -5\,\mu\mathrm{m}$. Those results are presented in Appendix A.4.

The lattice Boltzmann fluid has a dynamic viscosity $\mu = \mu^{\mathrm{water}}$ and is discretised on a grid with lattice spacing $a_{\mathrm{grid}} = r_{\mathrm{body}}$. Since all velocities are interpolated between lattice nodes, this resolution is fine enough to resolve the flow near the bacterium surface. To keep simulations stable, we choose a fluid mass density of $\rho = 1200\rho^{\mathrm{water}}$. This choice does not change the flow behaviour with respect to water since the Reynolds number $\mathrm{Re} \equiv \rho v_{\mathrm{swim}} r_{\mathrm{body}}/\mu \approx 0.017$ for a typical swimming velocity $v_{\mathrm{swim}} = 25\,\mu\mathrm{m\,s}^{-1}$ is much smaller than unity, even for this increased density.

Our simulations consider one bacterium and $N^{\mathrm{P}} = 1000$ phage particles in a fully periodic, cubic simulation domain with box length $L = 16\,\mu\mathrm{m}$. The volume fraction of phages $\phi = N^{\mathrm{P}} 4\pi (r^{\mathrm{P}})^3/3L^3 \approx 10^{-4}$ is very low, so we expect any hydrodynamic interactions between them to be negligible. Moreover, in Appendix A.4 we present evidence that there are no appreciable finite-size effects associated with the size of the simulation domain.

We set the encounter distance $d_{\mathrm{enc}} = r^{\mathrm{P}} = 50\,\mathrm{nm}$; the time scale for phage diffusion across this distance is $\tau_{\mathrm{cross}} \sim d_{\mathrm{enc}}^2 / D_{\mathrm{P}}^{\mathrm{t}} \approx 6 \times 10^{-4}\,\mathrm{s}$, so we choose $\Delta t = 1 \times 10^{-4}\,\mathrm{s}$ to adequately register phage encounters.

Each simulation is repeated N_{ensemble} times with different seeds, i.e., different initial conditions and noise realisations, to obtain the standard error of the mean of the quantities reported below. We choose $N_{\mathrm{ensemble}} \geq 5$, the exact numbers for each reported result can be found in the data set [175] that accompanies this work.

7.3 Results

7.3.1 Flow field

Before considering interactions with phages, we first verify that our simulation approach recapitulates the far-field dipolar flow field characteristic of swimming flagellated bacteria [254, 258]. This is indeed the case, as shown in Fig. 7.2, which shows the fluid flow field $\mathbf{u}(\mathbf{r})$ in the laboratory frame of reference. In Appendix A.4 we further show that the far field decay of the dipolar flow field is in close agreement to the theoretical expectation. Importantly, while the bacterium moves in the positive z-direction, our model for the flagellum-fluid interaction leads to fluid motion in the negative z-direction inside the flagellum, with swimming being force-free overall.

Having established that our simulations reproduce this characteristic dipolar flow field, we next investigate what its implications are for infection by phages. As described below, we use our simu-

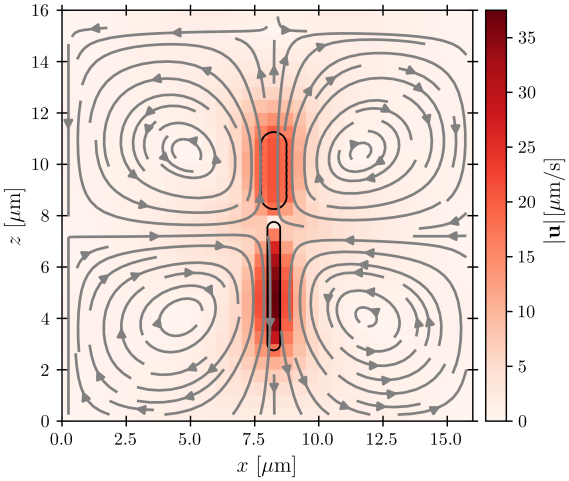

Figure 7.2. **Cross-section through the dipolar flow field generated by a swimming bacterium, in the stationary lab frame of reference.** This representative example is for the case of $v_{\text{swim}} = 20\,\mu\text{m}\,\text{s}^{-1}$ in the absence of thermal noise in the lab frame. Color scale and arrows show the magnitude and orientation of the local fluid velocity, respectively. The upper and lower black outlines show the cell body and flagellum, respectively; the cell is swimming in the $+z$ direction. Reproduced from Ref. [5] with permission from the Royal Society of Chemistry.

lations to examine phage interactions first with the cell body, then with the flagellum.

7.3.2 Phage infection of the cell body

To characterize how bacterial swimming and the associated hydrodynamic interactions (HI) influence how phages infect the cell body, we compute the infection rate J over a broad range of rep-

resentative swimming speeds v_{swim}, for a broad range of k^{att}, with or without HI included. Our results are presented in Fig. 7.3 for the limiting cases of $k^{\mathrm{att}} \to 0$ and $k^{\mathrm{att}} \to \infty$ for clarity; the intermediate values of k^{att} monotonically interpolate between these cases, as shown in Appendix A.4.5.

We first consider the case of rapidly-attaching phages ($k^{\mathrm{att}} \to \infty$). In the absence of HI, J increases approximately linearly with v_{swim} (blue $\times$, Fig. 7.3), as suggested previously [253]. Indeed, without HI, we expect that $J/c_0 \approx 4\pi D_{\mathrm{P}}^{\mathrm{t}} r_{\mathrm{eq}} + \pi r_{\mathrm{eq}}^2 v_{\mathrm{swim}}$; Here, the first term on the right hand side describes the flux of a diffusive species into a spherical, stationary, perfect absorber [267] and is given by the solution of Eq. (7.1) with $v_{\mathrm{swim}} = 0$, and the second term takes the motion of the absorber into account by calculating the rate at which its cross section explores the volume filled with a constant number density of phages that are absorbed upon contact. As shown by the dashed green line in Fig. 7.3, this prediction agrees well with our simulation results.

Incorporating HI strongly suppresses infection by phages, however. While J still increases monotonically with v_{swim}, the magnitude of this increase is considerably lessened by hydrodynamics (blue $\circ$, Fig. 7.3)—indeed, by as much as twofold at the largest swimming speed tested. Why is this the case?

Close inspection of the flow field around the cell body provides a clue: As shown in Fig. 7.2, the no-slip boundary condition on the cell body surface causes a region of fluid in its immediate vicinity to be dragged along with it as it swims. We expect that this region also advects surrounding phages along with the cell, pushing them

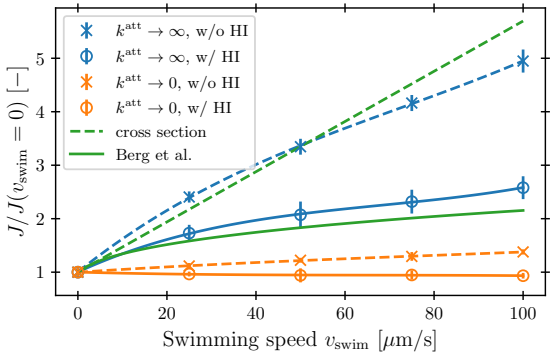

Figure 7.3. **Hydrodynamic interactions (HI) suppress the increase in phage infection rate on the cell body with swimming speed.** The infection rate J integrated over the cell body is computed from our simulations and normalized by its value when the bacterium is not swimming. Blue and orange points show the cases of rapidly- or slowly-attaching phages, respectively. Error bars represent the standard error of the mean over statistically independent simulations, blue and orange lines are polynomial fits to guide the eye. The dashed green line corresponds to a model of rapid phage infection through diffusion and uptake by the cell body cross section, neglecting HI. The solid green line shows the prediction of Berg and Purcell from a more simplified continuum model of a driven spherical bacterium. Adapted from Ref. [5] with permission from the Royal Society of Chemistry.

away from its forward-facing "head"; Consequently, these phages must rely primarily on passive thermal diffusion to cross this region and successfully infect the cell, independent of the bacterial swimming speed.

This effect is more clearly visualized in the reference frame that moves along with the bacterium. The relative flow field given by $\mathbf{u}^* = \mathbf{u} - v_{\text{swim}}\hat{\mathbf{e}}$, where the asterisk denotes quantities measured in this comoving frame, is shown in Fig. 7.4. We quantify the relative importance of phage advection and diffusion using the local Péclet number

$$\text{Pe}^*_{\text{phage}}(\mathbf{r}) \equiv |\mathbf{u}^*(\mathbf{r})| r_{\text{body}} / D^{\text{t}}_{\text{P}} \tag{7.6}$$

defined in this comoving frame; the iso-line of $\text{Pe}^*_{\text{phage}}(\mathbf{r}) = 1$ is shown by the dashed line. As expected, within the region bordered by the dashed line, the fluid is nearly at relative rest and $\text{Pe}^*_{\text{phage}}(\mathbf{r}) < 1$—confirming that any phages contained therein must rely primarily on thermal diffusion to infect the cell body. Any enhancement in the phage infection rate arising from bacterial swimming is therefore suppressed by this "protective shield" of fluid that surrounds the cell body.

This hydrodynamic effect manifests at smaller phage attachment rates ($k^{\text{att}} \to 0$), as well. When HI are not included, the swimming bacterium is not protected by the "shield" of quiescent fluid discussed above. Instead, as it swims, the cell collects and accumulates phages at its head, and J again increases approximately linearly with v_{swim}, as shown by the orange $\times$ in Fig. 7.3. In this case, the swimming bacterium does not appreciably remove contacting phages from the fluid, whereas in the case of $k^{\text{att}} \to \infty$,

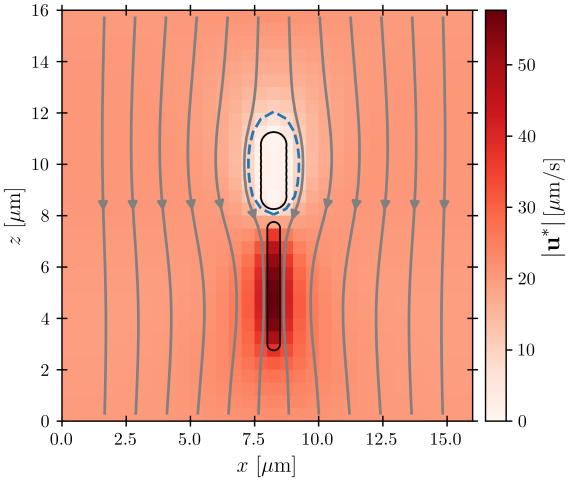

Figure 7.4. **Cross-section through the dipolar flow field generated by a swimming bacterium, in the cell's moving frame of reference.** The image shows the same flow field as in Fig. 7.2, but in the comoving frame. The cell is swimming in the $+z$ direction. The blue dashed line marks $\mathrm{Pe}^*_{\mathrm{phage}} = 1$. Reproduced from Ref. [5] with permission from the Royal Society of Chemistry.

phages are locally depleted from the vicinity of the cell upon contact and infection. Therefore, the dependence of J on v_{swim} is more modest for poorly-attaching phages; Indeed, when HI are included, there is no measurable dependence of J on v_{swim} (orange ∘, Fig. 7.3).

The protective influence of the hydrodynamic "shield" is also apparent in the spatial distribution of phage infection over the cell body, shown for the example of $v_{\mathrm{swim}} = 100\,\mu\mathrm{m\,s}^{-1}$ and $k^{\mathrm{att}} \to 0$ in Fig. 7.5. As expected, without HI (left panel), infections occur

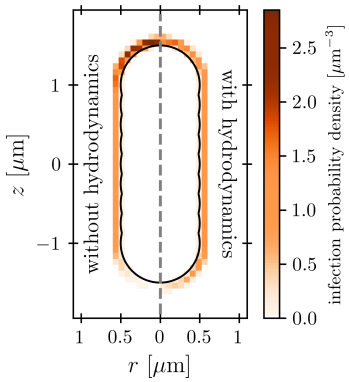

Figure 7.5. **Hydrodynamic interactions cause phages to be advected away from the head of the cell.** Color scale shows the probability density of phage infection over the surface of the cell body, for the example of $v_{\mathrm{swim}} = 100\,\mu\mathrm{m\,s}^{-1}$ and $k^{\mathrm{att}} \to 0$. The cell is swimming in the $+z$ direction. Without hydrodynamics, phages accumulate at its head, whereas when hydrodynamics are incorporated, the flow field established by swimming makes the distribution of infection sites more uniform along the cell body. Reproduced from Ref. [5] with permission from the Royal Society of Chemistry.

preferentially at the head of the cell. However, HI push phages away from the head of the cell, causing infections to be distributed more uniformly around the cell body (right panel). Figure 7.6 quantifies this difference for all the simulation conditions tested using the average z-position of phage infection relative to the cell body center of mass, i.e., the first moment of the infection probability density. Again, as shown by the difference between $\times$ and $\circ$ symbols, HI reduce the asymmetry of phage infection for both $k^{\mathrm{att}} \to 0$ and $k^{\mathrm{att}} \to \infty$ over all swimming speeds tested.

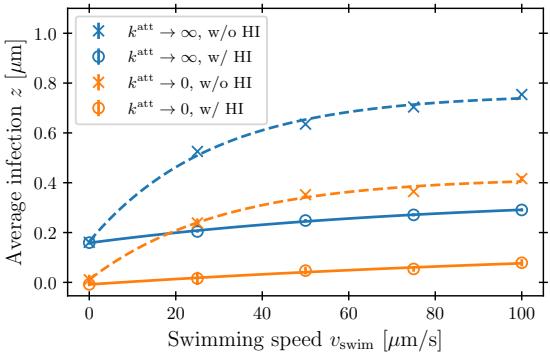

Figure 7.6. **Hydrodynamic interactions cause phages to be advected away from the head of the cell.** Symbols show the average position of phage infection positions along the bacterial symmetry axis relative to the cell body center. An average of $z > 0$ means the infection probability density is shifted towards the head of the cell. Blue and orange points show the cases of rapidly- or slowly-attaching phages, respectively. The lines are exponential fits to guide the eye. Error bars represent the standard error of the mean over statistically independent simulations, and are sometimes smaller than the symbol size. Adapted from Ref. [5] with permission from the Royal Society of Chemistry.

In their classic paper [255], Berg and Purcell did not consider the elongated shape of a swimming bacterium, the distinction between the cell body and flagellum, or the dipolar flow field established by swimming. Nevertheless, using a more simplified continuum model of an externally-forced sphere, they intuited the protective hydrodynamic effect uncovered by our simulations, noting that "The molecules [or in our case, phages] in front of the cell are carried out of its way along with the fluid it must push aside to move. The cell carries with it a layer of liquid that is practically

stationary in its frame of reference. Every molecule [or phage] that reaches the surface of the cell must cross this layer by diffusion." Remarkably, despite the simplifications made in their work, Berg and Purcell's prediction for the infection rate (solid green curve, Fig. 7.3) shows excellent agreement with the results of our more detailed simulations (blue ∘). One may not expect this agreement *a priori* given the marked difference between the actual dipolar flow field established by the swimming cell and the approximation used by Berg and Purcell. However, our results show that the essential qualitative feature of the low $\mathrm{Pe}^*_{\mathrm{phage}}$ region are independent of the shape and propulsion mechanism of the bacterium, justifying their simplifying assumptions *a posteriori*—but only for the case of the cell body. As we show in the next section, we find dramatically different behavior for the bacterial flagellum.

7.3.3 Phage infection of the flagellum

While the cell body drags a protective region of fluid with it, the flagellar bundle does not. Instead, because it is permeable to and exerts a force on the fluid, $\mathrm{Pe}^*_{\mathrm{phage}} \gg 1$ especially in the immediate vicinity of the flagellum, as seen by the dark red region of Fig. 7.4. As a result, we expect that hydrodynamic interactions are not protective as for the cell body, but instead, *promote* infection of the flagellum. Our simulations confirm this expectation, as shown in Fig. 7.7.

Unlike the case of the cell body, HI greatly *increase* the flagellar infection rate, as seen by comparing the ∘ and × points in Fig. 7.7—indeed, by nearly twofold at the largest swimming speed

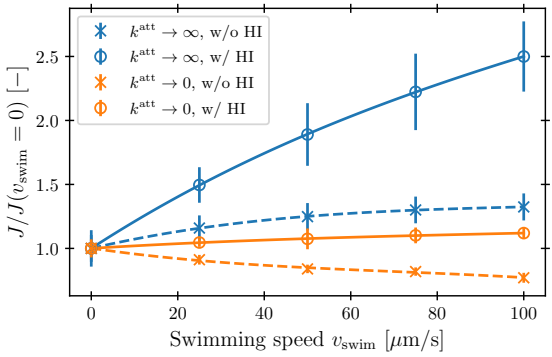

Figure 7.7. **Hydrodynamic interactions promote phage infection of the flagellum.** The infection rate J integrated over the flagellum is computed from our simulations for varying v_{swim} and normalized by its value when the bacterium is not swimming. Lines are polynomial fits to guide the eye. Error bars represent the standard error of the mean over statistically independent simulations. Adapted from Ref. [5] with permission from the Royal Society of Chemistry.

tested. In the absence of HI, J only increases marginally with v_{swim} for $k^{\mathrm{att}} \to \infty$. It even decreases with v_{swim} for $k^{\mathrm{att}} \to 0$, due to the cell body pushing phages radially outward upon contact. However, when HI are taken into account, the flagellum pumps in phage-laden fluid from the sides of the cell body and moves it through the space occupied by the flagellar bundle. Therefore, the volume of fluid coming in contact with the flagellum, and thus phage infection, increases with v_{swim}. Moreover, because the fluid is pumped along the $-\hat{\mathbf{e}}$ direction, we expect that phage infection is more likely to occur at the forward end of the flagellum with increasing v_{swim}. This expectation is confirmed quantitatively in

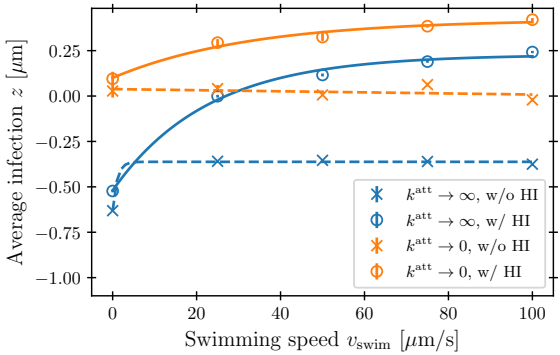

Figure 7.8. **Hydrodynamic interactions increase dependence of infection location on swimming speed.** Average position of phage infection positions along the bacterial symmetry axis relative to the flagellum center. An average of $z > 0$ means the infection probability density is shifted towards the forward end of the flagellum. For $k^{\mathrm{att}} \to \infty$, the attachment is shifted into the negative direction at $v_{\mathrm{swim}} = 0$ because the cell body depletes the region in front of the flagellum of phages. Lines are exponential fits to guide the eye. Error bars represent the standard error of the mean over statistically independent simulations. Adapted from Ref. [5] with permission from the Royal Society of Chemistry.

Fig. 7.8.

7.3.4 Total infection rate

Hydrodynamic interactions reduce phage infection of the cell body and promote phage infection of the flagellum. Figure 7.9 shows how for the total rate, these effects nearly cancel out the influence of hydrodynamics. For rapidly-attaching phages ($k^{\mathrm{att}} \to \infty$), there is no appreciable difference in infection rate for all swimming speeds

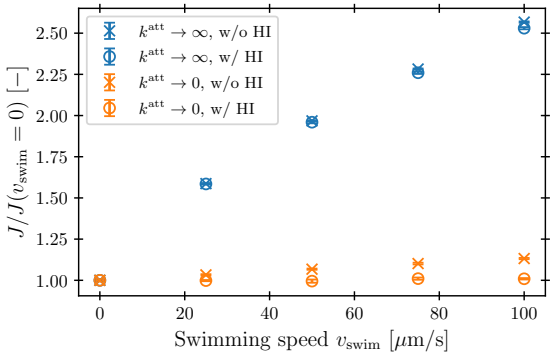

Figure 7.9. **Hydrodynamic interactions have a small influence on the total infection rate if phages are flagellotropic.** The infection rate J integrated over the entire bacterium comprising cell body and flagellum is computed from our simulations for varying v_{swim} and normalized by its value when the bacterium is not swimming. Blue and orange points show the cases of rapidly- or slowly-attaching phages, respectively. Error bars represent the standard error of the mean over statistically independent simulations.

considered, and for slowly-attaching phages, the difference is less than 20 %.

Considering the flow field in the comoving frame (see Fig. 7.4), we can explain why the the hydrodynamic effects cancel almost completely for $k^{\mathrm{att}} \to \infty$ rather than only partially: The two hydrodynamic effects — shielding of the cell body and pumping through the flagellar bundle — are not independent, because they affect the same material points of the fluid and thus the same phages. Following the stream lines starting in front of the bacterium, we see that they bend around the cell body and then

become focused inside the flagellar bundle. The phage population that leads to an increase of infection at the flagellum is thus the exact *same* phage population that previously was prevented from infecting the cell body because it was advected around it. For $k^{\mathrm{att}} \to \infty$ this means that every phage that would have infected the cell body if there were no hydrodynamic interactions now infects the flagellum instead, leaving the total infection rate unaffected. This mechanism is robust with regard to the specific geometrical parameters of the cell body and the flagellar bundle as long as every streamline that passes through the flagellum corresponds to a location in front of the cell body that is covered by its cross section.

For $k^{\mathrm{att}} \to 0$ the cancellation of hydrodynamic effects is less complete because here it is more relevant how long the phages stay in contact and not just if they make contact. Thus, the specific relative length and surface area difference between cell body and flagellar bundle determines the extent to which the total attachment rate is influenced by the inclusion of hydrodynamics.

7.4 Conclusions

Using coarse-grained molecular dynamics simulations of a swimming bacterium that explicitly treat its cell body and flagellum separately, with hydrodynamic interactions incorporated via coupling to a lattice Boltzmann fluid, our work has shed new light on the influence of swimming on infection by phages. We find that while swimming increases the rate at which both the cell body and

flagellar propeller are infected by phages, hydrodynamic interactions strongly *suppress* this increase at the cell body, but conversely *enhance* this increase at the flagellar bundle. This difference in infection arises from the characteristic dipolar flow field generated by a swimming bacterium, which advects phages away from the cell body, but pumps phage-laden fluid into the flagellum. The total infection rate, combining infections of the cell body and the flagellum, is almost independent of the inclusion of hydrodynamic effects because it's the very same phages that get advected around the cell body which get pumped into the flagellar bundle. Hence, while our results corroborate the findings of Berg and Purcell for the cell body, our work provides a counterpoint to their conclusion that "in a uniform medium motility cannot significantly increase the cell's acquisition of material [in our case, phages]." Experimentally testing these predictions—i.e., by combining direct visualization of phage infection [268] with optical trapping of swimming cells [269]—will be an important direction for future work.

Altogether, our findings highlight the pivotal influence of hydrodynamics on the interactions between bacteria and phages, as well as other diffusible species—i.e., nutrients, toxins, or signalling molecules—in microbial environments. They also provide a new perspective on the biophysical tradeoffs associated with bacterial swimming. While swimming can be beneficial by enabling bacteria to escape from harmful environments, find new resources, and colonize new terrain, it can also be costly—not only because of the additional energy it requires of the cell, but also because it is often thought to increase the probability of encountering sur-

rounding phages. Our results demonstrate that this latter cost is not appreciable for the cell body, due to the protective "shield" of fluid established by hydrodynamics, but is appreciable for the flagellar bundle, which pumps surrounding phages in. We conjecture that this may in part be why many phages have, over billions of years of evolution, developed ways to exploit bacterial swimming for their benefit by targeting the flagellum [117, 260]. Swimming bacteria may, in turn, have evolved localised defence countermeasures against phage infection such as through modification of specific surface receptors or production of outer membrane vesicles as decoys [270]. Investigating how these biological and chemical processes, combined with the hydrodynamic effects illuminated by our work, influence phage-bacteria interactions will be a useful avenue for future research.

Chapter 8

Emergence of chemotactic strategies with multi-agent reinforcement learning

This chapter contains in large parts text that is taken verbatim from S. J. Tovey, C. **Lohrmann**, and C. Holm, "Emergence of Chemotactic Strategies with Multi-Agent Reinforcement Learning", Machine Learning: Science and Technology, accepted manuscript (2024), a publication to which I contributed the physics aspects of the simulations, data interpretation and co-writing of the manuscript draft.

8.1 Introduction

For the last results chapter, we will take a step back from the now familiar bacterial model and explore how the framework of stochastic active dynamics as a model for bacterial motion can be used in combination with new numerical tools like reinforcement learn-

ing (RL). This chapter introduces the scientific field of machine learning and its application to the control of active agents such as bacteria or artificial microrobots. As an exemplary use case, we will study what kinds of strategies (in the sense of motility patterns akin to the ones presented in Chapter 6) can be learned such that the agent achieves chemotaxis, i.e., directed motion towards the source of a chemical, see Section 1.2.2.

Previous reviews have discussed the function of biological microswimmers in great detail [189, 271], elucidating the mechanisms and strategies behind their movement. However, understanding the emergence of this behaviour and judging its optimality is critical as scientists strive to construct the artificial counterparts of biological microswimmers. Learning chemotaxis *in silico* has been the focal point of several research papers aimed at reproducing or better understanding biological microswimmers through the use of reinforcement learning [272–275]. In their 2021 study, Hartl *et al.* [274] applied a genetic algorithm to the problem of learning shape deformations for navigation in static and dynamic environments. They found that the neural networks learned a movement closely resembling that of run-and-tumble motion. In another 2021 study, Muiños-Landin *et al.* [275] applied Q-learning to navigation strategies in self-thermophoretic particles from which they again see the emergence of run-and-tumble motion. They further investigated the effects of temperature on the learning process, identifying that models trained at higher temperatures took longer to learn their emergent strategy. Finally, our previous work [9] directly addressed the role of temperature in the emergent strategy of

RL-driven microswimmers by studying chemotaxis learning by the actor-critic reinforcement learning algorithm. It was found that, while the efficacy of chemotaxis changed with different temperatures, the same run-and-tumble strategy arose from the majority of agents trained at different temperatures. While it is clear that RL algorithms can and, in fact, seemingly often do learn run-and-tumble type patterns for chemotaxis problems, what impact this has on our understanding of biological microswimmers and even optimal design of artificial swimmers is not clear. In this chapter, we study the natural limitations on emergent chemotaxis by training actor-critic RL models using prolate, oblate, and spherical agents of different sizes and with different swim speeds in environments subject to translational and rotational Brownian motion. In this way, we hope to identify how optimal RL algorithms are for the learning task and to identify, if any exist, optimal size/speed combinations of microswimmers in these environments, which may guide our interpretation of biological microswimmers as well as advise the design of artificial ones. Furthermore, by investigating the deployment of the RL algorithms close to conditions where agents will be dominated by rotational and translational Brownian motion, we can explore the emergence of different navigation strategies that may be leveraged in the treatment of biological or artificial swimmers, essentially peering into the minds of bacteria as they navigate environments.

8.2 Theory

8.2.1 Actor-critic reinforcement learning

Reinforcement learning concerns itself with the interactions between an agent and its environment within which the agent gradually learns to achieve a desired task [276]. The agent is typically provided with a set of actions $\{\mathfrak{a}\}$ it may perform and uses a policy, $\pi(\mathfrak{a}_t|\mathfrak{s}_t)$ to decide at time t, based on its current state, $\mathfrak{s}_t$, what the best action $\mathfrak{a}_t$ will be such that it maximises a reward, $\mathfrak{r}(\mathfrak{s}_t)$. Over the course of one or many simulations, this policy will be updated so that the agent becomes more efficient at accomplishing this task and maximises its reward, yielding the optimal policy

$$\pi' = \arg\max_{\pi} \langle \mathfrak{r}(\mathfrak{s}_t|\pi) \rangle. \tag{8.1}$$

Deep reinforcement learning accomplishes this task using deep neural networks as the policy π [277]. For our investigations, the actor-critic approach to deep reinforcement learning has been adopted due to its flexibility and efficacy [278, 279]. In actor-critic reinforcement learning, the actor takes on the role of the policy π_θ, parameterized by θ, taking as input the current state of the agent and returning a distribution over possible actions from which one is selected. The critic takes on the role of a value function, $\mathfrak{C}_\omega^{\pi_\theta}$, the objective of which is to describe the expected return of an agent starting in state $\mathfrak{s}_t$ and following policy π. During training, the actor is tasked with maximising the finite-horizon return of its policy

$$\mathfrak{J}(\pi_\theta) = \left\langle \sum_{t=0}^{\mathfrak{T}} \log \pi_\theta(\mathfrak{a}_t|\mathfrak{s}_t) \cdot \mathfrak{A}^{\pi_\theta}(\mathfrak{s}_t, \mathfrak{a}_t) \right\rangle_\tau, \tag{8.2}$$

where $\mathfrak{T}$ is the episode length as explained below, $\langle\cdot\rangle_\tau$ an average over trajectories, and $\mathfrak{A}^{\pi_\theta}$ the so-called advantage. The advantage

$$\mathfrak{A}_t^{\pi_\theta} = \mathfrak{R}_t(\mathfrak{s}_t, \mathfrak{a}_t) - \mathfrak{C}_\omega^{\pi_\theta}(s_t) \tag{8.3}$$

combines the critic's value function and the actual rewards measured from the simulation that is used as training input. In our studies, we use simple decay function

$$\mathfrak{R}_t = \sum_{t'=t}^{\mathfrak{T}} \epsilon^{t'-t} \mathfrak{r}(\mathfrak{s}_{t'}), \tag{8.4}$$

with a decay factor $\epsilon < 1$. Unlike traditional supervised learning schemes, where training is performed on each data point individually, here, the policy is applied $\mathfrak{T}$ times and data is collected over this episode. Then, using the trajectory segment and the reward function $\mathfrak{r}$, the return $\mathfrak{J}$ of the policy over the entire episode is calculated.

$\mathfrak{J}(\pi_\theta)$ is maximised by way of gradient ascent on the actor parameters with updates taking the form

$$\theta' = \theta + \eta \cdot \nabla_\theta \mathfrak{J}(\pi_\theta), \tag{8.5}$$

where θ' is the new set of parameters after the training step and η the learning rate.

Recalling that the actor output is a distribution over actions, should the advantage $\mathfrak{A}$ be negative, i.e., the critic believes a better trajectory could have been chosen, the log probability of these actions will be discouraged. If this number is positive, the actor has outperformed the expectation of the critic and the policy is reinforced.

The critic network $\mathfrak{C}_\omega$ is trained directly on the chosen expected returns function via the Huber loss $\mathfrak{L}(\mathfrak{R}_t, \mathfrak{C}_\omega(\mathfrak{s}_t))$, where

$$\mathfrak{L}(x,y) = \begin{cases} \frac{1}{2} \cdot |x-y|^2 & \text{, for } |x-y| \leq \delta, \\ \delta \cdot (|x-y| - \frac{1}{2}\delta) & \text{, otherwise,} \end{cases} \tag{8.6}$$

with $\delta = 1$ in this study. Such an update procedure is referred to as simple or vanilla policy gradient [280]. More sophisticated approaches exist, e.g., proximal policy optimization [281], but for this study, the simpler approach sufficed.

8.2.2 Multi-agent reinforcement learning

In our simulations, we work with not one, but many agents simultaneously, moving from the general concept of reinforcement learning into multi-agent reinforcement learning (MARL) [282]. Here, all agents share a single actor and critic network and at the update time, also the experience that they have gathered. During the simulations, each agent asks the actor for an action to take individually and collects its own reward. At the time of the update, $\mathfrak{J}(\pi_\theta)$ becomes,

$$\mathfrak{J}_{\text{MARL}} = \frac{1}{N} \sum_i^N \mathfrak{J}_i(\pi_\theta), \tag{8.7}$$

where i sums over the agents in the system and J_i is simply Eq. (8.2) for a single agent. In this way, the experience of each agent is accumulated and updated together.

The field of MARL has a a vast set of definitions with respect to how individual agents interact and share knowledge in order to

achieve the problem they are training on [283]. In this work, a decentralized Markov decision process is used to describe how the agents in the system interact. The system is considered decentralized as each agent receives only local information regarding its environment and a local reward for its own actions. During training, these rewards and local states are summed over and in doing so, the agents share the knowledge with one another.

8.3 Methods

8.3.1 RL implementation

All reinforcement learning and all simulations have been handled through the open-source software package SwarmRL [10]. SwarmRL is a Python library built to combine molecular dynamics engines or real-world experiments with classical control and reinforcement learning algorithms. All machine learning uses the JAX [284] and Flax [285] libraries.

8.3.2 Agent model

Because the focus of this chapter lies more on reinforcement learning and the interpretation of the learned strategies, the bacterial model is much simpler than the one used in the previous chapters. Agents are represented by just one coarse-grained molecular dynamics particle, which follows the overdamped, active Brownian equations of motion 2.21 and 2.23 in $d = 2$ dimensions without hydrodynamic interactions. The simulation domain is a $1\,\mathrm{mm} \times 1\,\mathrm{mm}$

periodic domain and we consider 10 interacting agents. We choose a time step $\delta t = 0.005\,\mathrm{s}$, the active forces and torques are updated every $\Delta t = 0.1\,\mathrm{s}$. In all cases, unless otherwise specified, when referring to time in this investigation, we refer to the number of times an action is computed for each agent in the simulation.

For spherical agents, we use the WCA potential as introduced in Section 3.1.2.1 with $\epsilon^{\mathrm{LJ}} = k_{\mathrm{B}}T$ and varying particle size $\sigma^{\mathrm{LJ}} = 2r_{\mathrm{body}}$. Particle anisotropy is captured by anisotropic friction coefficients, see Section 2.2.3.1, and an anisotropic interaction between agents. We use the Gay-Berne potential V^{GB} as introduced in Section 3.1.2.2 with aspect ratio $l_{\mathrm{GB}} = 3$ for the prolate particles and $l_{\mathrm{GB}} = \frac{1}{3}$ for the oblates. We choose $\sigma^0_{\mathrm{GB}} = \sigma^{\mathrm{LJ}}$ and $\epsilon^0_{\mathrm{GB}} = \epsilon^{\mathrm{LJ}}$.

The study consideres three agent shapes: oblate, prolate, and spherical. Figure 8.1 displays renderings of these agents for "radius" $1\,\mu\mathrm{m}$ constructed using the Vedo Python package [286]. To make the radii comparable between spherical and anisotropic particles, we use the radius of a volume-equivalent sphere as the "radius" r_{body} of the spheroids.

To quantify the relative importance of active and passive motion, we define translational and rotational Péclet numbers

$$\mathrm{Pe}^{\mathrm{trans,\,rot}} = \frac{\tau^{\mathrm{diff}}_{\mathrm{trans,\,rot}}}{\tau^{\mathrm{act}}_{\mathrm{trans,\,rot}}}. \tag{8.8}$$

Here,

$$\tau^{\mathrm{diff}}_{\mathrm{rot}} = \frac{1}{2D^{\mathrm{r}}} = \frac{\gamma^{\mathrm{r}}}{2k_BT}, \quad \tau^{\mathrm{act}}_{\mathrm{rot}} = \frac{2\pi}{\omega_{\mathrm{act}}}, \tag{8.9}$$

are the timescale of decorrelation of the particle director through rotational diffusion and the timescale for one active rotation, re-

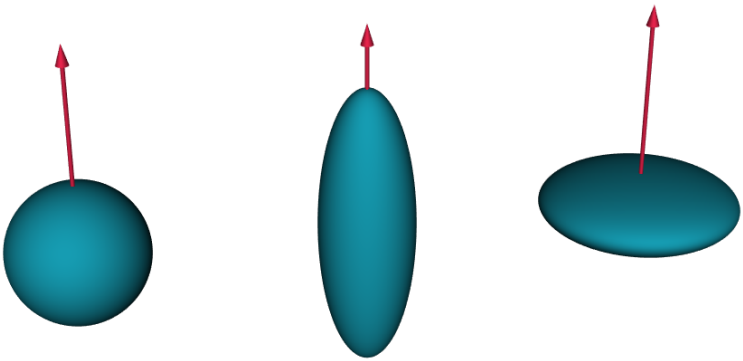

Figure 8.1. Graphical representation of the three agent shapes considered in this study: spherical (left), prolate (center), and oblate (left). They all have the same volume. Reproduced from Ref. [6] with permission from IOP Publishing..

spectively. For the translational degrees of freedom we have

$$\tau_{\text{trans}}^{\text{diff}} = \frac{r_{\text{body}}^2}{D^{\text{t}}} = \frac{r_{\text{body}}^2 \gamma^{\text{t}}}{k_B T}, \quad \tau_{\text{trans}}^{\text{act}} = \frac{r_{\text{body}}}{v_{\text{swim}}}, \tag{8.10}$$

as the timescale for diffusion of one particle radius and the timescale for swimming of one particle radius, respectively. In regimes where $\text{Pe}^{\text{trans, rot}} \gg 1$ the dynamics will be dominated by active motion and when $Pe^{trans,rot} \ll 1$, it will resemble passive diffusion.

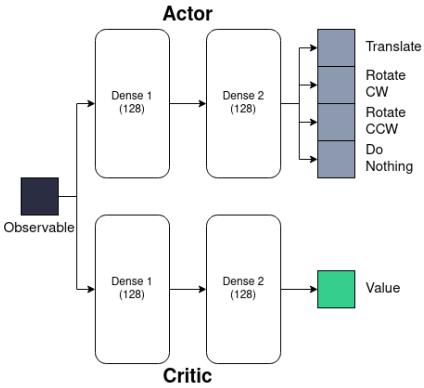

Figure 8.2. Representation of actor-critic reinforcement learning architectures. Reproduced from Ref. [6] with permission from IOP Publishing.

8.3.3 Reinforcement learning parameters

In our investigations, the actor-critic approach to reinforcement learning is utilised with a network architecture displayed in Figure 8.2. A two-layer network, each with 128 units, is deployed for both the actor and the critic, along with ReLU activation functions. During the training, each network is trained for 10000 episodes, each of which consists of 20 applications of the policy. Each episode would be 2 s in real time. Updates of the network are handled by the Adam optimizer [287] using a learning rate of 0.002. For each swim speed and agent size, 20 reinforcement learning runs were performed to collect statistics.

8.3.4 Actions

Agents are endowed with the ability to perform four distinct actions

$$\mathcal{A} = \begin{cases} \text{Translate:} & v_{\text{swim}} = n \cdot 2r_{\text{body}}\,\text{s}^{-1},\ \omega_{\text{act}} = 0.0 \\ \text{Rotate CCW:} & v_{\text{swim}} = 0,\ \omega_{\text{act}} = 10.472\,\text{s}^{-1} \\ \text{Rotate CW:} & v_{\text{swim}} = 0,\ \omega_{\text{act}} = -10.472\,\text{s}^{-1} \\ \text{Do Nothing:} & v_{\text{swim}} = 0,\ \omega_{\text{act}} = 0.0, \end{cases} \tag{8.11}$$

where n is a scaling factor that we vary during the experiment. The rotation speed was chosen to be similar to that of *E. coli* [84]. In line with Ref. [288], we argue that agent volume is proportional to its swimming speed. Therefore, the action velocity is measured in body lengths.

As the state description $\mathfrak{s}_t$, agents do not receive full information of the system which would include the position of the chemical source that is the target of chemotaxis. Instead, the description is designed to resemble a bacterium sensing changes of chemical concentration, defined mathematically by

$$\mathfrak{o}_i(t) = f\left(|\mathbf{r}_i(t) - \mathbf{r}_s|\right) - f\left(|\mathbf{r}_i(t - \Delta t) - \mathbf{r}_s|\right), \tag{8.12}$$

where $\mathfrak{o}_i$ is the observable for the i^{th} agent, $f(r) = r^{-1}$ is the field chosen to represent the chemical being sensed, and $\mathbf{r}_s$ denotes the position of the source of the field. To encourage chemotaxis, agents are rewarded using a similar function

$$\mathfrak{r}_i(t) = \begin{cases} \mathfrak{o}_i & \text{if } \mathfrak{o}_i > 0 \\ 0 & \text{else.} \end{cases} \tag{8.13}$$

This way, movement towards the source is encouraged, but movement away is not explicitly discouraged. We further refrain from using an absolute measure of the field in this study as it would not resemble the natural sensing abilities of the bacteria [289].

8.3.5 Computational methods

Training and deployment of the reinforcement learning models was performed on the University of Stuttgart SimTech compute cluster. Each simulation and training routine utilised six threads of an AMD EPYC 7702 CPU node, and all simulations were run in parallel. Due to the system sizes and machine learning being performed, no GPUs were required for these experiments. Training of each model required approximately twenty-four hours, and the deployment simulations were approximately six hours. The simulations and models were analysed on the same cluster hardware.

8.4 Results

Due to the similarity in the results and the amount of analysis, only the plots for the spherical agent analysis are shown in the main manuscript. All other plots are included in Appendix A.5.1, and any deviations between results are mentioned here.

8.4.1 Probability of emergent chemotaxis

This investigation aims to identify limits on emergent chemotaxis in RL agents in the hope that such limits cross over into biology,

allowing us to study natural biological processes using RL as a valid surrogate model. These limits suggest formulating a phase diagram with forbidden regions where this learning is impossible. To this end, all simulations were collected where during the final 50 % of the deployment trajectory all particles remained below 15 µm from the source of the field. This distance was determined based on the visual observation that no model that had successfully learned chemotaxis was farther away from the source than this distance. The successful simulations were used to compute the probability of learning chemotaxis by rationing them against the total number of simulations performed for a single speed and agent size. Figure 8.3 shows the computed phase diagram, where the color corresponds to the probability of successfully learned chemotaxis. Interestingly, it appears that smaller, faster agents are more likely to learn an effective chemotaxis policy. Suppose we equate the difficulty the RL algorithm has in training a policy with the real-world problem of evolving a suitable structure for life. In that case, these results suggest a trade-off between speed and size when learning how to perform chemotaxis.

The most critical component of Fig. 8.3 is the explanation of the phase boundary in physical terms. We consider the ratios between Brownian motion and the active motion described by Eqs. (8.9) and (8.10) as the main determinants of agent behaviour in this study. The green lines in Fig. 8.3 correspond to the agent radius and speed values for which the aforementioned Péclet numbers are 1.0 for translational (solid) and rotational (dashed) diffusion. The translational Péclet number forms a boundary where the RL

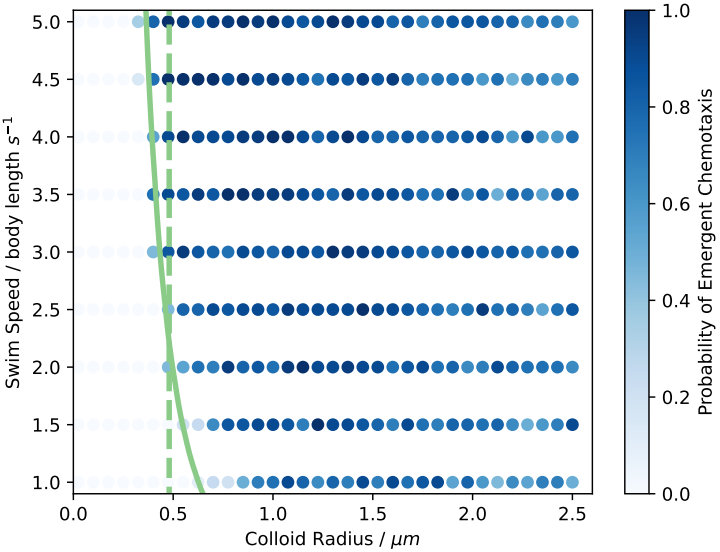

Figure 8.3. Probability of successful chemotaxis emerging from RL studies. Raw data from the experiment. The colour of each point corresponds to the number of RL simulations that successfully learned how to perform chemotaxis. The green lines indicate the theoretical values at which translational (solid) and rotational (dashed) diffusion becomes dominant compared to the active motion of the agents.

agents can no longer learn successful chemotaxis. The rotational diffusion boundary appears less strict, particularly for the faster agents, where it appears that with enough translational activity, the agents can overcome having rotational diffusion dominate over active rotation. The alignment of our simulation results with the physical boundaries we identified suggests that as soon as it is physically possible for an RL agent to learn chemotaxis, it does so. Later, we will discuss the very few cases of successful chemotaxis that were learned in the "forbidden" region.

8.4.2 Learning efficiency

Next, we look at how the reward received from the reinforcement learning process changed depending on the size and speed of the agents. This measure will indicate how easy it was for the model to learn the policy required to perform chemotaxis. Figure 8.4 outlines the results of this study in a similar manner to Fig. 8.3. In the figure, the point's colour corresponds to the total reward accumulated by the agents during all 10'000 training episodes. In order to compute the colour values in Fig. 8.4, we corrected the size difference between the agents. In the original simulations, an explicit distance to the source is used in the reward computation. However, this biases the results such that smaller agents will achieve higher rewards as they can approach the source more closely. Therefore, the rewards in Fig. 8.4 were computed by converting the reward from distance to the number of body lengths from the source. We can see that the reward diagrams roughly mirror the results shown in Fig. 8.3 with larger discrepancies between the larger and smaller

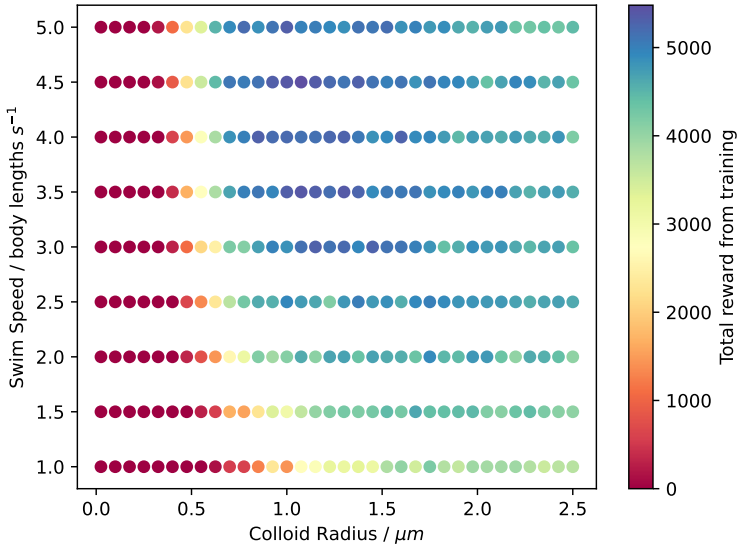

Figure 8.4. Probability of successful chemotaxis emerging from RL studies. Raw data from the experiment. The colour of each point corresponds to the maximum reward achieved by the agents during the 10'000 episodes. Reproduced from Ref. [6] with permission from IOP Publishing.

agents. Namely, the rewards achieved by small and fast agents are noticeably larger than those of the bigger agents. This effect is particularly evident in the prolate and oblate simulations (appendix Figs. A.14 and A.18). It is likely due to larger and faster agents hopping over the intended target instead of remaining on it without moving.

8.4.3 Policy efficiency

It is clear from the previous section that microswimmers of different sizes and speeds differ in their probability of emergent chemotaxis. However, what the differences are, if any, between their adopted strategy still needs to be determined. To identify these differences, the deployment simulations were analysed to compute the final equilibrium distance of the agents around the source as well as after how many action updates they reached this distance. Figure 8.5 displays the results of this investigation. The left panel shows the equilibrium distance of the agents as a function of radius for all studied swim speeds. For radii $r_{\text{body}} \gtrsim 1\,\mu\text{m}$, we see a linear trend, as the limiting factor for getting closer to the source becomes overshooting the target as a result of agent size and speed. The left non-linear side of the plot also contains interesting features. Aside from the lowest speed, the minimum distance from the source of the chemical field is achieved at a similar agent size for all of the different speeds, with faster agents being able to achieve slightly better equilibrium distances with smaller bodies.

In Fig. 8.5 (right), we show the average time the agents need reach the equilibrium distance. For the smaller agents, as is per-

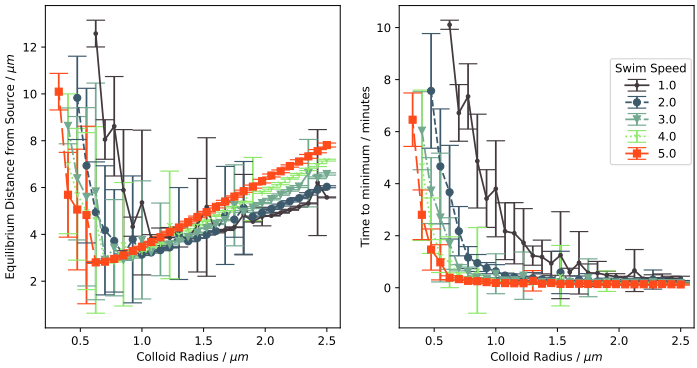

Figure 8.5. (left) Mean distance from the source for each swim speed and agent size. A clear minimum in each plot suggests an optimal size dependent on swim speed. (right) Rate of convergence to the source for different swim speeds and sizes. Interestingly, the convergence rate of larger agents is relatively similar, suggesting some redundancy in larger body sizes and swim speeds.

haps intuitive, the faster agents can move themselves to the source faster than their slower counterparts. However, this relationship fades for larger agents as we see that after approximately 1 µm radii, all agent sizes and speeds converge at similar times except for the slowest one. The time to minimum converges slightly above 25 s. The results also suggest that after 0.5 µm radius, there is no conceivable benefit and, in fact, due to the larger equilibrium distance, perhaps even a detriment in being larger. Interestingly, the most unstable equilibrium distances, identified by large variance in mean value and distance from the source, occur close to or within

the region displayed in Fig. 8.3 where rotational diffusion overpowers the active rotation of the agents. This strong environmental effect could cause instability in these models as they must rely solely on their active translation to achieve chemotaxis.

8.4.4 Emergent policies

As a final investigation, we determine whether the emergent policy of the RL agent differs for changing physical properties and shapes. Studying the particles' trajectory alone is almost impossible as they look very similar upon visual inspection. Therefore, to find differences in strategy, the trained models are given artificial test data $\{\mathfrak{o}_i^\star\}$, $i \in [1, \ldots, 1000]$ over a domain $\mathfrak{o}_i^\star \in (-10.0, 10.0)$ and the probability of selecting each of the four actions is computed from the network outputs. This encodes each learned policy's reaction to all relevant inputs and thus captures the whole policy in one high-dimensional point. In order to identify any structure in this 4000-dimensional data, we study the two-component t-distributed stochastic neighbourhood embedding (t-SNE) [290] of the vectors that represent the trained models, as implemented in the sklearn Python package [291]. Figure 8.6 outlines the results of the t-SNE for the policy data with a perplexity of 300 and principle-component-analysis (PCA) initialisation. Examining the t-SNE plots, we see the emergence of four groups, one of which is seemingly divided into two smaller subgroups. Using this information, we perform k-means clustering [292] on the probability vectors to split them into four clusters. The probability of the outcome of each policy is listed in Table 8.1 along with the explained variance

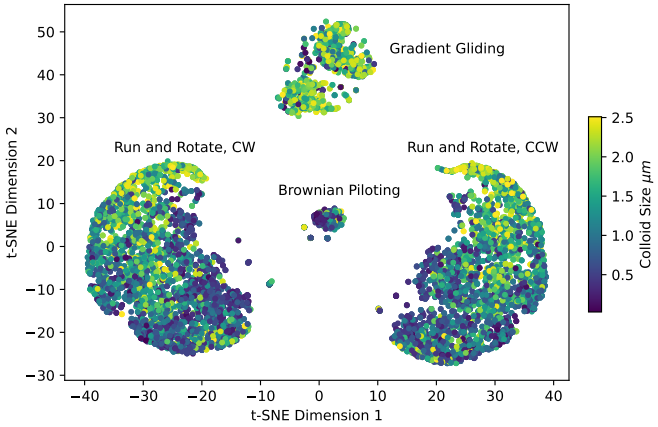

Figure 8.6. t-SNE embedding of the policy vectors for all successful agents in the study. Four large groups are formed, corresponding to the policies learned by the agents. The colour in these diagrams corresponds to the size of the studied agents.

from a PCA decomposition of the probability vectors. The probabilities are computed by examining the number of points clustered into each class by the k-means algorithm, which we assign a policy name by directly examining the action probabilities of the agents mapping into the class. The diagrams used to perform this mapping are included in Appendix A.5, where we show the probabilities of each action being taken for all agent sizes, shapes, and speeds.

We also perform PCA decomposition on the probability vectors to identify how much each policy explains the data distribution. In this approach, we see that 5.9 % of the data belongs to components with a smaller than one percent impact on the variance of the PCA. When we examine the policies in this region, they are typically

made up of combinations of the more dominant policies with very few exceptions. These policies may explain the splitting in the medium-sized group in Fig. 8.6.

Policy Name	Percentage Learned (K-Means)	Explained Variance (PCA)
Run and Rotate	83.49	83.5
Gradient Gliding	12.88	7.1
Brownian Piloting	3.63	3.5
Exotic Policies	0.0	5.9

Table 8.1. Percentage of agents which learned specific policy along with the explained variance of the principle components for each policy identified.

The remainder of the section will discuss each emergent policy in detail, including some policies poorly captured by the embedding methods.

▶ Run and Rotate

In the vast majority of cases (83 %), the agents learned a policy strikingly similar to the run-and-tumble approach to chemotaxis found in nature. Upon positive input to the network, i.e., movement towards the source of the gradient, the agents chose to translate with probability 1 (see Fig. 8.7a) and b)), corresponding to a prolonged run phase. Upon experiencing a negative input to the network, signifying a movement away from the source of the gradient, the agents rotate either CW or CCW, akin to a tumble event. The strategy that our RL agents learned is thus equivalent to bacterial chemotaxis with infinite sensitivity, i.e., infinite runs as long as the direction is correct and instant tumbles if it is not. Interestingly, once the agents chose one direction to rotate, they did not use the other one. CW vs CCW selection was even throughout the

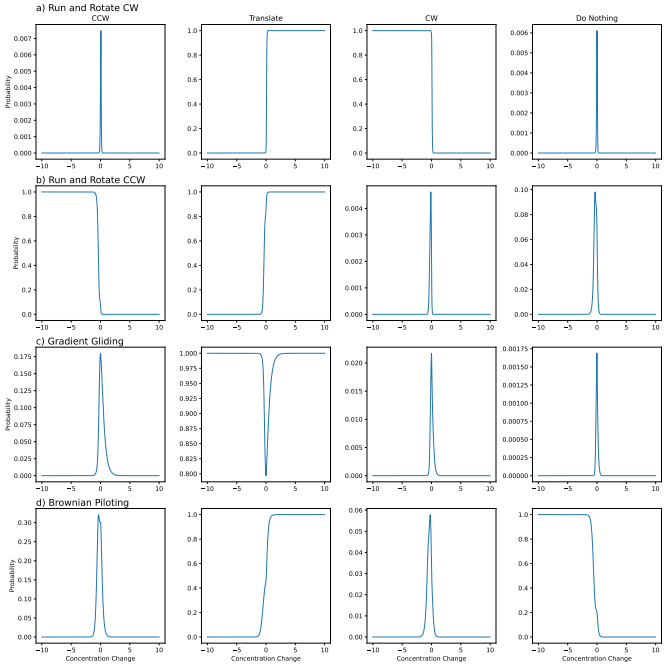

Figure 8.7. Examples of the dominant emergent policies found during the investigation. a) and b) are the run and rotate policy for CW and CCW directions. As the input to the network becomes negative, the agents decide to rotate and as they are moving towards the source, they translate. c) The policy where for most inputs, the agent will translate, but when the input is small, the agent may also decide to rotate. d) Do nothing when negative and translate when positive. Reproduced from Ref. [6] with permission from IOP Publishing.

simulations, with no preferred direction discovered, as is expected from the symmetry of the problem.

▶ Gradient gliding

For large agents, some took translate for most inputs, only rotating for minimal changes in concentration. Even in these cases, the strategy has a high probability of translation, as shown in Fig. 8.7c) The strategy works because the large agents are not strongly affected by thermal noise and the potential is spherically symmetric. Initially, they just translate until by chance, they move tangentially to an equiconcentration line where the sensed concentration change is very small. There, they sometimes rotate to keep themselves close to the equiconcentration line, while oversteering to move closer to the source in a spiral. Far from the source, oversteering by a large amount is beneficial, because it sends the agent on a trajectory that climbs the gradient faster. Close to the source, oversteering can become a problem because it can rotate the agent away from the source, at which point it will move down the gradient. The ratio between translate and rotate probability at small concentration change sets the turning radius, which is optimised to keep all agents circling around the source at large times.

This strategy is common amongst the chosen policies, with somewhere between 7 % and 12 % of agents opting for this approach. The discrepancy in percentage arises due to the spurious policies discussed in a later section. We label this policy gradient gliding as the agents generally follow a translation path with very small adjustments made under low gradient changes.

▶ Brownian piloting

An alternative policy, referred to here as Brownian piloting, was seen particularly in the case of smaller agents where rotational Brownian motion overcomes the active rotation. The agents learned to do nothing when experiencing negative network inputs and to translate if they see a positive one, see Fig. 8.7d). In this way, the agents do not fight against the Brownian forces, but instead use them instead of active rotation. The strategy demonstrates that small agents can still successfully learn to navigate toward sources of nutrition. Overall, this policy was adopted in 3.6 % of cases.

▶ Combinations

We noticed combinations and variations of the above mentioned strategies in many cases where classification was unsuccessful, accounting for approximately 5.9 % of emergent policies. For example, some smaller agents in Brownian-dominated regimes performed active rotation in both CW and CCW directions for negative inputs and translate for positive. We identify this policy as more or less equivalent to Brownian piloting as the active rotation will not yield more than simply relying on Brownian rotation. In other cases, the onset of translation was delayed or accelerated, yielding slight variations of run-and-rotate. As these points combined mixtures of the more dominant policies and yet did not occur often, the clustering algorithms could not successfully separate them into distinct classes.

In summary, the results tell us that in the cases where active translation and rotation are possible and dominate over Brownian

effects, the agents often learn to perform a run-and-rotate strategy. In cases where Brownian effects dominate active motion, the agents learn to adapt to this environment by performing only actions that move them into a new environment by using the Brownian forces to their advantage.

8.5 Conclusion

In this study, we have investigated the role of size and swim speed on the emergent strategy of microscopic active agents learning chemotaxis via multi-agent actor-critic reinforcement learning. Our simulations demonstrated that intelligent agents can learn chemotactic behaviour, even in environments where Brownian random forces begin to dominate over active motion. In such regimes, we found that the chemotaxis was not optimal in terms of the agents' final distance from the source of the chemical gradient or the speed at which they made it to the source. However, they could consistently reach their target. Interestingly, we saw that as the Péclet number grew above one and active motion dominated the Brownian forces and torques, the learned policies converged quickly to a similar equilibrium distance and time.

After studying the policy efficiency, we looked into the strategies adopted by the agents to perform chemotaxis. We identified one dominant strategy that occurs in 83.5 % of the cases we studies. We found that its working mechanism is very similar to that of bacterial chemotaxis: Translate forward when the sensed concentration change is positive, rotate when the concentration change is

negative. We also identified other strategies that leverage equiconcentration lines or use Brownian noise to their advantage. Overall, we have identified that reinforcement learning can replicate natural behaviour of organisms. Or, from a different perspective, that nature evolved a chemotaxis strategy that is very similar to the one optimized by the machine learning algorithm.

Our RL approach allows us to present the agents with near infinite possibilities in their choice of strategy and, without human bias, let them find the optimal one. After the fact, we can analyse the strategy by investigating the reaction to certain sensory input. Interestingly, policies are not easily differentiated when looking at the trajectories alone. Only by studying the neural networks can we see how the agents make decisions. Such an insight might guide us in understanding how real-world organisms navigate their environments, and perhaps, how to disrupt, as in quorum quenching [293], or support, as in quorum enhancement [294], this navigation. We found strategies that, to the best of our knowledge, were not described before. RL is therefore a useful tool for discovery of strategies that can provide clues for the design of artificial microagents, especially in the regime of strong thermal noise. A further point of interest would be to identify natural biological swimmers who have evolved such less common swimming patterns or can outperform the emergent strategies of the RL agents.

Chapter 9

Conclusion and outlook

In this thesis, a simulation model of motile bacteria was introduced and applied to five systems in which bacteria are subject to interactions with a complex environment. The model builds on previous work [172], but adds significant extensions. The geometric detail, especially of the flagellar bundle, was improved, different motility strategies implemented, and models for surface attachment, cell growth and division developed. This enabled research into bacterial accumulation (Chapter 4), biofilm initiation (Chapter 5), porous media exploration (Chapter 6), and phage-bacteria hydrodynamic interactions (Chapter 7). Combined with machine learning methods, a simplified version of the model was used to study bacterial chemotaxis in noisy environments (Chapter 8). For the application-specific summaries and conclusions I refer to the respective Sections 4.4, 5.4, 6.4, 7.4 and 8.5.

Here, I want to focus on the bigger picture and future challenges. The particle resolved model with coupling to lattice Botzmann hydrodynamics has proven a viable tool for investigations into bacteria on the micrometer scale. It provides just enough

detail to capture cell shape via steric interactions, hydrodynamic interactions on the scale of the flow field features generated by swimming, and coarse grained biological functions like cell growth and division. The simplicity of the algorithm and the relatively small number of particles that comprise a cell make the model efficient, enabling simulations of hundreds to thousands of bacteria over the relevant time scales of minutes and hours.

The micrometer focus makes our model unique in the multitude of other models used to describe bacteria [132]. Many other modeling approaches focus on the sub-micrometer scale, resolving bacteria and their flagella in high detail [26, 295–298]. This enables a very accurate description, especially of the hydrodynamics involved in bacterial swimming. The price to pay for this accuracy is computational cost. For highly resolved simulations, usually a supercomputer is employed to obtain trajectories on the order of seconds. Parameter studies become very costly or unfeasible. In this thesis however, usually more than one parameter is varied and many simulations per parameter set are needed for good statistics. For example, in Chapter 7 and Appendix A.4, we present results of simulations for 5 swim speeds $\times$ 4 attachment rates $\times$ 2 swimmer types (pusher/puller) $\times$ 2 types of particle coupling (with/without hydrodynamics) $\times$ 5 noise realisations, where each simulation tracks the bacterium and 1000 phages for about two minutes of simulated time, running for one day on one CPU core. The total computational cost for the related publication [5] including its supplementary information is thus around 400 core days. This could be done with reasonable time investment on a modern

workstation or overnight on a small HPC system. Of course, more nuanced questions can be answered with more detailed models, but sometimes details and nuance stand in the way of forming qualitative conclusions that reach beyond the simplified model used to motivate such conclusions.

Particle based simulation models for active matter like the active Brownian particle (ABP), that are commonly used in theoretical physics, have a similar length scale focus as the model we use. However, they typically do not aim to represent bacteria, but more abstract active particles lacking any biological detail such as shape or non-trivial motility patterns [132]. Our model thus fills a gap between highly abstracted active objects and highly detailed biological organisms.

On the coarse side of the detail spectrum, continuum methods for motile cells, but especially for biofilms, are popular [210–213]. They enable simulations of very large systems over long times, but necessarily lack particle detail. This particle detail might be required when biofilms are young and consist of a relatively small number of cells. The growing colony is then better described as an agglomeration of cells rather than as a material.

Mixed pseudoparticle-continuum models such as the ones developed by Picioreanu and Kreft are probably the most similar models to ours in the sense that they use some particle dynamics coupled to a lattice Boltzmann description of fluids [202–205]. However, the time propagation in these models does not follow physical equations of motion, but rather a push-and-shove algorithm that has no concept of force and is thus not able to realise a

two-way coupling between particles and fluid. These methods certainly are viable in many cases and have been applied to various systems and geometries, but especially for soft biofilms, a more physics-rooted approach like ours is needed to account for internal biofilm dynamics and the back-coupling to fluid flow.

I believe that our model sits in a previously unoccupied gap of complexity, detail level and computational efficiency. It will therefore continue to be a valuable tool for physicists, engineers and biologists to answer questions beyond the applications that are presented in this thesis. In the last paragraphs I will outline some interesting projects that I think are worthwhile pursuing using the methods presented in the previous chapters.

Expanding on the research into the efficiency of exploration of porous media, one could introduce nontrivial external flow conditions. Then, the influence of different motility patterns on spreading and accumulation behaviour along or across the flow direction in large porous systems could be investigated. Alternatively, one could study chemotaxis in such confined systems, coming even closer to (medical) applications of microscopic agents that perform tasks at predefined locations.

The biofilm model could be extended to account explicitly for the nutrients that are transported by flow and enable cell growth. In the lattice Boltzmann framework, this can be achieved using the lattice electrokinetics algorithm. This algorithm couples diffusion and reaction of dissolved chemical species to the same fluid that bacteria interact with in the current model.

In the study of phage infection, the role of the shape of the

phages in the hydrodynamic interaction has so far been neglected. Some phages are highly anisotropic with long filaments on the scale of the characteristic scales of flow features that are generated by swimming bacteria. Understanding how this impacts the infection process could lead to deeper insights into the clinically relevant infection process. A more ambitious project would be modeling the flagellar bundle in greater detail by explicitly capturing helical flagella and their rotation. Then, the influence of near field hydrodynamics *inside* the flagellar bundle could be studied.

All these research avenues are within reach by comparatively simple extension of the bacterial model presented in this thesis and are left as an exercise to the reader.

Appendix A

Additional information for results chapters

A.1 Additional information for Chapter 4: The influence of motility on bacterial accumulation in a microporous channel

This chapter contains in large parts text that is taken verbatim from M. Lee, C. **Lohrmann**, K. Szuttor, H. Auradou, and C. Holm, "The influence of motility on bacterial accumulation in a microporous channel", Soft Matter **17**, 893 (2021), a publication to which I contributed preparation of figures and co-writing of the manuscript draft.

A.1.1 Parameter choice

The parameters for the lattice Boltzmann simulations in simulation units are:

$$\begin{aligned} \text{LB grid spacing:} \quad & a_{\text{grid}} = 1, \\ \text{LB time step:} \quad & \Delta t = 1, \\ \text{LB fluid density:} \quad & \rho = 1, \\ \text{LB kinematic viscosity:} \quad & \mu/\rho = 0.1, \\ \text{LB bare friction coefficient:} \quad & \tilde{\gamma} = 0.25. \end{aligned}$$

The parameters for the molecular dynamics simulations in simulation units are:

$$\begin{aligned} \text{MD time step:} \quad & \delta t = \frac{\Delta t}{5} = 0.2, \\ \text{Effective diameter of a bead:} \quad & \sigma^{\text{LJ}} = 1, \\ \text{WCA potential strength:} \quad & \epsilon^{\text{LJ}} = 1, \\ \text{Thermal energy:} \quad & k_{\text{B}}T = 0 \end{aligned}$$

At a low Reynolds number, the flow velocity scales linearly with the external force density. In the case where the system is $(L, H, W) = (500\,\mu\text{m}, 200\,\mu\text{m}, 20\,\mu\text{m})$ with a periodic boundary condition in the x direction, the average flow speed in simulation units is given by

$$\langle |\mathbf{u}| \rangle = 17.7 \times \mathbf{f}^{\text{ext}}. \tag{A.1}$$

On the other hand, when the system is constructed as $(L, H, W) = (500\,\mu\text{m}, 500\,\mu\text{m}, 20\,\mu\text{m})$ with a periodic boundary condition in the

x and y directions, the average flow speed scales as

$$\langle |\mathbf{u}| \rangle = 40.1 \times \mathbf{f}^{\text{ext}}. \tag{A.2}$$

The swimmer speed is determined by the dipole force strength

$$v_{\text{swim}} = \tilde{\gamma} F_{\text{swim}}, \tag{A.3}$$

where

$$\begin{aligned} v_{\text{swim}} &= 6.67 \times 10^{-5} \\ F_{\text{swim}} &= 7.52 \times 10^{-5} \\ \tilde{\gamma} &= 0.89. \end{aligned} \tag{A.4}$$

in simulation units.

The parameters listed in simulation units can be related to those of the experiment done by Miño *et al.* [187] by specifying conversion factors for the length C_s, time C_t, and mass C_m.

Starting with the length conversion factor, we match the radius of the obstacle

$$\text{Radius:} \quad R = 32 a_{\text{grid}} = 80\,\mu\text{m},$$

which yields the length conversion factor:

$$C_x = 2.5\,\mu\text{m}.$$

The mass conversion factor can be found by matching the LB fluid density with the density of water:

$$\begin{aligned} 10^{-15}\,\text{kg}/\mu\text{m}^3 = 1 C_\rho = 1 \frac{C_m}{C_x^3} \\ \rightarrow C_m = 1.56 \times 10^{-14}\,\text{kg}. \end{aligned}$$

The last conversion factor, the time, can be found by comparing the time scales of the simulation and the experiment. We relate the swimmer's swimming velocity. *E. coli* bacteria swim at around 24 µm/s. In our simulations, our swimmers swim at $v_{\text{swim}} = 6.67 \times 10^{-5} \frac{C_m}{C_\tau}$, thus the time conversion factor is

$$24\,\mu\text{m/s} = 6.67 \times 10^{-5} \frac{C_m}{C_\tau}$$
$$\rightarrow C_\tau = 6.94 \times 10^{-6}\,\text{s}.$$

Note that this time conversion factor is 10 times larger than the value that one would have obtained via the viscosity of water. This is because we scale up the velocities of the experiment by a factor of 10. It is possible as long as the system is at sufficiently low Reynolds numbers (Re). Our simulation and the experiment show $\text{Re} \sim 10^{-2}$ and $\text{Re} \sim 10^{-3}$, respectively.

These three conversion factors uniquely map any number that carry a dimensionality in our simulation to its physical counterpart.

A.2 Additional information for Chapter 5: A novel model for biofilm formation in porous media flow

This chapter contains in large parts text that is taken verbatim from C. **Lohrmann** and C. Holm, "A novel model for biofilm initiation in porous media flow", Soft Matter **19**, 6920 (2023), a

publication to which I contributed the modelling, simulations, data analysis and writing of the manuscript draft.

A.2.1 Surface attachment in flow with increased attachment time

Complementary to Fig. 5.3 of the main text, Fig. A.1 shows the histogram of attachment angles on a cylindrical obstacle for motile bacteria, but with an increased average time-to-attachment $\langle t_{\mathrm{attach}} \rangle = 10\,\mathrm{s}$. This time is much larger than the time $2R_{\mathrm{cyl}}/v_{\mathrm{swim}} = 1.6\,\mathrm{s}$ it takes a bacterium to travel the diameter of a cylinder. Many encounters are therfore needed until a bacterium attaches to a surface. This constitutes the opposite limit compared to the instantaneous attachment discussed in the main text. Yet, the qualitative features of the histogram are the same, with a large probability of downstream attachment ($\Theta < \pi/2$) and a peak at $\Theta = 0$. This shows that the exact value of $\langle t_{\mathrm{attach}} \rangle$ does not influence the qualitative phenomenon of preferential attachment on the downstream end of obstacles.

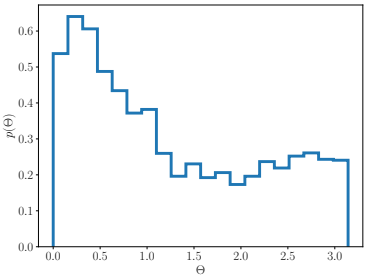

Figure A.1. Normalized histogram of the angular position of attachment for $\langle t_{\mathrm{attach}} \rangle = 10\,\mathrm{s}$. Reproduced from Ref. [3] with permission from the Royal Society of Chemistry.

A.2.2 Parameters for simulations

In the following sections we list the parameters needed to reproduce all simulations we performed. The section headings correspond to the respective sections in the main text. The symbols used here are introduced in the main text.

A.2.2.1 Qualitative biofilm morphologies

Table A.1 lists the parameters that are common to all simulations that show the qualitative biofilm morphologies. Table A.2 lists the parameters that differ between the four simulations. $\dot{\gamma}_{\mathrm{wall}}$ denotes the shear rate at the planar walls, the force applied to the fluid to achieve this shear rate is calculated from the Poiseuille flow profile as

$$\mathbf{f}^{\mathrm{ext}} = \frac{2\dot{\gamma}_{\mathrm{wall}}\mu}{h}\mathbf{e}_x. \tag{A.5}$$

The simulations are meant as a showcase of model capabilities and not to model a specific system. We use units of $c_{\text{length}} = 1\,\mu\text{m}$, $c_{\text{time}} = 1\,\text{s}$, $c_{\text{density}} = \rho_{\text{water}} = 1000\,\text{kg/m}^3$.

Table A.1. Common parameters for qualitative biofilm morphology simulations.

Symbol	δt	Δt	Δt	a_{grid}	ρ	μ
Value	0.05	3.45	0.2	1	1	0.1
Symbol	h	$\tilde{\gamma}$	r_{growth}	r_{body}	$l_{\text{body, max}}$	
Value	20	1.5	0.002	0.5	3	
Symbol	t_{attach}	r_{attach}	r_{bond}	r_{detach}	N_{anchor}	
Value	0.01	0.55	0.55	0.65	2	

Table A.2. Parameters for the individual biofilm morphology simulations.

	ϵ^{LJ}	k_{harm}	$\dot{\gamma}_{\text{wall}}$
Sphere	0.05	15	0
Flat	0.00005	15	0.05
Rolling	0.005	0.00001	0.05
Intermediate	0.02	15	0.05

A.2.2.2 Determination of model parameters

We choose units of $c_{\text{energy}} = \epsilon^{\text{LJ}}$, $c_{\text{length}} = 1\,\mu\text{m}$, $c_{\text{time}} = 1\,\text{s}$. Dynamic parameters (such as the friction coefficient $\tilde{\gamma}$) have no influence on the determination of all static properties like the biofilm tensile strength. They only affect the speed of convergence. Since we report tensile strength as a dimensionless quantity by dividing out the energy scale ϵ^{LJ}, we are free to set that value to 1.

Table A.3. Parameters for determination of biofilm tensile strength

Symbol	δt	Δt	ϵ^{LJ}	$\tilde{\gamma}$	r_{growth}	r_{body}
Value	0.035	2.765	1	0.4	0.0025	0.5
Symbol	t_{attach}	r_{attach}	r_{bond}	k_{harm}	r_{detach}	N_{anchor}
Value	0.01	0.75	0.6	15	0.8	2
Symbol	$l_{\mathrm{body,\ max}}$	cylinder radius	initial cylinder height			
Value	3	4.5	7.5			

A.2.2.3 Simulation of biofilm formation in porous media

Table A.4. Simulation parameters for biofilm formation simulation

Symbol	δt	Δt	Δt	a_{grid}	ρ
Value	0.006 s	12 s	0.03 s	1 µm	1000 kg m^{-3}
Symbol	μ	h	τ_2	$\lvert\mathbf{f}^{\mathrm{ext}}\rvert$	r_{body}
Value	1×10^{-3} Pa s	10 µm	1 h	40 N m^{-3}	0.5 µm
Symbol	$l_{\mathrm{body,\ max}}$	t_{attach}	r_{attach}	k_{harm}	r_{detach}
Value	3 µm	0.001 s	0.75 µm	8×10^{-2} kg s^{-2}	1 µm
Symbol	N_{anchor}	f			
Value	2	2×10^{-6}			

A.3 Additional information for Chapter 6: Optimal motility strategies for self-propelled agents to explore porous media

Figure A.2 shows $D_{\mathrm{eff}}^{\mathrm{t}}$ as a function of mean pore radius r_{p} for all investigated motility strategies, analogously to Fig. 6.4. Here however, the radius $R_{\mathrm{sphere}} = 10\,\mu\mathrm{m}$ is twice as large as in the geometry used in the Chapter 6. The qualitative behaviour and order of the curves is the same as in Fig. 6.4, leading us to believe that the results presented in Chapter 6 are independent of the

specific size of the grains that make up the porous medium.

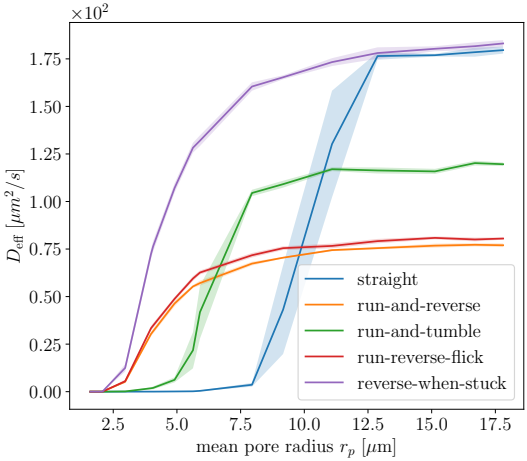

Figure A.2. Effective diffusion coefficient as a function of mean pore radius, for $R_{\text{sphere}} = 10\,\mu\text{m}$.

A.4 Additional information for Chapter 7: Influence of bacterial swimming and hydrodynamics on infection by phages

This chapter contains in large parts text that is taken verbatim from C. **Lohrmann**, C. Holm, and S. S. Datta, "Influence of bacterial swimming and hydrodynamics on attachment of phages", Soft Matter **20**, 4795 (2024), a publication to which I contributed the modelling, simulations, data analysis and writing of the manuscript

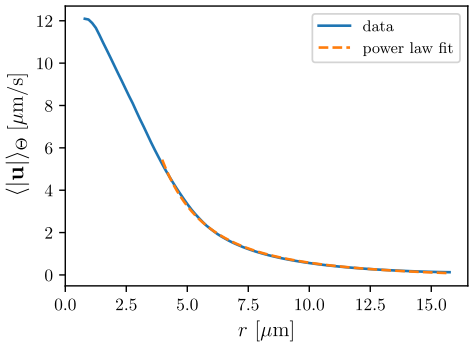

Figure A.3. Angle-averaged flow field around the swimmer as a function of distance. The power law fit yields a far-field exponent $\alpha = -2.12(3)$.

draft.

A.4.1 Far field decay of the swimming flow field

In Fig. A.3 we show the decay of the flow field $\langle |\mathbf{u}| \rangle_\Theta (r)$ generated by the swimming bacterium. Here, $\langle \cdot \rangle_\Theta (r)$ refers to an average over all angles Θ at distance r from the center location between cell body and flagellar bundle. Numerically, these values are obtained from linear interpolation of the lattice Boltzmann grid. We fit a power law function $f(r) = a \cdot r^\alpha$ to obtain the exponent α governing the leading order behaviour far from the cell. Our simulations yield $\alpha = -2.12(3)$, which is very close to the theoretically expected exponent $\alpha^{\text{dipole}} = -2$, showing that our model captures the swimming flow field well.

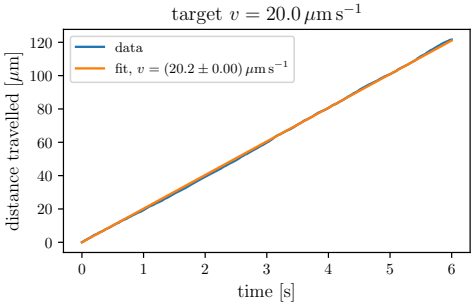

Figure A.4. Bacterium distance travelled and swim speed fit. Reproduced from Ref. [5] with permission from the Royal Society of Chemistry.

A.4.2 Bacterium and phage model calibration

Figure A.4 shows that using our choice of bacterial effective friction coefficient $\tilde{\gamma}$ and determining the corresponding effective mobility leads to the desired swim speed of the bacterium. In Fig. A.5 we show that applying the grid correction to the phage friction coefficient γ^P leads to the correct diffusion coefficient of the phages.

A.4.3 Determination of infection rate

Figure A.6 shows exemplary encounter data for a single simulation and the fit that is used to determine the infection rate.

A.4.4 Exclusion of finite size and density effects

In Fig. A.7 we show that the infection rate is independent of the box size and independent of the phage density.

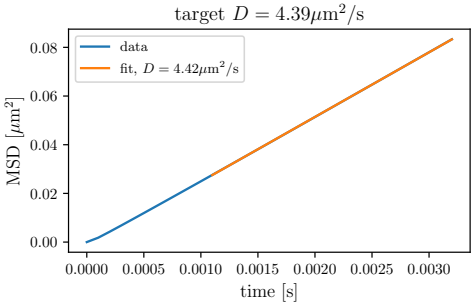

Figure A.5. Phage mean squared displacement and diffusion coefficient fit. Reproduced from Ref. [5] with permission from the Royal Society of Chemistry.

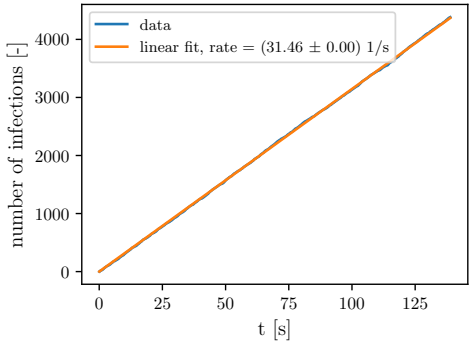

Figure A.6. Number of infection vs time for one simulation with hydrodynamics, $k^{att} \to \infty$ and $v_{swim} = 100\,\mu m\,s^{-1}$. Reproduced from Ref. [5] with permission from the Royal Society of Chemistry.

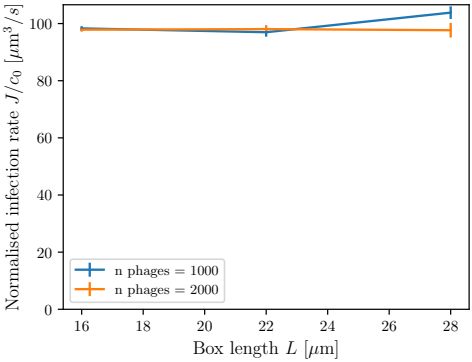

Figure A.7. Infection rate as a function of simulation box length for different numbers of phages. Simulations performed with hydrodynamics at $v_{\text{swim}} = 25\,\mu\text{m}\,\text{s}^{-1}$ and $k^{\text{att}} \to \infty$. Reproduced from Ref. [5] with permission from the Royal Society of Chemistry.

A.4.5 Finite attachment rate

Figure A.8 and Fig. A.9 show the results for infection rate and location on the body and flagellum, respectively. The data for $k^{\text{att}} \to 0, \infty$ are the same as in the corresponding figures in the main text. For intermediate attachment rates, the curves show the same qualitative behaviour as in the two limiting cases.

A.4.6 Puller swimmers

Figure A.10 and Fig. A.11 show results for infection rate and position for the body and flagellum, respectively. To obtain this data, puller type swimmers with the flagellum in front of the cell body were simulated.

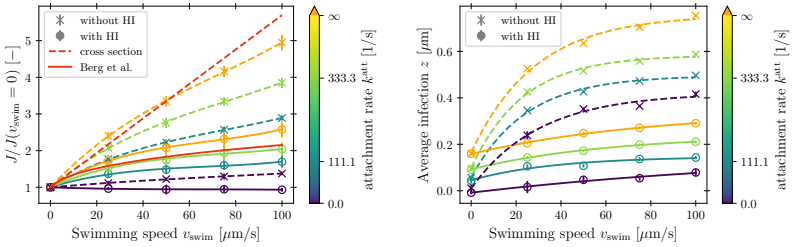

■ *Figure A.8.* **Pusher** bacterium: Infection rate and positions on the **cell body** for finite attachment rate. Polynomial/exponential fits are shown to guide the eye. Reproduced from Ref. [5] with permission from the Royal Society of Chemistry.

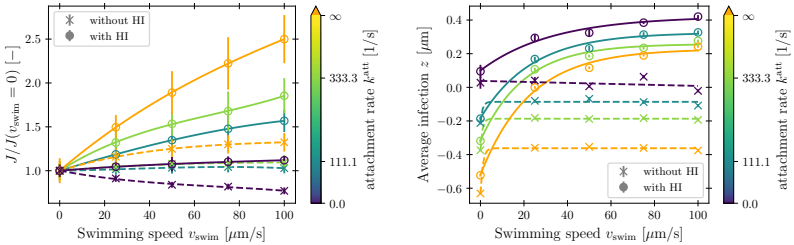

■ *Figure A.9.* **Pusher** bacterium: Infection rate and positions on the **flagellum** for finite attachment rate. Polynomial/exponential fits are shown to guide the eye. Reproduced from Ref. [5] with permission from the Royal Society of Chemistry.

Phages in the swimming direction are taken up by the flagellum before they can reach the front of the cell body. Therefore, in simulations without hydrodynamics, the main mechanism of infection rate increase on the cell body – uptake of more phages in the front – is strongly reduced. As a result, the infection rate increase

is much smaller than for pushers and is also not captured by the cross sectional model.

When hydrodynamic interactions are considered, there is almost no increase in infection rate on the cell body regardless of k^{att}. For the pusher, the infection rate increases with v_{swim} because the region with $\mathrm{Pe}^*_{\mathrm{Phage}} < 1$ shrinks around the forward end of the cell body and phages have to cross less distance by diffusion. For the puller, the shape of $\mathrm{Pe}^*_{\mathrm{Phage}} < 1$ around the forward end of the cell body is roughly independent of the swim speed as it is mainly determined by the details of the gap between cell surface and the propelling part of the flagellum. Therefore, the only increase of infection rate comes from phages that arrive from the sides, leading to the small influence of motility. Unsurprisingly, the model of Berg et al. cannot be employed for puller bacteria and flagellotropic phages, because now the flagellum is the main collector of phages instead of the cell body.

The dependence of the infection location on the cell body is qualitatively the same as in the pusher case, except that the curves are shifted to negative values at $v_{\mathrm{swim}} = 0$ because of the sink of phage concentration now in front of the cell body.

For the flagellum, the qualitative observations and explanations for the behaviour of infection rate and location are the same as in the pusher case.

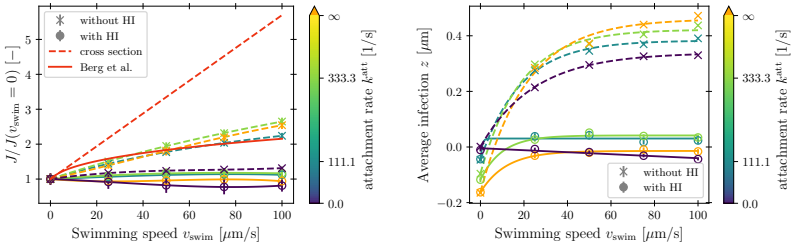

Figure A.10. **Puller** bacterium: Infection rate and positions on the **cell body** for finite attachment rate. Polynomial/exponential fits are shown to guide the eye. Reproduced from Ref. [5] with permission from the Royal Society of Chemistry.

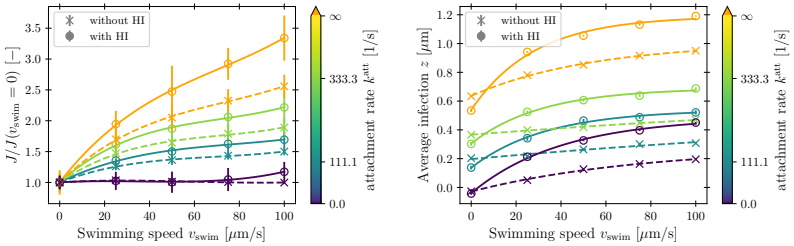

Figure A.11. **Puller** bacterium: Infection rate and positions on the **flagellum** for finite attachment rate. Polynomial/exponential fits are shown to guide the eye. Reproduced from Ref. [5] with permission from the Royal Society of Chemistry.

A.5 Additional information for Chapter 8: Emergence of chemotactic strategies with multi-agent reinforcement learning

This chapter contains in large parts text that is taken verbatim from S. J. Tovey, C. **Lohrmann**, and C. Holm, "Emer-

gence of Chemotactic Strategies with Multi-Agent Reinforcement Learning", Machine Learning: Science and Technology, accepted manuscript (2024), a publication to which I contributed the physics aspects of the simulations, data interpretation and co-writing of the manuscript draft.

A.5.1 Shape studies

As discussed in the manuscript, we performed the chemotaxis study for spherical, prolate, and oblate particles. Here we display and discuss the results not presented in the main manuscript.

A.5.1.1 Sphere

While most of the sphere results are presented in the main manuscript, the raw policy plots are presented here. Note, bl in the figure stands for body lengths. The sphere policy diagrams outline the majority of the policies discussed in the main text. On the x axis, the change in gradient is plotted and on the y, the colloid shape. The colour of the diagram represents the probability of an action being taken and each column corresponds to a single action. The rows are the different swim speeds from one to five body lengths per second. The diagrams show the forbidden region in the chemotaxis below approximately 0.5 µm. After this point, we see the emergence of non-zero probabilities as the networks have learned to perform chemotaxis.

A.5.1.2 Oblate

The oblate particles demonstrated similar behaviour to the spherical colloids, not showing any unique policy deviations.

A.5.1.3 Prolate

The prolate simulations were similar to both the spherical and oblate studies.

A.6 Code and data availability

All code and data that support the results presented in Chapters 5 to 7 can be found in the data repositories [173–175] associated with the respective publications.

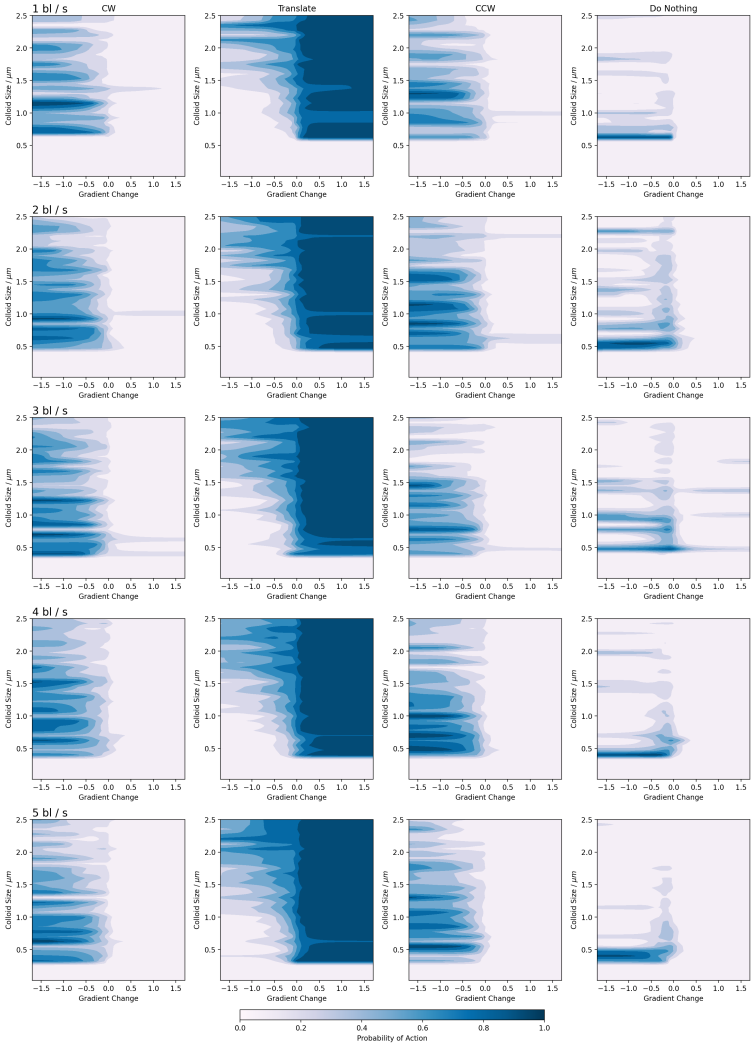

■ *Figure A.12.* Emergent policy of the spherical microswimmers for all speeds and sizes. Reproduced from Ref. [6] with permission from IOP Publishing..

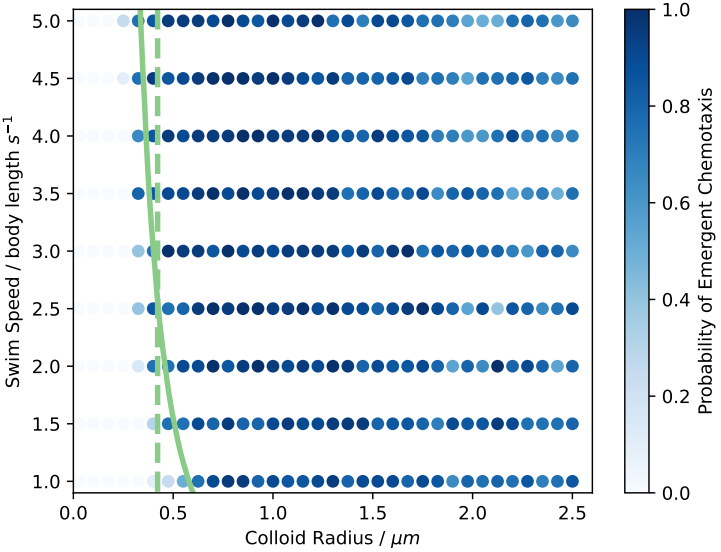

Figure A.13. The probability of emergent chemotaxis for the oblate particles along with the theoretical boundaries from the Péclet numbers. Reproduced from Ref. [6] with permission from IOP Publishing..

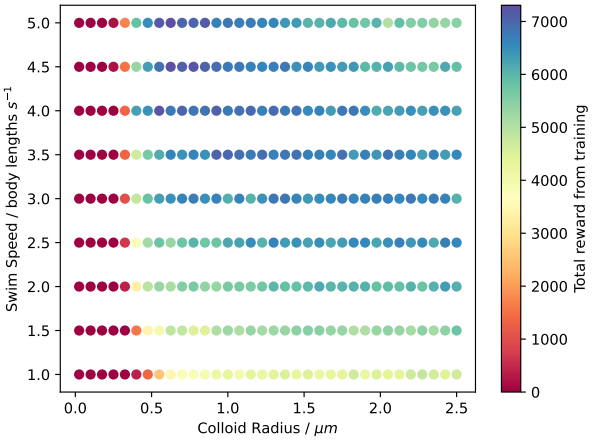

Figure A.14. Reward phase diagram computer from the oblate simulations. In this case, we see the best training emerges again in the smaller but fast region of the diagram. While the width of the colloids is corrected for, more complex geometric conditions may be impacting these results. Reproduced from Ref. [6] with permission from IOP Publishing..

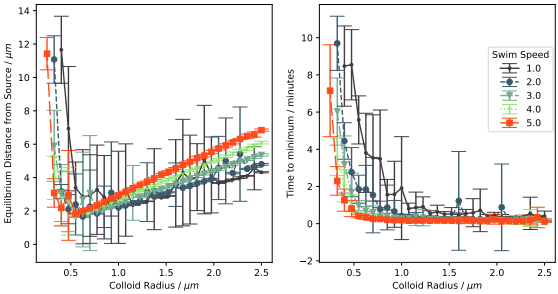

Figure A.15. Policy efficacy for the oblate particles appears almost identical to the spherical particles. Reproduced from Ref. [6] with permission from IOP Publishing..

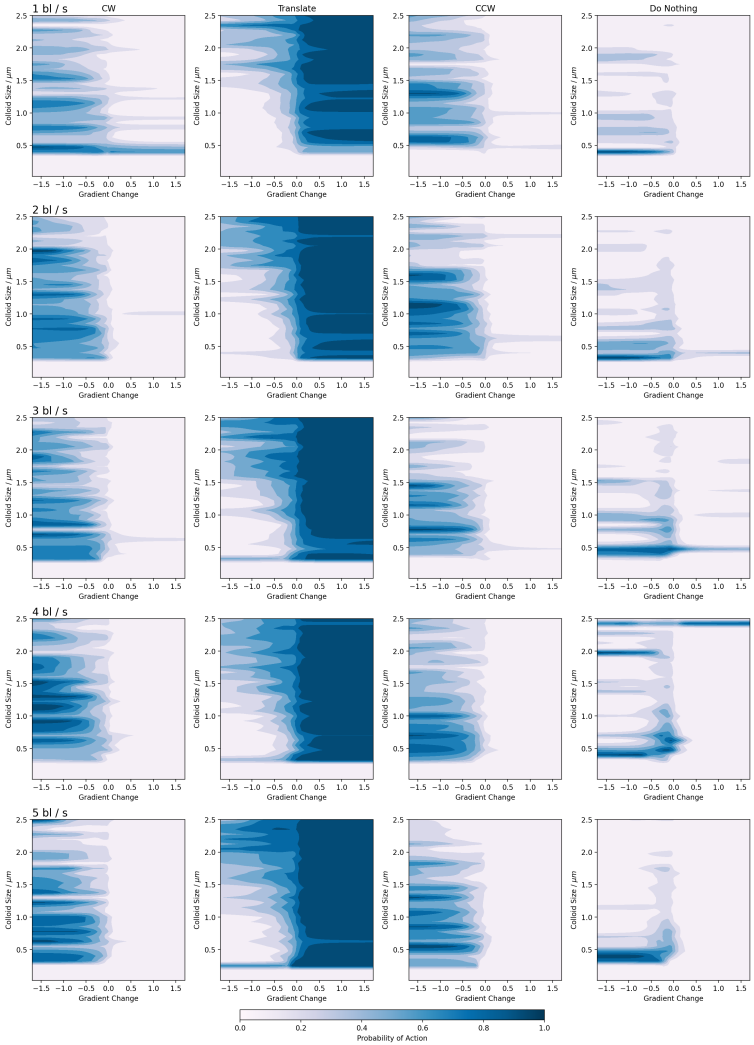

Figure A.16. Emergent policy diagram for the oblate particles. Reproduced from Ref. [6] with permission from IOP Publishing..

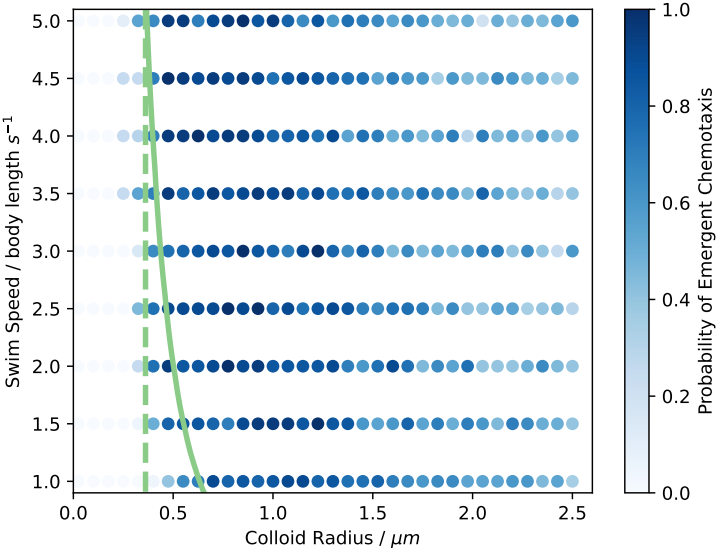

Figure A.17. The probability of emergent chemotaxis for the prolate particles along with the theoretical boundaries from the Péclet numbers. Reproduced from Ref. [6] with permission from IOP Publishing..

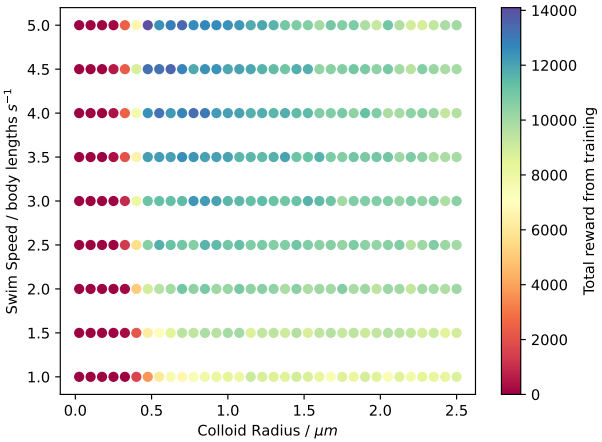

Figure A.18. Reward phase diagram computer from the prolate simulations. In this case, we see the best training emerges again in the smaller but fast region of the diagram. While the width of the colloids is corrected for, more complex geometric conditions may be impacting these results. Reproduced from Ref. [6] with permission from IOP Publishing..

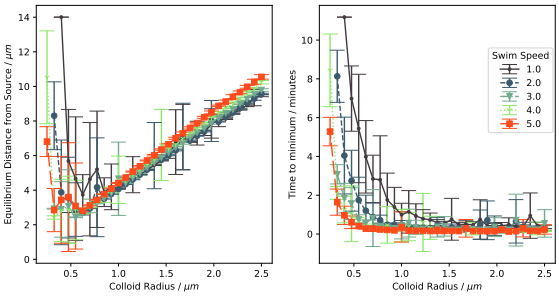

Figure A.19. Policy efficacy for the prolate particles appears almost identical to the spherical particles.

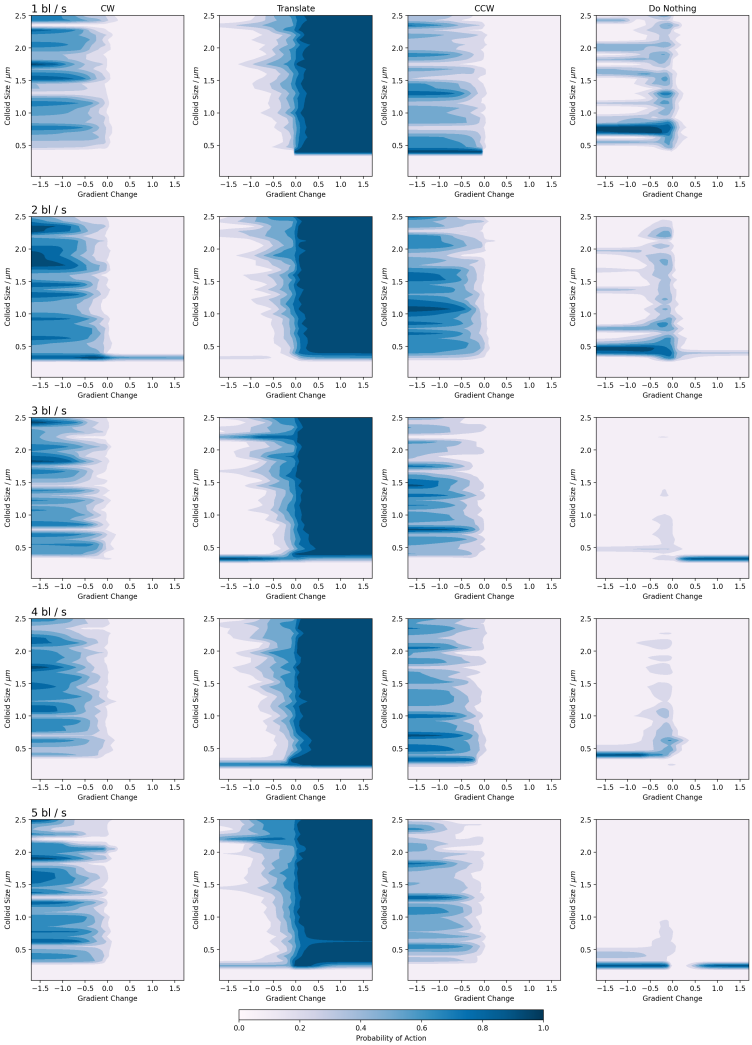

Figure A.20. Emergent policy diagram for the prolate particles. Reproduced from Ref. [6] with permission from IOP Publishing.

Appendix B

Miscellaneous

B.1 Scientific curriculum vitae

- 2005–2013 Abitur: Ludwig-Uhland-Gymnasium Kirchheim Teck

- 2013–2016 Bachelor of Science, Physics: University of Stuttgart.
  Thesis supervision: H. Cartarius, 1st Institute for Theoretical Physics

- 2016–2018 Master of Science, Physics: University of Stuttgart.
  Thesis supervision: U. Seifert, 2nd Institute for Theoretical Physics

- 2019–2024 Philosophiae Doctor, Physics: University of Stuttgart.
  Supervision: C. Holm, Institute for Computational Physics

B.2 Zusammenfassung in deutscher Sprache

In der Natur unterliegen Bakterien Wechselwirkungen mit komplexen Umgebungen. Komplexität kann durch, zum Beispiel, geometrische Begrenzung, externen Fluss oder durch andere Partikel entstehen, die in derselben Flüssigkeit suspendiert sind. Diese Dissertation berichtet über die Entwicklung und Anwendung eines numerischen Modells für schwimmende Bakterien in solch komplexen Umgebungen.

Das bakterielle Modell basiert auf vergröberter Molekulardynamik, das die Trajektorien einzelner Teilchen auflöst, aber physikalische Interaktionen auf der Mikrometerskala abstrahiert. Bakterien werden als starre Stäbe dargestellt, die aus mehreren Molekulardynamik-Teilchen bestehen. Ihre Dynamik wird durch physikalische Bewegungsgleichungen beschrieben, einschließlich Wechselwirkungen mit einer Flüssigkeit, mit geometrischen Begrenzungen oder mit anderen Partikeln. Bei Bedarf werden hydrodynamische Wechselwirkungen unter Verwendung des Gitter-Boltzmann-Algorithmus einbezogen.

Biologische Details jenseits der physikalischen Parameter wie Form und Masse werden in einer ebenso vergröberten Weise beschrieben, wobei nur die relevanten Merkmale für jede Anwendung modelliert werden. Die Fortbewegung wird durch eine fiktive Antriebskraft realisiert, die durch eine entgegengesetzte Kraft auf die Flüssigkeit ausgeglichen wird, die den Antriebsmechanismus imitiert. Unterschiedliche Bewegungsmuster wie Schwimmen-und-Taumeln, Schwimmen-und-Umkehrungen oder Schwimmen-Umkehren-Drehen werden durch Änderungen der Antriebskraft

und Lenkdrehmomente modelliert. Das Anhaften an Oberflächen über (nicht-)reversible Bindungen erfolgt durch lösbare Bindungen, die aus der Erforschung von Polymeren bekannt sind. Zellwachstum und -teilung werden durch Änderungen in der Konfiguration der einzelnen Partikel modelliert, die den bakteriellen Stab bilden.

Das Modell für Bakterien wird verwendet, um mehrere relevante Fragen im Bereich der Erforschung schwimmender Bakterien zu beantworten: Die erste Frage betrifft die Akkumulation von Bakterien und die Bildung von Biofilmen, also Kolonien wachsender Bakterien, in porösen Medien. "Wie beeinflusst externer Fluss die Initiierung und Bildung von Biofilmen?" Diese Dissertation trägt auf zwei Arten zur Beantwortung dieser Frage bei. In der planktonischen Phase, das heißt wenn Bakterien durch die Flüssigkeit schwimmen und nach Oberflächen suchen, an die sie sich anheften können, führt das Zusammenspiel zwischen bakteriellem Schwimmen und externem Fluss zu dem überraschenden Ergebnis, dass Zellen am *stromabwärts* liegenden Ende fester Körner anheften anstatt an den stromaufwärts liegenden Enden, wo man naiv Ansammlung und Anhaftung erwarten würde. Dies wird durch das Identifizieren von Bereichen erklärt, in denen Bakterien mit dem externen Fluss konkurrieren können, und Bereichen, in denen der externe Fluss stärker ist als der bakterielle Vortrieb, abhängig von der Schwimmrichtung. Bakterien, die stromaufwärts in Gebieten mit geringem externem Fluss schwimmen, können keine Zonen mit starkem Fluss überqueren und landen daher *hinter* den Flussbarrieren, die die Regionen mit starkem Fluss verursachen. In der Wachstumsphase des Biofilms, also wenn Bak-

terien bereits an der Oberfläche gebunden sind und sich replizieren, um eine Kolonie zu bilden, untersuchen wir das Zusammenspiel zwischen der Steifheit des Biofilms und der Stärke des externen Flusses. Wir stellen fest, dass weichere Biofilme aufgrund der viskosen Belastungen, die der externe Fluss verursacht, eine komplexere Wachstumsdynamik aufweisen und eine Verzögerung bei der Permeabilitätsreduktion zeigen.

Die zweite Frage bleibt im Bereich poröser Medien, betrifft jedoch eine derart starke geometrische Begrenzung, dass sie die Größenordnung einzelner Zellen erreicht. "Welche ist die optimale Bewegungsstrategie für ein Bakterium, um effizient eine poröse Umgebung zu erkunden?" In der Natur nutzen Bakterien verschiedene Bewegungsmuster, das heißt zeitliche Abfolgen von Vorwärtsschwimmen und (aktiver) Rotation. Wir untersuchen die Fähigkeit von vier Mustern, gerades Schwimmen, Schwimmen-und-Taumeln, Schwimmen-und-Umkehrungen oder Schwimmen-Umkehren-Drehen, ungeordnete poröse Medien zu erkunden. Wir stellen fest, dass für große Poren gerades Schwimmen und Schwimmen-und-Taumeln am effizientesten sind, weil sie offene Bereiche effizient nutzen. In kleinen Poren wird das Taumeln unterdrückt, was Umkehren zur einzigen praktikablen Optione für das Entkommen aus kleinen Poren macht. Durch Optimierung der Schwimmparameter für jede Porengröße kann Schwimmen-und-Umkehrungen die anderen Muster übertreffen, aber die Umgebung muss im Voraus bekannt sein, um die Optimierung zu ermöglichen. Wir schlagen daher eine adaptive Bewegungsstrategie vor, die erfordert, dass Bakterien feststellen können,

ob sie feststecken, und dann eine Umkehr initiieren. Diese Strategie erfordert kein vorheriges Wissen über die Umgebung und übertrifft die Strategien mit festen Mustern in Bezug auf Erkundungseffizienz.

Die dritte Frage geht noch weiter ins Detail und beschäftigt sich mit den hydrodynamischen Wechselwirkungen im Maßstab unterhalb der Zellgröße. "Was ist der Einfluss des bakteriellen Schwimmens auf den Infektionsprozess zwischen Phagen und Bakterien?" Phagen sind Viren, die Bakterien töten, aber physischen Kontakt mit ihrer Beute benötigen, um die Infektion zu initiieren. Das durch schwimmende Bakterien erzeugte Strömungsfeld hat einen Einfluss auf die Annäherung der Phagen an die Zelle. Mit zunehmender Schwimmgeschwindigkeit steigt die Infektionsrate, jedoch sublinear. Wenn das Bakterium vorwärts bewegt, bewegt es eine Menge Flüssigkeit mit sich, die den Zellkörper vor einfallenden Phagen abschirmt. Der Effekt auf das Flagellum ist das Gegenteil. Da es Flüssigkeit rückwärts pumpt, um das Bakterium vorwärts zu bewegen, kommt es bei schneller Bewegung mit einem größeren Volumen Flüssigkeit und damit einer größeren Anzahl von Phagen in Kontakt. Die Studie zeigt den wichtigen Einfluss der hydrodynamischen Wechselwirkungen zwischen Phagen und Bakterien. Wenn man das hydrodynamische Feld vernachlässigt hätte, hätte man die Infektionsrate am Zellkörper stark überschätzt und die Infektionsrate am Flagellum stark unterschätzt.

Als Ausblick auf weitere Anwendungsfelder befasst sich die vierte Frage mit dem Verhalten von Bakterien in nichthomogenen Umgebungen. "Was ist der Einfluss von Größe und

Geschwindigkeit bakterieller Zellen auf die Fähigkeit, chemotaktische Bewegung auszuführen?" Chemotaxis ist die gerichtete Bewegung zur Quelle einer chemischen Substanz, basierend auf der Wahrnehmung der Konzentration jener Substanz. Bakterien besitzen die Fähigkeit, sich durch Anpassung der Dauer von geradem Schwimmen und zufälliger Richtungsänderung im Mittel entlang eines Gradienten zu bewegen. Wir verwenden eine Methode des maschinellen Lernens, das *bestärkende Lernen* (engl. "reinforcement learning"), um zu untersuchen, ob simulierte Teilchen ebenfalls solch eine Strategie entwickeln können. Wir stellen fest, dass in einem sehr großen Parameterbereich eine Strategie gelernt wird, die der natürlicher Organismen sehr ähnlich ist. Durch Vergleich der Zeitskalen für aktive und Brown'sche Translation und Rotation finden wir physikalische Grenzen, jenseits derer ein Lernen dieser Strategie unmöglich wird. Wir finden jedoch auch neuartige Strategien, die sich die Brown'sche Bewegung zu Nutze machen, anstatt gegen sie anzukämpfen. Diese Strategien könnten bei der Entwicklung menschgemachter Mikroroboter als Inspiration dienen.

Insgesamt haben wir die Anwendbarkeit unseres bakteriellen Modells in verschiedenen komplexen Umgebungen demonstriert. Ob es sich um geometrische Begrenzung, externen Fluss oder hydrodynamische Wechselwirkungen handelt, können wir die relevante Physik auf Zellskala mithilfe der in dieser Dissertation vorgestellten Werkzeuge beschreiben. Natürlich sind nicht alle Fragen bezüglich schwimmender Bakterien in komplexen Umgebungen beantwortet. Bei der Erweiterung der Forschung zur Ef-

fizienz der Erkundung poröser Medien könnte man nicht-triviale externe Flussbedingungen einführen. Dann könnte der Einfluss verschiedener Bewegungsmuster auf das Ausbreitungsverhalten entlang oder quer zur Flussrichtung in großen porösen Systemen untersucht werden. Das Biofilmmodell könnte um die explizite Berücksichtigung der Nährstoffe erweitert werden, die durch den Fluss transportiert werden und Zellwachstum ermöglichen. Im Gitter-Boltzmann-Rahmen kann dies durch den Einsatz des Gitter-Elektrokinetik-Algorithmus erreicht werden, der Diffusion und Reaktion an dieselbe Flüssigkeit koppelt, mit der Bakterien im aktuellen Modell interagieren. Bei der Untersuchung der Phageninfektion wurde die Rolle der Form der Phagen in der hydrodynamischen Interaktion bisher vernachlässigt. Einige Phagen sind stark anisotrop mit langen Filamenten auf der Skala der charakteristischen Strömungsmerkmale, die durch schwimmende Bakterien erzeugt werden. Das Verständnis, wie dies den Infektionsprozess beeinflusst, könnte zu tieferen Einblicken in den klinisch relevanten Infektionsprozess führen.

All diese Forschungsrichtungen sind durch eine vergleichsweise einfache Erweiterung des hier vorgestellten bakteriellen Modells erreichbar und werden dem Leser als Übung überlassen.

B.3 Erklärung der Selbständigkeit

Die eingereichte Dissertation zum Thema *Motile bacteria in complex environments* stellt meine eigenständig erbrachte Leistung dar. Ich habe ausschließlich die angegebenen Quellen und Hilfsmittel benutzt. Wörtlich oder inhaltlich aus anderen Werken übernommene Angaben habe ich als solche kenntlich gemacht. Die Richtigkeit der hier getätigten Angaben bestätige ich und versichere, nach bestem Wissen die Wahrheit erklärt zu haben.

Stuttgart, 16 Juli 2024: _____

Christoph Lohrmann

B.4 Erklärung zur Übereinstimmung der digitalen Version mit der vorgelegten Printversion der Dissertation

Hiermit erkläre ich, Christoph Lohrmann, geboren am 03.10.1994, dass das von mir eingereichte pdf-Dokument zur Dissertation mit dem Thema *Motile bacteria in complex environments* in Inhalt und Wortlaut der ebenfalls eingereichten Printversion meiner Dissertationsschrift entspricht.

Stuttgart, 16 Juli 2024: _____

Christoph Lohrmann

Appendix C

Acknowledgements

The following acknowledgements contain lists of names that are sorted by alphabet to avoid drama. If you read this section, do not find your name, but think that you should be included, contact me and I will personally thank you for your contributions to this thesis and my general well being[1].

I would like to thank Petra and Wilhelm Lohrmann for bringing me into this world, raising and supporting me, and giving me every opportunity to become the person I am now.

I would like to thank Christian Holm for accepting me as a member of the ICP and guiding me through the PhD adventure.

I would like to thank all current and former ICP members, especially Adyant Agrawal, Alexander Reinauer, David Beyer, David Zimmer, Fabian Zills, Frank Huber, Henrik Stoß, Ingo Tischler, Jean-Noël Grad, Julian Hossbach, Kartik Jain, Keerthi Radhakrishnan, Konstantin Nikolaou, Lorenz Meyer, Maximilian Hörl, Marc Sauter, Mariano Brito, Michel Mom, Philipp Stärk, Robert

[1] If this applies to you but you do not have my contact information, think again if your contribution to the thesis and my well being is truly that great.

Schuh, Rudolf Weeber, Samuel Tovey, Simon Gravelle, Simon Koppenhoefer, Simone Blümlein and Tilman Kleiner for making my years at the institute inspiring, productive and also fun. Special shout outs go to Frank, Simone and Jean-Noël for providing the technical and administrative support without which I would not have survived the PhD. Special shout outs also go to the people that challenged me physically at the ICP patio or at the gym: Lorenz, Michel, David Z and Konsti. Thanks to my bachelor and master thesis mentees Alex, Simon, Maximilian and Robert for your trust and for keeping me sharp. Thanks to Sam for writing a ton of papers to which I could contribute.

I would like to thank Sujit Datta for the opportunity to spend time at Princeton University (twice!) and everything I learned there. I want to thank the Datta Lab members, especially Ahmed Al Harraq, Alejandro Martínez-Calvo, Anna Hancock, Babak Vajdi Hokmabad, Carolina Trenado Yuste, Craig Singiser, Danielle Sclafani, Emily Chen, Hongbo Zhao, Jenna Anne Ott, Joanna Schneider, Meera Ramaswamy, Navid Bizmark, Sanjana Kamath, Sebastian Gonzalez La Corte, Victoria Grace Muir and Yejoon Seo for welcoming me in their midst not only at work but also outside the lab.

I also want to thank the Princeton CBE G1 cohort of 2023, especially Austin Fan, Christina Kim, Elizabeth Wall, Emily Ostermann, Gracyn Reynolds, Illya Lyadov, Joshua Miller, Kushan Bahl, Matthew Pekarcik, Nathan Tran, Nathanial 'Nate' Hess, Philippe Baron, Quinn Gallagher, Sanjana Kamath, Shannon Zhang, Tohn Borjigin and Wesley Oliver for making me feel at

home far from home. Special shout outs go to the gymnasium brothers Phil, Illya, Wes and Matt; the volleyball Dawgs, the flag football Dawgs (you know who you are); and the climbing crew Emily and Christina. Very special thanks to Phil and Tohn for providing a roof over my head, making the second Princeton trip possible. Thanks to the Procter hall, Yeh and Hoagie Haven kitchen staff for culinary excellence.

I would like to thank the people of SFB1313, especially Alexander Jaust, Alixa Sonntag, Arndt Wagner, Benjamin Bursik, Dongwon Lee, Edward Coltman, Elissa Eggenweiler, Felix Weinhardt, Holger Class, Johannes Hommel, Johannes Muller, Katharina Heck, Kerem Bozkurt, Kilian Weishaupt, Melanie Lipp, Nikos Karadimitriou, Stefanie Kiemle, Theresa Schollenberger, Vahid Joekar-Niassar and Zubin Trivedi for productive collaborations, an insight into the research world beyond physics, and the good times at the various SFB related events. I thank the SFB1313 itself for funding, especially for the trip to MOLSIM in Amsterdam and the research stay in Princeton.

Thanks to Timur Koyuk, Konsti and Sam for helpful comments on the thesis draft.

Finally, I would like to thank all my family and not university-related friends for their continued support, time and love.

Bibliography

[1] D. Strickland, "Prize announcement", `https://www.nobelprize.org/prizes/physics/2018/prize-announcement`, [Online; accessed 27-February-2024], Nobel Prize Outreach AB, 2018.

[2] M. Lee, C. **Lohrmann**, K. Szuttor, H. Auradou, and C. Holm, "The influence of motility on bacterial accumulation in a microporous channel", Soft Matter **17**, 893 (2021).

[3] C. **Lohrmann** and C. Holm, "A novel model for biofilm initiation in porous media flow", Soft Matter **19**, 6920 (2023).

[4] C. **Lohrmann** and C. Holm, "Optimal motility strategies for self-propelled agents to explore porous media", Phys. Rev. E **108**, 054401 (2023).

[5] C. **Lohrmann**, C. Holm, and S. S. Datta, "Influence of bacterial swimming and hydrodynamics on attachment of phages", Soft Matter **20**, 4795 (2024).

[6] S. J. Tovey, C. **Lohrmann**, and C. Holm, "Emergence of Chemotactic Strategies with Multi-Agent Reinforcement Learning", Machine Learning: Science and Technology, accepted manuscript (2024).

[7] A. Wagner, E. Eggenweiler, F. Weinhardt, Z. Trivedi, D. Krach, C. **Lohrmann**, K. Jain, N. Karadimitriou, C. Bringedal, P. Voland, *et al.*, "Permeability Estimation of Regular Porous Structures: A Benchmark for Comparison of Methods", Transport in Porous Media **138**, 1 (2021).

[8] S. Tovey, F. Zills, F. Torres-Herrador, C. **Lohrmann**, M. Brückner, and C. Holm, "MDSuite: comprehensive post-processing tool for particle simulations", Journal of Cheminformatics **15**, 19 (2023).

[9] S. Tovey, D. Zimmer, C. **Lohrmann**, T. Merkt, S. Koppenhoefer, V.-L. Heuthe, C. Bechinger, and C. Holm, "Environmental effects on emergent strategy in micro-scale multi-agent reinforcement learning", 2023, arXiv:2307.00994.

[10] S. Tovey, C. **Lohrmann**, T. Merkt, D. Zimmer, K. Nikolaou, S. Koppenhöfer, A. Bushmakina, J. Scheunemann, and C. Holm, "SwarmRL: Building the future of smart active systems", submitted to *Journal of Micro and Bio Robotics*.

[11] S. Koppenhöfer, C. **Lohrmann**, and C. Holm, "Phase transition of a lattice of rotating rods in a smart active bath", in preparation.

[12] S. Tovey, L. Aigner, F. Zills, C. **Lohrmann**, M. Fleck, N. Hansen, and C. Holm, "Configuration space exploration through the minimum membership kernel", in preparation.

[13] C. Bechinger, R. D. Leonardo, H. Löwen, C. Reichhardt, G. Volpe, and G. Volpe, "Active particles in complex and

crowded environments", Reviews of Modern Physics **88**, 045006 (2016).

[14] A. Bricard, J.-B. Caussin, D. Das, C. Savoie, V. Chikkadi, K. Shitara, O. Chepizhko, F. Peruani, D. Saintillan, and D. Bartolo, "Emergent vortices in populations of colloidal rollers", Nature communications **6**, 7470 (2015).

[15] P. Galajda, J. Keymer, P. Chaikin, and R. Austin, "A wall of funnels concentrates swimming bacteria", Journal of bacteriology **189**, 8704 (2007).

[16] S. E. Hulme, W. R. DiLuzio, S. S. Shevkoplyas, L. Turner, M. Mayer, H. C. Berg, and G. M. Whitesides, "Using ratchets and sorters to fractionate motile cells of Escherichia coli by length", Lab on a Chip **8**, 1888 (2008).

[17] P. Denissenko, V. Kantsler, D. J. Smith, and J. Kirkman-Brown, "Human spermatozoa migration in microchannels reveals boundary-following navigation", Proceedings of the National Academy of Sciences **109**, 8007 (2012).

[18] M. E. Cates and J. Tailleur, "Motility-induced phase separation", Annual Review of Condensed Matter Physics **6**, 219 (2015).

[19] P. Pietzonka, É. Fodor, C. Lohrmann, M. E. Cates, and U. Seifert, "Autonomous engines driven by active matter: Energetics and design principles", Physical Review X **9**, 041032 (2019).

[20] T. Ekeh, M. E. Cates, and É. Fodor, "Thermodynamic cycles with active matter", Physical Review E **102**, 010101 (2020).

[21] P. Pietzonka and U. Seifert, "Entropy production of active particles and for particles in active baths", Journal of Physics A: Mathematical and Theoretical **51**, 01LT01 (2017).

[22] T. Speck, "Stochastic thermodynamics for active matter", Europhysics Letters **114**, 30006 (2016).

[23] E. Lauga and T. R. Powers, "The hydrodynamics of swimming microorganisms", Reports on Progress in Physics **72**, 096601 (2009).

[24] J. Elgeti, R. G. Winkler, and G. Gompper, "Physics of microswimmers — single particle motion and collective behavior: a review", Reports on Progress in Physics **78**, 056601 (2015).

[25] S. Y. Reigh, R. G. Winkler, and G. Gompper, "Synchronization and bundling of anchored bacterial flagella", Soft Matter **8**, 4363 (2012).

[26] J. Clopés and R. G. Winkler, "Flagellar arrangements in elongated peritrichous bacteria: bundle formation and swimming properties", The European Physical Journal E **44**, 1 (2021).

[27] J. Elgeti and G. Gompper, "Microswimmers near surfaces", The European Physical Journal Special Topics **225**, 2333 (2016).

[28] J. J. Molina, Y. Nakayama, and R. Yamamoto, "Hydrodynamic interactions of self-propelled swimmers", Soft Matter **9**, 4923 (2013).

[29] J. D. Wheeler, E. Secchi, R. Rusconi, and R. Stocker, "Not Just Going with the Flow: The Effects of Fluid Flow on Bacteria and Plankton", Annual Review of Cell and Developmental Biology **35**, 213 (2019).

[30] R. P. Feynman, "There's plenty of room at the bottom", Engineering and Science **23**, 22 (1960).

[31] L. Wang, A. Kaeppler, D. Fischer, and J. Simmchen, "Photocatalytic TiO2 micromotors for removal of microplastics and suspended matter", ACS applied materials & interfaces **11**, 32937 (2019).

[32] M. Zarei and M. Zarei, "Self-propelled micro/nanomotors for sensing and environmental remediation", Small **14**, 1800912 (2018).

[33] J. Katuri, X. Ma, M. M. Stanton, and S. Sánchez, "Designing micro-and nanoswimmers for specific applications", Accounts of chemical research **50**, 2 (2017).

[34] H. Zhou, C. C. Mayorga-Martinez, S. Pané, L. Zhang, and M. Pumera, "Magnetically driven micro and nanorobots", Chemical Reviews **121**, 4999 (2021).

[35] A. Ghosh and P. Fischer, "Controlled propulsion of artificial magnetic nanostructured propellers", Nano letters **9**, 2243 (2009).

[36] W. F. Paxton, K. C. Kistler, C. C. Olmeda, A. Sen, S. K. St. Angelo, Y. Cao, T. E. Mallouk, P. E. Lammert, and V. H. Crespi, "Catalytic nanomotors: autonomous movement of striped nanorods", Journal of the American Chemical Society **126**, 13424 (2004).

[37] R. Golestanian, T. B. Liverpool, and A. Ajdari, "Propulsion of a molecular machine by asymmetric distribution of reaction products", Physical Review Letters **94**, 220801 (2005).

[38] M. De Corato, X. Arqué, T. Patiño, M. Arroyo, S. Sánchez, and I. Pagonabarraga, "Self-propulsion of active colloids via ion release: Theory and experiments", Physical review letters **124**, 108001 (2020).

[39] H.-R. Jiang, N. Yoshinaga, and M. Sano, "Active motion of a Janus particle by self-thermophoresis in a defocused laser beam", Physical Review Letters **105**, 268302 (2010).

[40] J. R. Gomez-Solano, S. Samin, C. Lozano, and P. Ruedas-Batuecas, "Tuning the motility and directionality of self-propelled colloids", Scientific Reports **7**, 14891 (2017).

[41] J. M. Walter, D. Greenfield, C. Bustamante, and J. Liphardt, "Light-powering Escherichia coli with proteorhodopsin", Proceedings of the National Academy of Sciences **104**, 2408 (2007).

[42] N. Pellicciotta, O. S. Bagal, V. C. Sosa, G. Frangipane, G. Vizsnyiczai, and R. D. Leonardo, "Light Controlled Biohybrid Microbots", Advanced Functional Materials, 2214801 (2023).

[43] G. Vizsnyiczai, G. Frangipane, C. Maggi, F. Saglimbeni, S. Bianchi, and R. Di Leonardo, "Light controlled 3D micromotors powered by bacteria", Nature communications **8**, 15974 (2017).

[44] G. Frangipane, D. Dell'Arciprete, S. Petracchini, C. Maggi, F. Saglimbeni, S. Bianchi, G. Vizsnyiczai, M. L. Bernardini, and R. Di Leonardo, "Dynamic density shaping of photokinetic E. coli", Elife **7**, e36608 (2018).

[45] P. Gotovtsev, "Microbial Cells as a Microrobots: From Drug Delivery to Advanced Biosensors", Biomimetics **8**, 109 (2023).

[46] O. Schauer, B. Mostaghaci, R. Colin, D. Hürtgen, D. Kraus, M. Sitti, and V. Sourjik, "Motility and chemotaxis of bacteria-driven microswimmers fabricated using antigen 43-mediated biotin display", Scientific reports **8**, 9801 (2018).

[47] K. Bente, A. Codutti, F. Bachmann, and D. Faivre, "Biohybrid and bioinspired magnetic microswimmers", Small **14**, 1704374 (2018).

[48] D. Gong, N. Celi, D. Zhang, and J. Cai, "Magnetic biohybrid microrobot multimers based on chlorella cells for enhanced targeted drug delivery", ACS applied materials & interfaces **14**, 6320 (2022).

[49] J. Petit, S. M. García, B. Molle, R. Bendoula, and N. Ait-Mouheb, "Methods for drip irrigation clogging detection, analysis and understanding: State of the art and perspectives", Agricultural Water Management **272**, 107873 (2022).

[50] L. Mauclaire, A. Schürmann, M. Thullner, J. Zeyer, and S. Gammeter, "Sand filtration in a water treatment plant: biological parameters responsible for clogging", Journal of Water Supply: Research and Technology—AQUA **53**, 93 (2004).

[51] J. W. McKinley and R. L. Siegrist, "Soil clogging genesis in soil treatment units used for onsite wastewater reclamation: a review", Critical reviews in environmental science and technology **41**, 2186 (2011).

[52] W. Song, X. Liu, T. Zheng, and J. Yang, "A review of recharge and clogging in sandstone aquifer", Geothermics **87**, 101857 (2020).

[53] G. Tchobanoglus, F. Burton, and H. D. Stensel, *Wastewater engineering: treatment and reuse*, Vol. 95, 5 (American Water Works Association, 2003), page 201.

[54] G. Crini and E. Lichtfouse, "Wastewater treatment: an overview", Green adsorbents for pollutant removal: fundamentals and design, 1 (2018).

[55] D. Mujah, M. A. Shahin, and L. Cheng, "State-of-the-art review of biocementation by microbially induced calcite precipitation (MICP) for soil stabilization", Geomicrobiology Journal **34**, 524 (2017).

[56] Y. Wu, H. Li, and Y. Li, "Biomineralization induced by cells of Sporosarcina pasteurii: Mechanisms, applications and challenges", Microorganisms **9**, 2396 (2021).

[57] Y. S. Lee and W. Park, "Current challenges and future directions for bacterial self-healing concrete", Applied microbiology and biotechnology **102**, 3059 (2018).

[58] S. Joshi, S. Goyal, A. Mukherjee, and M. S. Reddy, "Microbial healing of cracks in concrete: a review", Journal of Industrial Microbiology and Biotechnology **44**, 1511 (2017).

[59] B. Wedeman and J. Palumbo, "The latest technology in art restoration? Bacteria", `https://www.cnn.com/style/article/bacteria-art-restoration`, [Online; accessed 2024-02-02], Oct. 26, 2021.

[60] C. Nething, M. Smirnova, J. A. Gröning, W. Haase, A. Stolz, and W. Sobek, "A method for 3D printing biocemented spatial structures using sand and urease active calcium carbonate powder", Materials & Design **195**, 109032 (2020).

[61] A. J. Phillips, R. Gerlach, E. Lauchnor, A. C. Mitchell, A. B. Cunningham, and L. Spangler, "Engineered applications of ureolytic biomineralization: a review", Biofouling **29**, 715 (2013).

[62] A. J. Phillips, A. B. Cunningham, R. Gerlach, R. Hiebert, C. Hwang, B. P. Lomans, J. Westrich, C. Mantilla, J. Kirksey, R. Esposito, and L. Spangler, "Fracture Sealing with

Microbially-Induced Calcium Carbonate Precipitation: A Field Study", Environmental Science & Technology **50**, 4111 (2016).

[63] A. J. Phillips, E. Troyer, R. Hiebert, C. Kirkland, R. Gerlach, A. B. Cunningham, L. Spangler, J. Kirksey, W. Rowe, and R. Esposito, "Enhancing wellbore cement integrity with microbially induced calcite precipitation (MICP): A field scale demonstration", Journal of petroleum science and engineering **171**, 1141 (2018).

[64] S. Xia, A. Davletshin, and W. Song, "Enhanced Oil Recovery through Microbially Induced Calcium Carbonate Precipitation", Energy & Fuels **37**, 14666 (2023).

[65] K. S. Ikuta, L. R. Swetschinski, G. R. Aguilar, F. Sharara, T. Mestrovic, A. P. Gray, N. D. Weaver, E. E. Wool, C. Han, A. G. Hayoon, *et al.*, "Global mortality associated with 33 bacterial pathogens in 2019: a systematic analysis for the Global Burden of Disease Study 2019", The Lancet **400**, 2221 (2022).

[66] A. Schulze, F. Mitterer, J. P. Pombo, and S. Schild, "Biofilms by bacterial human pathogens: Clinical relevance-development, composition and regulation-therapeutical strategies", Microbial Cell **8**, 28 (2021).

[67] P. S. Stewart and J. W. Costerton, "Antibiotic resistance of bacteria in biofilms", The lancet **358**, 135 (2001).

[68] R. M. Donlan, "Biofilms: microbial life on surfaces", Emerging infectious diseases **8**, 881 (2002).

[69] C. R. Arciola, D. Campoccia, and L. Montanaro, "Implant infections: adhesion, biofilm formation and immune evasion", Nature reviews microbiology **16**, 397 (2018).

[70] C. R. Epler Barbercheck, E. Bullitt, and M. Andersson, "Bacterial adhesion pili", Membrane Protein Complexes: Structure and Function, 1 (2018).

[71] N. Wadhwa and H. C. Berg, "Bacterial motility: machinery and mechanisms", Nature reviews microbiology **20**, 161 (2022).

[72] H. C. Berg and R. A. Anderson, "Bacteria swim by rotating their flagellar filaments", Nature **245**, 380 (1973).

[73] M. Silverman and M. Simon, "Flagellar rotation and the mechanism of bacterial motility", Nature **249**, 73 (1974).

[74] L. Turner, W. S. Ryu, and H. C. Berg, "Real-time imaging of fluorescent flagellar filaments", Journal of bacteriology **182**, 2793 (2000).

[75] N. C. Darnton, L. Turner, S. Rojevsky, and H. C. Berg, "On torque and tumbling in swimming Escherichia coli", Journal of bacteriology **189**, 1756 (2007).

[76] Y. Sowa and R. M. Berry, "Bacterial flagellar motor", Quarterly reviews of biophysics **41**, 103 (2008).

[77] J. P. Armitage and R. M. Berry, "Assembly and dynamics of the bacterial flagellum", Annual review of microbiology **74**, 181 (2020).

[78] Y. Magariyama, S. Sugiyama, K. Muramoto, Y. Maekawa, I. Kawagishi, Y. Imae, and S. Kudo, "Very fast flagellar rotation", Nature **371**, 752 (1994).

[79] Wikipedia contributors, "Formula One engines — Wikipedia, The Free Encyclopedia", `https://en.wikipedia.org/w/index.php?title=Formula_One_engines&oldid=1200452756`, [Online; accessed 27-February-2024], 2024.

[80] H. Hu, M. Santiveri, N. Wadhwa, H. C. Berg, M. Erhardt, and N. M. Taylor, "Structural basis of torque generation in the bi-directional bacterial flagellar motor", Trends in Biochemical Sciences **47**, 160 (2022).

[81] J. C. Deme, S. Johnson, O. Vickery, A. Aron, H. Monkhouse, T. Griffiths, R. H. James, B. C. Berks, J. W. Coulton, P. J. Stansfeld, *et al.*, "Structures of the stator complex that drives rotation of the bacterial flagellum", Nature Microbiology **5**, 1553 (2020).

[82] H. C. Berg, "The rotary motor of bacterial flagella", Annual review of biochemistry **72**, 19 (2003).

[83] T. Minamino, M. Kinoshita, and K. Namba, "Directional switching mechanism of the bacterial flagellar motor", Computational and structural biotechnology journal **17**, 1075 (2019).

[84] H. C. Berg and D. A. Brown, "Chemotaxis in Escherichia coli analysed by Three-dimensional Tracking", Nature **239**, 500 (1972).

[85] D. J. Webre, P. M. Wolanin, and J. B. Stock, "Bacterial chemotaxis", Current Biology **13**, R47 (2003).

[86] H. C. Berg, "Chemotaxis in bacteria", Annual Review of Biophysics and Bioengineering **4**, 119 (1975).

[87] G. H. Wadhams and J. P. Armitage, "Making sense of it all: bacterial chemotaxis", Nature reviews Molecular cell biology **5**, 1024 (2004).

[88] J. P. Armitage, "Behavioural responses of bacteria to light and oxygen", Archives of Microbiology **168**, 249 (1997).

[89] D.-P. Häder, M. Lebert, P. Richter, and M. Ntefidou, "Gravitaxis and graviperception in flagellates", Advances in Space Research **31**, 2181 (2003).

[90] M. Demir and H. Salman, "Bacterial thermotaxis by speed modulation", Biophysical journal **103**, 1683 (2012).

[91] M. Eisenbach and L. C. Giojalas, "Sperm guidance in mammals—an unpaved road to the egg", Nature reviews Molecular cell biology **7**, 276 (2006).

[92] E. Govorunova and O. Sineshchekov, "Chemotaxis in the green flagellate alga Chlamydomonas", Biochemistry (Moscow) **70**, 717 (2005).

[93] N. Vladimirov and V. Sourjik, "Chemotaxis: how bacteria use memory", Biological Chemistry **390**, 1097 (2009).

[94] S. H. Larsen, R. W. Reader, E. N. Kort, W.-W. Tso, and J. Adler, "Change in direction of flagellar rotation is the ba-

sis of the chemotactic response in Escherichia coli", Nature **249**, 74 (1974).

[95] W. G. Characklis and K. C. Marshall, *Biofilms*, eng, Wiley series in ecological and applied microbiology (Wiley, New York, 1990).

[96] L. Yang, Y. Liu, H. Wu, N. Høiby, S. Molin, and Z.-j. Song, "Current understanding of multi-species biofilms", International journal of oral science **3**, 74 (2011).

[97] R. Hengge, "Principles of c-di-GMP signalling in bacteria", Nature Reviews Microbiology **7**, 263 (2009).

[98] K. Quan, J. Hou, Z. Zhang, Y. Ren, B. W. Peterson, H.-C. Flemming, C. Mayer, H. J. Busscher, and H. C. van der Mei, "Water in bacterial biofilms: pores and channels, storage and transport functions", Critical reviews in microbiology **48**, 283 (2022).

[99] V. D. Gordon, M. Davis-Fields, K. Kovach, and C. A. Rodesney, "Biofilms and mechanics: a review of experimental techniques and findings", Journal of Physics D: Applied Physics **50**, 223002 (2017).

[100] E. S. Gloag, S. Fabbri, D. J. Wozniak, and P. Stoodley, "Biofilm mechanics: Implications in infection and survival", Biofilm **2**, 100017 (2020).

[101] A. Chevallereau, B. J. Pons, S. van Houte, and E. R. Westra, "Interactions between bacterial and phage communities in natural environments", Nat. Rev. Microbiol. **20**, 49 (2022).

[102] B. Koskella, C. A. Hernandez, and R. M. Wheatley, "Understanding the impacts of bacteriophage viruses: from laboratory evolution to natural ecosystems", Annu. Rev. Virol. **9**, 57 (2022).

[103] M. Breitbart, C. Bonnain, K. Malki, and N. Sawaya, "Phage puppet masters of the marine microbial realm", Nat. Microbiol. **3**, 754 (2018).

[104] S. A. Strathdee, G. F. Hatfull, V. K. Mutalik, and R. T. Schooley, "Phage therapy: From biological mechanisms to future directions", Cell **186**, 17 (2023).

[105] H. Brüssow, C. Canchaya, and W.-D. Hardt, "Phages and the evolution of bacterial pathogens: from genomic rearrangements to lysogenic conversion", Microbiology and molecular biology reviews **68**, 560 (2004).

[106] R. W. Hendrix, M. C. M. Smith, R. N. Burns, M. E. Ford, and G. F. Hatfull, "Evolutionary relationships among diverse bacteriophages and prophages: All the world's a phage", Proceedings of the National Academy of Sciences **96**, 2192 (1999).

[107] A. Mushegian, "Are there 10^{31} virus particles on earth, or more, or fewer?", Journal of bacteriology **202**, 10 (2020).

[108] H. G. Hampton, B. N. Watson, and P. C. Fineran, "The arms race between bacteria and their phage foes", Nature **577**, 327 (2020).

[109] J. Łoś, S. Zielińska, A. Krajewska, Z. Michalina, A. Małachowska, K. Kwaśnicka, and M. Łoś, "Temperate phages, prophages, and lysogeny", Bacteriophages: Biology, Technology, Therapy, 119 (2021).

[110] I. D. Hay and T. Lithgow, "Filamentous phages: masters of a microbial sharing economy", EMBO reports **20**, e47427 (2019).

[111] S. Markert, "Electron micrograph of T4 phages and Escherichia Coli cell", `https://twitter.com/sci_bastian/status/1636138908814651396/photo/1`, 2023.

[112] E. Stone, K. Campbell, I. Grant, and O. McAuliffe, "Understanding and exploiting phage–host interactions", Viruses **11**, 567 (2019).

[113] J. J. Dennehy and S. T. Abedon, "Adsorption: phage acquisition of bacteria", Bacteriophages: biology, technology, therapy, 93 (2021).

[114] S. Fernandes and C. São-José, "Enzymes and mechanisms employed by tailed bacteriophages to breach the bacterial cell barriers", Viruses **10**, 396 (2018).

[115] I. J. Molineux and D. Panja, "Popping the cork: mechanisms of phage genome ejection", Nature Reviews Microbiology **11**, 194 (2013).

[116] H. Deveau, J. E. Garneau, and S. Moineau, "CRISPR/Cas system and its role in phage-bacteria interactions", Annual review of microbiology **64**, 475 (2010).

[117] P. Katsamba and E. Lauga, "Hydrodynamics of bacteriophage migration along bacterial flagella", Physical Review Fluids **4**, 013101 (2019).

[118] S. A. Karabasov, M. A. Zaitsev, and D. A. Nerukh, "The nut-and-bolt motion of a bacteriophage sliding along a bacterial flagellum: a complete hydrodynamics model", Scientific Reports **13**, 9077 (2023).

[119] R. Brown, "A brief account of microscopical observations made in the months of June, July and August 1827, on the particles contained in the pollen of plants; and on the general existence of active molecules in organic and inorganic bodies", The philosophical magazine **4**, 161 (1828).

[120] A. Einstein, "Über die von der molekularkinetischen Theorie der Wärme geforderte Bewegung von in ruhenden Flüssigkeiten suspendierten Teilchen", Annalen der Physik **4** (1905).

[121] H. Risken, *The Fokker-Planck Equation*, 2nd edition (Springer, Berlin, 1989).

[122] L. Bachelier, "Théorie de la spéculation", in Annales scientifiques de l'École normale supérieure, Vol. 17 (1900), pages 21–86.

[123] J. Choi, M. Kwak, C. W. Tee, and Y. Wang, "A Black–Scholes user's guide to the Bachelier model", Journal of Futures Markets **42**, 959 (2022).

[124] D. S. Lemons and A. Gythiel, "Paul Langevin's 1908 paper "on the theory of brownian motion"["sur la théorie du mouvement brownien," cr acad. sci.(paris) 146, 530–533 (1908)]", American Journal of Physics **65**, 1079 (1997).

[125] P. Langevin, "Sur la théorie du mouvement brownien", Compt. Rendus **146**, 530 (1908).

[126] G. Stokes, "On the effect of internal friction of fluids on the motion of pendulums", Transactions of the Cambridge philosophical Society **9**, 106 (1850).

[127] R. Zwanzig, *Nonequilibrium statistical mechanics* (Oxford University Press, 2001).

[128] M. Von Smoluchowski, "Zur kinetischen theorie der brownschen molekularbewegung und der suspensionen", Annalen der physik **326**, 756 (1906).

[129] E. Guazzelli and J. F. Morris, *A physical introduction to suspension dynamics*, Vol. 45 (Cambridge University Press, 2011).

[130] R. G. Winkler, A. Wysocki, and G. Gompper, "Virial pressure in systems of spherical active Brownian particles", Soft matter **11**, 6680 (2015).

[131] C. W. Gardiner, *Handbook of stochastic methods*, 2nd, Springer Series in Synergetics (Springer, 1996).

[132] M. R. Shaebani, A. Wysocki, R. G. Winkler, G. Gompper, and H. Rieger, "Computational models for active matter", Nature Reviews Physics **2**, 181 (2020).

[133] B. ten Hagen, S. van Teeffelen, and H. Löwen, "Brownian motion of a self-propelled particle", Journal of Physics: Condensed Matter **23**, 194119 (2011).

[134] F. Weik, R. Weeber, K. Szuttor, K. Breitsprecher, J. de Graaf, M. Kuron, J. Landsgesell, H. Menke, D. Sean, and C. Holm, "ESPResSo 4.0–an extensible software package for simulating soft matter systems", The European Physical Journal Special Topics **227**, 1789 (2019).

[135] D. Frenkel and B. Smit, *Understanding molecular simulation: from algorithms to applications* (Academic Press San Diego, 2002).

[136] I. P. Omelyan, "On the numerical integration of motion for rigid polyatomics: The modified quaternion approach", Computers in Physics **12**, 97 (1998).

[137] C. Liu and Z. Li, "On the validity of the Navier-Stokes equations for nanoscale liquid flows: The role of channel size", AIP advances **1** (2011).

[138] A. Schlaich, M. Vandamme, M. Plazanet, and B. Coasne, "Bridging Microscopic Dynamics and Hydraulic Permeability in Mechanically-Deformed Nanoporous Materials", arXiv preprint arXiv:2403.19812 (2024).

[139] M. Bier, "Lecture notes for "Physik der Flüssigkeiten"", 2018.

[140] E. Lauga and H. A. Stone, "Effective slip in pressure-driven Stokes flow", Journal of Fluid Mechanics **489**, 55 (2003).

[141] E. M. Purcell, "Life at low Reynolds number", American journal of physics **45**, 3 (1977).

[142] W. Freiherr von Buddenbrock-Hettersdorff, *Untersuchungen über die Schwimmbewegungen und die Statocysten der Gattung Pecten*, Sitzungsberichte der Heidelberger Akademie der Wissenschaften, Mathematisch-Naturwissenschaftliche Klasse (Winter, Heidelberg, 1911).

[143] P. Bayly, B. Lewis, E. Ranz, R. Okamoto, R. Pless, and S. Dutcher, "Propulsive forces on the flagellum during locomotion of Chlamydomonas reinhardtii", Biophysical journal **100**, 2716 (2011).

[144] M. Lisicki, "Four approaches to hydrodynamic Green's functions–the Oseen tensors", arXiv preprint arXiv:1312.6231 (2013).

[145] S. E. Spagnolie and E. Lauga, "Hydrodynamics of self-propulsion near a boundary: predictions and accuracy of far-field approximations", Journal of Fluid Mechanics **700**, 105 (2012).

[146] M. Kuron, P. Stärk, C. Holm, and J. de Graaf, "Hydrodynamic mobility reversal of squirmers near flat and curved surfaces", Soft Matter **15**, 5908 (2019).

[147] S. Datta and D. K. Srivastava, "Stokes drag on axially symmetric bodies: a new approach", Proceedings-Mathematical Sciences **109**, 441 (1999).

[148] F. Perrin, "Mouvement brownien d'un ellipsoide-I. Dispersion diélectrique pour des molécules ellipsoidales", J. phys. radium **5**, 497 (1934).

[149] T. Krüger, H. Kusumaatmaja, A. Kuzmin, O. Shardt, G. Silva, and E. M. Viggen, "The lattice Boltzmann method", Springer International Publishing **10**, 4 (2017).

[150] J. J. Monaghan, "Smoothed particle hydrodynamics and its diverse applications", Annual Review of Fluid Mechanics **44**, 323 (2012).

[151] G. Gompper, T. Ihle, D. M. Kroll, and R. G. Winkler, "Multi-particle collision dynamics: A particle-based mesoscale simulation approach to the hydrodynamics of complex fluids", in *Advanced Computer Simulation Approaches for Soft Matter Sciences III*, edited by C. Holm and K. Kremer, Advances in Polymer Science 221 (Springer, Berlin, 2009), pages 1–87.

[152] P. L. Bhatnagar, E. P. Gross, and M. Krook, "A model for collision processes in gases. I. Small amplitude processes in charged and neutral one-component systems", Physical review **94**, 511 (1954).

[153] M. Bauer, S. Eibl, C. Godenschwager, N. Kohl, M. Kuron, C. Rettinger, F. Schornbaum, C. Schwarzmeier, D. Thönnes, H. Köstler, and U. Rüde, "waLBerla: A block-structured high-performance framework for multiphysics simulations", Computers & Mathematics with Applications **81** *Develop-*

ment and Application of Open-source Software for Problems with Numerical PDEs, 478 (2021).

[154] J. M. O. De Zarate and J. V. Sengers, *Hydrodynamic fluctuations in fluids and fluid mixtures* (Elsevier, 2006).

[155] A. J. C. Ladd, "Numerical simulations of particulate suspensions via a discretized Boltzmann equation. Part 1. Theoretical foundation", Journal of Fluid Mechanics **271**, 285 (1994).

[156] S. Chapman and T. Cowling, *The Mathematical Theory of Non-Uniform Gases* (Cambridge University Press, 1970).

[157] Z. Guo, C. Zheng, and B. Shi, "Discrete lattice effects on the forcing term in the lattice Boltzmann method", Physical review E **65**, 046308 (2002).

[158] M. Kuron, C. Stewart, J. de Graaf, and C. Holm, "An extensible lattice Boltzmann method for viscoelastic flows: complex and moving boundaries in Oldroyd-B fluids", European Physical Journal E **44** *Motile Active Matter*, 1 (2021).

[159] P. Ahlrichs and B. Dünweg, "Simulation of a single polymer chain in solution by combining lattice Boltzmann and molecular dynamics", The Journal of chemical physics **111**, 8225 (1999).

[160] V. Lobaskin and B. Dünweg, "A new model for simulating colloidal dynamics", New Journal of Physics **6**, 54 (2004).

[161] L. P. Fischer, T. Peter, C. Holm, and J. de Graaf, "The raspberry model for hydrodynamic interactions revisited. I. Periodic arrays of spheres and dumbbells", The Journal of Chemical Physics **143**, 084107 (2015).

[162] J. de Graaf, T. Peter, L. P. Fischer, and C. Holm, "The raspberry model for hydrodynamic interactions revisited. II. The effect of confinement", The Journal of Chemical Physics **143**, 084108, 084108 (2015).

[163] H. Darcy, *Les fontaines publiques de la ville de Dijon: exposition et application des principes à suivre et des formules à employer dans les questions de distribution d'eau*, Vol. 1 (Victor dalmont, 1856).

[164] J. de Graaf, H. Menke, A. J. Mathijssen, M. Fabritius, C. Holm, and T. N. Shendruk, "Lattice-Boltzmann hydrodynamics of anisotropic active matter", The Journal of chemical physics **144** (2016).

[165] J. E. Jones, "On the determination of molecular fields.—I. From the variation of the viscosity of a gas with temperature", Proceedings of the Royal Society of London. Series A, Containing Papers of a Mathematical and Physical Character **106**, 441 (1924).

[166] J. E. Lennard-Jones, "Cohesion", Proceedings of the Physical Society **43**, 461 (1931).

[167] J. D. Weeks, D. Chandler, and H. C. Andersen, "Role of Repulsive Forces in Determining the Equilibrium Structure

of Simple Liquids", The Journal of Chemical Physics **54**, 5237 (1971).

[168] R. A. X. Persson, "Modification of the Gay-Berne potential for improved accuracy and speed", The Journal of Chemical Physics **136**, 226101 (2012).

[169] J. G. Gay and B. J. Berne, "Modification of the overlap potential to mimic a linear site-site potential", The Journal of Chemical Physics **74**, 3316 (1981).

[170] J. de Graaf, A. J. Mathijssen, M. Fabritius, H. Menke, C. Holm, and T. N. Shendruk, "Understanding the onset of oscillatory swimming in microchannels", Soft Matter **12**, 4704 (2016).

[171] J. Saragosti, P. Silberzan, and A. Buguin, "Modeling E. coli tumbles by rotational diffusion. Implications for chemotaxis", PLOS ONE **7**, e35412 (2012).

[172] M. Lee, K. Szuttor, and C. Holm, "A computational model for bacterial run-and-tumble motion", The Journal of Chemical Physics **150**, 174111 (2019).

[173] C. Lohrmann and C. Holm, *Replication Data for: Lohrmann, Holm: A novel model for biofilm initiation in porous media flow* (DaRUS, 2023).

[174] C. Lohrmann and C. Holm, *Replication Data for: Lohrmann, Holm: Optimal motility strategies for self-propelled agents to explore porous media* (DaRUS, 2023).

[175] C. Lohrmann and C. Holm, *Replication Data for: Lohrmann, Holm, Datta: Influence of bacterial motility and hydrodynamics on phage bacteria encounters*, version V1 (DaRUS, 2023).

[176] T. R. Ginn, B. D. Wood, K. E. Nelson, T. D. Scheibe, E. M. Murphy, and T. P. Clement, "Processes in microbial transport in the natural subsurface", Advances in Water Resources **25**, 1017 (2002).

[177] T. Kaya and H. Koser, "Direct Upstream Motility in Escherichia coli", Biophysical Journal **102**, 1514 (2012).

[178] V. Kantsler, J. Dunkel, M. Blayney, and R. E. Goldstein, "Rheotaxis facilitates upstream navigation of mammalian sperm cells", eLife **3**, edited by A. A. Hyman, e02403 (2014).

[179] N. Figueroa-Morales, G. Leonardo Miño, A. Rivera, R. Caballero, E. Clément, E. Altshuler, and A. Lindner, "Living on the edge: transfer and traffic of E. coli in a confined flow", Soft Matter **11**, 6284 (2015).

[180] E. Lauga, W. R. DiLuzio, G. M. Whitesides, and H. A. Stone, "Swimming in Circles: Motion of Bacteria near Solid Boundaries", Biophysical Journal **90**, 400 (2006).

[181] A. J. Mathijssen, N. Figueroa-Morales, G. Junot, É. Clément, A. Lindner, and A. Zöttl, "Oscillatory surface rheotaxis of swimming E. coli bacteria", Nature communications **10**, 1 (2019).

[182] R. Rusconi and R. Stocker, "Microbes in flow", Current Opinion in Microbiology **25**, 1 (2015).

[183] G. Junot, N. Figueroa-Morales, T. Darnige, A. Lindner, R. Soto, H. Auradou, and E. Clément, "Swimming bacteria in Poiseuille flow: The quest for active Bretherton-Jeffery trajectories", EPL (Europhysics Letters) **126**, 44003 (2019).

[184] R. Rusconi, J. S. Guasto, and R. Stocker, "Bacterial transport suppressed by fluid shear", Nature physics **10**, 212 (2014).

[185] E. Secchi, A. Vitale, G. L. Miño, V. Kantsler, L. Eberl, R. Rusconi, and R. Stocker, "The effect of flow on swimming bacteria controls the initial colonization of curved surfaces", Nature Communications **11**, 1 (2020).

[186] J. Słomka, U. Alcolombri, E. Secchi, R. Stocker, and V. I. Fernandez, "Encounter rates between bacteria and small sinking particles", New Journal of Physics **22**, 043016 (2020).

[187] G. L. Miño, M. Baabour, R. Chertcoff, G. Gutkind, E. Clément, H. Auradou, and I. Ippolito, "E coli Accumulation behind an Obstacle", Advances in Microbiology **8**, 451 (2018).

[188] J. Elgeti and G. Gompper, "Wall accumulation of self-propelled spheres", Europhysics Letters **101**, 48003 (2013).

[189] J. Elgeti and G. Gompper, "Run-and-tumble dynamics of self-propelled particles in confinement", Europhysics Letters **109**, 58003 (2015).

[190] G. Volpe, I. Buttinoni, D. Vogt, H.-J. Kümmerer, and C. Bechinger, "Microswimmers in patterned environments", Soft Matter **7**, 8810 (2011).

[191] M. Zeitz, K. Wolff, and H. Stark, "Active Brownian particles moving in a random Lorentz gas", European Physical Journal E **40**, 23 (2017).

[192] S. E. Spagnolie, G. R. Moreno-Flores, D. Bartolo, and E. Lauga, "Geometric capture and escape of a microswimmer colliding with an obstacle", Soft Matter **11**, 3396 (2015).

[193] O. Sipos, K. Nagy, R. Di Leonardo, and P. Galajda, "Hydrodynamic Trapping of Swimming Bacteria by Convex Walls", Physical Review Letters **114**, 258104 (2015).

[194] R. Alonso-Matilla, B. Chakrabarti, and D. Saintillan, "Transport and dispersion of active particles in periodic porous media", Physical Review Fluids **4**, 043101, 043101 (2019), eprint: 1809.00086 (physics.flu-dyn).

[195] H.-C. Flemming and S. Wuertz, "Bacteria and archaea on Earth and their abundance in biofilms", Nature Reviews Microbiology **17**, 247 (2019).

[196] V. D. Gordon, M. Davis-Fields, K. Kovach, and C. A. Rodesney, "Biofilms and mechanics: a review of experimen-

tal techniques and findings", Journal of Physics D: Applied Physics **50**, 223002 (2017).

[197] R. Hartmann, P. K. Singh, P. Pearce, R. Mok, B. Song, F. Díaz-Pascual, J. Dunkel, and K. Drescher, "Emergence of three-dimensional order and structure in growing biofilms", Nature Physics **15**, 251 (2019).

[198] P. Stoodley, Z. Lewandowski, J. D. Boyle, and H. M. Lappin-Scott, "Oscillation Characteristics of Biofilm Streamers in Turbulent Flowing Water as Related to Drag and Pressure Drop", Biotechnology and Bioengineering **57**, 536 (1998).

[199] K. Drescher, Y. Shen, B. L. Bassler, and H. A. Stone, "Biofilm streamers cause rapid clogging", Proceedings of the National Academy of Sciences **110**, 4345 (2013).

[200] A. Martínez-Calvo, T. Bhattacharjee, R. K. Bay, H. N. Luu, A. M. Hancock, N. S. Wingreen, and S. S. Datta, "Morphological instability and roughening of growing 3D bacterial colonies", Proceedings of the National Academy of Sciences **119**, e2208019119 (2022).

[201] C. Zhang, Q. Kang, X. Wang, J. L. Zilles, R. H. Müller, and C. J. Werth, "Effects of Pore-Scale Heterogeneity and Transverse Mixing on Bacterial Growth in Porous Media", Environmental Science & Technology **44**, 3085 (2010).

[202] J.-U. Kreft, G. Booth, and J. W. T. Wimpenny, "BacSim, a Simulator for Individual-Based Modelling of Bacterial Colony Growth", Microbiology **144**, 3275 (1998).

[203] J.-U. Kreft, C. Picioreanu, J. W. T. Wimpenny, and M. C. M. van Loosdrecht, "Individual-Based Modelling of Biofilms", Microbiology **147**, 2897 (2001).

[204] D. A. G. von der Schulenburg, T. R. R. Pintelon, C. Picioreanu, M. C. M. Van Loosdrecht, and M. L. Johns, "Three-Dimensional Simulations of Biofilm Growth in Porous Media", AIChE Journal **55**, 494 (2009).

[205] L. A. Lardon, B. V. Merkey, S. Martins, A. Dötsch, C. Picioreanu, J.-U. Kreft, and B. F. Smets, "iDynoMiCS: Next-Generation Individual-Based Modelling of Biofilms", Environmental Microbiology **13**, 2416 (2011).

[206] J. W. Wimpenny and R. Colasanti, "A Unifying Hypothesis for the Structure of Microbial Biofilms Based on Cellular Automaton Models", FEMS Microbiology Ecology **22**, 1 (1997).

[207] C. Picioreanu, M. C. M. van Loosdrecht, and J. J. Heijnen, "A New Combined Differential-Discrete Cellular Automaton Approach for Biofilm Modeling: Application for Growth in Gel Beads", Biotechnology and Bioengineering **57**, 718 (1998).

[208] G. Pizarro, D. Griffeath, and D. R. Noguera, "Quantitative Cellular Automaton Model for Biofilms", Journal of Environmental Engineering **127**, 782 (2001).

[209] M. Aghajani Delavar and J. Wang, "Pore-Scale Modeling of Competition and Cooperation of Multispecies Biofilms for

Nutrients in Changing Environments", AIChE Journal **66**, e16919 (2020).

[210] K. Williamson and P. L. McCarty, "A Model of Substrate Utilization by Bacterial Films", Journal (Water Pollution Control Federation) **48**, 9 (1976), JSTOR: 25038465.

[211] O. Wanner and W. Gujer, "A Multispecies Biofilm Model", Biotechnology and Bioengineering **28**, 314 (1986).

[212] H. J. Eberl, D. F. Parker, and M. C. Vanloosdrecht, "A New Deterministic Spatio-Temporal Continuum Model for Biofilm Development", Journal of Theoretical Medicine **3**, 161 (2001).

[213] P. Cumsille, J. A. Asenjo, and C. Conca, "A Novel Model for Biofilm Growth and Its Resolution by Using the Hybrid Immersed Interface-Level Set Method", Computers & Mathematics with Applications **67**, 34 (2014).

[214] J. Zhang, "Lattice Boltzmann method for microfluidics: models and applications", Microfluidics and Nanofluidics **10**, 1 (2011).

[215] M. Rubinstein and R. H. Colby, *Polymer Physics* (Oxford University Press, Oxford, UK, 2003).

[216] E. Miller, T. Garcia, S. Hultgren, and A. F. Oberhauser, "The Mechanical Properties of E. Coli Type 1 Pili Measured by Atomic Force Microscopy Techniques", Biophysical Journal **91**, 3848 (2006).

[217] S. H. Lee, E. Secchi, and P. K. Kang, "Rapid formation of bioaggregates and morphology transition to biofilm streamers induced by pore-throat flows", Proceedings of the National Academy of Sciences **120**, e2204466120 (2023).

[218] C. J. Rupp, C. A. Fux, and P. Stoodley, "Viscoelasticity of Staphylococcus aureus Biofilms in Response to Fluid Shear Allows Resistance to Detachment and Facilitates Rolling Migration", Applied and Environmental Microbiology **71**, 2175 (2005).

[219] P. Pearce, B. Song, D. J. Skinner, R. Mok, R. Hartmann, P. K. Singh, H. Jeckel, J. S. Oishi, K. Drescher, and J. Dunkel, "Flow-Induced Symmetry Breaking in Growing Bacterial Biofilms", Physical Review Letters **123**, 258101 (2019).

[220] S. Aggarwal, E. H. Poppele, and R. M. Hozalski, "Development and Testing of a Novel Microcantilever Technique for Measuring the Cohesive Strength of Intact Biofilms", Biotechnology and Bioengineering **105**, 924 (2010).

[221] S. Aggarwal and R. M. Hozalski, "Determination of biofilm mechanical properties from tensile tests performed using a micro-cantilever method", Biofouling **26**, 479 (2010).

[222] C. L. Gaol, L. Ganzer, S. Mukherjee, and H. Alkan, "Investigation of clogging in porous media induced by microorganisms using a microfluidic application", Environmental Science: Water Research & Technology **7**, 441 (2021).

[223] D. L. Kurz, E. Secchi, F. J. Carrillo, I. C. Bourg, R. Stocker, and J. Jimenez-Martinez, "Competition between growth and shear stress drives intermittency in preferential flow paths in porous medium biofilms", Proceedings of the National Academy of Sciences **119**, e2122202119 (2022).

[224] K. Josef, J. Saranak, and K. W. Foster, "Linear systems analysis of the ciliary steering behavior associated with negative-phototaxis in Chlamydomonas reinhardtii", Cell motility and the cytoskeleton **63**, 758 (2006).

[225] J. Schwarz-Linek, J. Arlt, A. Jepson, A. Dawson, T. Vissers, D. Miroli, T. Pilizota, V. A. Martinez, and W. C. Poon, "Escherichia coli as a model active colloid: a practical introduction", Colloids and Surfaces B: Biointerfaces **137**, 2 (2016).

[226] A. Gong, S. Rode, U. B. Kaupp, G. Gompper, J. Elgeti, B. M. Friedrich, and L. Alvarez, "The steering gaits of sperm", Philosophical Transactions of the Royal Society B **375**, 20190149 (2020).

[227] J. R. Howse, R. A. Jones, A. J. Ryan, T. Gough, R. Vafabakhsh, and R. Golestanian, "Self-motile colloidal particles: from directed propulsion to random walk", Physical Review Letters **99**, 048102 (2007).

[228] J. Li, V. V. Singh, S. Sattayasamitsathit, J. Orozco, K. Kaufmann, R. Dong, W. Gao, B. Jurado-Sanchez, Y. Fedorak, and J. Wang, "Water-driven micromotors for rapid

photocatalytic degradation of biological and chemical warfare agents", ACS nano **8**, 11118 (2014).

[229] C. Lozano, B. Ten Hagen, H. Löwen, and C. Bechinger, "Phototaxis of synthetic microswimmers in optical landscapes", Nature communications **7**, 12828 (2016).

[230] T. Bäuerle, R. C. Löffler, and C. Bechinger, "Formation of stable and responsive collective states in suspensions of active colloids", Nature Communications **11**, 2547 (2020).

[231] H. Massana-Cid, C. Maggi, G. Frangipane, and R. Di Leonardo, "Rectification and confinement of photokinetic bacteria in an optical feedback loop", Nature Communications **13**, 2740 (2022).

[232] U. K. Cheang, H. Kim, D. Milutinović, J. Choi, and M. J. Kim, "Feedback control of an achiral robotic microswimmer", Journal of Bionic Engineering **14**, 245 (2017).

[233] M. A. Fernandez-Rodriguez, F. Grillo, L. Alvarez, M. Rathlef, I. Buttinoni, G. Volpe, and L. Isa, "Feedback-controlled active brownian colloids with space-dependent rotational dynamics", Nature communications **11**, 4223 (2020).

[234] U. Kei Cheang, K. Lee, A. A. Julius, and M. J. Kim, "Multiple-robot drug delivery strategy through coordinated teams of microswimmers", Applied physics letters **105** (2014).

[235] J. E. Johansen, J. Pinhassi, N. Blackburn, U. L. Zweifel, and Å. Hagström, "Variability in motility characteristics among marine bacteria", Aquatic microbial ecology **28**, 229 (2002).

[236] R. Stocker and J. R. Seymour, "Ecology and physics of bacterial chemotaxis in the ocean", Microbiology and Molecular Biology Reviews **76**, 792 (2012).

[237] L. Xie, T. Altindal, S. Chattopadhyay, and X.-L. Wu, "Bacterial flagellum as a propeller and as a rudder for efficient chemotaxis", Proceedings of the National Academy of Sciences **108**, 2246 (2011).

[238] J. Taktikos, H. Stark, and V. Zaburdaev, "How the motility pattern of bacteria affects their dispersal and chemotaxis", PloS one **8**, e81936 (2013).

[239] T. Bhattacharjee and S. S. Datta, "Bacterial hopping and trapping in porous media", Nature Communications **10**, 1 (2019).

[240] T. Bhattacharjee and S. S. Datta, "Confinement and activity regulate bacterial motion in porous media", Soft Matter **15**, 9920 (2019).

[241] C. Reichhardt and C. O. Reichhardt, "Active matter transport and jamming on disordered landscapes", Physical Review E **90**, 012701 (2014).

[242] N. A. Licata, B. Mohari, C. Fuqua, and S. Setayeshgar, "Diffusion of bacterial cells in porous media", Biophysical journal **110**, 247 (2016).

[243] T. Bertrand, Y. Zhao, O. Bénichou, J. Tailleur, and R. Voituriez, "Optimized diffusion of run-and-tumble particles in crowded environments", Physical Review Letters **120**, 198103 (2018).

[244] E. Irani, Z. Mokhtari, and A. Zippelius, "Dynamics of bacteria scanning a porous environment", Physical Review Letters **128**, 144501 (2022).

[245] C. Kurzthaler, S. Mandal, T. Bhattacharjee, H. Löwen, S. S. Datta, and H. A. Stone, "A geometric criterion for the optimal spreading of active polymers in porous media", Nature communications **12**, 7088 (2021).

[246] M. Hintsche, V. Waljor, R. Großmann, M. J. Kühn, K. M. Thormann, F. Peruani, and C. Beta, "A Polar Bundle of Flagella Can Drive Bacterial Swimming by Pushing, Pulling, or Coiling around the Cell Body", Scientific Reports **7**, 16771 (2017).

[247] B. L. Taylor and D. E. Koshland, "Reversal of flagellar rotation in monotrichous and peritrichous bacteria: Generation of changes in direction", Journal of Bacteriology **119**, 640 (1974).

[248] K. J. Duffy and R. M. Ford, "Turn Angle and Run Time Distributions Characterize Swimming Behavior for Pseudomonas Putida", Journal of Bacteriology **179**, 1428 (1997).

[249] H. C. Berg, *Random Walks in Biology* (Princeton University Press, 1993).

[250] V. D. Gordon and L. Wang, "Bacterial mechanosensing: the force will be with you, always", Journal of Cell Science **132**, jcs227694 (2019).

[251] J. T. Gostick, Z. A. Khan, T. G. Tranter, M. D. Kok, M. Agnaou, M. Sadeghi, and R. Jervis, "PoreSpy: A python toolkit for quantitative analysis of porous media images", Journal of Open Source Software **4**, 1296 (2019).

[252] S. T. Abedon, "Bacteriophage Adsorption: Likelihood of Virion Encounter with Bacteria and Other Factors Affecting Rates", Antibiotics **12**, `10.3390/antibiotics12040723` (2023).

[253] K. L. Joiner, A. Baljon, J. Barr, F. Rohwer, and A. Luque, "Impact of bacteria motility in the encounter rates with bacteriophage in mucus", Scientific Reports **9**, 1 (2019).

[254] K. Drescher, J. Dunkel, L. Cisneros, S. Ganguly, and R. Goldstein, "Fluid dynamics and noise in bacterial cell–cell and cell–surface scattering", Proceedings of the National Academy of Sciences **108**, 10940 (2011).

[255] H. Berg and E. Purcell, "Physics of chemoreception", Biophysical Journal **20**, 193 (1977).

[256] S. Friedlander, "Mass and heat transfer to single spheres and cylinders at low Reynolds numbers", AIChE journal **3**, 43 (1957).

[257] A. Acrivos and T. D. Taylor, "Heat and mass transfer from single spheres in Stokes flow", The Physics of Fluids **5**, 387 (1962).

[258] E. Lauga, "Bacterial Hydrodynamics", Annual Review of Fluid Mechanics **48**, 105 (2016).

[259] S. E. Spagnolie and E. Lauga, "Hydrodynamics of self-propulsion near a boundary: predictions and accuracy of far-field approximations", Journal of Fluid Mechanics **700**, 105 (2012).

[260] N. C. Esteves and B. E. Scharf, "Flagellotropic bacteriophages: opportunities and challenges for antimicrobial applications", International Journal of Molecular Sciences **23**, 7084 (2022).

[261] M. Schwartz, "The adsorption of coliphage lambda to its host: effect of variations in the surface density of receptor and in phage-receptor affinity", Journal of molecular biology **103**, 521 (1976).

[262] Z. J. Storms and D. Sauvageau, "Modeling tailed bacteriophage adsorption: Insight into mechanisms", Virology **485**, 355 (2015).

[263] A. Logg and G. N. Wells, "DOLFIN: Automated finite element computing", ACM Transactions on Mathematical Software (TOMS) **37**, 1 (2010).

[264] H.-W. Ackermann and H. Krisch, "A catalogue of T4-type bacteriophages", Archives of virology **142**, 2329 (1997).

[265] E. T. Barr, M. Harman, P. McMinn, M. Shahbaz, and S. Yoo, "The Oracle Problem in Software Testing: A Survey", IEEE Transactions on Software Engineering **41**, 507 (2015).

[266] A. Andino and I. Hanning, "Salmonella enterica: survival, colonization, and virulence differences among serovars", The Scientific World Journal **2015** (2015).

[267] M. von Smoluchowski, "Versuch einer mathematischen Theorie der Koagulationskinetik kolloider Lösungen", Zeitschrift für physikalische Chemie **92**, 129 (1918).

[268] E. Rothenberg, L. A. Sepúlveda, S. O. Skinner, L. Zeng, P. R. Selvin, and I. Golding, "Single-virus tracking reveals a spatial receptor-dependent search mechanism", Biophysical journal **100**, 2875 (2011).

[269] T. L. Min, P. J. Mears, L. M. Chubiz, C. V. Rao, I. Golding, and Y. R. Chemla, "High-resolution, long-term characterization of bacterial motility using optical tweezers", Nature methods **6**, 831 (2009).

[270] K. D. Seed, "Battling phages: how bacteria defend against viral attack", PLoS pathogens **11**, e1004847 (2015).

[271] J. Bastos-Arrieta, A. Revilla-Guarinos, W. E. Uspal, and J. Simmchen, "Bacterial Biohybrid Microswimmers", Frontiers in Robotics and AI **5**, `10.3389/frobt.2018.00097` (2018).

[272] S. Tovey, D. Zimmer, C. Lohrmann, T. Merkt, S. Koppenhoefer, V.-L. Heuthe, C. Bechinger, and C. Holm, "Environ-

mental effects on emergent strategy in micro-scale multi-agent reinforcement learning", 2023, arXiv:2307.00994 [physics.bio-ph].

[273] T. Mo, L. Zeng, Z. Wang, S. Kondrat, and G. Feng, "Symmetrizing cathode-anode response to speed up charging of nanoporous supercapacitors", Green Energy & Environment **7**, 95 (2022).

[274] B. Hartl, M. Hübl, G. Kahl, and A. Zöttl, "Microswimmers learning chemotaxis with genetic algorithms", Proceedings of the National Academy of Sciences **118**, e2019683118 (2021).

[275] S. Muiños-Landin, A. Fischer, V. Holubec, and F. Cichos, "Reinforcement learning with artificial microswimmers", Science Robotics **6**, eabd9285 (2021).

[276] R. S. Sutton and A. G. Barto, *Reinforcement Learning: An Introduction*, Second (The MIT Press, 2018).

[277] K. Arulkumaran, M. P. Deisenroth, M. Brundage, and A. A. Bharath, "Deep Reinforcement Learning: A Brief Survey", IEEE Signal Processing Magazine **34**, 26 (2017).

[278] A. G. Barto, R. S. Sutton, and C. W. Anderson, "Neuronlike adaptive elements that can solve difficult learning control problems", IEEE Transactions on Systems, Man, and Cybernetics **SMC-13**, 834 (1983).

[279] I. Grondman, L. Busoniu, G. A. D. Lopes, and R. Babuska, "A Survey of Actor-Critic Reinforcement Learning: Stan-

dard and Natural Policy Gradients", IEEE Transactions on Systems, Man, and Cybernetics, Part C (Applications and Reviews) **42**, 1291 (2012).

[280] R. S. Sutton, D. McAllester, S. Singh, and Y. Mansour, "Policy Gradient Methods for Reinforcement Learning with Function Approximation", in Advances in Neural Information Processing Systems, Vol. 12, edited by S. Solla, T. Leen, and K. Müller (1999).

[281] J. Schulman, F. Wolski, P. Dhariwal, A. Radford, and O. Klimov, "Proximal Policy Optimization Algorithms", 2017, arXiv:1707.06347 [cs.LG].

[282] S. Gronauer and K. Diepold, "Multi-agent deep reinforcement learning: a survey", Artificial Intelligence Review **55**, 895 (2022).

[283] F. A. Oliehoek, C. Amato, *et al.*, *A concise introduction to decentralized POMDPs*, Vol. 1 (Springer, 2016).

[284] J. Bradbury, R. Frostig, P. Hawkins, M. J. Johnson, C. Leary, D. Maclaurin, G. Necula, A. Paszke, J. VanderPlas, S. Wanderman-Milne, and Q. Zhang, "JAX: composable transformations of Python+NumPy programs", version 0.3.13, 2018.

[285] J. Heek, A. Levskaya, A. Oliver, M. Ritter, B. Rondepierre, A. Steiner, and M. van Zee, "Flax: A neural network library and ecosystem for JAX", version 0.6.9, 2023.

[286] M. Musy, G. Jacquenot, G. Dalmasso, J. Lee, R. de Bruin, J. Soltwedel, M. Tulldahl, Z.-Q. Zhou, RobinEnjalbert, A. Pollack, B. Hacha, F. Claudi, C. Badger, X. Lu, A. Sol, A. Yershov, B. Sullivan, B. Lerner, D. Hrisca, D. Volpatto, Evan, F. Matzkin, JohnsWor, mkerrinrapid, N. Schlömer, RichardScottOZ, and O. Schneider, "marcomusy/vedo: 2023.5.0", version v2023.5.0, 2023.

[287] D. P. Kingma and J. Ba, "Adam: A Method for Stochastic Optimization", 2017, arXiv:1412.6980 [cs.LG].

[288] A. G. Murray and G. A. Jackson, "Viral dynamics: a model of the effects of size, shape, motion and abundance of single-celled planktonic organisms and other particles", Marine Ecology Progress Series **89**, 103 (1992).

[289] A. Bren and M. Eisenbach, "How signals are heard during bacterial chemotaxis: protein-protein interactions in sensory signal propagation", en, J Bacteriol **182**, 6865 (2000).

[290] L. van der Maaten and G. Hinton, "Visualizing Data using t-SNE", Journal of Machine Learning Research **9**, 2579 (2008).

[291] F. Pedregosa, G. Varoquaux, A. Gramfort, V. Michel, B. Thirion, O. Grisel, M. Blondel, P. Prettenhofer, R. Weiss, V. Dubourg, J. Vanderplas, A. Passos, D. Cournapeau, M. Brucher, M. Perrot, and E. Duchesnay, "Scikit-learn: Machine Learning in Python", Journal of Machine Learning Research **12**, 2825 (2011).

[292] S. Lloyd, "Least squares quantization in PCM", IEEE Transactions on Information Theory **28**, 129 (1982).

[293] C. Grandclément, M. Tannières, S. Moréra, Y. Dessaux, and D. Faure, "Quorum quenching: role in nature and applied developments", FEMS Microbiology Reviews **40**, 86 (2015).

[294] R. García-Contreras, L. Nuñez-López, R. Jasso-Chávez, B. W. Kwan, J. A. Belmont, A. Rangel-Vega, T. Maeda, and T. K. Wood, "Quorum sensing enhancement of the stress response promotes resistance to quorum quenching and prevents social cheating", en, ISME J **9**, 115 (2014).

[295] A. Kitao and H. Hata, "Molecular dynamics simulation of bacterial flagella", Biophysical reviews **10**, 617 (2018).

[296] W. Lee, Y. Kim, C. S. Peskin, and S. Lim, "A novel computational approach to simulate microswimmers propelled by bacterial flagella", Physics of Fluids **33** (2021).

[297] J. Hu, M. Yang, G. Gompper, and R. G. Winkler, "Modelling the mechanics and hydrodynamics of swimming E. coli", Soft matter **11**, 7867 (2015).

[298] N. Watari and R. G. Larson, "The hydrodynamics of a run-and-tumble bacterium propelled by polymorphic helical flagella", Biophysical journal **98**, 12 (2010).